ASDEX CONTRIBUTIONS TO THE 14th EUROPEAN CONFERENCE ON CONTROLLED FUSION AND PLASMA PHYSICS

(Madrid, June 22 - 26, 1987)

IPP III/120 June 1987

MAX-PLANCK-INSTITUT FÜR PLASMAPHYSIK

8046 GARCHING BEI MÜNCHEN

MAX-PLANCK-INSTITUT FÜR PLASMAPHYSIK

GARCHING BEI MÜNCHEN

ASDEX CONTRIBUTIONS TO THE 14th EUROPEAN CONFERENCE ON CONTROLLED FUSION AND PLASMA PHYSICS

(Madrid, June 22 - 26, 1987)

IPP III/120 June 1987

Die nachstehende Arbeit wurde im Rahmen des Vertrages zwischen dem Max-Planck-Institut für Plasmaphysik und der Europäischen Atomgemeinschaft über die Zusammenarbeit auf dem Gebiete der Plasmaphysik durchgeführt.

ASDEX CONTRIBUTIONS TO THE 14th EUROPEAN CONFERENCE ON CONTROLLED FUSION AND PLASMA PHYSICS

(Madrid, June 22 - 26, 1987)

Pellet Injection with Improved Confinement in ASDEX

V. Mertens, M. Kaufmann, K. Büchl, G. Fussmann, O. Gehre, K. Graßie, O. Gruber, G. Haas, G. Janeschitz, M. Kornherr, K. Lackner, R.S. Lang, K.F. Mast, K. McCormick, J. Neuhauser, H. Niedermeyer, W. Sandmann, D. Zasche, H.P. Zehrfeld

Max-Planck Institut für Plasmaphysik, EURATOM Association
D-8046 Garching, Fed. Rep. of Germany

Z.A. Pietrzyk, University of Washington, Seattle, Wash., USA

Introduction :

An intensive campaign to study the consequences of repetitive pellet injection was carried out on ASDEX. It was possible to improve by pellet injection considerably the plasma confinement compared to earlier investigations /1/. In addition we could advance considerably the understanding of the relevant mechanisms. The dominant difference between the earlier and the recent experiments was different recycling in the plasma boundary and the divertor. While the earlier campaign aimed at low-recycling pellet injection (LRP) to study the genuine pellet fuelling, the second campaign aimed at an improvement of the density limit.

Experimental parameter :

The investigation concentrated on ohmically heated doulble null discharges in deuterium but discharges with additional neutral beam heating are considered as well. The ASDEX device was run typically at $B_t = 2.2$ tesla, $I_p = 380$ kA, $q_a = 2.7$. The density range was extended from $\overline{n_e} = 0.1 \times 10^{20}$ m^{-3} to $\overline{n_e} = 1.2 \times 10^{20}$ m^{-3}. The pellets with about 4.5×10^{19} deuterium atoms each were accelerated by a centrifuge to a velocity of 620 $\frac{\text{m}}{\text{s}}$ /2/ and yield penetration depths of roughly half the plasma radius. Normally up to 20 pellets were injected with a repetition rate of 30 ms. In typical cases of good confinement ASDEX was carbonized.

In a first campaign discharges were performed to demonstrate the potential of very low recycling at the plasma boundary by combining divertor operation and pellet fuelling. The pellet injection started at low density. Only a poor density build-up could be attained under these conditions. Figure 1 shows the successful density build-up in a typical high-recycling pellet injection (HRP) discharge beyond the gas puff (GP) density limit. The flat electron density profile starts to peak strongly with pellet injection whereas the temperature drops somewhat but the profile stays nearly self-similar.

The increase of the energy content and the improvement of the averaged energy confinement time is clearly seen in fig. 1; $\tau_E = 1.9 \times W_e/(P_{OH} - 1.9\dot{W}_e)$. W_e : energy content of the electrons; P_{OH} : ohmic heating power without correction for radiation.

In the pure GP phase the radiation profile is strongly peaked at the edge. During and after pellet injection when sawtooth activity is reduced the central radiation increases exponentially to a value comparable to the local power input without indication of saturation. Spectroscopic observation indicates Fe and/or Ti to be responsible for the rise of central radiation. Often nearly stationary density phases up to 230 ms duration could be observed after the last pellet. This phase is characterized by a very peaked pressure profile coinciding with a relatively flat temperature profile. The final breakdown seems therefore correlated to a violation of the ballooning criterion in the plasma centre. HRP discharges with neutral beam injection below $\sim$ 1 MW behave like ohmically heated discharges. The unsuccessful density build-up at higher neutral injection power seems to be correlated with a more peaked electron temperature profile and a specific MHD-activity triggered by the pellet.

Improved energy confinement with pellet injection was always correlated to a successful density build-up. The improvement of τ_E in HRP discharges compared to standard ohmically heated GP discharges by about a factor of 2 is demonstrated in fig. 2. The increase of τ_E starts with the first pellet and the enhancement lasts for times long compared with τ_E . The data may suggest that the pellets remove the reason for the τ_E roll-over because the peaked density profile in HRP discharges seems to establish a new type of discharge. This improvement of τ_E might be explained either by a local heat transport model or the profile consistency model of Furth /3/.

Discharges with proper edge conditioning (HRP) show distinct changes in bulk plasma particle transport with pellet injection. The observed peaking of the density profile can not be attributed to central deposition of pellets because the penetration depth is approximately half the minor radius and the peaking lasts up to 230 ms after the last pellet. Assuming that the particle transport i.e. the electron flux Γ may be interpreted by a diffusive and convective driving term with a diffusion coefficient D and an inward velocity V,

$$\Gamma(r) = -D(r) \times n'(r) - V(r) \times n(r),$$

nearly stationary phases are analyzed neglecting particle sources. Figure 3 shows typical electron density profiles and deduced ratios $\frac{V}{D}$ before and after pellet injection. In the inner two-thirds of the minor radius $\frac{V}{D}$ has increased by a factor of about 3 or more demonstrating the change in particle transport. During density build-up the following transport coefficients fit the observed electron flux in the inner region :

$$D(r) = 0.1 \text{ m}^2/\text{s} \quad \text{and} \quad V(r) = 1 \times \frac{r}{a} \text{ m/s}$$

(a: minor radius)

Reduced sawtooth activity and the correlated decreased outward flow of particles during a sawtooth disruption - compared to GP discharges - seems also to be a condition for the profile peaking. GP discharges without sawteeth show a similar peaking /4/. A macroscopic vertical electric field of the order of 10 V/m might explain an enlarged inward velocity. Calculation of the neoclassical current profiles show a small but significant increase of q on axis which reflects the increase of the collisionality with pellet injection.

In typical GP discharges there is a strict relation between the bulk plasma density and the edge density $n_s = 0.3 \times \overline{n_e}$. n_s is the density at the separatrix and $\overline{n_e}$ is the line-averaged bulk density /5/. The relative exponential density decay length in the scrape-off layer is practically independent of $\overline{n_e}$. In LRP discharges the particle density in the boundary exhibits large variation during pellet injection because the divertor walls are far from saturation and the neutral flux density in the divertor is low. This lack of saturation leads to a continuous outflow of the injected particles as seen in fig. 4a . In HRP discharges the high neutral flux density prevent loss of particles. The edge density stays nearly constant during the build-up of bulk density (fig. 4b) and the very small modulation of the edge density during pellet cycle indicate that the particle density in the boundary seems to be in equilibrium with the bulk density and the recycling. While the edge density behaviour is similar to GP discharges the ratio $n_s/\overline{n_e}$ decreases from its standard GP value consistent with the peaking of the bulk profile.

References :

/1/ G. Vlases et al, Proc. 12th Europ. Conf. on Contr. Fusion and Plasma Physics, Budapest 1985, 1 (1985) 78

/2/ W. Amenda, R.S. Lang, Proc. 13th Symp. on Fusion Technology, Varese 1984, 243

/3/ M. Kaufmann et al, Nucl. Fusion, to be published

/4/ F. Wagner et al, Proc. Invited Papers, 13th European Conf. on Contr. Fusion and Plasma Heating, Schliersee 1986, vol 28 9A, 1225

/5/ K. McCormick et al, J. Nucl. Mater., 145-147 (1987), 215

Figure Captions :

1 : The electron particle content N_e and the energy content W_e are shown together with the global energy confinement time τ_E as function of time. The density and temperature profile development can be seen from the $\frac{n_e(0)}{\overline{n_e}}$ and the $\frac{T_e(0)}{T_e(a/2)}$ traces.

2 : Energy confinement time τ_E as function of the line averaged density $\overline{n_e}$ for LRP, HRP and standard ASDEX GP discharges. All discharges are with ohmic heating only.

3 : The ratio of the inward drift velocity to the particle diffusion coefficient $\frac{V}{D} = \frac{n_e'}{n_e}$ together with density profiles (*dotted lines*) is given before (a) and after pellet injection (b).

4 : Electron density profiles at the plasma boundary for LRP (a) and HRP (b) discharges. In case (a) one pellet cycle is shown. The profile steepens by the pellet and flattens afterwords again. R_S : radius of the separatrix, t_p : pellet injection time.

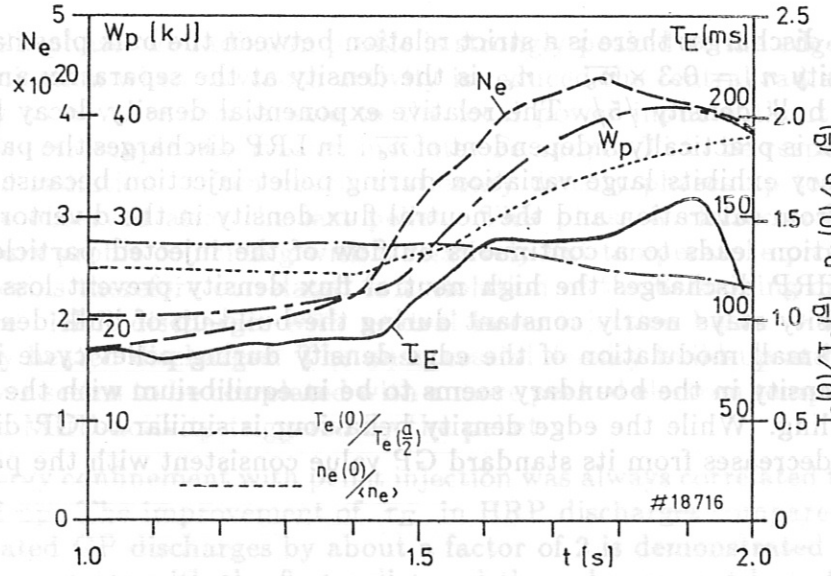

Fig. 1

Fig. 2

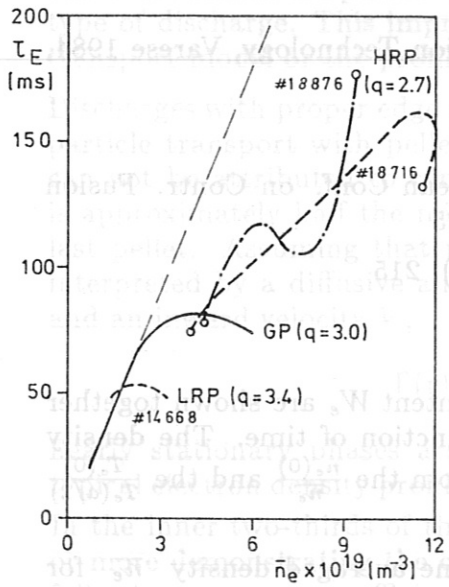

Fig. 3

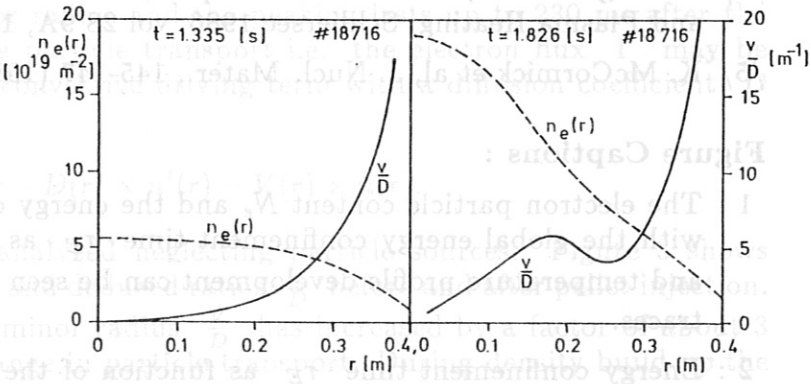

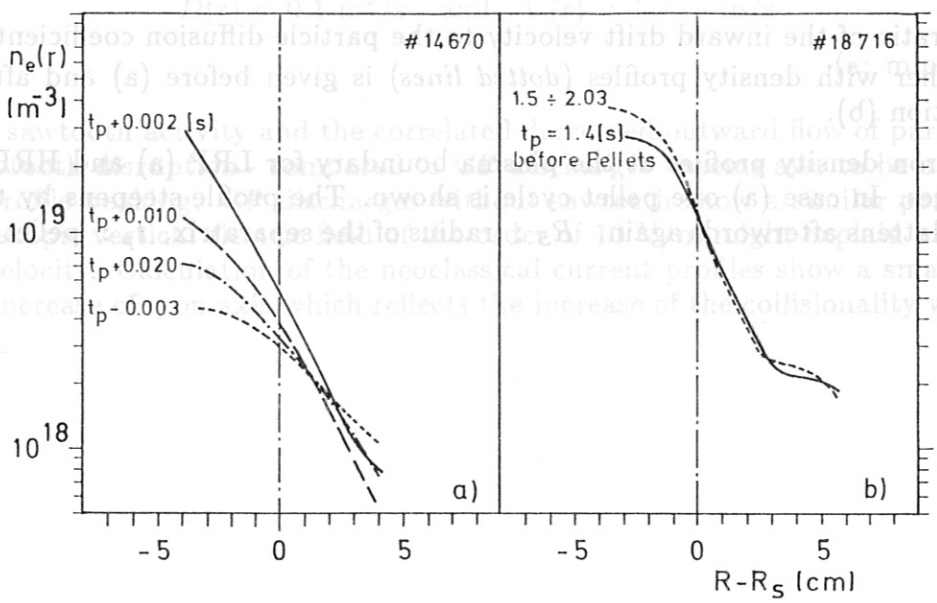

Fig. 4

RADIATION BEHAVIOUR OF GAS AND PELLET REFUELLED HIGH DENSITY DISCHARGES IN ASDEX

K.F. Mast, E.R. Müller, H.U. Fahrbach, H. Krause, R.S. Lang, P. McCarthy, W. Sandmann, D. Zasche, G. Becker H.B. Bosch, H. Brocken, A. Carlson, A. Eberhagen, G. Dodel[1] G. Fußmann, O. Gehre, J. Gernhardt, G. v.Gierke, E. Glock, O. Gruber, G. Haas, W. Herrmann, J. Hofmann, A. Izvozchikov[2], E. Holzhauer[1], K. Hübner[3], G. Janeschitz, F. Karger, M. Kaufmann, O. Klüber, M. Kornherr, K. Lackner, M. Lenoci, G. Lisitano, H.M. Mayer, K. McCormick, D. Meisel, V. Mertens, H. Murmann, J. Neuhauser, H. Niedermeyer, A. Pietrzyk[4], W. Poschenrieder, H. Rapp, A. Rudyj, F. Schneider, C. Setzensack, G. Siller, E. Speth, F. Söldner, K. Steinmetz, K.-H. Steuer, S. Ugniewski[5], O. Vollmer, F. Wagner

Max-Planck Institut für Plasmaphysik, Garching bei München, W. Germany
[1]University of Stuttgart, [2]Ioffe Institute, [3]University of Heidelberg,
[4]University of Washington, Seattle, USA, [5]Inst. for Nuclear Research, Swierk, Poland

Abstract. Pellet and gas refuelled high density divertor discharges in ASDEX are investigated with regard to their radiation behaviour and energy balance. Exclusively ohmically heated deuterium plasmas in a non-carbonized (NC), carbonized (C) and titanium gettered (DP) vacuum vessel are considered. In gas refuelled plasmas the radiation power profiles are hollow with a central emissivity $\epsilon(0) \leq 10\mathrm{mW/cm^3}$ in C and $\epsilon(0) \leq 40\mathrm{mW/cm^3}$ in NC and DP discharges. In C discharges P_{RAD}/P_Ω rises from 0.2 at $\bar{n}_e = 3.2 \cdot 10^{19} m^{-3}$ to 0.3 at the density limit. In NC and DP plasmas higher values from 0.3 to 0.45 are observed. Radiation from the X-points can amount to 14 % of P_Ω. In pellet refuelled discharges a central peaking of the emissivity ϵ is observed. A sudden transition from negligible or slow impurity accumulation to a fast rise could be detected in many discharges. In NC and DP pellet discharges a self-triggering of impurity accumulation was found. Measured inward drift velocities range from 60 cm/s to 130 cm/s at r=15 cm.

1. Global radiation behaviour and energy balance. This paper mainly deals with parametric studies of the total plasma radiation with a particular emphasis on X-point radiation from gas and pellet refuelled high density discharges in ASDEX. Three radiation zones are discernible with the bolometric diagnostics. The main plasma including the scrape-off layer, the regions around the two X-points and the divertor plasma [1].

Total X-point and main plasma radiation can be separated from two independent measurements of the total radiation in the main plasma chamber. Firstly with the wide-angle bolometers and secondly with the bolometer array both taking into account the X-point radiation with various weighting factors. Radial profiles of emissivity are derived by standard Abel-inversion technique.

Ohmically heated pellet and gas refuelled high density divertor discharges in deuterium are investigated with regard to their radiation behaviour and energy balance during current flattop. Carbonized (C), non-carbonized (NC) and titanium gettered (DP) discharges with safety factors q_a between 2.7 and 2.9 and plasma currents between 300 KA and 380 KA are considered here.

In gas refuelled discharges dW_p/dt the time derivative of stored plasma energy Wp is negligible small whereas during pellet injection dW_p/dt amounts up to 20 % of P_Ω and has to be taken into account in the power balance. The normalized total radiation of the main plasma $P_{RN} = P_{RAD}/(P_\Omega - \frac{dW_p}{dt})$ as a function of the line averaged electron density $\bar{n}_e$ during various gas refuelled discharges is shown in Fig. 1a.

In carbonized plasmas P_{RN} amounts to 0.2 at $\bar{n}_e = 3.5 \cdot 10^{19} m^{-3}$. NC and DP plasmas radiate about 0.35 at $\bar{n}_e = 3.5 \cdot 10^{19} m^{-3}$ owing to a higher content of metals, mainly of iron. At higher densities near the density limit gas refuelled discharges with $q_a > 2.7$ (no sharp limit was detected) show a nonlinear increase of P_{RN} with rising $\bar{n}_e$. This behaviour can be attributed mainly to a decrease of the electron temperature near the separatrix due to enhanced recycling losses and line radiation of low-Z impurities (C_{III}-lines). A correlation between edge peaking of radiation power profiles (carbonized and gettered plasmas) and nonlinear behaviour of P_{RN} with $\bar{n}_e$ can be deduced from Figs. 1a and 3.

The formation of a zone of enhanced radiation near the separatrix is observed just 10–20 ms before a density limit disruption occurs. Owing to an electronic integration time constant $\tau = 10ms$ the time resolution of the bolometric diagnostics is too poor to reveal details of the radiation profile evolution. This type of poloidal symmetric thermal instability which differs from the usual Marfe evolves on a longer time scale in JET due to its larger dimensions [2]. The normalized X-point radiation $P_{XN} = P_X/(P_\Omega - dW_p/dt)$ (Fig. 1b) enhances with increasing $\bar{n}_e$ similar as P_{RN} does. Maximum values of P_{XN}=0.14 are obtained and have to be considered in the energy balance. A titanium gettered discharge (#19514) serves as an example for a low $q_a = 2.1$ high density plasma. P_{RN} remains nearly constant until the density limit is reached and P_{XN} increases linearly with $\bar{n}_e$. The formation of a zone of enhanced edge radiation could not be detected.

In ASDEX a considerable increase of the line average density $\bar{n}_e$ and of the Murakami parameter $\bar{n}_e R/B_T$ was achieved by injecting series of deuterium pellets with a centrifuge [3,7]. We consider here only discharges with high central peaking of the density profiles during pellet injection.

A nonlinear enhancement of P_{RN} with rising $\bar{n}_e$ is observed in pellet refuelled (C, NC and DP) discharges qualitatively similar to gas refuelled plasmas. Starting from values characteristic to gas refuelled plasmas P_{RN} continuously rises until about 0.45

at the density limit (Fig. 2a). The relative increase of P_{RN} is highest in C discharges in contrast to gas refuelled discharges. Central peaking of the electron density and radiation power profile in pellet discharges is responsible for this behaviour. P_{XN} decreases with increasing $\bar{n}_e$ (Fig. 2b) owing to the high central radiation which reduces the power outflux in the scrape-off layer.

A correction of P_{RN} with the total radiation inside the inner half minor radius $P_{RAD}(a/2)$ yields nearly no variation of the corrected P_{XN} with $\bar{n}_e$. Near the density limit P_{XN} is usually smaller in pellet discharges than in gas refuelled discharges.

In pellet and gas refuelled discharges the normalized divertor radiation $P_{DN} = P_{DIV}/(P_\Omega - dW_p/dt)$ rises with $\bar{n}_e$ up to $\bar{n}_e \approx 5.5 \cdot 10^{19} m^{-3}$. Above $\bar{n}_e = 5.5 \cdot 10^{19} m^{-3}$ P_{DN} saturates which indicates the achievement of a high recycling regime in the divertor [1]. Near the density limit P_{DN} continuously decreases with $\bar{n}_e$ owing to the steady increase of the radiation in the main plasma P_{RN} and, thus, decreasing heat flux into the divertor.

The energy confinement time $\tau_E = W_p/(P_\Omega - dW_p/dt)$ shows a similar behaviour as P_{DN} near the density limit. The plasma energy W_p is derived from the diamagnetic signal, from kinetic data (twice the energy content of electrons) and from the equilibrium beta. Li is derived from the electron temerature profiles assuming neoclassical resistivity and neglecting diffusion of the poloidal magnetic field. All three energies agree better than within 10% and indicate the same trend with $\bar{n}_e$. The power on the divertor plates P_{cond} is measured with the thermographic diagnostics. Only a small fraction of the heating power is deposited on the divertor plates. The normalized power on the divertor plates $P_{CN} = P_{cond}/(P_\Omega - dW_p/dt)$ is smaller than 0.1 and reduces further near the density limit (Fig. 4). We conclude: a nonlinear rise of P_{RN} with $\bar{n}_e$ is observed in both gas and pellet refuelled C, NC and DP discharges with maximum values of $P_{RN} \approx 0.45$ at the density limit. X-point radiation plays an important role in the energy balance ($P_{XN} \leq 0.14$). Gas and pellet discharges show a different behaviour of P_{XN} with $\bar{n}_e$.

2. Profiles and impurity transport. The signal rise of the central channels of the bolometer camera originates either from a Marfe which is a low tempertaure thermal instability located at the plasma boundary [4] or from enhanced radiation from the plasma centre. A Marfe is accompanied by a strong increase of the line intensities from low ionization stages of low Z impurities, e.g. CIII lines ($T_e \approx 10eV$). In contrast radiation peaking at the plasma centre is indicated by a simultaneous rise of intensity of central soft X-ray channels and of Fe XVI lines. Considering spectroscopic, soft X-ray and bolometer signals we can separate Marfes from radiation peaking at the plasma centre.

Normalization of the radiation emitted from the outer half of the minor plasma radius to the total radiation P_{RAD} yields a quantitative parameter indicating the profile shape (Fig. 3). All gas refuelled discharges (with sawtooth activity during current flattop) show edge peaked radiation profiles. The central radiation power density in C discharges is less than $10mW/cm^3$ and in NC and DP discharges it is somewhat higher $\leq 40mW/cm^3$ but still negligible related to the central ohmic heating power $P_\Omega(0) \approx 200mW/cm^3$.

In low $q(q_a \leq 3)$ pellet discharges the central peaking of the density and the radiation power profile is correlated. During a typical discharge there is first a phase of negligible or slow impurity accumulation, which may suddenly turn into a fast accumulation at the plasma core. Three different scenarios for this transition are experimentally observed: a) one pellet is missing during a series of pellets (Fig. 5), b) after pellet injection if no density limit disruption occurs, c) in NC and DP discharges the q on axis may considerably rise above 1.0 owing to a pronounced flattening of the T_e-profile with rising central radiation power density (Fig. 6). A self-triggering of accumulation occurs then if $P_{RAD}(0)/P_\Omega(0) \geq 1$ (see also [6]).

Case a) is demonstrated in Fig. 5 for a discharge with density feed back. From t=1.5s until t=2.1s the T_e- and n_e-profiles remain nearly unchanged with a small rise of $n_e(0)(\leq 20\%)$. Strong sawtooth activity is observed during pellet injection which obviously prevents an accumulation of impurities averaged over a pellet cycle. After a last sawtooth possibly triggered by the pellet at t=1.89s a fast accumulation starts inside a minor radius r=10cm (Fig. 7). One finds from the chord-intensity profile in Fig. 7 a transport of impurities from the outer plasma regions $r > 10cm$ to the plasma core. It seems that the impurity accumulation is immediately stopped by the next pellet (Figs. 5,5a). A neoclassical theory [5] predicts from $\frac{dp_i}{dr}$ an inward drift velocity $v_D = 100cm/s$ at r=15 cm. At this position the maximum gradient of the pressure profile of plasma ions is observed. An inward drift velocity of $v_D = 65cm/s$ at r=15 cm is derived for case a) [5] which is in good agreement with theory. One can speculate that pellets change the outward transport of impurities by triggering sawteeth resulting in a higher cycle averaged diffusion coefficient. More details are given in [5].

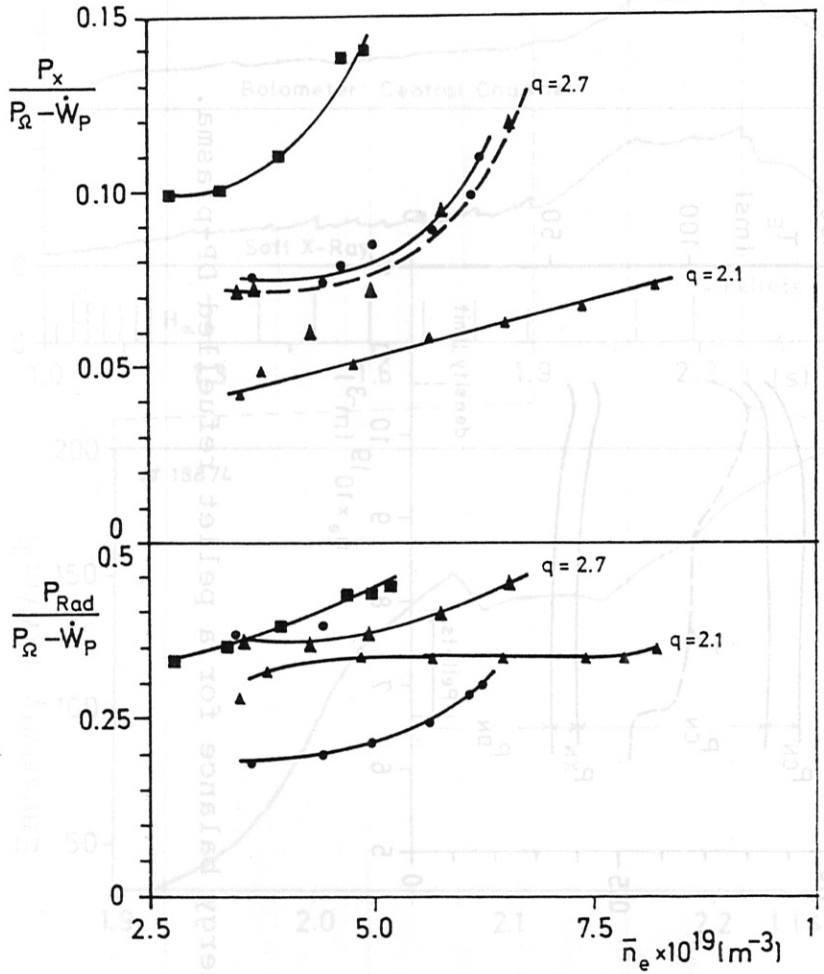

Fig. 1a,1b: Gas-refuelled

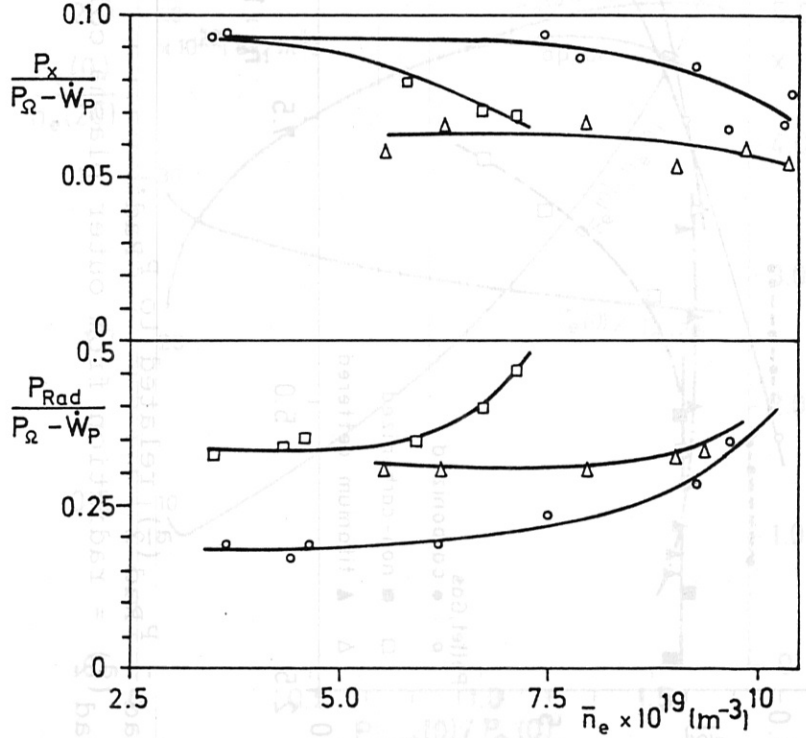

Fig. 2a,2b: Pellet-refuelled

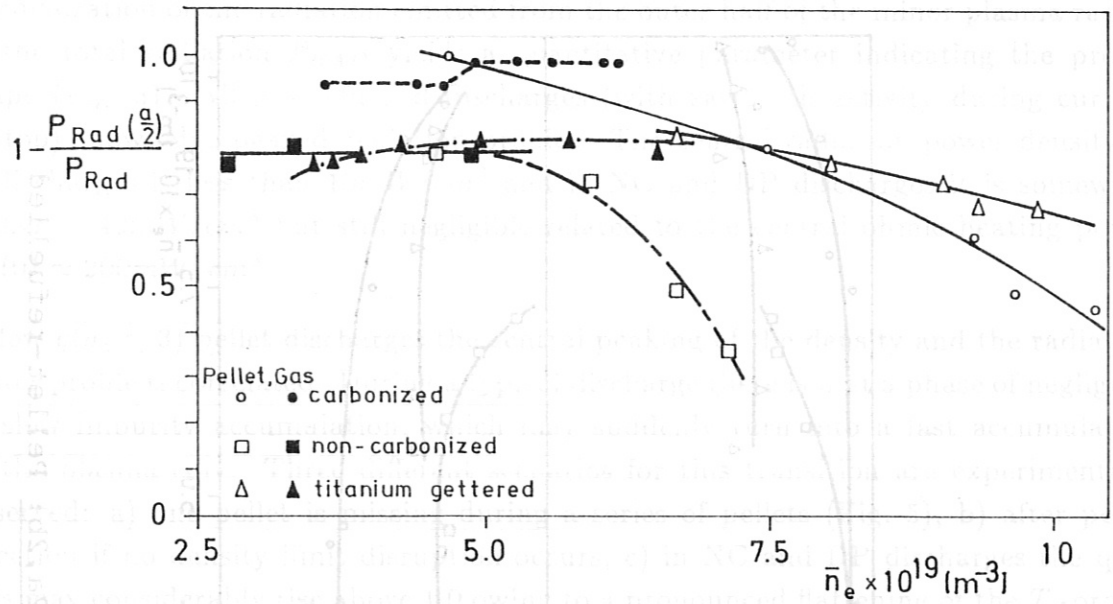

Fig. 3: $P_{Rad} - P_{Rad}(\frac{a}{2})$ related to P_{Rad}.
$P_{Rad}(\frac{a}{2})$ = radiation from outer plasma column $\frac{a}{2} \leqslant r \leqslant a$

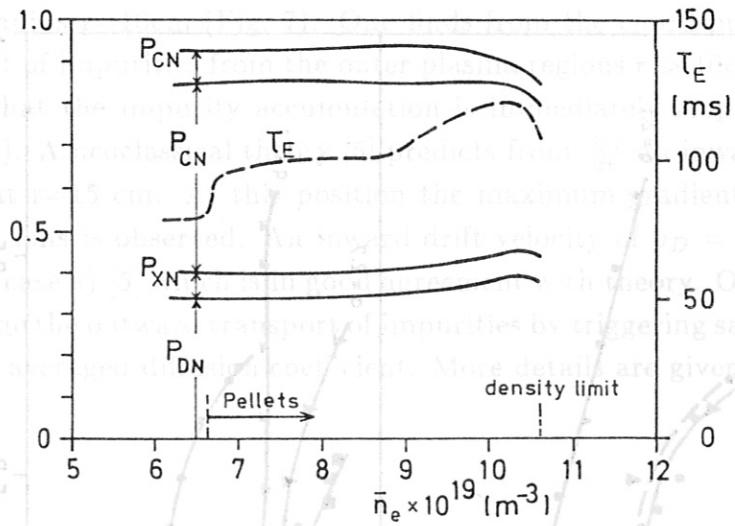

Fig. 4: Energy balance for a pellet refuelled DP-plasma.

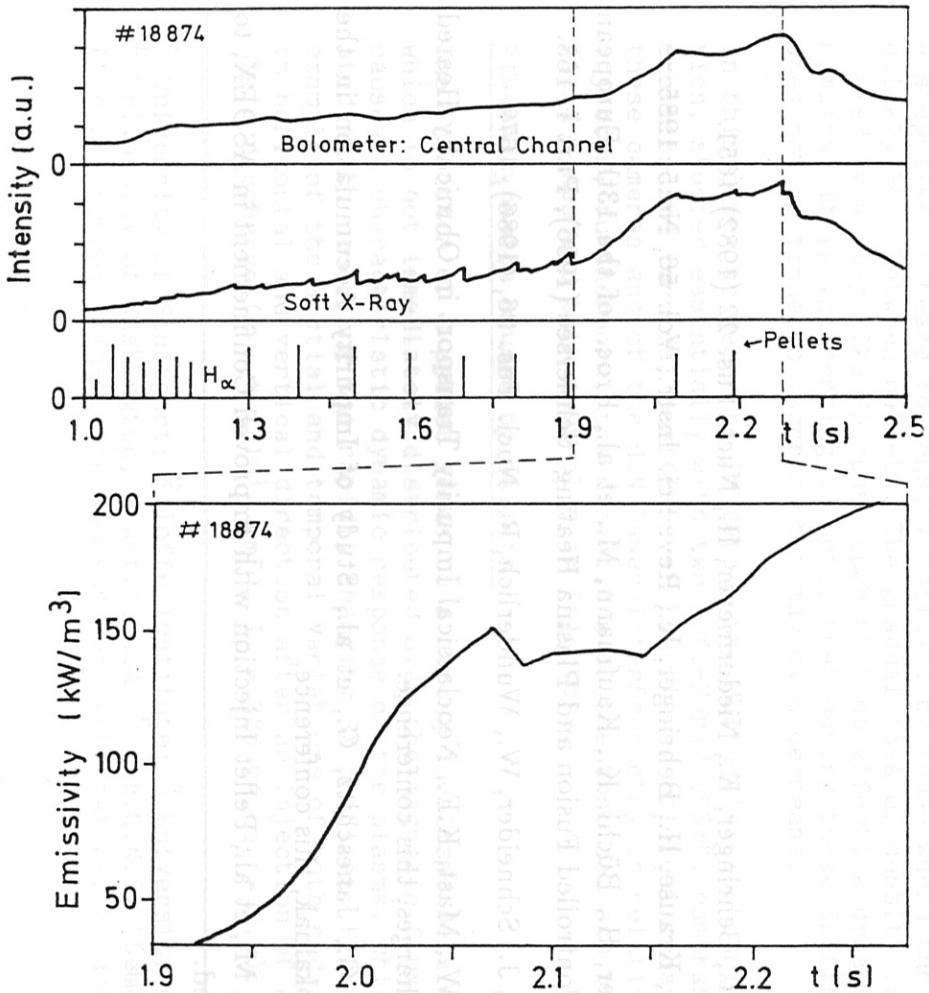

Fig: 5,5a:

Evolution of radiation power density on plasma axis.

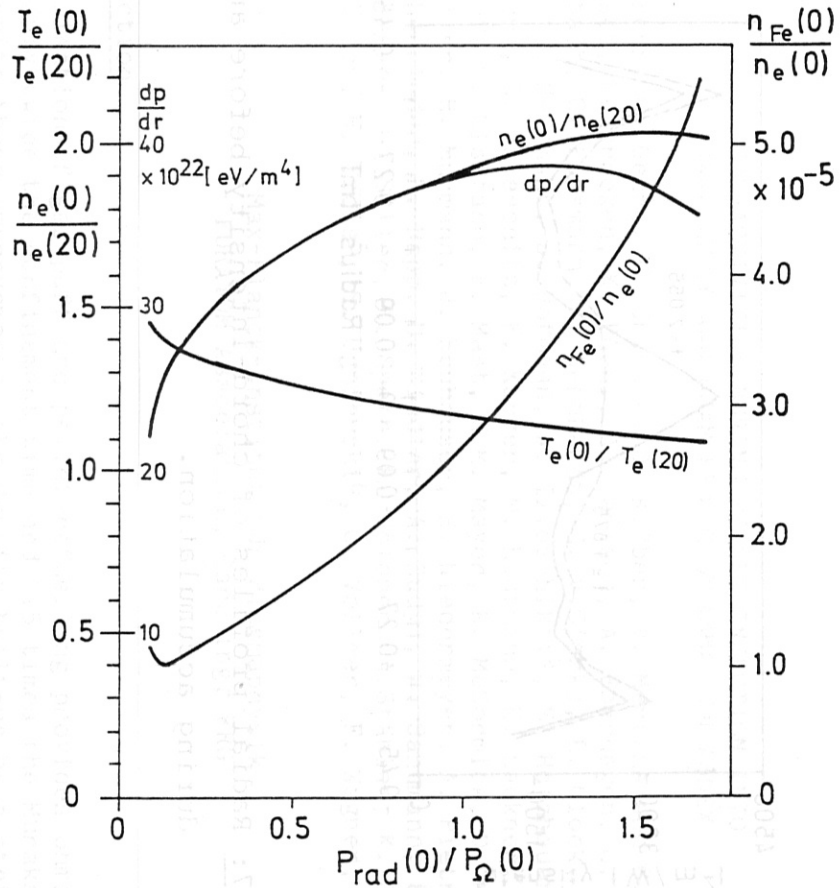

Fig. 6:

Effect of $P_{Rad}(0)/P_\Omega(0)$ on profile shape and impurity accumulation
$T_e(20) = T_e$ and $n_e(20) = n_e$ at r = 20 cm.

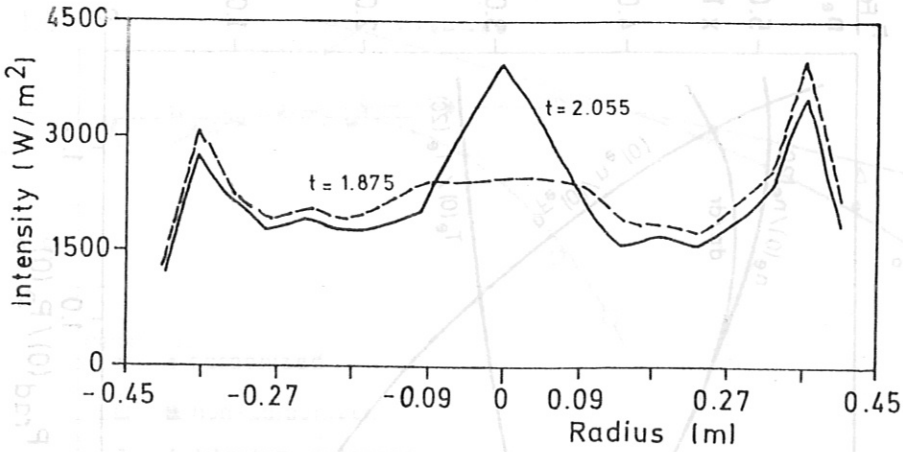

Fig. 7: Radial profiles of chord-intensity before and during accumulation.

References

/1/ Müller, E.R., Behringer, K., Niedermeyer, H., Nucl. Fus. 22 (1982) 1651.

/2/ Mast, K.F., Krause, H., Behringer, K., Rev. Sci. Instr., Vol. 56, No.5, 1985.

/3/ Niedermeyer, H., Büchl, K., Kaufmann, M., et al., Proc. of the 13th European Conf. on Controlled Fusion and Plasma Heating, Schliersee (1986), Part I, 168.

/4/ Neuhauser, J., Schneider, W., Wunderlich, R., Nucl. Fus. 26, (1986), 1679.

/5/ Feneberg, W., Mast, K.F., Neoclassical Impurity Transport in Ohmically Heated Pellet Discharges, this conference.

/6/ Fussmann, G., Janeschitz, G., et al., Study of Impurity Accumulation in the ASDEX Tokamak, this conference.

/7/ Kaufmann, M., et al., Pellet Injection with Improved Confinement in ASDEX, to be published.

MHD-ACTIVITIES DURING PELLET INJECTION INTO OHMICALLY AND BEAM HEATED PLASMAS ON ASDEX

M. Kornherr, O. Gehre, K. Grassie, O. Klüber, V. Mertens and G. Becker, H.S. Bosch, H. Brocken, K. Büchl, A. Carlson, A. Eberhagen, G. Dodel[1], H.-U. Fahrbach, G. Fussmann, J. Gernhardt, G. v.Gierke, E. Glock, O. Gruber, G. Haas, W. Herrmann, J. Hofmann, A. Izvozchikov[2], E. Holzhauer[1], K. Hübner[3], G. Janeschitz, F. Karger, M. Kaufmann, K. Lackner, R. Lang, M. Lenoci, G. Lisitano, F. Mast, H.M. Mayer, K. McCormick, D. Meisel, E.R. Müller, H. Murmann, J. Neuhauser, H. Niedermeyer, A. Pietrzyk[4], W. Poschenrieder, H. Rapp, H. Riedler, A. Rudyj, W. Sandmann, F. Schneider, C. Setzensack, G. Siller, E. Speth, F. Söldner, A.Stäbler, K. Steinmetz, K.-H. Steuer, N. Tsois[5], S. Ugniewski[6], O. Vollmer, F. Wagner, D. Zasche

Max-Planck-Institut für Plasmaphysik
EURATOM Association, Garching, FRG

Introduction

The combination of gas-puff and pellet refuelling provides ohmic discharges with nearly twice the confinement time and 1.5 times the Murakami limit /1/. Despite these improvements, the density built-up by a string of pellets (up to 80 pellets with maximally 700 m/s and up to 50 pellets per s) is not yet optimized. There are phases where the pellet refuelling leads to a step-like increase in density followed by those where the added mass is quickly lost between pellets. The gradual loss of density is often accompanied by a step-like decrease such that no effective density increase remains. It is interesting to note, that during these ineffective phases β does not continue to increase but may even decrease.

In this paper we describe in detail the MHD-activities during pellet injection, studied essentially with two soft-X-ray ("SX") cameras. Fig. 1 exhibits the toroidal positions of the viewed poloidal cross sections of these cameras and of the HCN-laser-interferometry in relation to the pellet injector, furthermore, the directions of the toroidal and poloidal magnetic field lines and both neutral beam injectors.

Plasma dynamics caused by pellets.

The injection of a pellet leads to a strong localized density disturbence, which is not immediately distributed over the magnetic flux surfaces, but causes a characteristic dynamic response of the plasma, which can be well studied by observing the rapidly changing SX profiles. Fig. 2 gives an example of the spatial and temporal variations of both radiation profiles in horizontal and vertical direction after an injection of a pellet into an ohmic discharge ($\bar{n} = 4 \times 10^{13}$ cm^{-3}, $I_p = 380$ kA, $q_a = 2.9$).

---

[1] University of Stuttgart; [2] Ioffe Institute; [3] University of Heidelberg; [4] University of Washington, Seattle, USA; [5] N.R.C.N.S. "Democritos", Athens, Greece; [6] Inst. for Nuclear Research, Swierk, Poland

Within a few hundred μs a poloidally strong asymmetric distribution of SX radiation develops. The measured signals of the chords crossing the outer and lower halfs of the plasma cross section decrease, while the signals of the inner and upper chords increase. This m=1 like structure rotates within the viewed cross section in direction of the poloidal magnetic field lines with a typical frequency of about 1 kHz and is damped after 2 - 10 cycles. Only the edge-localized channels (omitted in Fig. 1 and 2) show a different behaviour, namely a single positive spike due to the injected pellet.

After injection of a pellet into an ohmic discharge with reversed toroidal field and plasma current the maxima and minima of the SX signals become exchanged (cf. Fig. 3); also the direction of rotation alters and corresponds again to the direction of the poloidal field lines.

In this context the following observation from HCN-interferometry is of interest: Immediately after pellet injection the lower laser beam is deflected for both magnetic field directions. This diffraction indicates strong density gradients but in both cases within the lower plasma region, passing the HCN laser beam.

Sawtooth activity and accumulation.

The oscillatory mode described before finally leads to a new static SX profile. The integral radiation increases from pellet to pellet and the profile becomes more and more peaked. Already after a few pellets the sawtooth activity may increase and on the time scale of typically 20 msec after pellet injection one or more strong sawteeth occur. In the example of Fig. 4 strong sawteeth are observed after the third pellet, accompanied by distinct steps on the density trace.

Despite the broadening by sawteeth the density profiles remain strongly peaked in the case of pellet refuelling, which originates from an increased inward drift /2/. This enhanced drift causes also accumulation of impurities in the plasma center /3/. In this context compare also /4/.

In Fig. 5 two discharges are compared which only differ in plasma current. Smaller currents correspond to more peaked density profiles /5/. In both discharges a string of five pellets is injected and the temporal behaviour of the discharge is very similar. After the last pellet a strong sawtooth occurs. In case A strong sawteeth stop the further development of the accumulation phase and restore the original plasma parameters, in case B with smaller plasma current the sawteeth become suppressed and the enhanced inward drift leads to strong accumulation of electron density and heavy impurities in the plasma center.

Accumulation and sawtooth activity are competing processes and the temporal development of pellet refuelled ohmic discharges depends ultimately on the strenght of the two counteracting processes.

Pellet injection into NB-heated plasmas.

Up to now only preliminary results are achieved in pellet-refuelling of injection heated plasmas. In Fig. 6 we describe the history of a NBI heated plasma discharge ($\bar{n}$ = 1.4 x 10^{13} cm^{-3}, I_p = 320 kA, q_a = 3.3, power of NBI = 1.3 MW). During the initial ohmic phase we observe the typical step-like increase in density, which repeats immediately after switching off NBI; finally the transport mechanisms described before cause strong impurity accumulation resulting in a disruption.

At .6 s when two sources of the NBI-SE injector and one source of NBI-NW injector start operation, the averaged density decreases and the pellets injected thereafter effect only a small rise in density. SX radiation and density profiles change immediately after pellet injection in a way which is typical for a sawtooth event, both become flat within the central plasma region.

From 1.0 s two sources of NBI-NW and only one source of NBI-SE operate; at the same time the response of the plasma upon an injected pellet changes. First of all the pellet excites an m=1 mode of about 15 kHz near the inversion radius of SX, rotating opposite to the ion drift direction. This mode becomes completely damped after about 10 msec, but reappears once more with slightly reduced frequency and is finally terminated by a sawtooth event. At the same time we observe corresponding oscillations on Mirnov loops with m=4, n=1 structure, which is well explained by mode coupling due to geometrical effects /6/. There is no doubt, that this MHD-activity is triggered by the pellet, but it can also occur in NBI heated plasmas without pellet refuelling. SX radiation and density remain peaked up to the sawtooth event.

The broadening of the density profiles caused by the two kinds of sawtooth activity as described does not lead to an essential loss of particles. The additional mass of pellets is lost rather in a gradual way accompanied by simultaneous peaking density profiles.

References

/1/ H. Niedermeyer et al., Proc. 13th EPS, Schliersee 1986, part 1, p.168
/2/ V. Mertens et al., this conference
/3/ G. Fußmann et al., this conference
/4/ F. Mast et al., this conference
/5/ O. Gehre et al., Proc. 13th EPS, Schliersee 1986, part 1, p. 220
/6/ K. Grassie, to be published

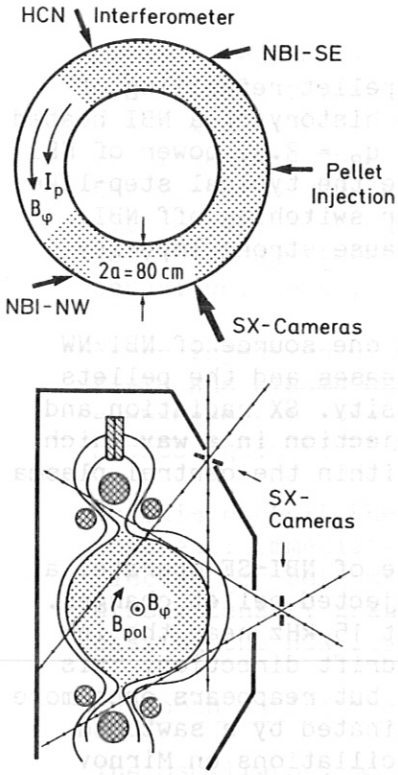

Fig.1: Schematic design of the ASDEX device.

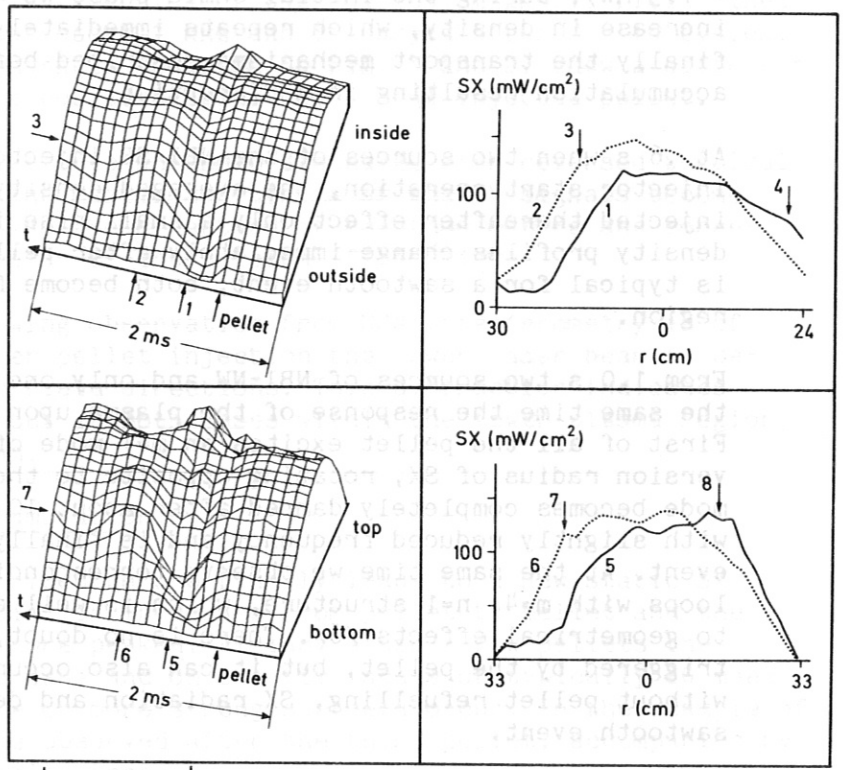

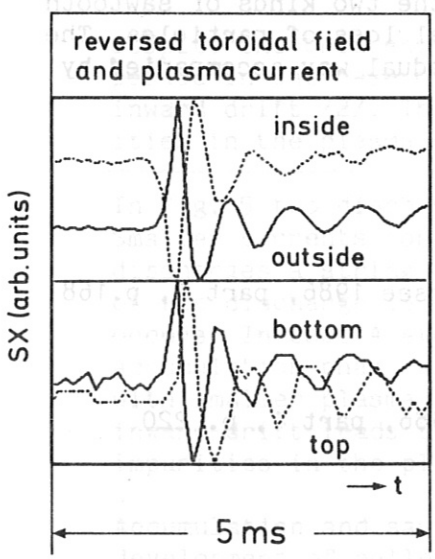

Fig.3 The temporal development of the same SX chords as shown in Fig. 2, but at reversed magnetic fields.

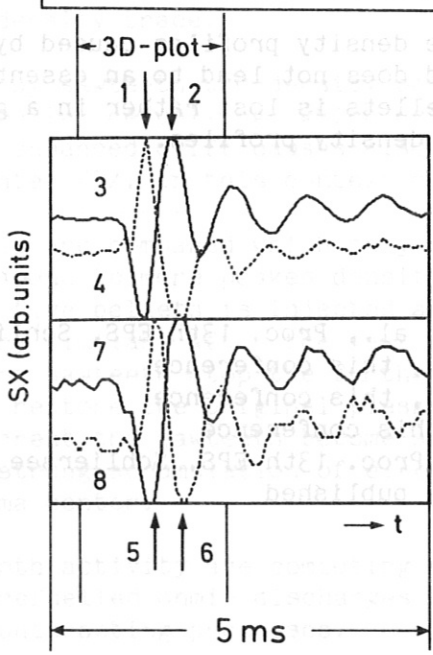

Fig.2: The spatial (above) and temporal development (left side) of SX radiation after pellet injection into an ohmic discharge. Identic numbers correspond to identic SX signals.

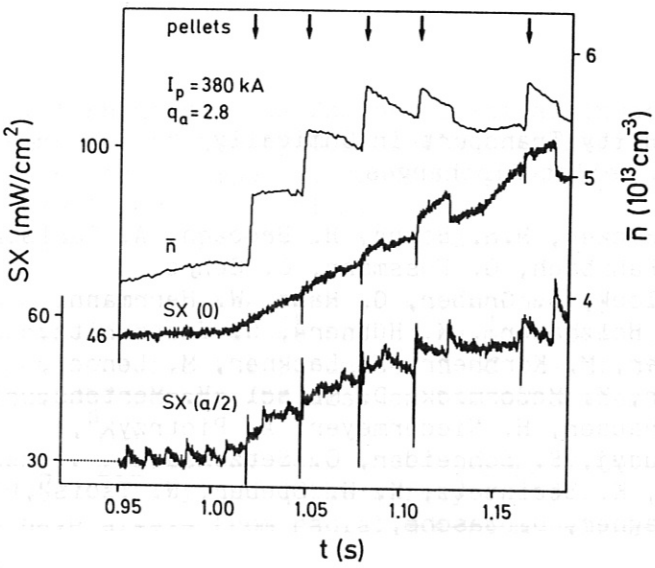

Fig.4 (above): Development of strong sawtooth activity after pellet injection.

Fig.5 (below): Comparison of two pellet refuelled ohmic discharges w/o and with accumulation, respectively.

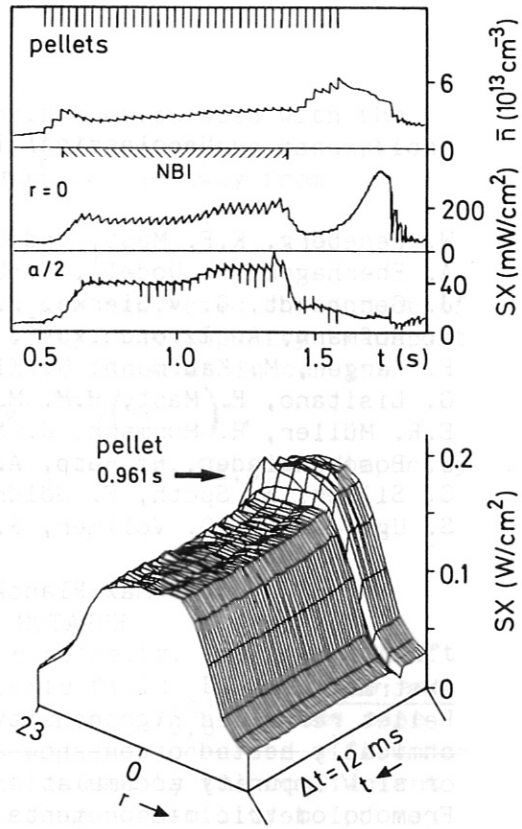

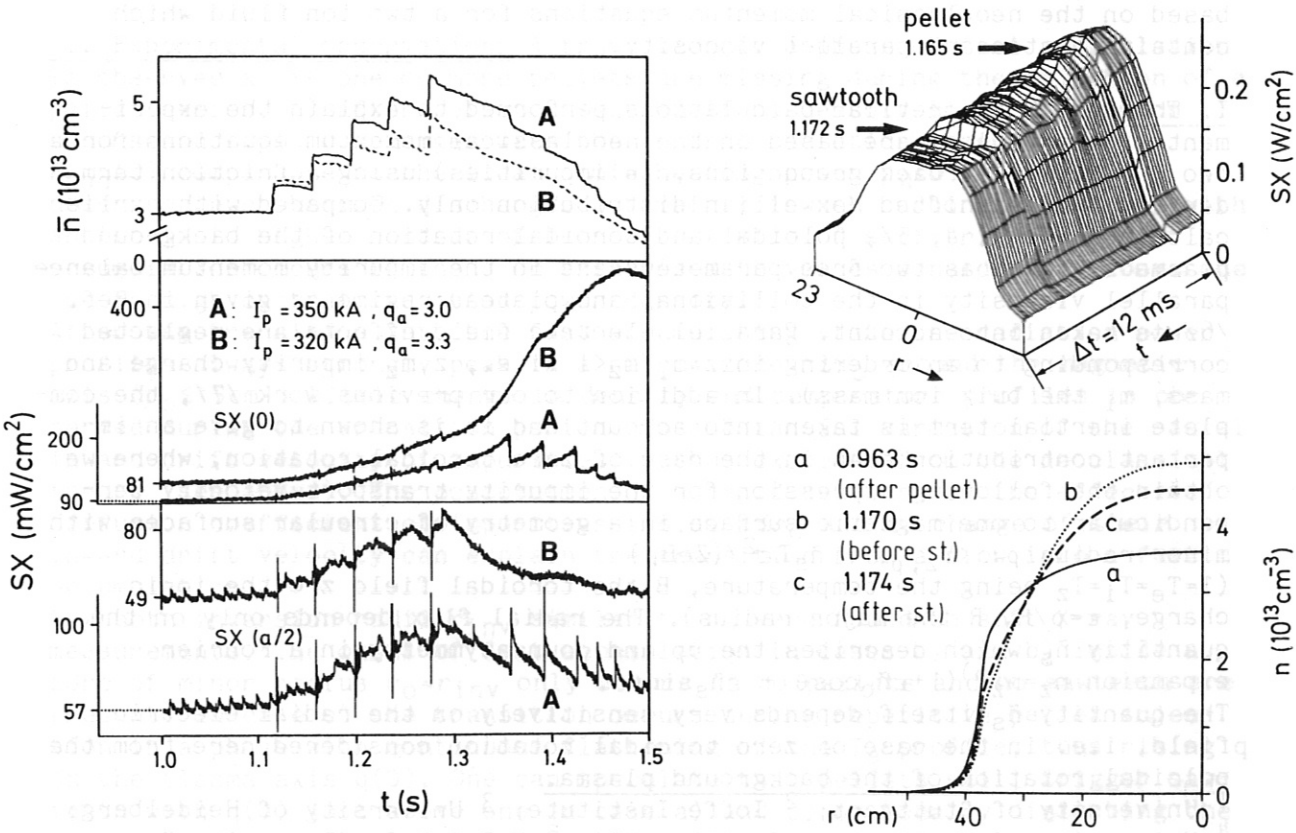

Fig.6: SX radiation and density profiles /5/ after pellet injection into a beam heated plasma. Two different cases can be well discriminated.

Neoclassical Impurity Transport in Ohmically Heated Pellet Discharges

W. Feneberg, K.F. Mast, and G. Becker, H.S. Bosch, H. Brocken, A. Carlson, A. Eberhagen, G. Dodel[1], H.-U. Fahrbach, G. Fussmann, O. Gehre, J. Gernhardt, G. v.Gierke, E. Glock, O. Gruber, G. Haas, W. Herrmann, J. Hofmann, A. Izvozchikov[2], E. Holzhauer[1], K. Hübner[3], G. Janeschitz, F. Karger, M. Kaufmann, O. Klüber, M. Kornherr, K. Lackner, M. Lenoci, G. Lisitano, F. Mast, H.M. Mayer, K. McCormick, D. Meisel, V. Mertens, E.R. Müller, H. Murmann, J. Neuhauser, H. Niedermeyer, A. Pietrzyk[4], W. Poschenrieder, H. Rapp, A. Rudyj, F. Schneider, C. Setzensack, G. Siller, E. Speth, F. Söldner, K. Steinmetz, K.-H. Steuer, N. Tsois[5], S. Ugniewski[6], O. Vollmer, F. Wagner, D. Zasche,

Max-Planck-Institut für Plasmaphysik
EURATOM Association, Garching, FRG

Abstract
Pellet refuelled high density divertor discharges in ASDEX which are ohmically heated often show a sudden transition from a status of negligible or slow impurity accumulation to a fast accumulation at the plasma core. From bolometric measurements we estimate the inward drift velocity of medium z impurities and compare the results with theoretical predictions based on the neoclassical momentum equations for a two ion fluid which contain inertia and parallel viscosity.

I. Theory The theoretical calculations performed to explain the experimental observations are based on the neoclassical momentum equations for a two ion fluid (i= back ground ions, z= impurities) using a friction term derived from a shifted Maxwellian distribution only. Compared with earlier calculations /3, 4, 5/, poloidal and toroidal rotation of the background plasma is taken as two free parameters and in the impurity momentum balance parallel viscosity in the collisional and plateau regime as given in Ref. /6/ is taken into account. Parallel electric field effects are neglected corresponding to an ordering in $z \cdot m_i/m_z < 1$ (i.e., z, m_z impurity charge and mass, m_i the bulk ion mass). In addition to our previous work /7/, the complete inertial term is taken into account and it is shown to give an important contribution even in the case of zero toroidal rotation, where we obtain the following expression for the impurity transport velocity perpendicular to one magnetic surface in a geometry of circular surfaces with minor radius ρ: $\langle V_{z,\rho} \rangle = \tilde{n}_s T \varepsilon^2/(ZeB\rho)$
($T=T_e=T_i=T_z$ being the temperature, B the toroidal field $z \cdot e$ the ionic charge, $\varepsilon=\rho/R$, R the major radius). The radial flux depends only on the quantitiy $\tilde{n}_s$ which describes the up and down asymmetry in a Fourier expansion $n_z=n_z^{(o)}(1+\varepsilon\tilde{n}_c\cos\theta + \varepsilon\tilde{n}_s\sin\theta)$.
The quantity $\tilde{n}_s$ itself depends very sensitively on the radial electric field, i.e. in the case of zero toroidal rotation considered here from the poloidal rotation of the background plasma.

[1] University of Stuttgart; [2] Ioffe Institute; [3] University of Heidelberg; [4] University of Washington, Seattle, USA; [5] N.R.C.N.S. "Democritos", Athens, Greece; [6] Inst. for Nuclear Research, Swierk, Poland;

Fig. 1 shows results for neoclassical inward drifts calculated with the parameters of two typical pellet discharges in ASDEX under the assumption of zero order impurity pressure gradient $p_Z^{(o)\prime}$ to be far away from accumulation equilibrium.

$$(p_i'/n_i >> P_Z^{(o)\prime}/z \cdot n_Z^{(o)}.$$

In opposite to the work of Rutherford /3/ which has neglected the effect of inertia and therefore has to be modified completely, the impurity transport depends beside the parameter Ω of collisionality defined as in our previous JET report /8/ also on the parameter $A^2 = V_{z,\Theta}^{2\ (o)} / \left(\frac{\varepsilon}{q} C_{z,s}\right)^2$, where $V_{z,\Theta}^{(o)}$ is the zero order impurity rotation velocity, $C_{z,s}$ the impurity sound velocity and q the safety factor.
We have always from radial momentum balance

$$V_{Z,\theta}^{(o)} = V_{i,\theta}^{(o)} - 1/eB\ (P_i'/n_i - P_Z^{(o)\prime}/zn_Z^{(o)}),$$

where $V_{i,\theta}^{(o)}$ is the bulk plasma poloidal rotation velocity. The inward drift has a maximum for $V_{Z,\theta}^{(o)}=0$, when the radial electric field E_ρ vanishes and is much smaller when the background plasma is at rest ($V_{i,\theta}^{(o)}=0$), the case which fits best to experiment. In this case theory even predicts a flow reversal for heavy impurities when $A^2 \geqq 2$ an effect caused by the coefficient of parallel viscosity and leading to an interesting possibility to prove the neoclassical theory.

II. Experimental observations A transition to a phase of fast accumulation is observed a) if one or more pellets are missing during the injection of a pellet series, b) after pellet injection if no density limit disruption occurs and c) in discharges with the central radiation power density $P_{rad}(0)$ comparable to the local ohmic heating power $p_\Omega(0)$. This is observed in carbonized discharges but mainly in non-carbonized plasmas with an intrinsic higher content of iron /1/. A kind of self-triggering of accumulation occurs if the q on axis rises to values considerably above one due to high central radiation power density.
After the transition into the fast accumulating state the radiation power profiles always strongly peak in a narrow zone $r \leqq r_o$ around the magnetic axis ($r_o \leqq 15$cm). Little change in density and temperature profiles is observed during the transition period. No substantial variation of the radial inward drift velocity of impurities is thus expected from the neoclassical theory (see above). The postulation of a rapid decrease of the effective diffusion coefficient of impurities inside $r \leqq r_o$ and no change of their inward drift velocity can explain the transition from a slow into a fast accumulation.
Sawtooth inversion radii r_{inv} similar to r_o were found in soft X-ray measurements. The onset of fast accumulation in cases a) and b) inside a zone of minor radius $r_o \approx r_{inv}$ only occurs if no pellets and no sawteeth are present. In case c) the transition occurs during repetitive pellet injection in a phase with continuous flattening of the T_e-profile, thus rising q on the plasma axis q(0). One can speculate that pellets still trigger sawteeth with q(0) just above one in case a) and b) by locally disturbing the n_e- and T_e-profile. A further rise of q(0) owing to increasing

$p_{rad}(0)/p_\Omega(0)$ suppresses the sawtooth activity during pellet injection. A simple analytical model is derived in order to estimate the accumulation of impurities on the plasma axis. The linearised transport equation for impurities with charge Z in cylindrical approximation is

$$-D_z(r)\cdot r\cdot\frac{\partial^2 n_z}{\partial r^2}-(D_z(r)+r\frac{dD_z}{dr})\frac{\partial n_z}{\partial r}+V_{DZ}(r)\cdot r\frac{\partial n_z}{\partial r}+(V_{DZ}(r)+\frac{dV_{DZ}}{dr}\cdot r)\,n_z=-r\frac{\partial n_z}{\partial t} \qquad (1)$$

with $n_z(r,t)$=density, $v_z(r)$= inward drift velocity (neoclassical) and $D_z(r)$=effective diffusion coefficient of impurities Z.
We define $D_z(r)$ as

$t<0$ $D_z(r)=D_i$ $\leftarrow (r\leq r_o)$ $\quad D_z(r)=D_o(r_o<r<a)$ (r_o=15 cm, a=plasma minor radius = 40 cm)
$t\geq 0$ $D_z(r)=D_a$ $\swarrow$

Expansion of $v_z(r)$ near the axis yields $v_z=V_{D1}\cdot r$ ($v_{D1}<0$). Fast impurity accumulation starts at t=0 and no saturation of $n_z(0,t)$ is experimentally observed until a density limit disruption occurs. For a time interval $0\leq t\leq t_A$ (t_A is estimated below) we define the velocity for outward diffusion at $r=r_o$

$$V_{DIF}=\frac{dn_z(r,0)}{dr}\cdot D_z(r)/n_z(r,0)_{/r=r_o} \qquad (2)$$

A time t_A is defined at which the increase of V_{DIF} at $r=r_o$ is
$\Delta V_{DIF}=V_{DIF}(r_o,t_A)-V_{DIF}(r_o,0)=0.3\cdot V_z(r_o)$
and an experimentally detectable decrease of the time constant τ is expected. Equation 1 is simplified to

$$V_z^*(r)\cdot r\frac{dn_z}{dr}+(V_z^*+\frac{dV_z^*}{dr}\cdot r)n_z(r,t)=-r\frac{\partial n_z}{\partial t} \qquad (3)$$

$v_z^*(r)=V_z(r)+V_{DIF}(r)=V_{D_1}(1-D_a/D_i)\cdot r=V_D^*\cdot r.$
Starting from a quasi-stationary impurity distribution $n_z(r,0)=n_o\cdot\exp((v_{D1}/2D_i)r^2)$ $(r\leq r_o)$ at t=0, the distribution of impurities z evolves as

$$n_z(r,t)=n_o\cdot\sum_{l=0}^{\infty}\frac{(-1)^l}{l!}(\frac{r}{\lambda\cdot a})^{2l}\cdot\exp(2|V_D^*|(l+1)t) \qquad (4)$$

$1/\lambda\cdot a=(|V_{D1}|/(2D_i))^{0.5}$
and the central density of impurities is $n_z(0,t)=n_o\cdot e^{2/v_D^*\cdot t}$

Figure 2 represents t_A/τ_O ($\tau_O<\tau$, $\tau_O=1/(2|V_{D1}|)$ $\tau=1/2|V_D^*|$) as an upper limit of t_a/τ. Experimentally we always find $t_A/\tau>1$ (Fig. 3) and thus $t_A/\tau_O>1$. We deduce from Fig. 2 the ratio D_a/D_i to be always less than 0.3. The inward drift velocity at $r=r_O$ is derived from the experimental τ as $V_z(r_o)=r_o/2\cdot\tau$ and should always be smaller than the theoretical value.

The concentration of iron (the dominating metal in ASDEX /2/) on the plasma axis is derived from $p_{rad}(0)$ and $n_e(0)$ assuming coronal equilibrium. We always find a constant τ during accumulation and no saturation (Fig. 3).

Conclusion The theoretically predicted inward drift velocity at r=15 cm, V_z = 75 cm/s for #18716 and V_z = 110 cm/s for #18874 agree well with the bolometrically detected V_z = 43 cm/s for #18716 and V_z = 63 cm/s for #18874. The experimental values of V_z are always smaller than the theoretical V_z.

References

/1/ Mast, K.F., Müller, E.R., et al., Radiation Behaviour of Gas and Pellet refuelled High density discharges in ASDEX, this conference.
/2/ Fußmann, G., Journal of Nuclear Materials 145-147 (1987) 96-104.
/3/ Rutherford, P.H., Phys. of Fluids, 17, 9 (1984).
/4/ Burrel, K.H., Ohkawa, T., Wong, S.K., Phys. Rev. Lett., 47, 7 (1981).
/5/ Stacey, W.M.Jr., Sigmar, D.J., et al., Nucl. Fus. 25, 4 (1985).
/6/ Callen, J.D., et al., IAEA-CN-47, Kyoto, Nov. 1986.
/7/ Feneberg, W., Kornherr, M., Smeulders, P., et al., Budapest, Sept. 1985.
/8/ Feneberg, W., Mast, F.K., Gottardi, N., Martin P., JET-R(86)07.

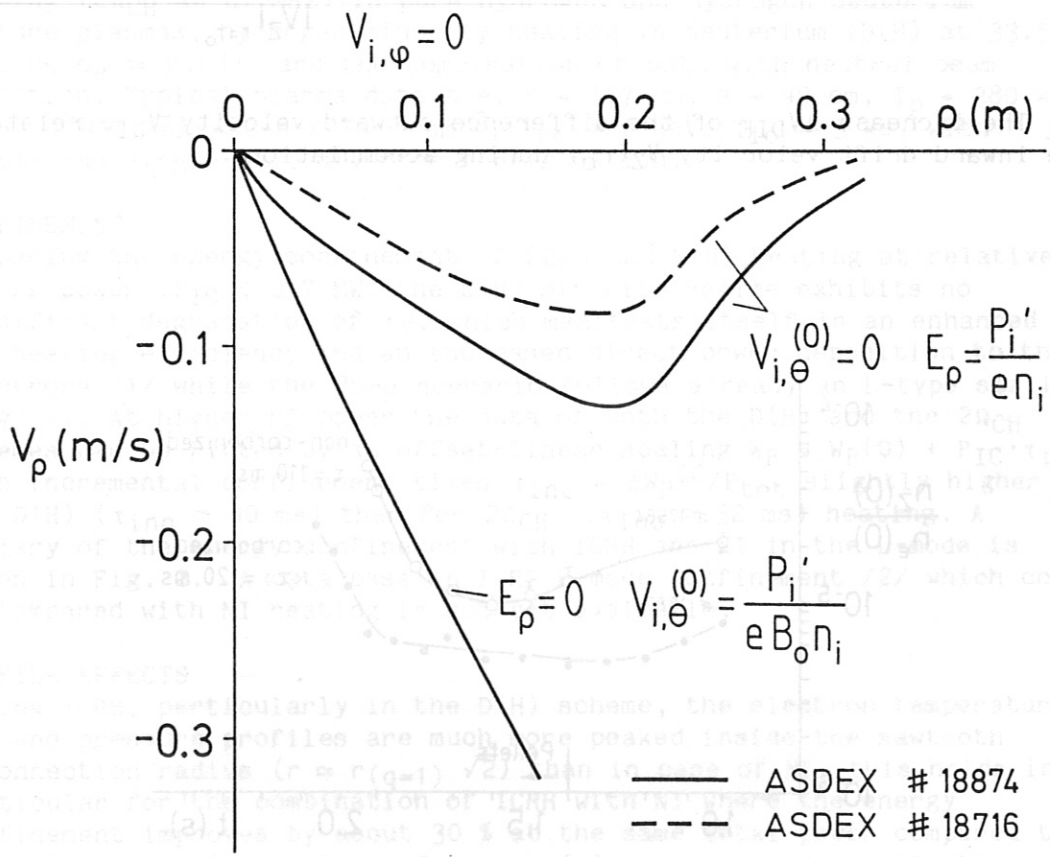

Fig.1: Neoclassical impurity inward drifts calculated for iron in a typically ASDEX pellet discharge for two different rotation velocities. $Z(\rho)$ from corona equilibrium.

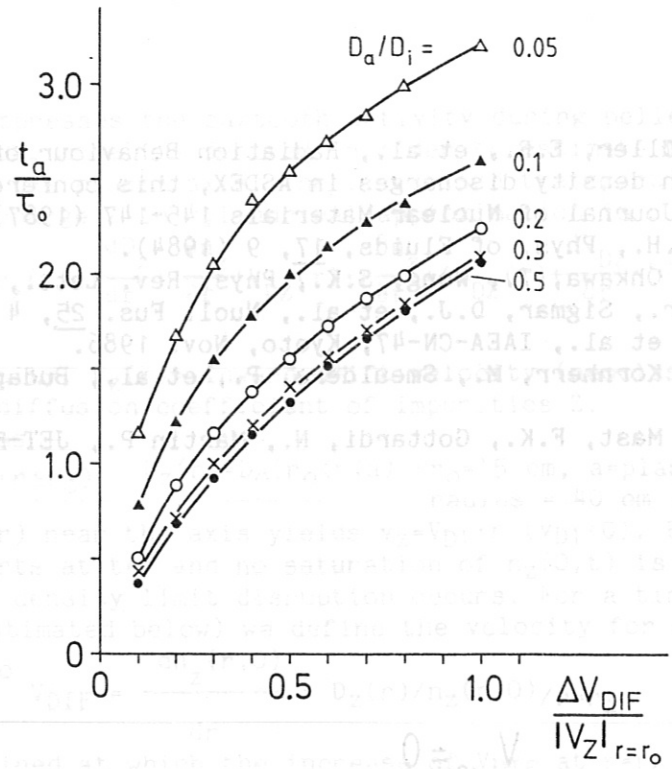

Fig.2: The increase ΔV_{DIF} of the difference outward velocity V_{DIF} related to the inward drift veloc ity $V_Z(r_o)$ during accumulation.

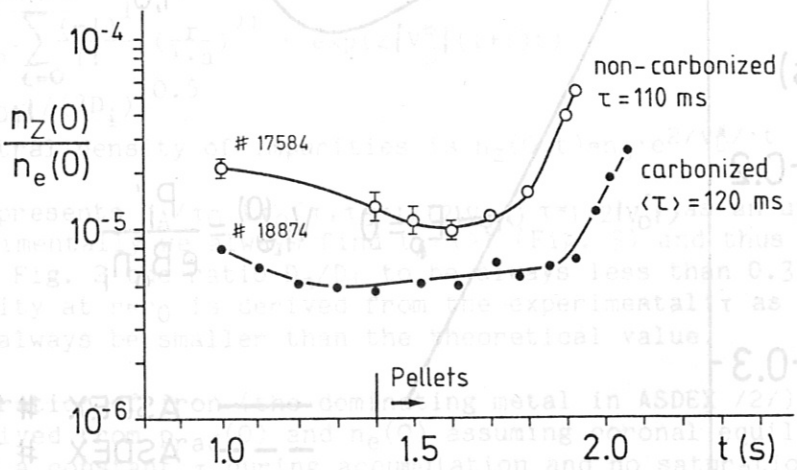

Fig.3: #17584: non carbonized pellet discharge in D_2. The dominating metal is iron $n_Z(0) \approx n_{Fe}(0)$.
#18874: carbonized pellet discharge. The T_e-profile is constant for 1.5 s≤t≤2.1 s
($T_e(0)$=780 eV = 30 eV). The time constant τ represents an average value for iron and titanium.

CONFINEMENT AND PROFILE EFFECTS DURING ICRF HEATING ON ASDEX

K. Steinmetz, M. Brambilla, A. Eberhagen, F. Wagner, F. Wesner, J. Bäumler, G. Becker, W. Becker, F. Braun, R. Fritsch, G. Fussmann, O. Gehre, J. Gernhardt, G. v.Gierke, E. Glock, O. Gruber, G. Haas, J. Hofmann, F. Hofmeister, G. Janeschitz, F. Karger, O. Klüber, M. Kornherr, K. Lackner, G. Lisitano, F. Mast, H.-M. Mayer, K. McCormick, D. Meisel, V. Mertens, E.R. Müller, H. Murmann, H. Niedermeyer, J.-M. Noterdaeme, W. Poschenrieder, S. Puri, H. Rapp, H. Röhr, J. Roth, F. Schneider, C. Setzensack, G. Siller, F. Söldner, E. Speth, K.-H. Steuer, O. Vollmer, H. Wedler, D. Zasche

Max-Planck-Institut für Plasmaphysik,
EURATOM Association, D-8046 Garching, F.R.G.

INTRODUCTION

Various high power heating scenarios in the ion cyclotron range of frequencies (ICRF) have been studied on ASDEX up to a power of $P_{IC} \simeq$ 2.3 MW launched by two low-field side antennae: Hydrogen second harmonic heating ($2\Omega_{CH}$ at 67 MHz) in pure hydrogen and hydrogen-deuterium mixture plasmas, hydrogen minority heating in deuterium (D(H) at 33.5 MHz, $n_H/n_e \simeq 0.05$), and the combination of both with neutral beam injection. Typical plasma data are: R = 167 cm, a = 40 cm, I_p = 380 kA, $B_o \simeq$ 2.24 T, $\bar{n}_e$ = 2-6 x 10^{13} cm^{-3}, $T_{eo} \simeq$ 2 keV, $T_{io} \simeq$ 3 keV with double and single-null divertor configuration.

CONFINEMENT

Comparing the energy confinement of $2\Omega_{CH}$ and D(H) heating at relatively low rf power (P_{IC} < 0.7 MW) the D(H) minority regime exhibits no significant degradation of τ_E, which manifests itself in an enhanced ion heating efficiency and an increased direct power deposition to the electrons /1/ while the $2\Omega_{CH}$ scenario follows already an L-type scaling (Fig. 1). At higher rf power the data of both the D(H) and the $2\Omega_{CH}$ schemes can be fitted by an offset-linear scaling $W_p = W_p(0) + P_{IC} \cdot \tau_{inc}$ with incremental confinement times $\tau_{inc} = \Delta W_p^{IC}/P_{tot}$ slightly higher for D(H) ($\tau_{inc} \simeq$ 40 ms) than for $2\Omega_{CH}$ ($\tau_{inc} \simeq$ 32 ms) heating. A summary of the energy confinement with ICRH and NI in the L-mode is given in Fig. 2. A data base on ICRF H-mode confinement /2/ which could be compared with NI heating is not yet available.

PROFILE EFFECTS

During ICRH, particularly in the D(H) scheme, the electron temperature /2/ and pressure profiles are much more peaked inside the sawtooth reconnection radius ($r \simeq r_{(q=1)} \sqrt{2}$) than in case of NI: this holds in particular for the combination of ICRH with NI where the energy confinement improves by about 30 % at the same total power compared to pure NI heating (Fig. 3). As far as $n_e(r)$ is concerned the electron density profiles remain essentially unchanged at the plasma boundary (between separatrix and antennae) /3/ whereas $n_e(r)$ becomes slightly

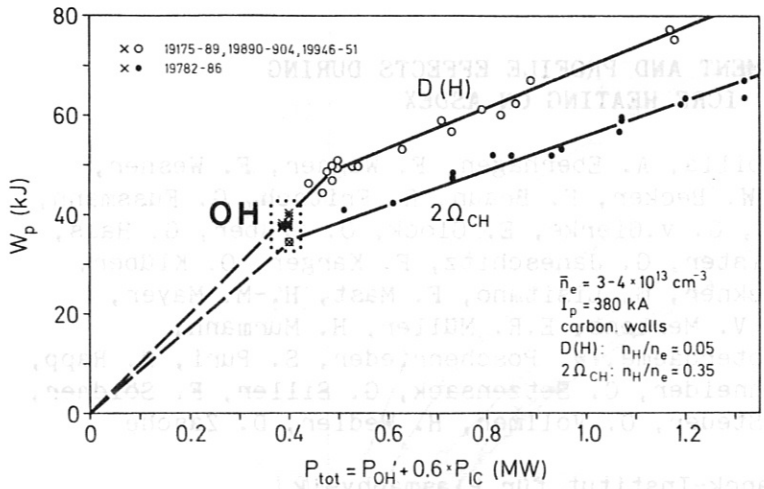

Fig. 1: Plasma energy content for $2\Omega_{CH}$ and D(H) heating versus total power (note the ICRH power absorption α = 0.6).

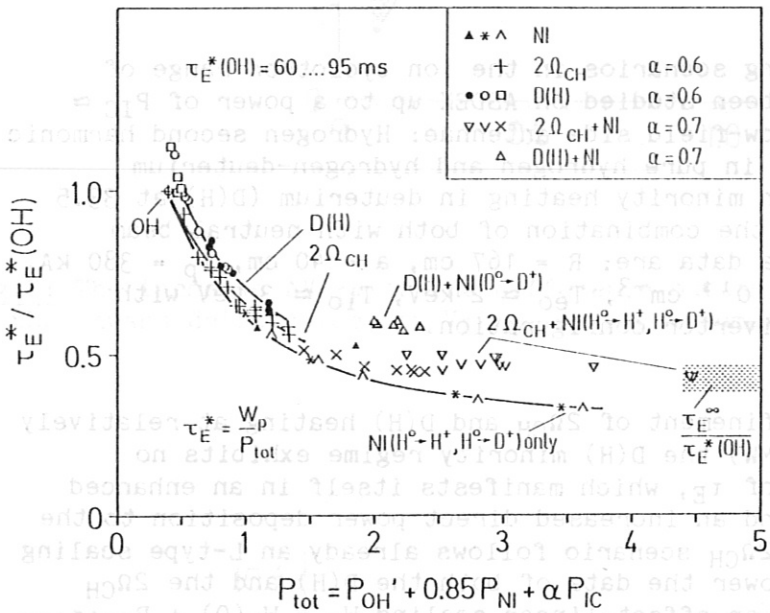

Fig. 2: Gross energy confinement times for ICRH ($2\Omega_{CH}$, D(H)), NI and ICRH+NI heating.

peaked with ICRH in the plasma centre. Whether the peakedness of the profiles and the absence or reduction of plasma rotation (in case of ICRH + NI) is directly related to the slight improvement of τ_E with ICRH is not yet clear.

The extent of temperature profile shaping has been attempted to test by varying the ICRF power deposition by either 1) shifting the $2\Omega_{CH}$ resonance layer radially while keeping q_a = 3.3 = constant, or 2) workingwith two $2\Omega_{CH}$ resonance layer positions simultaneously, excited by two antennae operating at different frequencies (67 MHz for r_{res} ~ 0 cm, and 61.9 MHz for $r_{res} \simeq a/2$ = 20 cm) and variable power (P^{IC}_{tot} = 0.9 MW), combined with a small amount of NI heating (P_{NI} = 0.4 MW): In case of primarily off-axis rf power deposition neither a significant alteration of electron temperature (Fig. 4) and pressure profiles outside q = 1 nor a

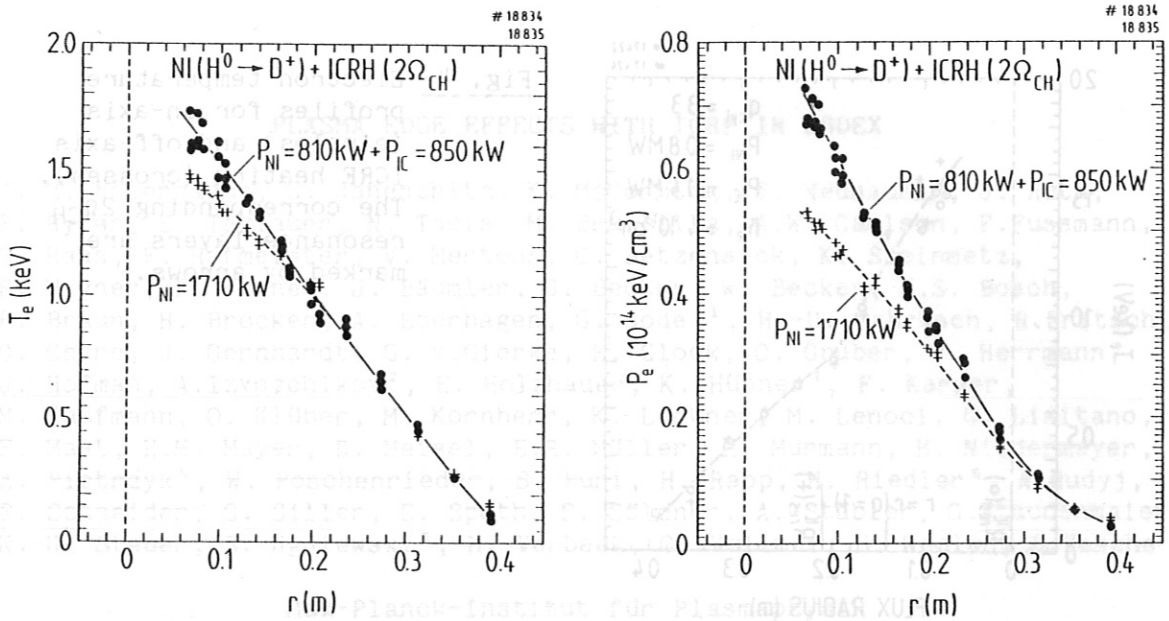

Fig. 3: Electron temperature and pressure profiles obtained with pure NI and ICRH+NI heating at the same total power.

change of the gross energy confinement time with respect to on-axis deposition have been observed, i.e. the electron profiles are widely invariant to the rf power distribution in the plasma. No information is so far available on ASDEX of the ion temperature profiles with ICRH in these conditions; investigations at JET /4/ indicate a relatively strong flattening of $T_i(r)$ with off-axis deposition.

DIRECT ELECTRON HEATING

An enhanced direct electron heating, $p_e = 1.5\, n_e(r)\, dT_e(r)/dt$, determined via the initial slope of $T_e(t)$ after the sawtooth crash, is found close to the $2\Omega_{CH}$ resonance layer, in particular with off-axis deposition. The observations can be interpreted by electron heating via ion Bernstein waves (IBW) as predicted by theory /5/, which are weakly damped along their propagation towards the inner plasma region. This is illustrated in Fig. 5 where direct electron heating is measured on axis and at r = 10 cm whereasthe resonance layers are located at r_{res} = 0 cm and 20 cm. With increasing ratio of off-axis to on-axis rf power direct electron heating is enhanced not only 10 cm towards the plasma centre (with respect to the off-axis resonance) but also on-axis where p_e does not decrease, although the rf power is reduced there.

SUMMARY

High power ICRF heating experiments on ASDEX and their comparison with NI heating have shown a unique confinement structure which appears to be inherent to tokamak plasmas. Although profiles are much more peaked with ICRH, their shapes are found to be invariant to modifications of the rf power deposition profiles. Studies on direct electron heating indicate that ion Bernstein waves generated via mode conversion at the $2\Omega_{CH}$ resonance layer(s) propagate more than 20 cm towards the inner plasma region while being absorbed along their path.

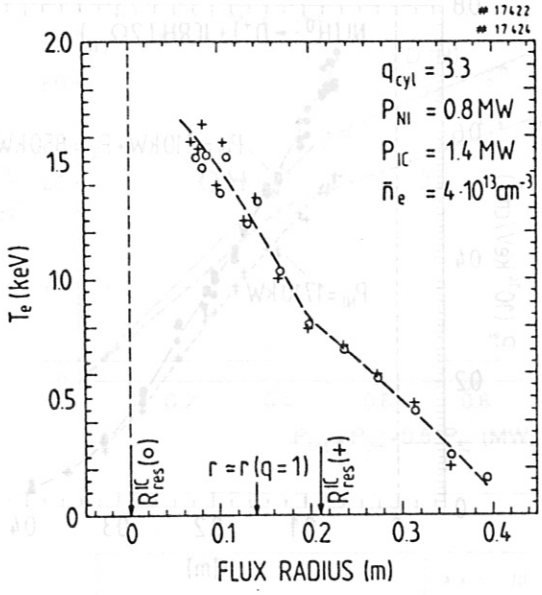

Fig. 4: Electron temperature profiles for on-axis (circles) and off-axis ICRF heating (crosses). The corresponding $2\Omega_{CH}$ resonance layers are marked by arrows.

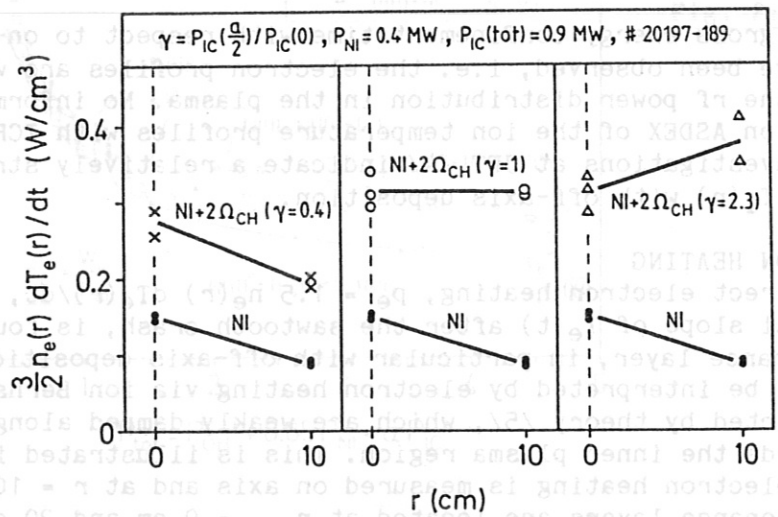

Fig. 5: Direct electron heating power density at r = 0 and r = 10 cm due to varying off-axis ICRF power deposition $\gamma = P_{IC}(a/2)/P_{IC}(0)$.

REFERENCES

/1/ K. Steinmetz et al., Plasma Physics and Contr. Fusion 28, 235 (1986).

/2/ K. Steinmetz et al., 13th Europ. Conf. on Contr. Fus. and Plasma Heating, EPS Schliersee, Vol. II, 21 (1986).

/3/ J.-M. Noterdaeme et al., this conference

/4/ J. Jacquinot et al., RF HEATING ON JET, Proc. 11th Conf. on Plasma Phys. and Contr. Nucl. Fus. Research, Kyoto (1986).

/5/ M. Brambilla, IPP-Report 5/15 (1987).

PLASMA EDGE EFFECTS WITH ICRF IN ASDEX

J.-M. Noterdaeme, G. Janeschitz, K. McCormick, J. Neuhauser, J. Roth, F. Ryter, E. Taglauer, N. Tsois, M. Brambilla, A.W. Carlson, F.Fussmann, G. Haas, F. Hofmeister, V. Mertens, C. Setzensack, K. Steinmetz, F. Wagner, F. Wesner, J. Bäumler, G. Becker, W. Becker, H.S. Bosch, F. Braun, H. Brocken, A. Eberhagen, G. Dodel[1], H.-U. Fahrbach, R.Fritsch, O. Gehre, J. Gernhardt, G. v.Gierke, E. Glock, O. Gruber, W. Herrmann, J. Hofman, A.Izvozchikov[2], E. Holzhauer, K. Hübner[3], F. Karger, M. Kaufmann, O. Klüber, M. Kornherr, K. Lackner, M. Lenoci, G. Lisitano, F. Mast, H.M. Mayer, D. Meisel, E.R. Müller, H. Murmann, H. Niedermeyer, A. Pietrzyk[4], W. Poschenrieder, S. Puri, H. Rapp, H. Riedler[6], A.Rudyj, F. Schneider, G. Siller, E. Speth, F. Söldner, A. Stäbler, G.Staudenmaier, K.-H. Steuer, S. Ugniewski[5], H. Verbeek, O. Vollmer, H. Wedler, D.Zasche

Max-Planck-Institut für Plasmaphysik
EURATOM Association, D-8046 Garching
[1] University of Stuttgart, [2] Ioffe Institute, [3] University of Heidelberg, [4] University of Washington, Seattle, USA, [5] Inst.for Nuclear Research, Swierk, Poland, [6] Schiedel-Stiftung, Austria

Introduction: The boundary plasma plays a major role in the understanding of the multiple aspects of an RF heated plasma: the coupling of RF waves, the impurity content of the plasma, or even its overall confinement properties. The difficulty to measure the boundary plasma especially with RF is compounded by the fact that machine specific aspects have a much larger impact on the plasma boundary than at the plasma center. Systematic tendencies are however recognized. In the following we give an overview of plasma boundary data (n_e,Te electric fields in the scrape off layer) and report on Fe flux measurements in the divertor and on evidence of a local impurity production mechanism. We then propose an explanation for the enhanced impurity content of the plasma during ICRF, which is also consistent with earlier measurements /1,2,3/.

Boundary density evolution: In standard ICRH discharges the density evolution, measured with the Li beam diagnostic /4/ is as follows: As the separatrix is moved outwards, due to β_p effects, the density at a fixed radial position increases (Fig. 1a). Normalised to the position of the separatrix, however, the density there is constant (Fig. 1b) with at low plasma current a small increase of the gradient length (Fig. 1c). The density at the antenna limiter stays constant. This results in a steepening of the density gradient close to the antenna.

Edge temperature evolution: In the last experimental period the Langmuir probes in the main chamber were disturbed by the ICRF and the edge laser scattering system did not cover in the case of ICRF the separatrix region (the plasma is shifted outward for a good antenna coupling). There is, however, substantial experience (incl. numerical simulation) from ohmic and neutral injection heated discharges with an unshifted plasma where all diagnostics are working. Taking the divertor data (density,

temperature, CIII, bolometer etc.) and the main chamber edge density during ICRH, it is quite obvious that the power input into the divertor and hence the midplane temperature are substantially increased in normal ICRH discharges. This is in agreement with observations on JET and TEXTOR. RF theory /5/ also predicts that a few per cent of the power can be deposited in the boundary through collisional absorption on the electrons (the mechanism being that the electrons take up energy with their $\tilde{E}$ x B drift and thermalize it if $\nu_{ei} >> \nu_{ICRH}$, cold electrons with large ν_{ei} are preferentially heated). Close to the separatrix this is a small fraction compared to the large power outflux from the main plasma. It can, however, strongly influence the temperature and potential in the low energy scrape off layer wing.

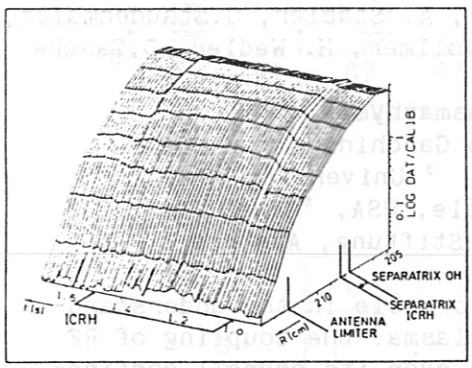

Fig.1a: Density evolution at the boundary

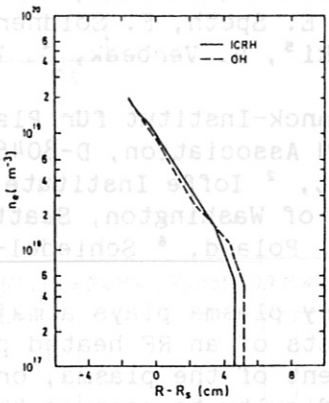

Fig.1b: Normalized to the position of the separatrix

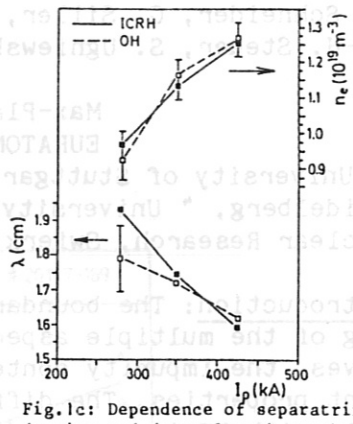

Fig.1c: Dependence of separatrix density and decay length at the separatrix with plasma current

Floating potential measurement in the divertor: In fact, a substantial influence is observed e.g. in the floating potential in the divertor /6/. During ICRH, a strong negative peak is observed in the outer scrape-off layer wing just inside the last flux surface entering the divertor (which is also the surface directly in front of the antenna). This may be connected with the spurious edge heating mentioned above. The detailed structure of the floating potential profile depends on the heating scenario (OH, $2\omega_c$, minority, addition of NI) and on the position of the resonance layer. There are indications that there is a correlation between enhanced impurity content of the plasma and the observed radial potential pattern: Figures 2 a,b,c show how this profile changes as one goes from a case (a) resulting in a large to a case (c) resulting in a much reduced impurity content of the plasma. Note the appearance of an intermediate region with a radially inward electric field. Those radial electric fields will affect the transport in the scrape off layer, the exact mechanism, however, remains unclear.

Measurements of Fe fluxes: A divertor collector probe was used to measure the Fe fluxes in front of the divertor target plate /7/. Assuming toroidal and poloidal symmetry, those fluxes can be related to the Fe fluxes originating from the main chamber walls (Fig. 3a). Spectroscopic measurements of the Fe XVI line intensity, as a function of power, are shown in Fig. 3b. Using an impurity transport code /8/, which neglect electric fields in the scrape-off, the absolute Fe XVII

line intensities and the absolute X-ray signals can be converted into absolute Fe fluxes (Fig. 3a). In the case of NBI, the measured fluxes in the divertor, as well as the fluxes calculated by the code are in good agreement with those calculated /9,10/ from CX sputtering using data from the neutral particle diagnostics. In the case of ICRH, however, the fluxes calculated from the Fe XVI intensity are much higher than those measured by the divertor probe or calculated from CX sputtering. One has either to assume that the Fe flux measurements in the divertor were not representative of the fluxes in the main chamber or that the scrape off transport model in the code is incomplete in the case of ICRF heating.

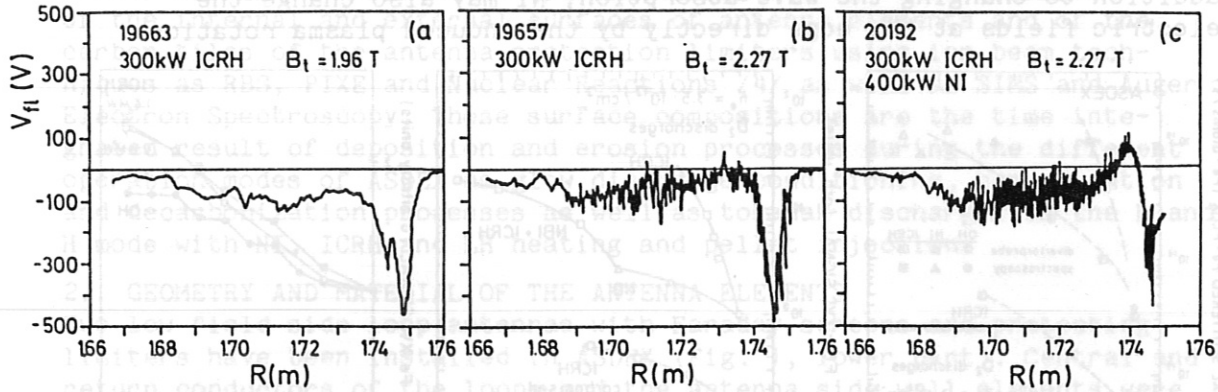

Fig.2: Floating potential in the divertor chamber
a) ICRH alone, non optimal position of resonance layer
b) ICRH alone, optimal position of the resonance layer
c) ICRH with NI

Evidence of local impurity production: There are several indications for localised impurity sources in the main chamber during ICRH. The development of the Fe XVI line intensity over a dozen of shots after wall carbonisation is shown in Fig. 4. The values for OH and ICRH were normalized at shot 18782. The faster shot to shot increase during ICRH, relative to the OH part of the pulse can only be explained by a strong local erosion due to the RF. Surface analysis of the carbon protection limiters of the antenna indicate the presence of a local Fe source /11/. A similar conclusion was reached by the JFT-2M group /12/, when they protected the antenna neighbourhood with graphite. The divertor probe could underestimate the amount of Fe originating from such local spots because much may be locally redeposited.

Discussion: In view of the now accumulated data we can propose an hypothesis for the increased impurity content in the plasma during ICRH. Earlier explanations, based mainly on the anticorrelation of wave absorption and the impurity content in the plasma /1,2,/ have emphasized increased impurity production with, however, the mechanism still to be identified. More recently, in view of the Fe measurements in the divertor, an increased penetration of neutrals through the scrape-off layer was put forward as an hypothesis/13/. Model calculations, however, show that this would require a major reduction of the boundary temperature which was not substantiated in normal discharges.
Consistent with earlier measurements and with both the measured Fe flux in the divertor, and the boundary parameters during RF, the higher impurity concentrations can be related to two effects: 1) a changed

transport in the SOL, because of radial electric fields at the edge, originating from a changed plasma potential, and 2) a strongly localised Fe source due to strong electric fields in the vicinity of the antenna. The anticorrelation between absorption and impurity production, seen for example in B_t scans /2/ and in the beneficial effect of NI can be explained as follows. Bad absorption would result in a strong local standing wave near the antenna /5/, which increases the impurity production directly in this region, and in larger RF fields at the plasma edge /14/, which, through acceleration of particles there, could change the plasma potential and thus the transport in the scrape off. In addition to changing the wave absorption, NI may also change the electric fields at the edge directly by the induced plasma rotation.

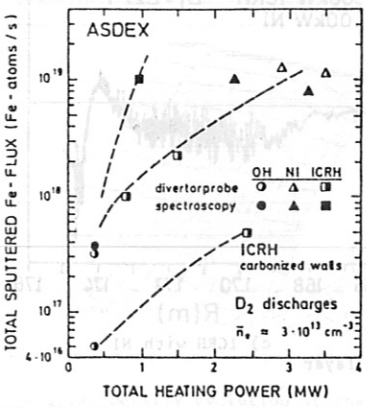

Fig.3a: Fe fluxes as calculated from the divertor probe and from the Fe intensity lines

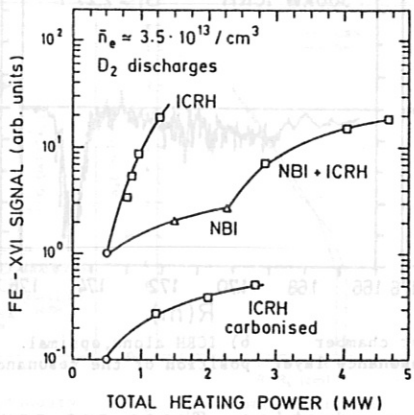

Fig.3b: Measured Fe XVI intensities

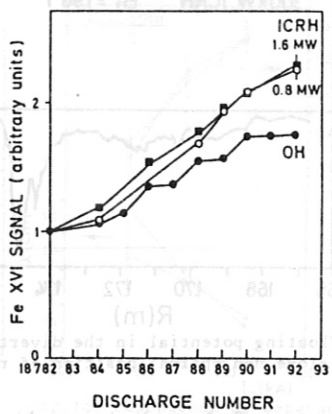

Fig.4: Normalized evolution of the Fe XVI signal

Summary: The evolution of n_e and T_e at the plasma boundary during the RF, together with measurements of the floating potential in the divertor, and the analysis of Fe collector probes in the divertor and of the antenna limiter indicate that the enhanced impurity concentration in a ICRF heated plasma is due to a combination of changed transport in the scrape-off layer because of electric fields, and an increased local production of impurities, related to large electric fields in the direct antenna neighbourhood.

References

/1/ G. Fussmann et al., Europhys.Conf.Abstr. (1985) Vol. 9F, I, 195
/2/ G. Janeschitz et al., Europhys.Conf.Abstr.(1986) Vol.10C,I, 407
/3/ C. Setzensack, IPP Report III Feb. 1987
/4/ K. McCormick, J.Nucl.Mat. 121 (1984) 48
/5/ M. Brambilla et al., this conference, and private communication
/6/ N. Tsois et al., this conference
/7/ E. Taglauer, J.Nucl.Mat. 128-129 (1984) 141
/8/ G. Fussmann, Nucl. Fus. 26 (1986) 983
/9/ H. Verbeek et al., as /1/, Vol. 9F, II, 583
/10/ G. Staudenmaier, J.Nucl.Mat. 145-147 (1987) 539
/11/ R. Behrisch et al., this conference
/12/ H. Tamai et al., JAERI-M 86-143, Tokai,Sept. 1986
/13/ J. Roth, IPP Jahresbericht 1986
/14/ R. Van Nieuwenhove et al., this conference

DEPOSITION AND EROSION AT THE OPEN AND CLOSED ICRH ANTENNAE OF ASDEX

R. Behrisch, F. Wesner, M. Wielunski[1], J.-M. Noterdaeme, E. Taglauer,
Max-Planck-Institut für Plasmaphysik,
EURATOM Association, D-8046 Garching

1. INTRODUCTION

In the ASDEX tokamak ICRH has been applied with two antennae and a total RF generator power of 3 MW for about one and a half years between 1984 and April 1986. Second harmonic and minority heating modes in Deuterium and Deuterium-hydrogen mixture plasmas have been investigated /1/. In April 1986 the antennae were dismanteled to be exchanged by watercooled ones. This gave the possibility to investigate the surface composition of the internal and external surfaces of antenna elements and of the carbon tiles of the antenna protection limiters using ion beam techniques as RBS, PIXE and Nuclear Reactions /4/ as well as SIMS and Auger Electron Spectroscopy. These surface compositions are the time integrated result of deposition and erosion processes during the different operation modes of ASDEX as glow discharge conditioning, carbonization and decarbonization processes as well as tokamak discharges in the L and H mode with NI, ICRH and LH heating and pellet injection.

2. GEOMETRY AND MATERIAL OF THE ANTENNA ELEMENTS

Two low field side loop antennae with Faraday screens and protecting limiters have been installed in ASDEX (Fig. 1, lower part). Central and return conductors of the loops and the antenna side wall elements were silver coated. The limiters were made of graphite mushrooms brazed into copper blocks, the copper being protected against particle bombardment by stainless steel plates at the side seen by the plasma. The Faraday screen was composed of TiC coated rods with different cross sections: the screen of one antenna consisted of T-shaped rods and was almost opaque while at the other antenna circular rods formed an optically open array /2,3/.

3. EXPERIMENTAL RESULTS

The surfaces of the dismanteled limiter elements and Faraday rods showed almost no visible modifications due to the plasma operation, while all parts below the Faraday screen of the optically open antenna - mainly the central conductor - showed a remarkable pattern of dark and bright stripes correlated with the position of the Faraday rods.
The distribution of metals and deuterium found on the TiC-coated Faraday rods and on the center conductor of the optically open antenna are shown in Fig. 2. In contrary to initial expectations carbon due to carbonization processes is almost homogeneously distributed and the dark stripes located in the shadow regions of the Faraday rods on the central conductor show a deposition of Fe and O. The bright stripes show clear maxima of D-implantation.
The distribution of wall material (Fe + Cr + Ni) and of Deuterium on the different Faraday rods is shown in Fig. 3. The concentration of both is clearly larger in front of the plasma than behind. The maxima of metals

---

[1] Guest scientist from Institute of Nuclear Research, Warshaw - Poland

are found at the sides or at half-shadowed surface parts of the rods while Deuterium shows a more homogeneous distribution with maxima rather in front of the plasma.
The deposition of silver on the inner surface of the opaque screen is much smaller than in the case of the optically open one (Fig.3) indicating that silver from the Ag-plated inner antenna surfaces is only eroded by particles coming from outside and not by arcing in the antenna. This is in agreement with the result, that the electrical strength in the open antenna is not worse compared to the closed one up to the tested level /2/.
The small content of tantalum and tungsten is possibly an impurity originating from the TiC coating process.
Figure 1 (upper side) shows the toroidal variation of the surface composition of the Faraday screen elements and of the protection limiters facing the plasma. While the D-concentration is similar for screen and limiter elements, the concentration of wall material (Fe + Cr + Ni) on the screen is considerably smaller than on the limiters.
The amount of Ti, Cu and Ag, measured on the carbon limiter blocks is much larger than at other areas of the torus, thus indicating sources in the direct neighbourhood: the TiC-coated Faraday screen, copper blocks of the limiter elements and the antenna side walls (Fig. 1).

4. POSSIBLE INTERPRETATIONS

The measured surface composition is the integrated result of deposition and erosion processes during tokamak operation and conditioning glow dicharges. Figure 4 shows schematically the relevant particle fluxes for both cases. During tokamak operation electrons and ions follow predominantly the mgnetic field lines, superposed by drift and plasma rotation movements. In addition, there are runaway electrons, energetic ions on drift orbits and charge exchange (D) neutrals moving in random directions. During the glow discharge the plasma (D^+) ions are accelerated in the sheath potential and move perpendicularly towards the wall and antenna structure. Their energy is of the order of a few 100 eV and thus sufficient to cause sputtering. Shadowing is only possible for charged particles.
The stripes inside the open antenna (Fig. 2) can be explained as being the result of random deposition of sputtered, not ionized wall material (Fe+Ni+Cr), possibly predominantly during glow discharges, and erosion at the unshadowed areas below the slits between Faraday rods by D-ions during the glow discharges. The profiles shown in Fig. 3 can also be explained by this shadow effect.
In order to explain the surface composition shown in Fig. 1, glow and tokamak discharges have to be taken into account. Since D-ions at plasma operations would be shadowed from the screen by the limiters, the almost homogeneous D content, implanted with energies below about 1 keV, is obviously the result of glow discharge ions and/or CX-neutrals in tokamak discharges. The small maxima at the ion side of the limiters can be due to an additional ion implantation in tokamak discharges.

The small Fe + Cr + Ni content on the screen situated more than 5 mm behind the first unshadowed magnetic surface could in principle be the result of an ion deposition during tokamak discharges, which is largely

reduced due to the shadowing limiters. But the maxima at the sides of the screen rods (Fig. 3) and limiter elements (Fig. 1, mainly at the left one) may rather indicate a homogeneous deposition and a subsequent erosion during tokamak discharges (the erosion during glow discharges should be similar at Faraday rods and limiters). In this case a special ion accelerating process by ICRH just in front of the active antenna area would have to be assumed to explain the erosion.This would be in agreement with the increase of antenna material impurity observed at ICRH operation in JET /5/. The Fe+Cr+Ni maxima at the outer limiter sides are comparable with the deposition on carbon limiters previously used in ASDEX /6/. They may be enlarged by the direct neighbourhood of the stainless steel plate protecting the copper blocks, while Cu and Ag may originate from the Cu blocks and the Ag coating of the Faraday screen support.

SUMMARY

The measured surface composition of the ICRH antenna and protecting limiter elements, dismanteled after an operation time of one and a half year, showed an implanted Deuterium and metal content which can only be explained by combined deposition and erosion processes during tokamak operation and glow discharge conditioning. Some results also indicate a special ion accelerating process during ICRH just in front of the active part of the antenna.

REFERENCES

/1/ K. Steinmetz et al., Proc. 11th Conf. on Plasma Phys. and Contr. Nucl. Fusion Research, Kyoto (1986).

/2/ J.-M. Noterdaeme et al., Proc. 13th Europ. Conf. on Contr. Fus. and Plasma Heating, Vol. II, 137 (1986)

/3/ J.-M.Noterdaeme et al., Proc.14th Symp.on Fus.Techn.,Vol.I, 795 (1986)

/4/ R. Behrisch et al., J.Nucl.Mat. 145-147, 731 (1987)

/5/ K.H. Behringer et al., see Ref. /2/, Vol. I, 176 (1986)

/6/ R. Behrisch et al., J. Nucl. Mat. 128-129, 470 (1984).

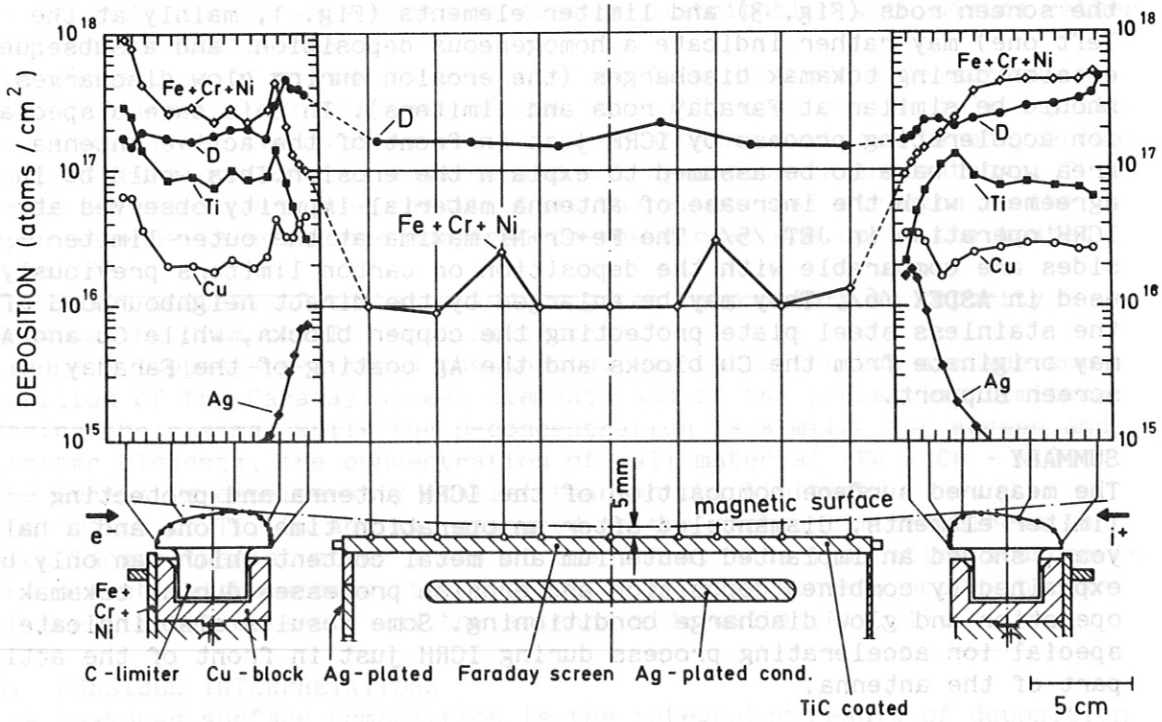

Fig. 1: Cross section of the antenna and protection limiters (lower part), and distribution of deuterium and metal depositions in toroidal direction.

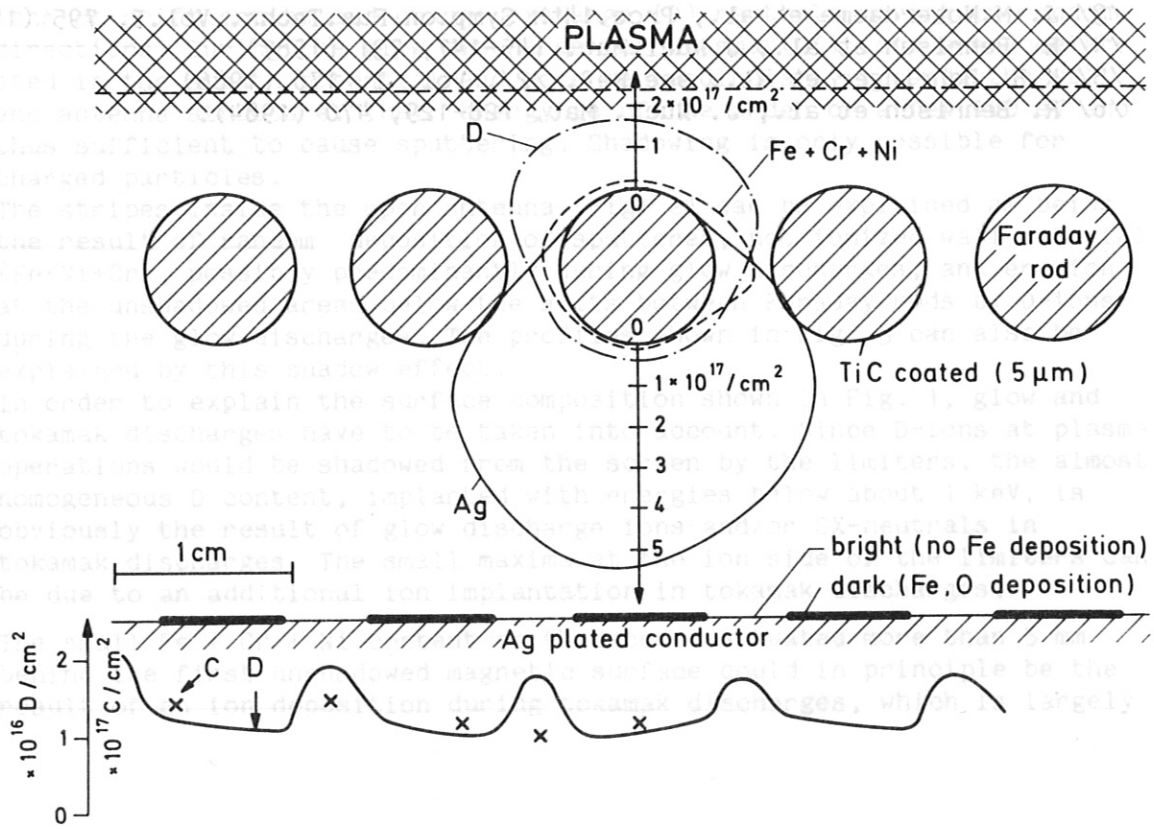

Fig. 2: Stripe pattern on the central conductor and surface composition on central conductor and on the rods of an open Faraday screen.

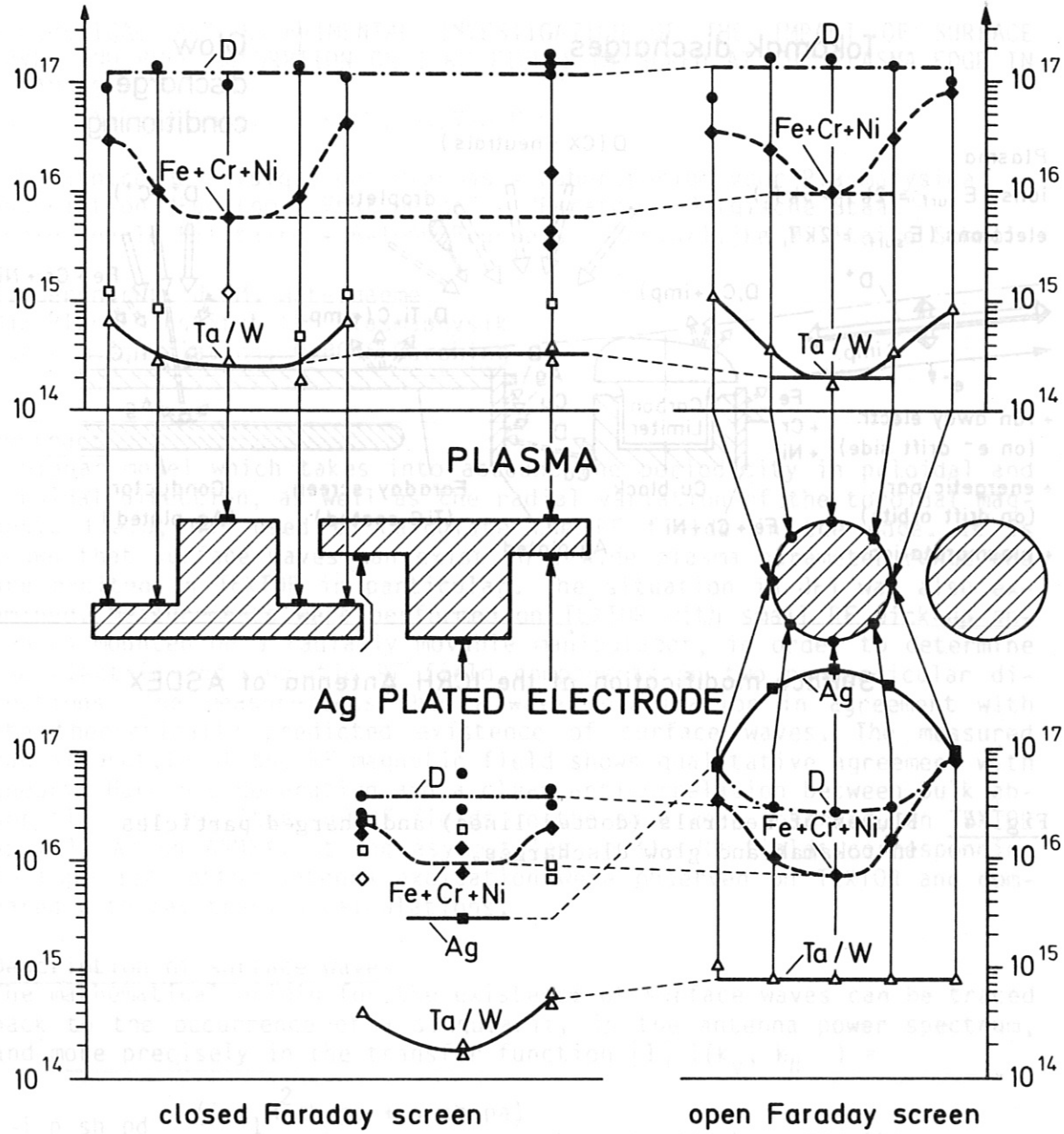

Fig. 3: Surface composition on the rods of the opaque and the optically open Faraday screen. The maxima at the sides and at shadowed parts can be explained by the lower density of eroding particles. Silver is found at the central conductor of the open antenna only.

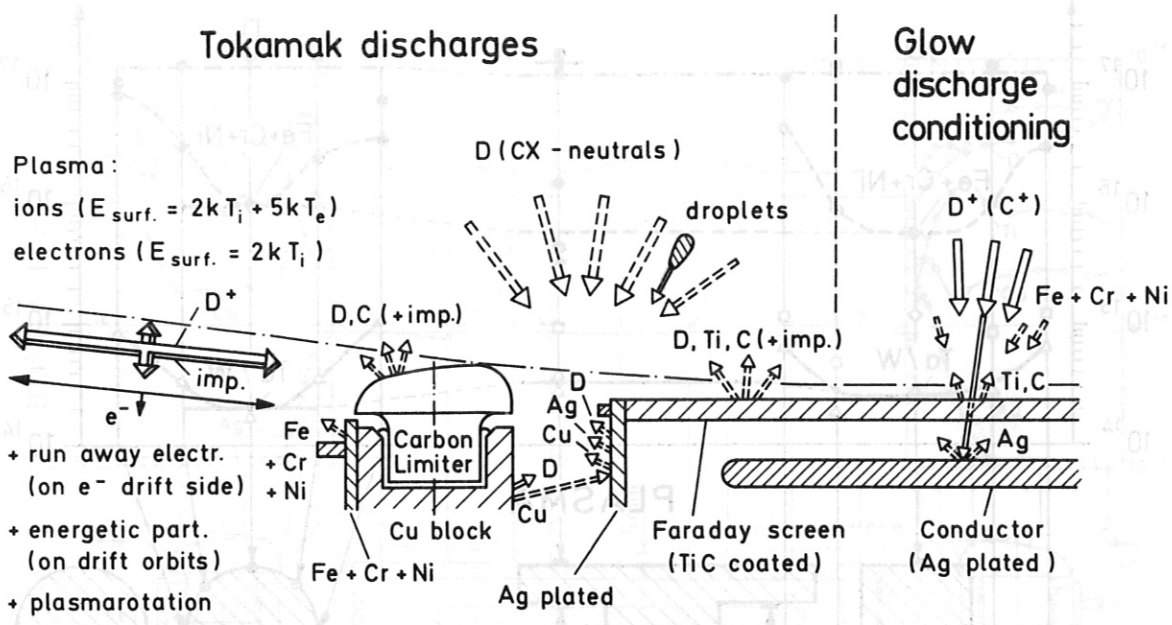

Surface modification at the ICRH Antenna of ASDEX

Fig. 4: Fluxes of neutrals (dotted lines) and charged particles in tokamak and glow discharges.

THEORETICAL AND EXPERIMENTAL INVESTIGATION OF THE IMPACT OF SURFACE WAVES AND BULK ABSORPTION ON ICRH FIELDS MEASURED AT THE PLASMA EDGE IN TOKAMAKS

R. Van Nieuwenhove, R. Koch, G. Van Oost

Laboratoire de Physique des Plasmas - Laboratorium voor Plasmafysica
Association "Euratom - Etat Belge" - "Euratom - Belgische Staat"
Ecole Royale Militaire - B-1040 Brussels - Koninklijke Militaire School

J. Gernhardt, J.-M. Noterdaeme
Max-Planck-Institut für Plasmaphysik
Euratom Association, D-8046 Garching

Abstract

A planar model which takes into account the periodicity in poloidal and toroidal direction, as well as the radial variation of the toroidal magnetic field, was used to calculate the RF fields in the edge. It is shown that surface waves can exist in a wide plasma parameter range and are excited in TEXTOR in particular. The situation in JET was also examined. Measurements were performed on TEXTOR with small RF pick-up antennas mounted on a radially movable manipulator, in order to determine the electric and magnetic RF field components in two perpendicular directions. The measurements show a wave polarization in agreement with the theoretically predicted existence of surface waves. The measured radial profile of the RF magnetic field shows qualitative agreement with theory. Harmonic generation and a clear anticorrelation between bulk absorption and amplitude of RF fields in the edge were observed, on TEXTOR as well as on ASDEX. Strong asymmetries in the RF fields corresponding to top- and bottom antenna excitation were observed on TEXTOR and compared with ray tracing calculations.

Description of surface waves

The mathematical origin for the existence of surface waves can be traced back to the occurrence of a singularity in the antenna power spectrum, and more precisely in the transfer function [1] $T(k_y, k_{//}) = \frac{-i\ p\ sh\ pd}{H^2} \frac{(i\ \xi_1 H^2 ch\ pa + p\ sh\ pa)}{\Delta}$ where k_y and $k_{//}$ are the poloidal and toroidal components of the wave vector, ξ_1 is proportional to the surface impedance of the inhomogeneous plasma for which only the cold magnetosonic wave is considered. Surface waves correspond to particular roots of $\Delta = i\ \xi_1 H^2 ch\ p(a + d) + p\ shp(a + d)$. $H^2 = k_0^2 - k_{//}^2$, $p^2 = k_y^2 - H^2$, all other notations are given in [1]. A contour plot of the imaginary part of T as a function of k_y and $k_{//}$ is shown in Fig. 1 for typical TEXTOR parameters. Due to the discretisation of k_y and $k_{//}$, $|\Delta| = 0$ is only approximately fulfilled, leading to maxima instead of infinities in T. The amplitude of these maxima, which reflect how strongly these waves are excited, may fluctuate considerably during a single plasma discharge due to large density fluctuations in the edge.

The periodic structure of the maxima is also a consequence of the discretisation of k_y and $k_{//}$. From Fig. 1 one can see that the maxima are located at low values of $k_{//}$ (2 to 4 m^{-1}) and high, positive values of k_y (order 30 m^{-1}). This high k_y value is characteristic of surface waves, for which k_y^2 must be larger than $k_\perp^2$ everywhere in the plasma; as $k_x = \sqrt{k_\perp^2 - k_y^2}$, $k_x \sim ik_y$ resulting in a radial decay of the form $\exp(-k_y x)$ with a decay length of about 3 cm. The effect of an increased edge density is a vertical shift of the dispersion curve (Fig. 1) towards somewhat higher values of $k_{//}$. The model calculation also shows that when collisions are taken into account, they transfer energy from the reactive part of the power spectrum into the active part, leading to power deposition in the edge. A simple phenomenological collision frequency model was used with frequencies of typically $\simeq$ 4 MHZ for usual edge conditions. The presence of surface waves does not lead to a significant additional power absorption. Even in their absence, the model shows that about 1 % of the power launched by the ICRH antennas is lost in the scrape-off layer (SOL). The order of magnitude of this power can account for the observed electron temperature increase in the SOL. In order to depict some of the distinct features of the surface wave, the magnetic induction poloidal (B_y) and toroidal (B_z) components are plotted (Fig. 2-a,b). B_z has approximately the same profile as in the absence of a surface wave, whereas By shows a periodic behaviour in the z direction with high maxima. Around these maxima B_y is larger than B_z, in contrast with the classical picture of the bulk plasma fast wave polarization. The profile of the poloidal electric field is shown in Fig. 2-c. Calculations for JET also show the possibility to excite surface waves even with k shaping.

Experimental set-up

On TEXTOR, the experiments were performed with two excitation antennas, one extending over the top half and one over the bottom half of the same poloidal cross-section. The RF pick-up probes were located at the low field side in the equatorial plane at a distance 1.15 m toroidally away from the ICRH antennas. For the magnetic measurements stainless steel single turn loops with a wire thickness of 1 mm were used. On ASDEX the measurements were only performed with a radial electric probe. The RF signals were either rectified by linear RF demodulators or connected to a spectrum analyser, after which they were fed to a CAMAC ADC.

Experimental results

The relation between the bulk absorption and the amplitude of the RF fields in the edge was obtained in a series of discharges in which the minority ^3He concentration was gradually changed. Figure 3 shows that all field components have a minimum at a ^3He concentration of around 3 % which is the optimal condition for central electron heating. The same anticorrelation between bulk absorption and minimum RF fields in the edge was observed on ASDEX, where the position of the resonance layer was varied during a toroidal magnetic field scan (Fig. 4). Figure 3 shows a B_y component that can be larger than or comparable to B_z depending on the ^3He concentration. The presence of surface waves seems necessary to explain the magnitude of B_y, while a flat B profile, which is

ding on the ^{3}He concentration. The presence of surface waves seems necessary to explain the magnitude of B_y, while a flat B profile, which is observed experimentally (Fig. 5), seems in agreement with theoretical profiles obtained in their absence. The extreme sensitivity of the surface wave excitation to density, seen theoretically, and the above-mentioned facts therefore suggest that surface waves may really be present in TEXTOR but that their excitation can be strongly dependent on operating conditions and might be time-averaged out in the profiles of Fig. 5, obtained in a series of shots. The second and third harmonics were observed on the electric and magnetic fields, with amplitudes of respectively 70 % and 5 % of the signal at the generator frequency. The high amplitude of these harmonics on the electric fields could be caused by the nonlinear sheath recification effect at the ICRH antenna or at the receiving probe [2]. Similar observations were also made on ASDEX. It was also observed that the RF fields in the edge produced by the bottom antenna could be 8 times larger than those of the top antenna at equal power levels. Ray tracing calculations could not explain this asymmetry, even taking into account the modified ion cyclotron wave [3]. However ray tracing neglects tunneling, which can be very high in the ^{3}He minority case [4] and might explain the observed asymmetries.

Acknowledgement
The authors like to thank D. Van Eester for the ray tracing calculations.

References

1) A.M. Messiaen et al., Proc. 4th Int. Symp. Heat. Tor. Plasma, Rome, 1 (1984) 315
2) F.M. Skiff et al., PPPL-2116, Princeton, 1984
3) K. Appert et al., Plasma Physics and Contr. Fusion, 28, (1986) 133, D.W. Faulconer et al., This conference
4) R. Koch et al., This conference

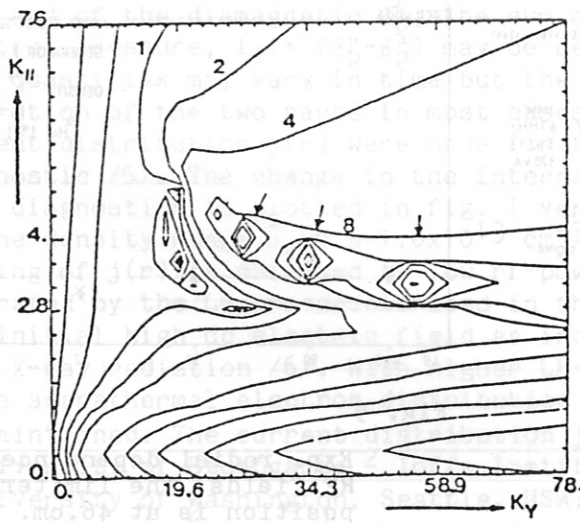

Fig. 1
Contour plot of $T(k_y, k_{//})$ in arbitrary units. The maxima are indicated by arrows.

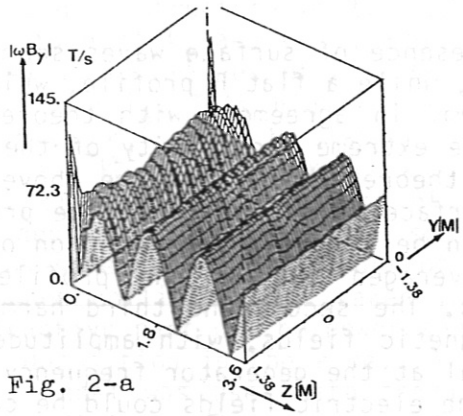

Fig. 2-a

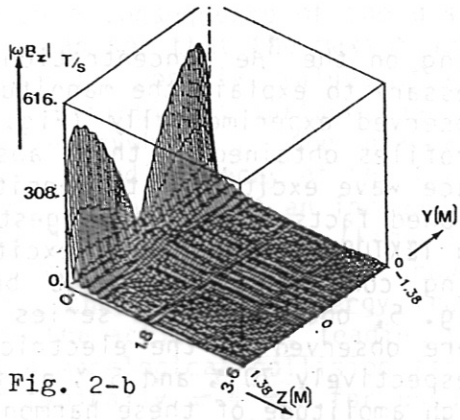

Fig. 2-b

Theoretical By and Bz profiles; the z and y-axes are resp. the tor. and pol. directions. The two antennas are located at $|z| \leq 8.7$ cm and are fed at y=0 . The length of each antenna is 1.37 m. The short circuit current is 1 A.

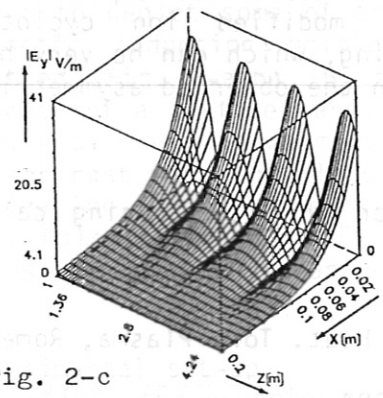

Fig. 2-c

Theoretical pol. electric field profile in tor. and radial (X) direction at y=0. The antenna screen is at X=0.9 cm.

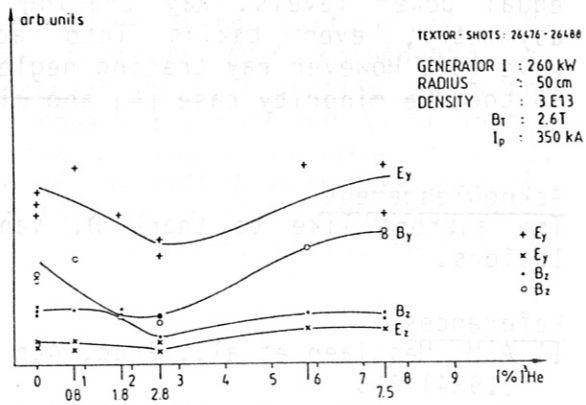

Fig. 3

RF field components in the edge measured during a ^{3}He scan.

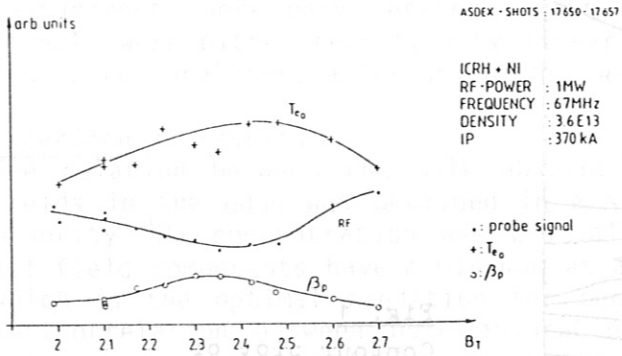

Fig. 4

BT scan; Te_o is the central electron temperature, β is the pol. Beta and RF is the probe signal.

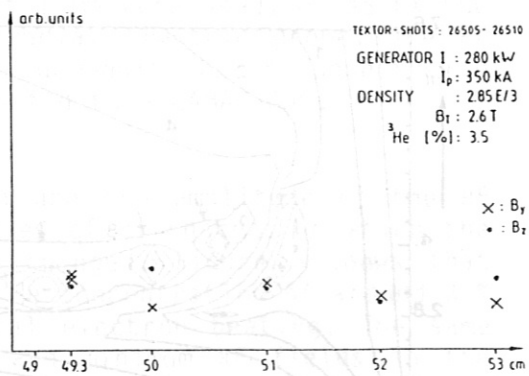

Fig. 5

Exp. radial dependence of RF fields. The limiter position is at 46.cm.

PROFILE CONTROL WITH LOWER HYBRID WAVES ON ASDEX

F.X. Söldner, K. McCormick, F. Leuterer, and G. Becker, H.S. Bosch, H. Brocken, A. Carlson, A. Eberhagen, G. Dodel[1], H.-U. Fahrbach, G. Fussmann, O. Gehre, J. Gernhardt, G. v.Gierke, E. Glock, O. Gruber, G. Haas, W. Herrmann, J. Hofmann, A. Izvozchikov[2], E. Holzhauer[1], K. Hübner[3], G. Janeschitz, F. Karger, M. Kaufmann, O. Klüber, M. Kornherr, K. Lackner, M. Lenoci, G. Lisitano, F. Mast, H.M. Mayer, D. Meisel, V. Mertens, E.R. Müller, M. Münich, H. Murmann, J. Neuhauser, H. Niedermeyer, A. Pietrzyk[4], W. Poschenrieder, H. Rapp, H. Riedler, A. Rudyj, F. Schneider, C. Setzensack, G. Siller, E. Speth, K. Steinmetz, K.-H. Steuer, N. Tsois[5], S. Ugniewski[6], O. Vollmer, F. Wagner, D. Zasche, M. Zouhar

Max-Planck-Institut für Plasmaphysik,
EURATOM Association, Garching, FRG

Introduction

Optimization of plasma current profiles may be a way to provide stability against MHD modes /1/. With inductive current drive, however, external control is impeded by the link between current density and electron temperature profiles. RF current drive therefore has been proposed for local profile shaping /2/. The largest current drive efficiency in a wide range of experimental applications has been obtained with Lower Hybrid current drive. Modification of the current profile and decoupling of $j(r)$ and $T_e(r)$ were demonstrated on ASDEX /3, 4/. In this paper the correlation between current profile changes and the behavior of MHD modes is studied. Local profile shaping by tailoring of the launched LH wave spectrum is investigated. The impact on electron density and temperature profiles and the relevance of profile consistency are discussed.

The form of the current density profile $j(r)$ can be characterized by the internal inductance l_i. From the two independent measurements of $\beta_p^{equ} + l_i/2$ and of the diamagnetic $\beta_p^{\perp}$, the sum of l_i and of the anisotropy in electron pressure, $l_i + (\beta_p^{\parallel} - \beta_p^{\perp})$ may be determined. With LH current drive both quantities may vary in time but the different time scales allow separation of the two parts in most cases. Direct measurements of the current distribution $j(r)$ were made for typical cases also with a Li-beam diagnostic /5/. The change in the internal inductance Δl_i as determined by both diagnostics is plotted in fig. 1 versus rf-power for LH-current drive in the density range $\bar{n}_e = 0.5\text{-}1.6 \times 10^{13}$ cm^{-3}. An increase of l_i and therefore peaking of $j(r)$ is obtained at low rf-power. The suprathermal electrons generated by the LH are accelerated in this case to very high energies by the initial high dc electric field as indicated by a continuous increase of hard X-ray radiation /6/. With higher LH-powers the loop voltage is reduced and a suprathermal electron distribution with an upper boundary of ~400 keV is maintained. The current distribution $j(r)$ broadens under these con-

[1] University of Stuttgart; [2] Ioffe Institute; [3] University of Heidelberg; [4] University of Washington, Seattle, USA; [5] N.R.C.N.S. "Democritos", Athens, Greece; [6] Inst. for Nuclear Research, Swierk, Poland;

ditions and l_i decreases as P_{LH} increases. The current distribution therefore is closely related to the form of the electron distribution function which is determined by the combination of inductive and rf-current drive. At high LH-power strong central electron heating results in a peaking of $T_e(r)$ while $j(r)$ is flattened. Thus, the resistive link between current and temperature profiles is then removed with LH-current drive.

Sawtooth oscillations are strongly influenced by modifications of the current profile. Peaking of $j(r)$ at low P_{LH} leads to an augmentation of the sawtooth amplitude. Above a threshold LH-power sawteeth are completely suppressed when $j(r)$ is flattened such that $q>1$ in the whole plasma /7/. Sawteeth can also be stabilized by this method in the presence of strong additional heating from NBI /8/. In the sawtooth-free phase higher central electron temperatures are obtained. The electron density also peaks with the steady-state profile being similar to that just before the sawtooth crash.

Steady-state sawtooth-free discharges can be maintained for the whole duration of the rf pulse ($\leq$1.5 s) with LH powers slightly above the threshold for sawtooth stabilization (30-50 % of the power required for complete current drive). If the LH power is further increased MHD modes with mode numbers $m=2,3$ /$n=1$ may be activated. The various regimes are shown in fig. 2 for a density scan with LH-current drive at constant power P_{LH}=750 kW. Δl_i is plotted together with a signal from Li-beam measurements $\Delta\theta_p(r=15\ cm)$ which is proportional to the change in fractional plasma current inside r=15 cm. At low density strong broadening of $j(r)$ with a resulting reduction of the internal inductance $-\Delta l_i$ up to 0.3 leads to the onset of m=2 modes several hundred ms after the stabilization of sawteeth. The total plasma current is driven by the LH in this density range. With increasing density the drop in l_i decreases. Sawteeth are still stabilized up to $\bar{n}_e=1.6\times10^{13}\ cm^{-3}$ where $-\Delta l_i\approx0.15$. Steady state discharges stable against sawteeth and other MHD modes are thus obtained in the density range $\bar{n}_e\approx0.8\text{-}1.6\times10^{13}\ cm^{-3}$. Towards higher densities the signal $\Delta\theta_p(r=15\ cm)$ decreases faster than $-\Delta l_i$. Above $\bar{n}_e=2\times10^{13}\ cm^{-3}$ the current distribution is no longer modified in the central region while the total current profile still broadens. This may be explained by a local flattening of $j(r)$ by the LH which is shifted towards the periphery with increasing density. With edge current drive a redistribution of the current in the center is not seen during pulse times of 1s possibly due to the long inductive time constants.

m=2 modes are readily destabilized by LH-current drive at low q(a). They appear shortly after suppression of sawteeth. In experiments at q(a)=2.1, m=2 modes are triggered immediately after begin of the rf pulse. In most cases they give rise to major disruptions. Sawteeth could not be stabilized under these conditions. With decreasing q(a) rf-generated modifications of the Ohmic $j(r)$ profile therefore increasingly provoke mode activity for the LH spectra investigated here. This may be caused by a steepening of $\nabla_r j(r)$ in the region of the q=2 surface due to the current redistribution.

Optimization of the current profile with respect to all modes therefore requires selective modification of j(r) with external control of the local absorption of the LH waves. In a series of experiments the shape of the LH wave spectrum was varied by adjusting the power fed into each one of the waveguides of the grill antenna /9/. Thereby $\bar{N}_{\parallel}$ could be varied in the range $1.9<\bar{N}_{\parallel}<3.2$ with highly directional current-drive spectra. The plasma current was kept constant at 300 kA by feedback control. The variation during LH of the residual Ohmic power input P_{OH}^{LH}, of Δl_i and $\Delta\theta_p(r=15\ cm)$ are shown in fig. 3. The results with a wider grill ($\bar{N}_{\parallel}(\Delta\phi=\pi)=3$) at $\Delta\phi=105^{o}$, $\bar{N}_{\parallel}=1.65$ are also included in this figure. With increasing $\bar{N}_{\parallel}$ the current-drive efficiency is reduced as expected from theory. Therefore the additional Ohmic input P_{OH}^{LH} has to be increased. The change of the current profile characterized by Δl_i and $\Delta\theta_p(r=15\ cm)$, however, is enhanced with increasing $\bar{N}_{\parallel}$, i.e. with decreasing rf-driven current. This can be explained only by a shift of the LH current deposition zone to larger radii and a resulting flattening of j(r) closer to the plasma surface. This is confirmed by local current profile measurements. They show also an increase of $-\Delta l_i$ with $\bar{N}_{\parallel}$ but simultaneously a decrease of the change of j(r) in the center:

$\bar{N}_{\parallel}=1.65$: $-\Delta l_i=0.04$, $\Delta q(0)=0.3$

$\bar{N}_{\parallel}=3.1$: $-\Delta l_i=0.16$, $\Delta q(0)=0.11$.

The displacement of the LH deposition zone is also clearly seen in the modification of the electron temperature profiles as shown in fig. 4. The ratio $T_e^{LH}(r)/T_e^{OH}(r)$ of the local values is calculated at each radius; the points in fig. 4 refer to the actual data points, the solid lines to fitted analytic profiles for $T_e(r)$. This form of local normalization of the profiles leads to a better criterion for profile consistency which then would require a constant factor of temperature change for all radii, i.e. straight horizontal lines in fig. 4. With LH-current drive, strong electron heating is achieved in the center for low $\bar{N}_{\parallel}$, while edge heating and cooling of the center are observed at high $\bar{N}_{\parallel}$. This shows that a large variety of electron temperature profiles can be obtained with LH current drive which are not subject to profile consistency.

As shown in these experiments, the form of current and temperature profiles is governed by the local deposition of LH power. The position of the absorption zone can be varied externally by varying the launched wave spectrum. This allows for an active control of plasma profiles, where sawteeth and MHD modes with higher m numbers might be suppressed simultaneously.

References

/1/ A.H. Glasser, et al., Phys. Rev. Lett. 38, 234 (1977)
/2/ A.H. Reiman, Phys. Fluids 26, 1338 (1983)
/3/ K. McCormick, et al., 12th Europ. Conf. on Contr. Fusion and Plasma Physics, Budapest 1985, Vol. I, p. 199
/4/ K. McCormick, et al., Phys. Rev. Lett. 58, 491 (1987)
/5/ K. McCormick, et al., 13th Europ. Conf. on Contr. Fusion and Plasma Physics, Schliersee, 1986, Vol. Vol. II, p. 323
/6/ F.X. Söldner, et al., internal report IPP II/111 (1986)
/7/ F.X. Söldner, et al., Phys. Rev. Lett. 57, 1137 (1986)
/8/ F.X. Söldner, et al., ref. 5, Vol. II, p. 319
/9/ F. Leuterer, et al., ref. 5, Vol. II, p. 409

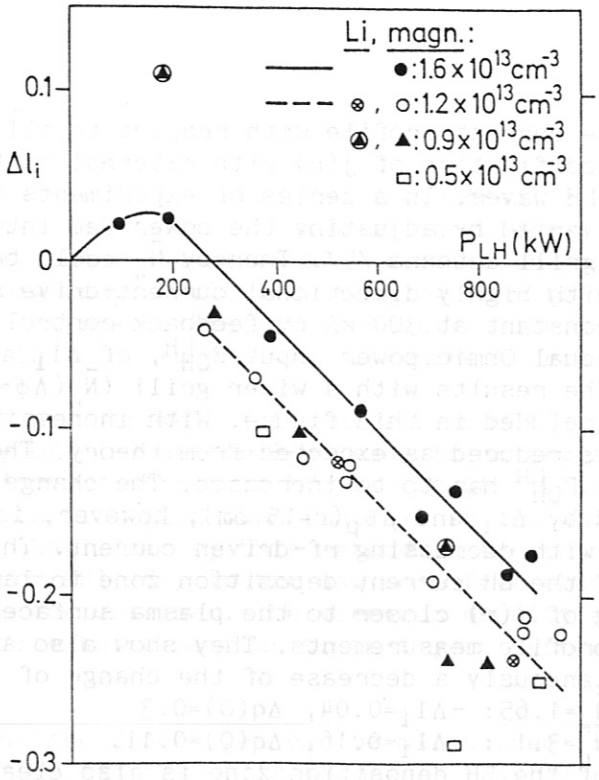

Fig. 1: Variation of Δl_i with P_{LH} during LH-current drive, from magnetic and Li-beam measurements.

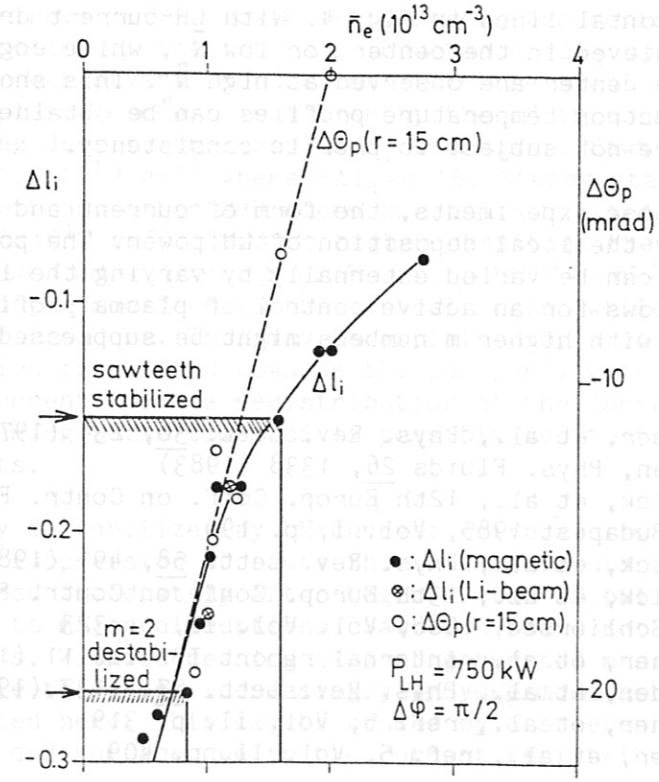

Fig. 2: Variation of Δl_i and of the monitor signal $\Delta\theta_p$ (r=15 cm) with $\bar{n}_e$. I_p = 300 kA, B_t = 2.17 T, q(a) = 3.5.

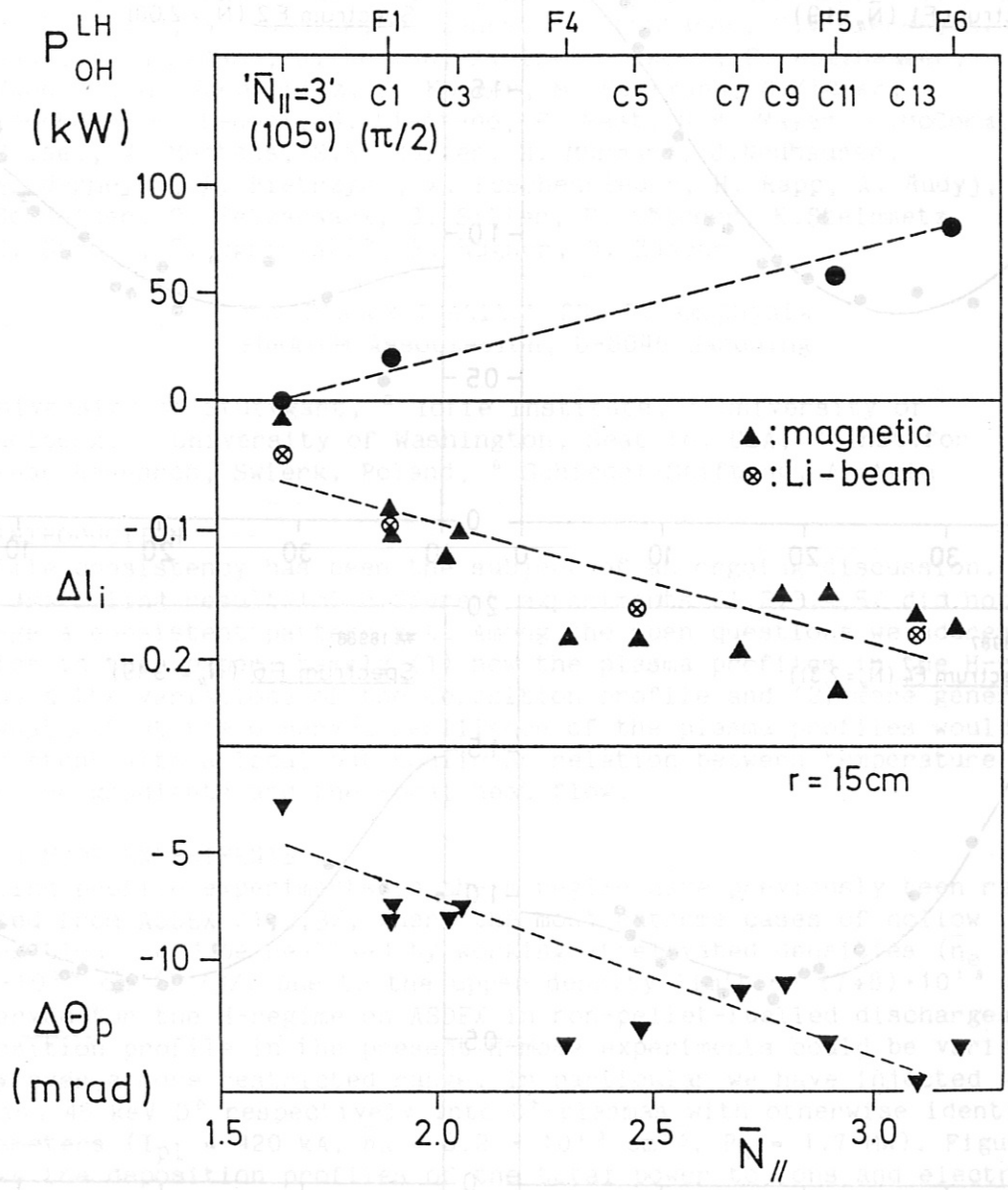

Fig. 3: Residual Ohmic power input P_{OH}^{LH}, Δl_i and $\Delta\theta p$(r=15 cm) for LH-current drive with P_{LH}=350 kW at different $\bar{N}_{\parallel}$. P_{LH}=350 kW at different $\bar{N}_{\parallel}$. I_p=300 kA, B_t=2.17 T.

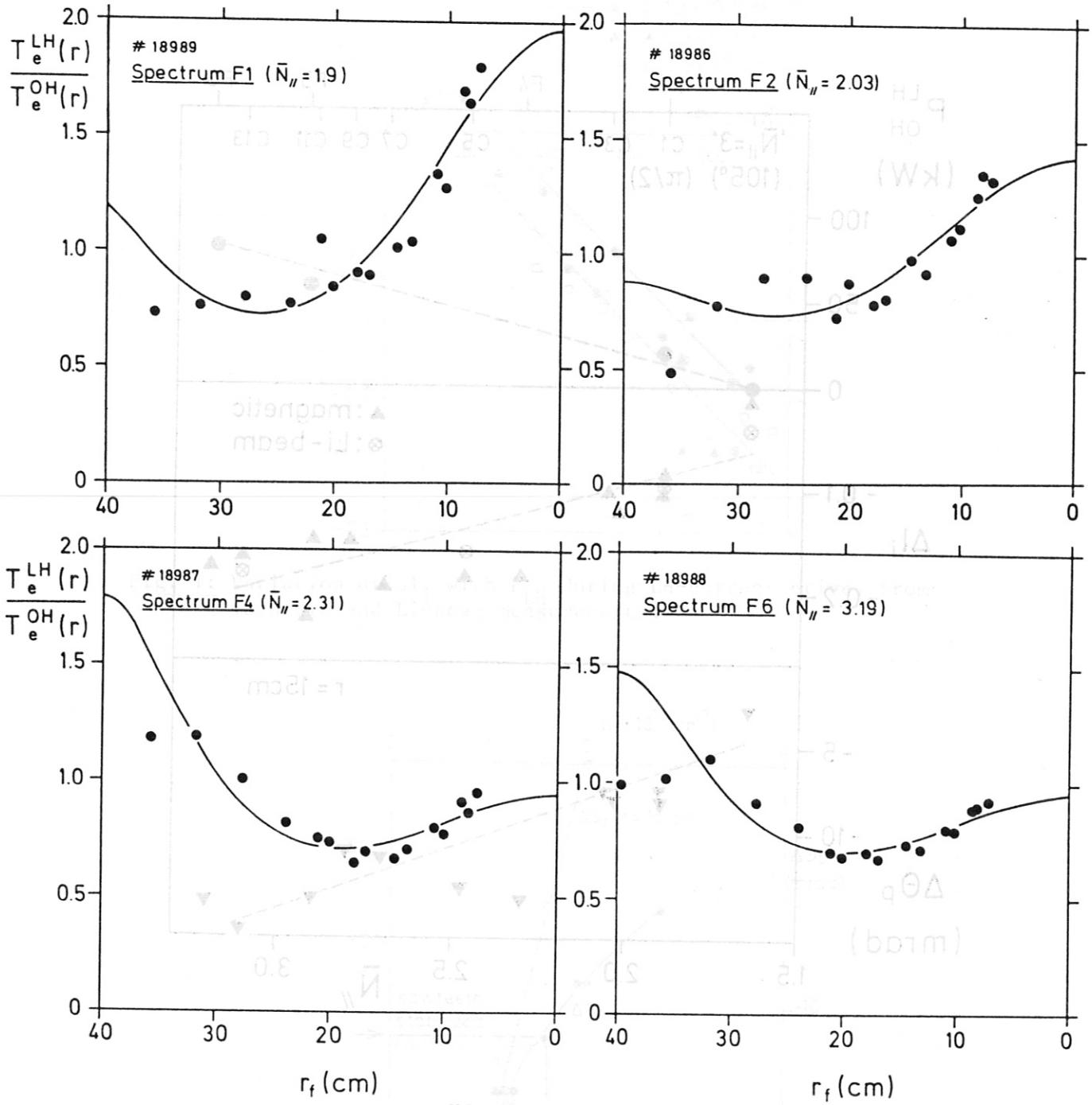

Fig. 4: Change of the electron temperature profile for different LH-current drive spectra.

RESPONSE OF PLASMA PROFILES TO NEUTRAL BEAM POWER DEPOSITION IN ASDEX

E. Speth, O. Gruber, K. Lackner, H. Riedler[6], A. Stäbler, O. Vollmer, G. Becker, H.S. Bosch, H. Brocken, A. Carlson, A. Eberhagen, G. Dodel[1], H.-U. Fahrbach, G. Fußmann, O. Gehre, J. Gernhardt, G.v.Gierke, E. Glock. G. Haas, W. Herrmann, J. Hofman, A. Izvozchikov[2], E. Holzhauser, K. Hübner[3], G. Janeschitz, F. Karger, M. Kaufmann, O.Klüber, M. Kornherr, M. Lenoci, G. Lisitano, F. Mast, H.M. Mayer, K.McCormick, D. Meisel, V. Mertens, E.R. Müller, H. Murmann, J.Neuhauser, H. Niedermeyer, A. Pietrzyk[4], W. Poschenrieder, H. Rapp, A. Rudyj, F. Schneider, C. Setzensack, G. Siller, F. Söldner, K.Steinmetz, K.-H. Steuer, S. Ugniewski[5], F. Wagner, D. Zasche

Max-Planck-Institut für Plasmaphysik
EURATOM Association, D-8046 Garching

[1] University of Stuttgart, [2] Ioffe Institute, [3] University of Heidelberg, [4] University of Washington, Seattle, USA, [5] Inst.for Nuclear Research, Swierk, Poland, [6] Schiedel-Stiftung, Austria

1. INTRODUCTION

Profile consistency has been the subject of an ongoing discussion. From the prevailing results of different experiments /1,2,3,4,5/ did not emerge a consistent pattern yet. Among the open questions we address two topics in this paper: namely (1) how the plasma profiles in the H-regime respond the variations of the deposition profile and (2) more generally, to what extent the observed resilience of the plasma profiles would be consistent with a local but nonlinear relation between temperature - or pressure gradients and the local heat flow.

2. H-MODE EXPERIMENTS

Heating profile experiments in the L-regime have previously been reported from ASDEX /1,2,3/, where the most extreme cases of hollow deposition could be realised by working at elevated densities ($\bar{n}_e$ = $1.1 \cdot 10^{14}$ cm^{-3}) /3/. Due to the upper density limit of $(7 \div 8) \cdot 10^{13}$ cm^{-3} observed for the H-regime on ASDEX in non-pellet-fuelled discharges, the deposition profile in the present H-mode experiments could be varied only over a more restricted range. In particular we have injected 40 keV H^0 and 45 keV D^0 respectively into D^+-plasmas with otherwise identical parameters (I_{pl} = 420 kA, $\bar{n}_e = 6.2 \cdot 10^{13}$ cm^{-3}, P_N = 1.7 MW). Figure 1 shows the deposition profiles of the total power to ions and electrons as computed with the FREYA-code including the ohmic power. The subsequent response of the pressure profiles is shown in Fig. 2: there is no significant difference. The beam-induced change on plasma composition and the known isotope effect on confinement should be small, since the profiles analysed are taken 150 msec after the beams are turned on.

Table 1

	No. 13 079 (45 keV $D^0 \rightarrow D_2$)	No. 13 381 (40 keV $H^0 \rightarrow D_2$)
$T_e(0)$	(1.33 ± 0.15) keV	(1.25 ± 0.17) keV
τ_E (a)	58 msec	51 msec
$\tau_{Ee}(0)$	158 msec	96 msec

(Concerning the rather lowish global confinement times (for the H-mode) one should note that the burst frquency of the ELM's dramatically increases when approaching the upper density limit in the H-mode; consequently the confinement time is considerably reduced in comparison to the medium density cases or the quiescent H*-mode.)

3. NONLOCAL HEAT TRANSFER

Theoretical examinations by other groups have shown the incompatibility of predictions of standard first principle drift wave theories with the experimentally observed T_e-profiles. This resilience has led to the proposition /6/ that a globally acting principle has to be invoked to explain their very weak variation with any change of power deposition. As an alternative explanation, we compare the response predicted by empirical heat transport laws containing a nonlinear relation between temperature- or pressure-gradients and the local heat flow.
For the stated purpose of a rather qualitative illustration we make a number of simplifying assumption which otherwise would have to be viewed critically. So we do not distinguish between electron and ion transport (assuming $T_e = T_i$). We use in the following calculations two heat transport models, a linear one

$$q_{heat} = - f_1(r) \cdot \nabla p \qquad (1)$$

and a quadratic one

$$q_{heat} = f_2(r) \cdot (\nabla p)^2 \qquad (2)$$

with f_1 and f_2 chosen as $f_1(r) = f_2(r) = (1 + (r/a)^2)^3$. Only relative variations will be considered, so that no absolute coefficient values need to be specified (q_{heat} ... radial heat flux density).

As a realistic example we consider the two extreme deposition profiles reported in /2/, which are more or less identical to the ones in Fig. 1. The corresponding unnormalised profiles are shown in Figs. 3a and 3b. They show, in spite of the large apparent difference in the power deposition, a remarkable small difference already for the linear transport model case, which is further diminished when changing over to the quadratic transport law.
The above examples show that on the basis of presently available data it seems difficult to rule out a local, nonlinear transport law as an explanation of the observed profile resilience in tokamaks. A nonlinear transport law of the form (2) would automatically link profile resilience to confinement degradation with power as globally observed in

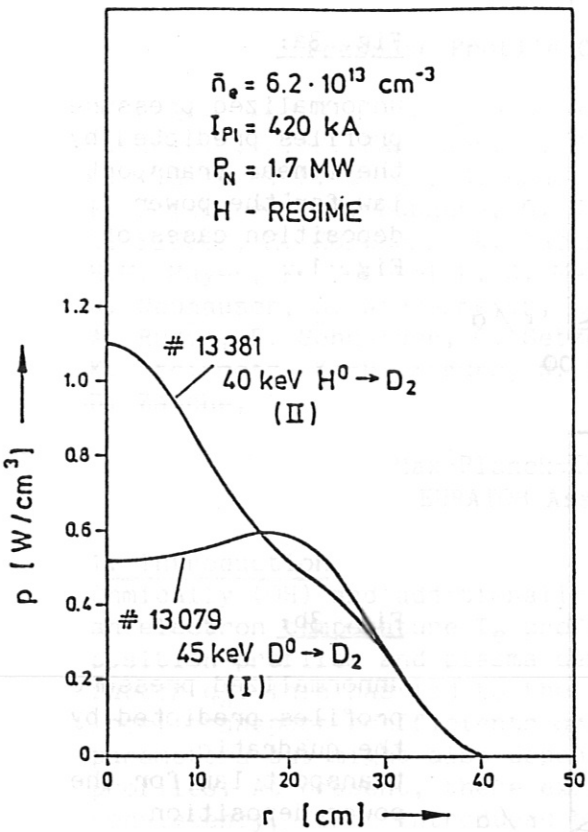

Fig. 1:
Deposition profiles of the total power to ions and electrons including ohmic power.

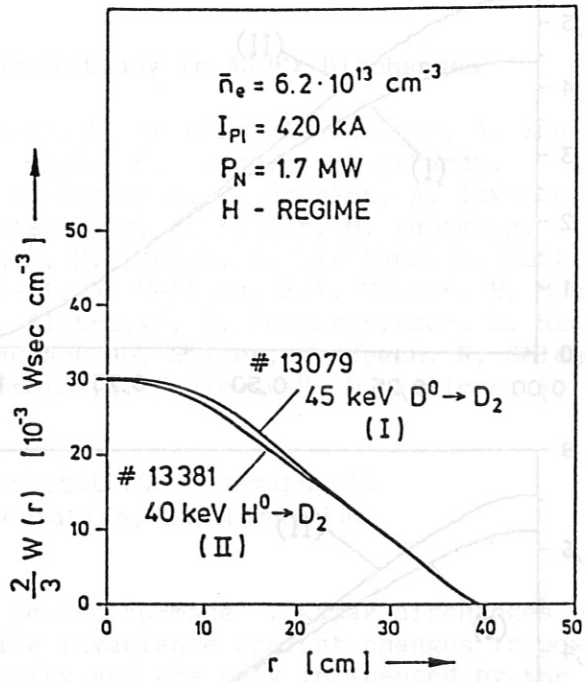

Fig. 2:
Resulting experimental pressure profiles for the power deposition cases of Fig. 1
$2/3\ W(r)=\int n_e(r)(T_e(r)+T_i(r))dV$
The T_i-profiles not being known precisely, electron pressure and ion pressure form factors were assumed to be identical and the integrated energy content was normalised to the diamagnetic signal (fast ions neglected).

Typical parameters of the two cases are compared in Table 1. Although the Te-profiles (not shown here) establish the well-known differences to those in the L-regime, (pedestal at the edge) their shape agrees within the error bars, and also the previous findings in the L-regime concerning deposition profile changes /1/ are valid: $\tau_{Ee}(0)$ shows a 60% enhancement, $\tau_E(a)$ is about 15 % higher, $T_e(0)$ is marginally higher for hollow deposition. Thus the conclusions drawn previously /1,2/ for profile invariances in the L-Regime appear to be applicable to the H-regime too at least within the range of presently accessible deposition profiles.

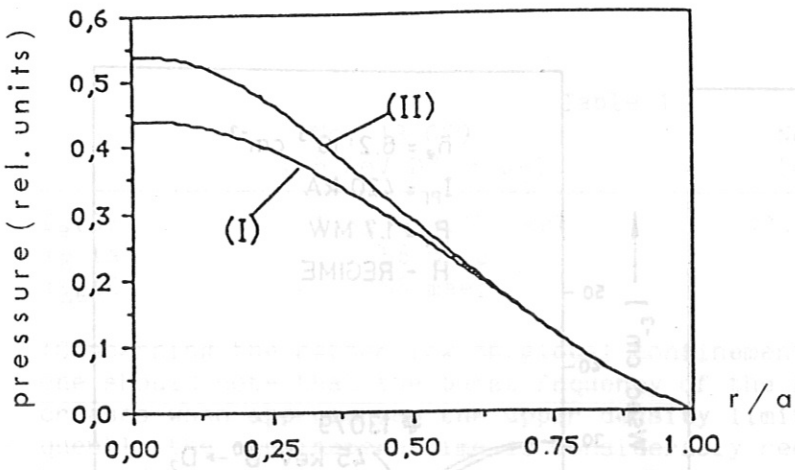

Fig. 3a:

unnormalized pressure profiles predicted by the linear transport law for the power deposition cases of Fig. 1.

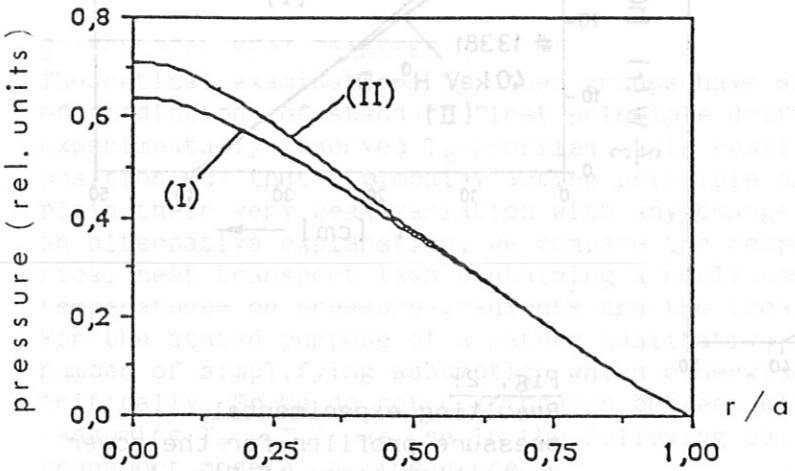

Fig. 3b:

unnormalized pressure profiles predicted by the quadratic transport law for the power deposition cases of Fig. 1.

L-discharges. Power independence of confinement times as observed in ASDEX H-mode discharges could however be made compatible with strong profile resilience e.g. by an ansatz $q_{heat} \sim (\nabla p/p) \cdot \nabla p$. The considerations can of course not rigorously disprove the explanation that plasma profile shapes are determined by some non-local principle. One so far unanswered argument in favour of such a more global explanation is the sharp transition between L- and H-mode behaviour, and the obvious non-existence of mixed situations where part of the plasma volume is in the L- and the other in the H-regime.

REFERENCES

/1/ E. Speth et al., Proc. 12th EPS Conference, Budapest (1985), Vol. II, 284

/2/ F. Wagner et al., Phys. Rev. Lett. 56 (1986) 2187

/3/ E. Speth et al., Proc. 13th EPS Conference, Schliersee (1986), Vol. II, p. 281

/4/ R.J. Goldston et al., ibid. P. 41

/5/ J.G. Cordey et al., Proc. 11 Int. IAEA Conf., Kyoto (1986) paper A-II-3.

/6/ H.P. Furth, Plasma Physics and Contr. Fus. 28, 9A (1986) 1305

Pressure Profile Consistency in ASDEX Discharges

O. Gruber and G. Becker, H.S. Bosch, H. Brocken, A. Carlson, A. Eberhagen, G. Dodel[1], H.-U. Fahrbach, G. Fussmann, O. Gehre, J. Gernhardt, G. v.Gierke, E. Glock, G. Haas, W. Herrmann, J. Hofmann, A. Izvozchikov[2], E. Holzhauer[1], K. Hübner[3], G. Janeschitz, F. Karger, M. Kaufmann, O. Klüber, M. Kornherr, K. Lackner, M. Lenoci, G. Lisitano, F. Mast, H.M. Mayer, K. McCormick, D. Meisel, V. Mertens, E.R. Müller, H. Murmann, J. Neuhauser, H. Niedermeyer, A. Pietrzyk[4], W. Poschenrieder, H. Rapp, A. Rudyj, F. Schneider, C. Setzensack, G. Siller, E. Speth, F. Söldner, K. Steinmetz, K.-H. Steuer, N. Tsois[5], S. Ugniewski[6], O. Vollmer, F. Wagner, D. Zasche,

Max-Planck-Institut für Plasmaphysik
EURATOM Association, Garching, FRG

1. Introduction

Ohmically (OH) and additionally heated "L-mode" Tokamak discharges exhibit an electron temperature T_e profile invariance against changes in power deposition profiles and plasma density and are only influenced by the safety factor q_a. This has led to the concept of "profile consistency" where the local transport coefficients are not only a function of local plasma parameters but might also depend on non-local processes adjusting the T_e profiles. At present, there exists no coinvincing model for this profile consistency, first introduced by B. Coppi to describe the current density behaviour and the connected T_e profiles of Ohmic heated plasmas. But if the thermal transport is governed, for instance, by electromagnetic modes, not only the current density should show a canonical profile, but also the pressure (p) gradient profiles. Moreover, these profiles can adjust after changes of the heating deposition much faster than the current density, and any deviation from the canonical profile might then result in an additional heat transport which can be expected to act complementory on ion and electrons.

According to Kadomtsev /1/, a pressure profile consistency arises from the existence of relaxed states with thermal and poloidal field minimized subject to a single (constant current) or two constraints (constant current and helicity of the magnetic field). With such a strong principle the resulting pressure and current density profiles depend on the ratio q_a/q_o only and, depending on the constraint, are finite or zero, respectively, at the plasma boundary r=a. Profiles for both cases approach each other at high q_a/q_o. In this paper we examine the total pressure profile shapes in all phases of ASDEX discharges (OH, L and H mode) and compare them with the T_e profiles.

2. T_e and pressure profiles in OH and L mode discharges

There is no commonly agreed format of the T_e profile normalization showing an invariance for different operating conditions. With increasing order of

[1] University of Stuttgart; [2] Ioffe Institute; [3] University of Heidelberg; [4] University of Washington, Seattle, USA; [5] N.R.C.N.S. "Democritos", Athens, Greece; [6] Inst. for Nuclear Research, Swierk, Poland;

the profile consistency quality, the possibilities proposed are: $T(0)/\langle T\rangle$, $T(r)/T(a/2)$ or $\ln(T(r)/T(a/2)$ and $1/T\cdot dT/dr$. Using the normalizaiton $T(r)/T(a/2)$ ASDEX T_e-profiles coincide within the error bars and discharge to discharge variations outside the q=1 surfaces ($r_{q=1}\approx a/q_a$) for all OH- and L-mode discharge conditions as is shown in Fig. 1 (Thomson scattering measurements). Data from discharges are used for which transport analyses with the TRANSP code have been carried out including stationary and unstationary discharge phases and the following parameter variations: I_p=300÷440 kA, $\bar{n}_e$=1÷11·$10^{19}m^{-3}$; $P_h\leqq$3.8 MW; strong on- and off-axis heating deposition profiles /2/ and pellet refuelled discharges /3/.
For different q_a-values deviations can be seen at radii $r<r_{q=1}$, but differences exist also in the confinement zone between q=1 and q=2 (which is roughly at $r_{q=2}\approx a/\sqrt{q_a/2}$). This is more clearly demonstrated in Fig. 2 showing for the same discharges the radial profiles of the upper and lower bounds of the normalized T_e scale length r_{Te} given by the inverse logarithmic derivative $r_{Te}/a = -(T_e/dT_e/dr)/a$. Part of the q_a-dependence is certainly due to the T_e-flattening inside the sawtooth region. At fixed q_a there is a weak T_e profile response to changes in the heating profile yielding broader profiles, i.e. higher r_{Te}, with increasing off-axis heat deposition. The latter is obtained by using a lower energy/nucleon of the injected fast neutrals or an increasing density (beam deposition at larger radii, broader resistivity profile due to higher collisionality and reduced $T_e(0)$).

The total kinetic pressure profiles are obtained by using the TRANSP analyses code. Input data are the $n_e(r,t)$ and $T_e(r,t)$ profiles measured by a 16-spatial channel multi-pulse Thomson scattering system and supplemented by a HCN-laser interferometer and ECE diagnostic (4 channels both), the bolometrically measured profiles of the radiation losses and global parameters like the loop voltage V_L, I_p, $\beta_{p\perp}$ from diamagnetic flux measurements and $\beta_{p_\parallel}+l_i/2$ as deduced from poloidal fields and fluxes. Lacking a measurement of the full ion temperature T_i profiles for all discharges we assume a spatially constant enhancement factor α of about 2 to 3 of the ion heat diffusivity χ_i over the neoclassical value as calculated by Chang and Hinton, checking the resulting T_i profiles for their compatibility with the available neutron production and T_i measurements (passive and active CX diagnostic, Doppler broadening of impurity lines). The calculated kinetic pressures include also the contributions due to the anisotropic fast beam ions (using Monte Carlo calculations for the deposition and slowing-down of the beam particles) and are in good agreement with the magnetically measured ones. Fig. 3 shows the pressure scale length r_p for the discharges of Fig. 1 and 2 exhibiting a somewhat stronger separation of the two q_a data sets, which are not in disagreement with the Kadomtsev p(a)=0 pressure profiles. The influence of the χ_i assumption was estimated by taking α-values between 1 and 5, yielding r_p variations below 10%.

3. H-mode profiles

The invariance of the pressure profiles is even more impressive if we look at their time development during single discharges as is shown for a β-limit discharge in Fig. 4. Fig. 4a demonstrates the strong T_e profile variation at the L/H mode transition where the T_e profile flattens in the

center (higher r_{Te}) and develops shoulders towards the boundary. After reaching β_{max} the T_e profiles flatten even more in the center due to increasing central radiation losses /4, 5/. As also the density profiles form shoulders in the H-mode, the electron pressure (p_e) profiles do the same (see Fig. 4b) but are by far not comparable to the second class of Kadomtsev-profiles with $p(a)\neq 0$ which would have nearly constant r_p for $0.5a<r<a$. Contrary to p_e, the total pressure profile is nearly time independent. In this discharge, the fast ions contribute up to 40 % of the pressure and a comparable amount to the pressure gradient and the ion temperature is well above T_e. The universality of the p profile shape is also demonstrated by comparing H-mode discharges both with H^o and D^o injection, i.e. different deposition profiles (see Fig. 5). The disappearance of the q_a-dependence might be partly caused by the lack of sawteeth.

4. Conclusions

The total pressure profiles of ASDEX discharges exhibit a canonical shape which is preserved also in the H-mode contrary to a changing T_e profile shape. There exists one exception namely the high confinement pellet refuelled discharges revealing a steeper pressure gradient and smaller scale lengths /3/. For instances in a q_a=2.5 ohmic pellet discharge the r_p/a profile is about at the lower bound of the gas fuelled discharges shown in Fig. 3. This might be related to the process limiting the pressure shape yielding a lower bound for the r_p profile which is nearly reached in these pellet discharges. It is interesting that only in the pellet discharges η_i-values below 1 are observed over a large part of the plasma column.

References

/1/ B. Kadomtsev, IAEA-Meeting on Confinement in Tokamaks with Intense Heating, (Nov. 1986), Kyoto

/2/ O. Gruber, et al., Proc. 13th Europ. Conf. on Contr. Fusion and Plasma Heating, Schliersee 1986, Europhys. Conf. Abstr. **10C** Part I (1986) 248.

/3/ G. Vlases, O. Gruber, M. Kaufmann, et al., Nucl. Fusion, **27** (1987) 351
M. Kaufmann, et al., to be published in Nucl. Fusion

/4/ O. Gruber, et al., Proc. 11th Conf. on Plasma Phys. and Contr. Nucl. Fus. Research, Kyoto, 1986

/5/ O. Gruber, et al., Proc. 12th Europ. Conf. on Contr. Fusion and Plasma Physics, Budapest 1985, Europhys. Conf. Abstr. 9F, Part I(1985) 18

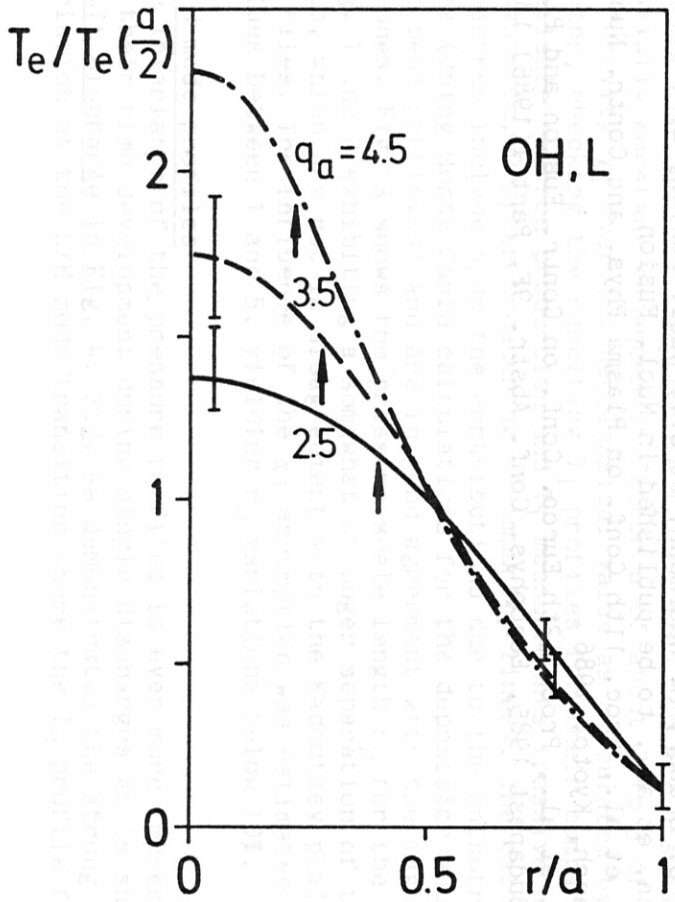

Fig.1: Averaged T_e profiles normalized to $T_e(a/2)$ vs. flux surface radius r in ohmic and L-mode discharges at q_a= 2.5±0.1, and q_a=3.5 ± 0.2, and for a comparison discharge at q_a=4.5.

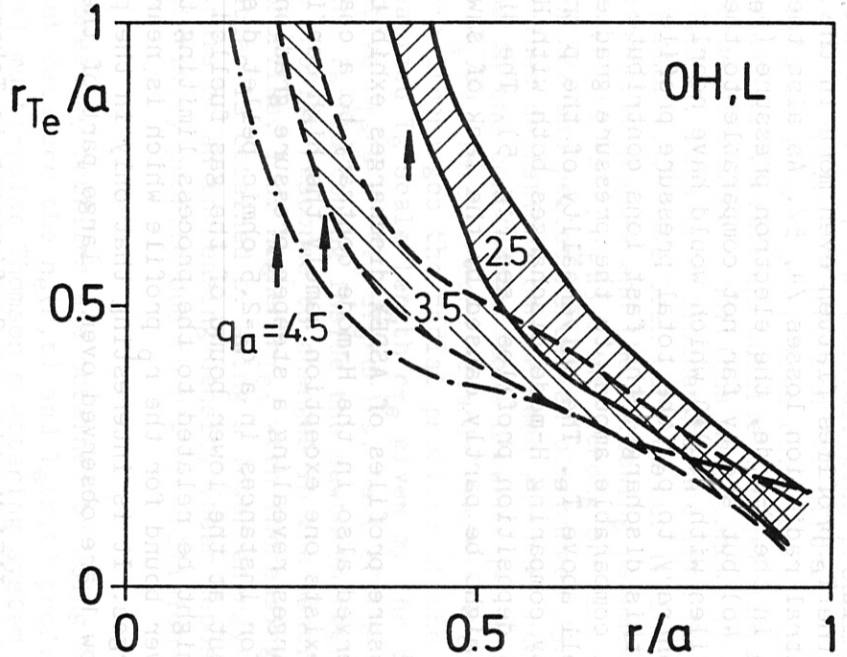

Fig.2: Radial profiles of the upper and lower bounds of the T_e scale length $r_{Te}=-T_e/(dT_e/dr)$ normalized to a for the discharges used in Fig. 1 (OH, L-mode).

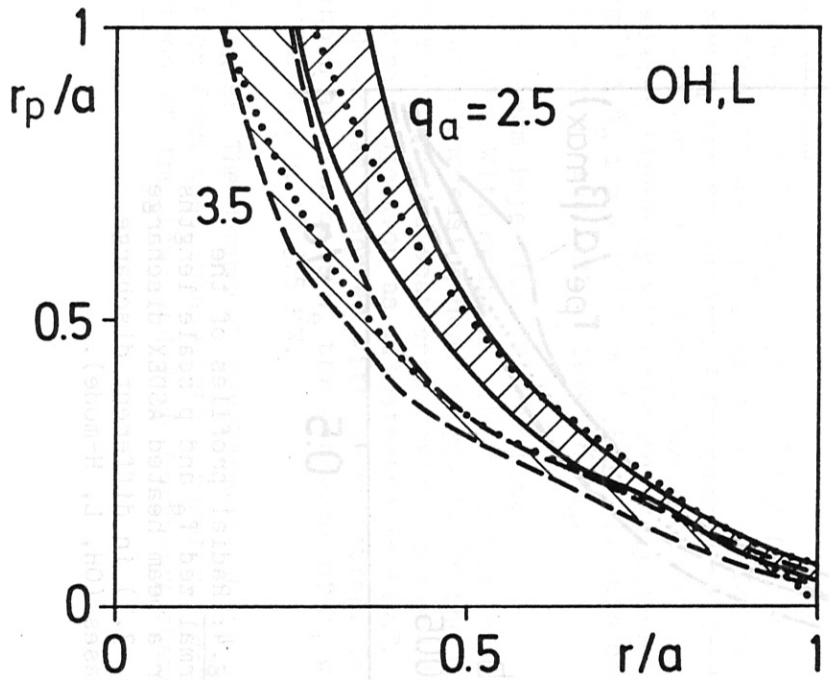

Fig.3: Radial profiles of the upper and lower bounds of the normalized pressure scale length r_p/a (OH, L-mode). The dotted lines are the Kadomtsev pressure profiles with p(a)=0 for q_a=2.5 and 3.5.

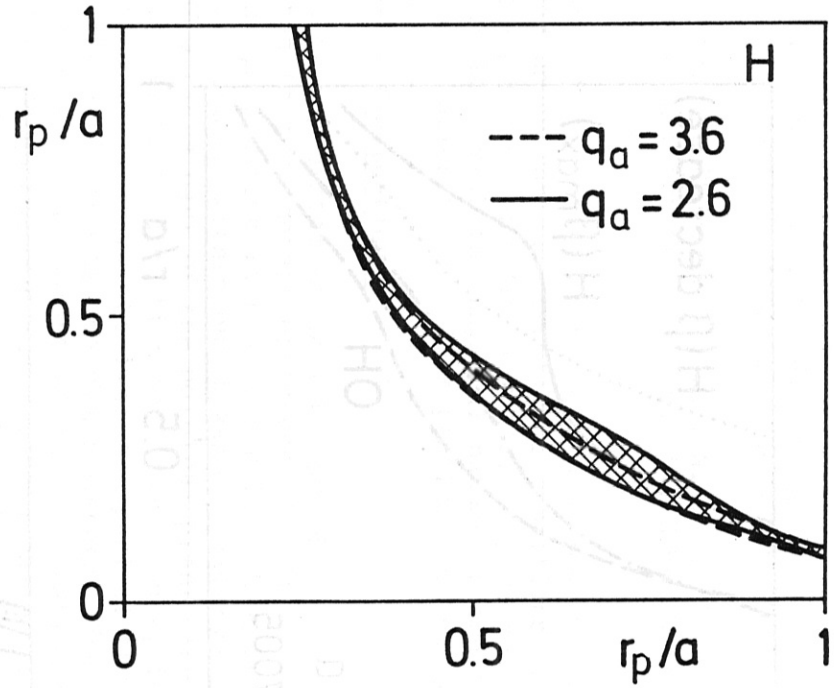

Fig.5: Radial profiles of the bounds of the normalized pressure scale length for beam-heated H mode discharges.

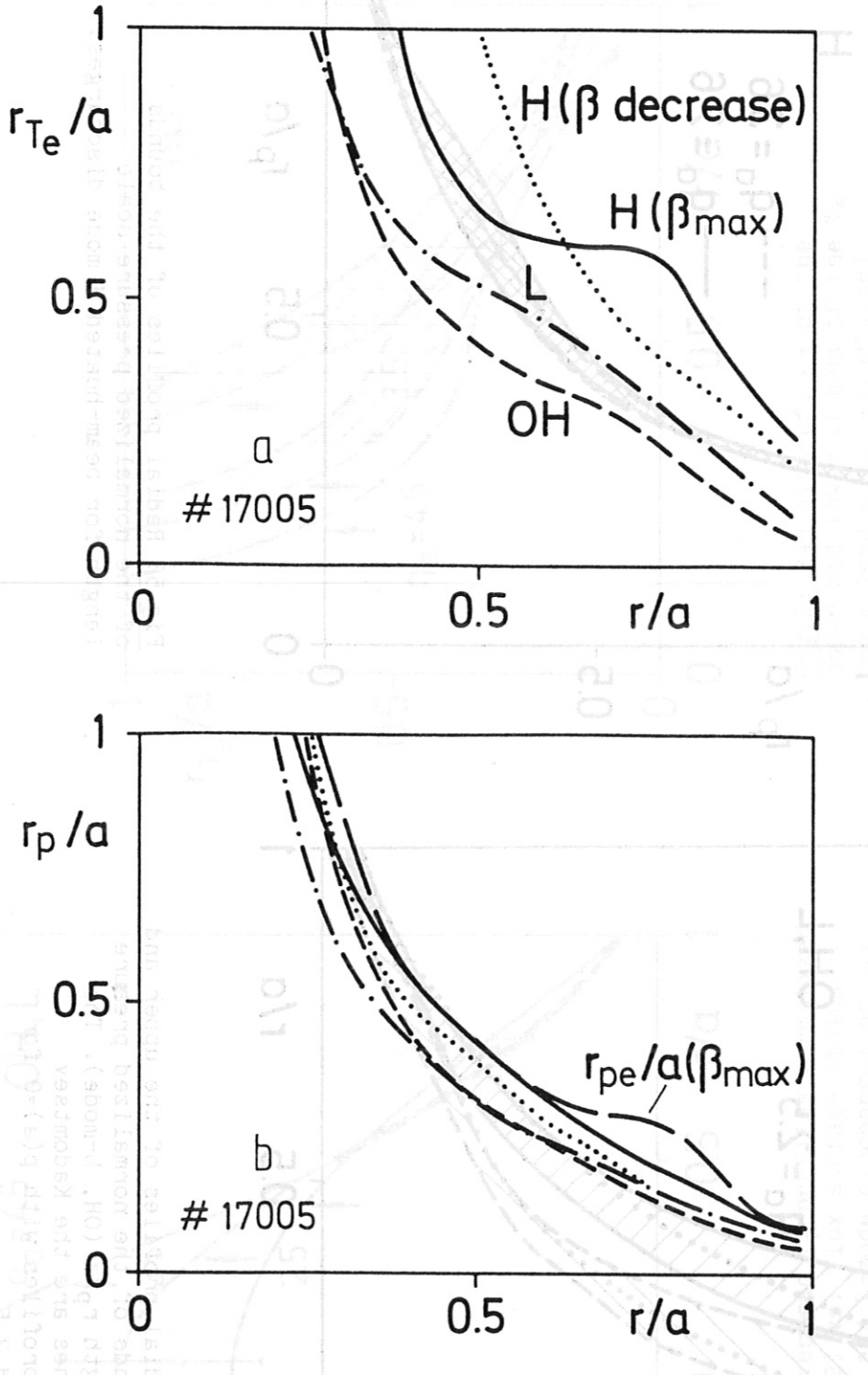

Fig.4: Radial profiles of the normalized T_e and p scale lengths for a beam heated ASDEX discharge (q_a=3.7) in different discharge phases (OH, L, H-mode).

MEASUREMENT OF DENSITY TURBULENCE AND BROADBAND MAGNETIC FLUCTUATIONS ON ASDEX

G. Dodel, E. Holzhauer, and J. Massig
Institut für Plasmaforschung, Universität Stuttgart, Fed. Rep. of Germany

J. Gernhardt, ASDEX-, ICRH-, LH-, NI-, and Pellet-Teams,
Max-Planck-Institut für Plasmaphysik, EURATOM-Association, Garching, FRG

Broadband fluctuations of the electron density and the magnetic field were observed under various operational conditions of ASDEX using a laser scattering experiment and Mirnov coils, respectively. The aim of such measurements is to reveal the physical nature of the fluctuations and their possible correlation to anomalous particle and energy transport properties.

1. Density fluctuations.

The scattering system using a 119 µm CH_3OH laser and homodyne detection is described in more detail elsewhere [1]. It is able to detect density fluctuations propagating in nearly vertical direction. Movable optics allow a stepwise $k_\perp$-scan within one tokamak discharge and a shot to shot spatial scan of a large part of the poloidal plane. The spatial resolution is ± 1 cm in the vertical direction and depends on $k_\perp$ in the horizontal direction. For $k_\perp \leq 10\ cm^{-1}$, where the dominant part of the fluctuation spectrum is found, the measurements are chord-averaged. The $k_\perp$ resolution is ± 3.2 cm^{-1}.

The temporal development of the fluctuation spectra could be monitored with fixed frequency channels. Plateau phases of the tokamak discharge allowed frequency spectra to be scanned continuously with a spectrum analyzer.

a) Ohmic heating
In the range $5\ cm^{-1} \leq k_\perp \leq 20\ cm^{-1}$ the frequency integrated scattered power $P_s(k_\perp)$ decreases as $k_\perp^{-\alpha}$, where $\alpha \approx 4$. The frequency power spectra $P_s(f)$ for fixed $k_\perp$ are broadband. A frequency roll-off on the order of 6 dB/100 kHz is observed above 100 kHz. The root of the frequency integrated power $P_s^{1/2}$ scales linearly with the mean electron density $\bar{n}_e$ in the range $5 \times 10^{12}\ cm^{-3} \leq \bar{n}_e \leq 5 \times 10^{13}\ cm^{-3}$ (Fig. 1). This corresponds to a nearly constant relative fluctuation level $\tilde{n}_e/n_e$.

b) Neutral beam injection (NI) heating.
L-discharges: With neutral injection the frequency spectra $P_s(f)$ become broader with increasing heating power. In the majority of L-discharges the frequency integrated scattered power increased above the ohmic level during neutral injection as illustrated in Fig.2. A maximum enhancement by a factor of ~9 was observed with co-injection. In a series of counter-injection shots at constant n_e the increase of P_s with P_{NI} was approximately linear for P_{NI} up to 3.5 MW.

H-discharges: The temporal development of the fluctuation spectra at the transition from the L-phase into a burstfree H-phase is shown in Fig. 3. A comparison of the low- and high frequency channels shows a broadening of

the spectrum and a decrease in the frequency integrated scattered power although the line density $\bar{n}_e$ increases. A similar observation was reported in [3]. There is evidence for a shift in the $k_\perp$ spectrum towards longer fluctuation wavelengths. In contrast to the sharp L-H transition indicated by the D_α- monitor in the divertor chamber the frequency integrated scattered power changes on a much longer time scale, which corresponds to the global change in the density and temperature profiles.

In normal H-discharges with edge-localized modes the behaviour of the scattering signals is irregular.

c) Ion cyclotron resonance heating.
The scattering signals increase above the ohmic level for $k_\perp \leqq 5\ cm^{-1}$ as reported also by [4]. Density fluctuations with $k_\perp \leqq 7.5\ cm^{-1}$ are observed at the heating frequency (33.5 and 67 MHz).

d) Lower hybrid heating and current drive.
No significant changes in the low-frequency density fluctuations with respect to the ohmic phase are found.

e) Sawtooth activity.
Precursors to the sawtooth crash in the soft X-ray signals are observed in the frequency range > 500 kHz. There is experimental evidence that they are localized only inside the q=1 surface. Increased fluctuations below 500 kHz are also found outside the q=1 surface, but only after the sawtooth crash [1].

f) Pellet injection.
An increase of the scattered signal is observed which starts with the ablation of the pellet. For single pellets the scattered signal decreases with the relaxation of the radial density profile [1].

In order to obtain a conclusive picture of the nature of the density turbulence and possible correlations to anomalous transport properties the measurements will be extended to wavenumbers below $5\ cm^{-1}$.

2. Magnetic fluctuations.

Mirnov coils in the limiter shadow of ASDEX were used to demonstrate the existence of broadband magnetic fluctuations with radial and poloidal components. Above about 70 kHz the temporal evolution of these spectra is distinctly different from the coherent Mirnov oscillations and their harmonics at lower frequencies.

If we assume that the field due to current disturbances decays like a vacuum field outside the plasma boundary in a cylindrical geometry, we can estimate the dominant poloidal mode number. For L-mode discharges with NI the plasma position, and thus the distance to the Mirnov coil, were varied. From the observed radial decay length a value of $m \geqq 10$ is deduced. Typical fluctuation levels at the probe position were $\tilde{B}_r/B_t \approx 10^{-5}$. From 70 kHz to 200 kHz the spectral power density drops by a factor of 10. No qualitative

difference was seen in the temporal development of the radial and poloidal field components.

a) Ohmic heating.
The power spectra of the magnetic fluctuations are not correlated with those of the density fluctuations. During a linear density ramp the signal power of the magnetic fluctuations decreased slightly in contrast to the density fluctuations (Fig. 1).

b) Additional heating (L-phase).
The signal power increases for all types of heating used and the frequency spectrum broadens. An example recorded during an L-discharge with NI is given in Fig. 2.

c) Additional heating (H-phase).
After the transition into a burstfree H-phase the signal power begins to increase again as shown in Fig.4. When edge localized modes, indicated by spikes in the D_α signal, appear, the magnetic fluctuation signal is strongly modulated.

d) Sawtooth activity.
In the presence of sawteeth (during additional heating) the fluctuations suddenly increase at the time of the sawtooth crash, similarly to the D_α-signal observed in the divertor chamber [2].

e) Influence of boundary layer.
The magnetic probe signals seem to depend on conditions in the plasma boundary layer, as can be seen in the case of gas puffing or the modulation by edge localized modes.

3. Summary.

Significant but distinct changes in the fluctuation spectra have been observed in the various operating regimes of ASDEX. When comparing the behaviour of the density and magnetic field fluctuations it should be kept in mind that the two diagnostics have different spatial weighting functions, defined by the scattering volume in the former case and by the distance from the probe and the mode number m in the latter case. Further experiments will be needed before a comparison with proposed theoretical models for the fluctuations and their propagation mechanism inside the plasma can be made.

References

[1] Dodel, G., Holzhauer, E., Massig, J., Vogel, T., Ignacz, P., ASDEX-, ICRH-, LH-, NI-, and Pellet-Teams, in "Basic and Advanced Diagnostic Techniques for Fusion Plasmas", Varenna (Italy), Sept. 1986, Vol.II, p.589 DOC. CEC EUR-10797 EN.
[2] IPP Garching, Annual Report 1986, p. 15
[3] Crowley, T., and Mazzucato, E., Nucl. Fusion 25, (1985), 507
[4] TFR Group, and Truc, A., Plasma Phys., 27, (1985), 1057

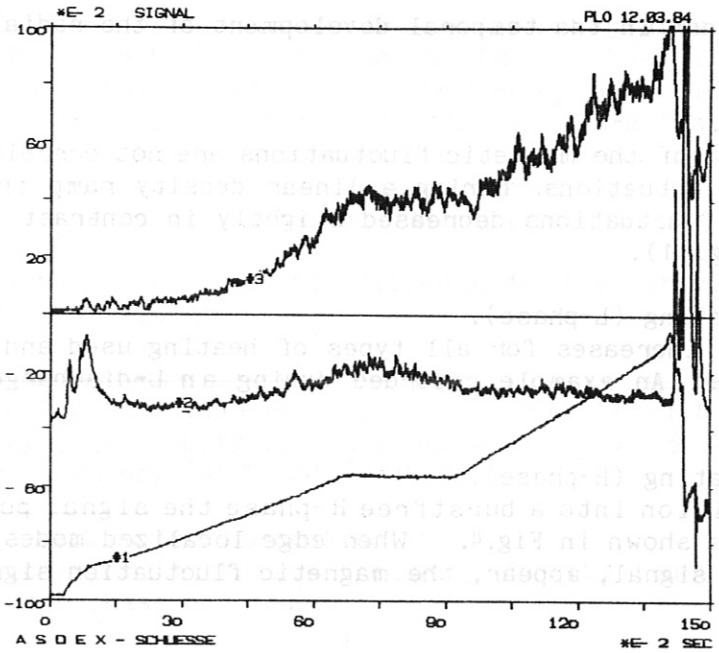

Fig.1 Density- and magnetic fluctuation signals in a shot with density ramping. From top to bottom: rms-scattering signal $P_s^{1/2}$; f = 100 ± 15 kHz; $k_\perp$ = 7.5 cm^{-1}. Magnetic signal power; f = 100 ± 15 kHz. Line electron density $\bar{n}_e$. (Full time interval of abscissa: 1.5 s).

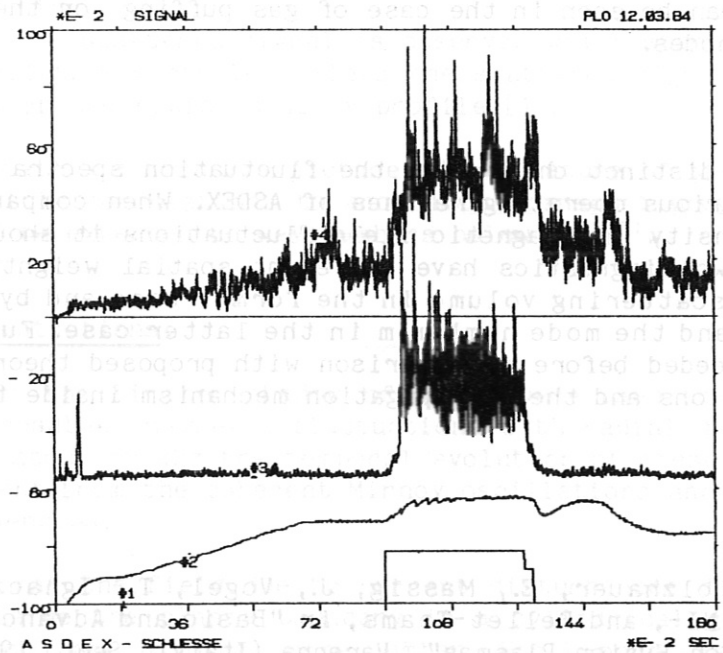

Fig.2 Density- and magnetic fluctuation signals in an L-discharge with NI. From top to bottom: Scattering signal P_s; f = 60 kHz - 1600 kHz; $k_\perp$ = 7.5 cm^{-1}. Magnetic signal power; f = 100 ± 15 kHz. Line electron density $\bar{n}_e$. NI beam monitor; P_{NI} = 2.64 MW. (Full time interval of abscissa: 1.8 s)

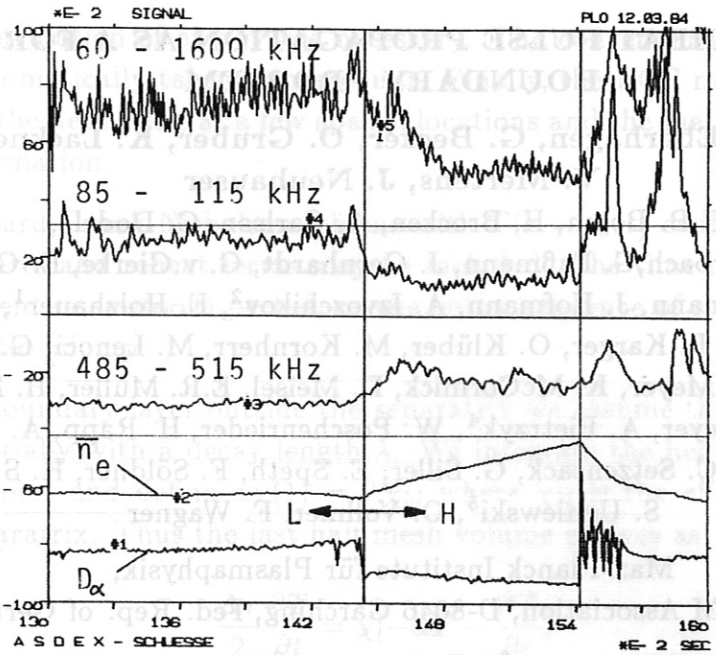

Fig.3 Density fluctuation signals in different frequency channels at the transition from an L-phase into a burstfree H-phase. $k_\perp = 5\ cm^{-1}$. Lower traces: line electron density $\bar{n}_e$ and D_α-monitor. (Full time interval of abscissa: 300 ms).

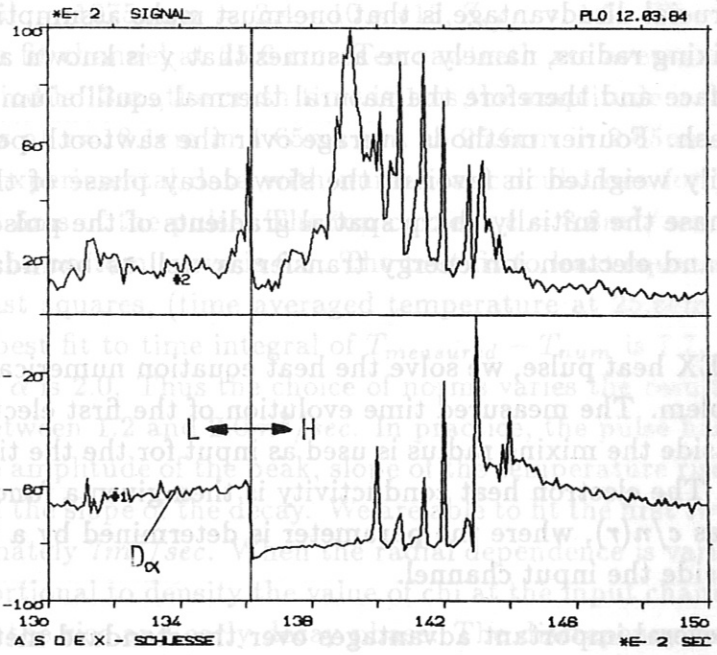

Fig.4 Magnetic fluctuation signal power at the transition from an L-phase into a burstfree H-phase followed by edge localized modes; f = 100 ± 15 kHz. Lower trace: D_α-monitor. (Full time interval of abscissa: 200 ms).

ASDEX HEAT PULSE PROPAGATION AS A FORCED BOUNDARY PROBLEM

K.S. Riedel, A. Eberhagen, G. Becker, O. Gruber, K. Lackner, O. Gehre
V. Mertens, J. Neuhauser
H.B. Bosch, H. Brocken, A. Carlson, G. Dodel[1],
H.U. Fahrbach,G. Fußmann, J. Gernhardt, G. v.Gierke, E. Glock,
G. Haas, W. Hermann, J. Hofmann, A. Izvozchikov[2], E. Holzhauer[1], K. Hübner[3],
G. Janeschitz, F. Karger, O. Klüber, M. Kornherr, M. Lenoci, G. Lisitano,
F. Mast, H.M. Meyer, K. McCormick, D. Meisel, E.R. Müller, H. Murmann,
H. Niedermeyer, A. Pietrzyk[4], W. Poschenrieder, H. Rapp, A. Rudyj,
F. Schneider, C. Setzensack, G. Siller, E. Speth, F. Söldner, K. Steinmetz,
S. Ugniewski[5], O. Vollmer, F. Wagner

Max-Planck Institute für Plasmaphysik,
EURATOM Association, D-8046 Garching, Fed. Rep. of Germany

[1]University of Stuttgart, [2]Ioffe Institute, [3]University of Heidelberg,
[4]University of Washington, Seattle, USA, [5]Inst. for Nuclear Research, Swierk, Poland

Traditionally, two types of methods are used to determine the eletron heat conductivity, χ: initial value and Fourier. Initial value analyses compare the observed temporal evolution during the rise phase of the heat pulse with Kadomtsev's model for sawtooth reconnection. The crucial disadvantage is that one must make assumptions about the plasma inside the mixing radius, namely one assumes that χ is known and unchanged inside the $q = 1$ surface and therefore the natural thermal equilibrium is the temperature before the crash. Fourier methods average over the sawtooth period and thus the results are heavily weighted in favor of the slow decay phase of the heat pulse. During this latter phase the initially sharp spatial gradients of the pulse have relaxed and Ohmic heating and electron ion energy transfer as well as boundary conditions become important.

To analyze the ASDEX heat pulse, we solve the heat equation numerically as a forced boundary value problem. The measured time evolution of the first electron cyclotron emission channel outside the mixing radius is used as input for the the time dependent boundary condition. The electron heat conductivity is then given a functionally parametrized form such as $c/n(r)$, where the parameter is determined by a best fit to the channels located outside the input channel.

This approach has several important advantages over the standard method of fitting the arrival time of the peak of the pulse to a theoretically initialized perturbation. The region inside the mixing surface, where the conductivity may be anomalously large, is excluded from consideration. No assumptions on the position of the $q = 1$ surface or

the radial redistribution of energy are necessary. The conversion of magnetic energy into heat is automatically taken into account. Finally, the ECE measurements give a time history of the heat pulse at a few spatial locations and the method makes effective use of this information.

We use a standard Crank-Nicholson scheme with $T(r = r_o, t)$ evolving in time. Convective, dissipative and reheat terms may be included. The time interval may be the rise phase, the entire sawtooth period, or the entire sequence of sawteeth to simulate the effect of pulse pile up.

To model the boundary layer outside the separatrix we assume that the temperature decays exponentially with a decay length λ. We integrate the heat equation over the last half grid point and define $\alpha\chi(1) = \lambda\chi_{bl}$ where χ_{bl} is the effective conductivity outside the separatrix. Thus the last half mesh volume evolves as

$$\frac{\Delta r}{2}\frac{\partial T}{\partial t} = \chi[-\alpha T - \frac{\partial T}{\partial r}]$$

where the minus denotes the inside derivative. Since the boundary layer is believed to be a highly nonlinear function we treat α as a free parameter. Results which depend sensitively on α are of little value.

The method is tested on a standard Ohmic discharge with the following parameters, $q(a) = 3.3, T(0) = 1075ev, n = 2.4 * 10 * *13, Z_{eff} = 1.3$. The input channel is at 18.1cm and the fit channel at 25.6 cm. Ten sawteeth are averaged over the sawtooth period.The period is 13ms,the crash time is 1ms,the amplitude is 90ev,and the peak of the pulse arives at r=18.1cm in 1.65ms and at 25.6cm in 2.65ms. Figure 1 compares the smoothed experimental data with numerical calculations for $\chi = c * n(.47)/n(r)$ during the first 5ms of the pulse. The top curve is $c = 8.8m^2/sec$, the middle curve is $7.7m/sec$ and the bottom curve is 6.5. The best fit to least squares integral is 7.35, to the relative least squares, (time averaged temperature at 25.6cm normallized to 1.0) is 6.8 and the best fit to time integral of $T_{measured} - T_{num}$ is 7.7. The boundary heat flux parameter α is 2.0. Thus the choice of norms varies the result by 5%. The power balance χ is between 1.2 and $2.0m^2/sec$. In practice, the pulse has four characteristic parameters,the amplitude of the peak, slope of the temperature rise ,the time of arrival of the peak and the slope of the decay. We are able to fit the first two parameters with a chi of approximately $7m^2/sec$. When the radial dependence is varied from constant to inversely proportional to density the value of chi at the input channel varies only a few percent during the rise and early decay phase. The discrepency between the observed and computed time of arrival of the peak is larger. Since in fitting the peak we are essentially specifying the second derivative of $T(t)$, the poorer fit is to be expected. It may also be partially related to the presence of convection.

The temporal decay depends on both the assumed radial profile of χ and on the heat transfer parameter α. As α decreases, the rate of increase of χ with radius must increase. Figures 3a,b,c give the computed values of the temperature at $r = 25.6$ for $\alpha = 0.1, 2.0$ and 40.0 respectively. In each case, the top curve is $\chi = 7.3m^2/sec$, the middle curve is $7.3n(.475)/n(r)$ and the bottom curve has a inverse square dependence on density. Clearly the boundary condition determines the radial variation of χ.

We now analyze the same case with the initial value approach and determine χ by fitting the differential time of arrival of the peak at 18.1 and 25.6. We assume a parabolic current profile and initialize the code with the perturbation given by conservation of energy and flux. The experimental temperature and density profiles are used. For a differential time of arrival of 1ms we find $\chi = 4.1m^2/sec$. The temporal evolution at 18.1 and 25.6 cm are displayed in Fig 3a,b. The amplitude of the temperature pertubation just outside the mixing radius is in good agreement with theory. The actual crash time of one msec is comparable with the time of arrival. The difference in arrival times occurs because the initial value approach assumes that the crash is instananeous. The forced boundary value approach automatically took this into account. For neutral beam cases, the crash time is .1ms and the agreement will be better.

The most disturbing discrepency is the surprisingly large magnitude of the heat pulse away from the mixing radius. The theoretical prediction is based on a dipole character of the initialization. By assuming thermal equilibrium after the crash is the temperature before the crash, there is a net lack of thermal energy inside the $q = 1$ surface. This absence of heat mixes with the excess outside the inversion radius and causes a rapid decay. If the conductivity inside the $q = 1$ surface were greatly enhanced after the crash, the natural profile would be the flat final profile. Thus the heat pulse would propagate like a monopole localized between the inversion and mixing radii.

The experimental observations in ASDEX and TFTR seem to suggest that the temperature at the $q = 1$ surface is held constant throughout the sawtooth period. This is an intermediate case between a dipole and a monopole.

In conclusion, the forced boundary value method allows quantitative analysis of the time evolution of the measured signals. The major source of error are the spatial resolution of the ECE spectrometer and the lack of knowledge of the correct boundary condition. By averaging over several shots it should be possible to determine both the physical boundary condition and the radial profile of χ. For the sample ohmic case analyzed here we find that the heat pulse conductivity is a factor of four to five higher than the power balance conductivity and that the initial valve approach significantly underestimates the heat pulse χ.

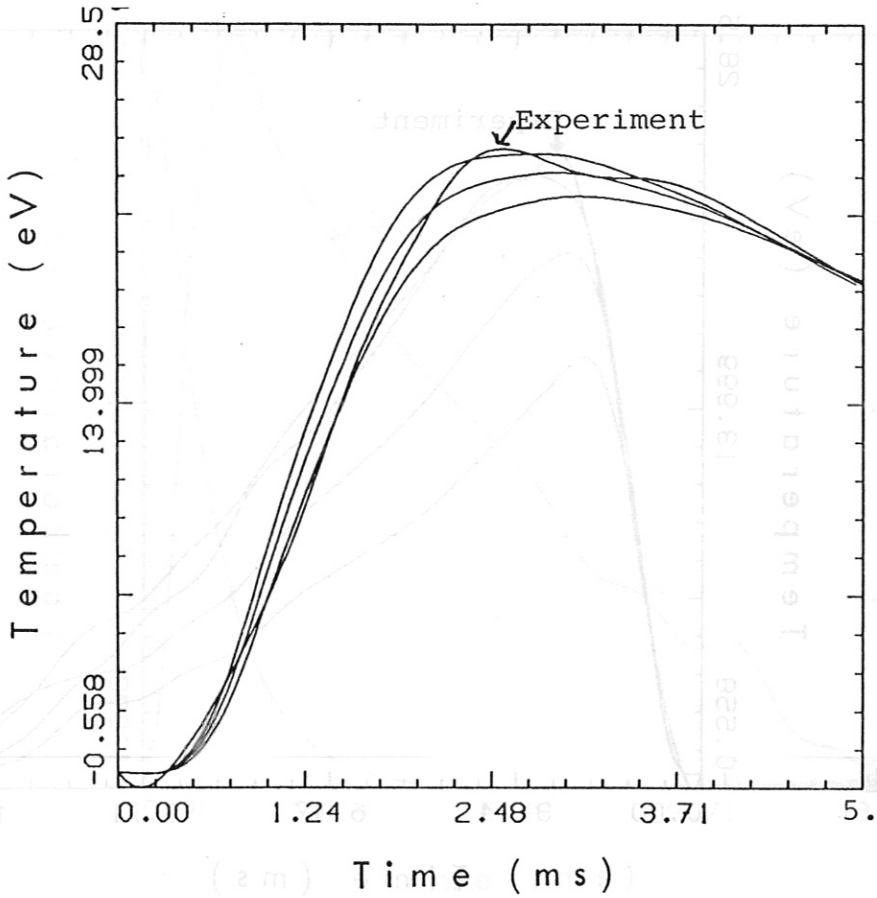
28.5
13.999
-0.558
Temperature (eV)
Experiment
0.00
1.24
2.48
3.71
5.
Time (ms)

Fig. 1

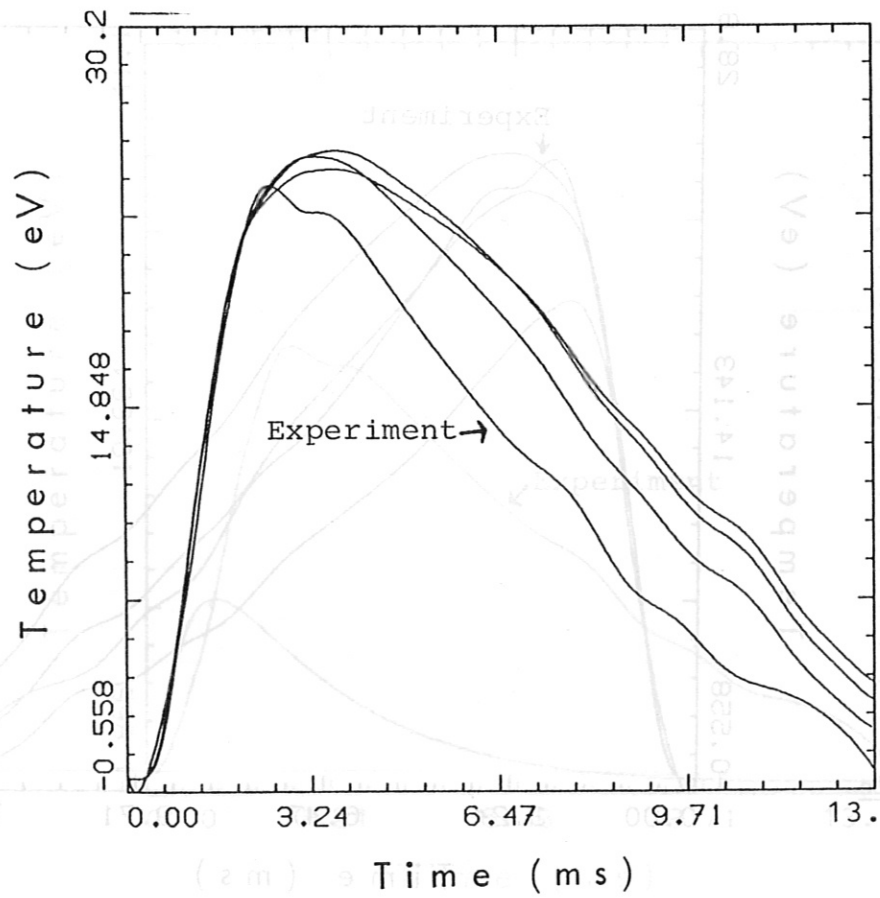
30.2
14.848
-0.558
Temperature (eV)
Experiment
0.00
3.24
6.47
9.71
13.
Time (ms)

Fig. 2a

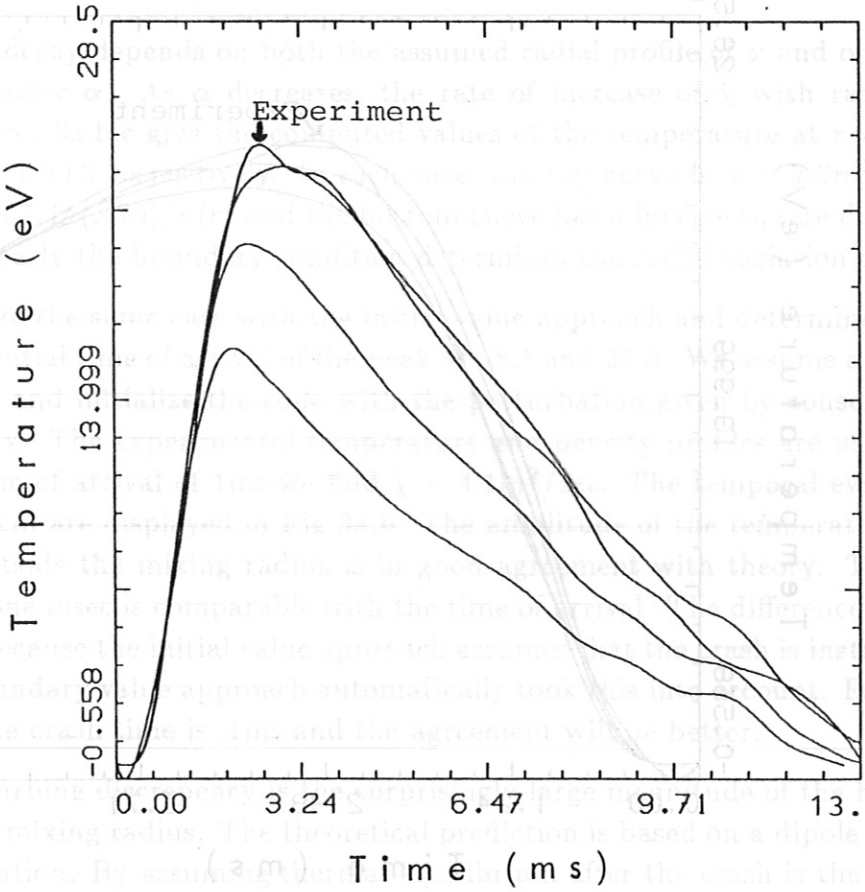
28.5
13.999
-0.558
Temperature (eV)
Experiment
0.00
3.24
6.47
9.71
13.
Time (ms)

Fig. 2b

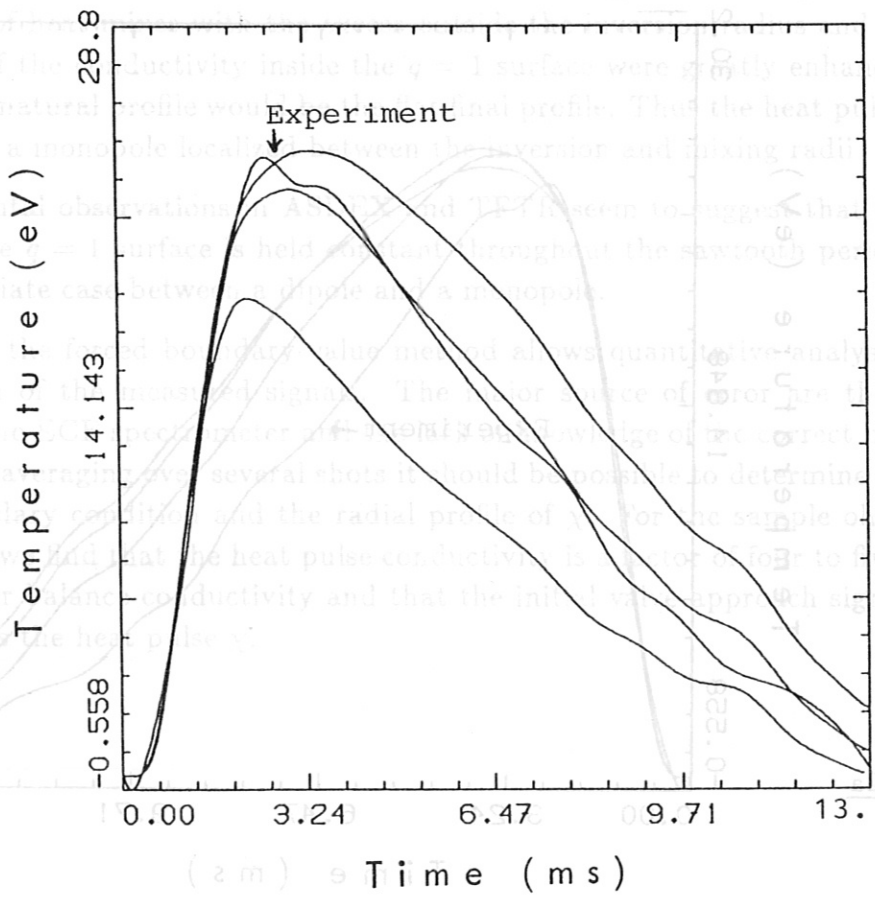
28.8
14.143
-0.558
Temperature (eV)
Experiment
0.00
3.24
6.47
9.71
13.
Time (ms)

Fig. 2c

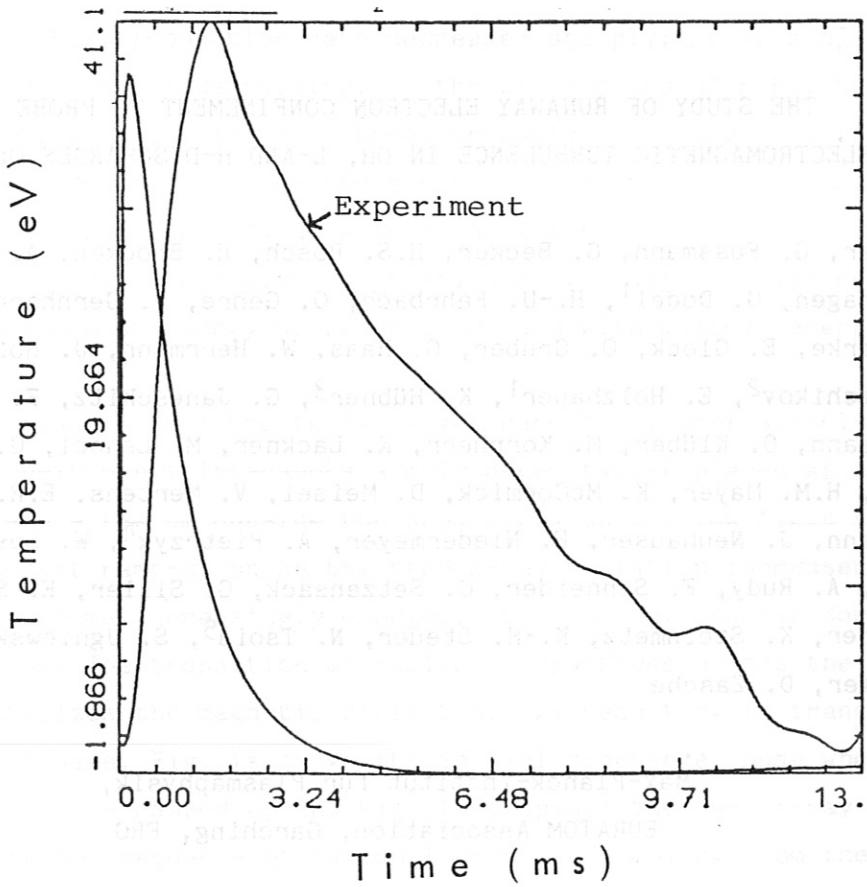
41.1
19.664
-1.866
Temperature (eV)
Experiment
0.00
3.24
6.48
9.71
13.
Time (ms)

Fig. 3a

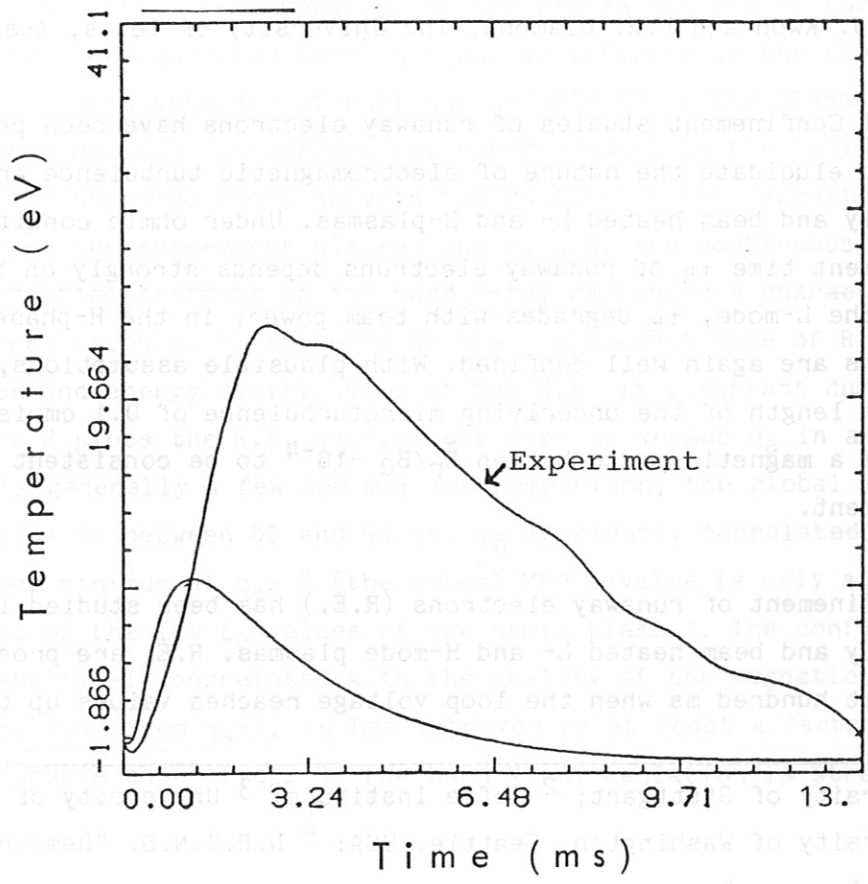
41.1
19.664
-1.866
Temperature (eV)
Experiment
0.00
3.24
6.48
9.71
13.
Time (ms)

Fig. 3b

THE STUDY OF RUNAWAY ELECTRON CONFINEMENT TO PROBE THE ELECTROMAGNETIC TURBULENCE IN OH, L-AND H-DISCHARGES OF ASDEX

F. Wagner, G. Fussmann, G. Becker, H.S. Bosch, H. Brocken, A. Carlson, A. Eberhagen, G. Dodel[1], H.-U. Fahrbach, O. Gehre, J. Gernhardt, G. v.Gierke, E. Glock, O. Gruber, G. Haas, W. Herrmann, J. Hofmann, A. Izvozchikov[2], E. Holzhauer[1], K. Hübner[3], G. Janeschitz, F. Karger, M. Kaufmann, O. Klüber, M. Kornherr, K. Lackner, M. Lenoci, G. Lisitano, F. Mast, H.M. Mayer, K. McCormick, D. Meisel, V. Mertens, E.R. Müller, H. Murmann, J. Neuhauser, H. Niedermeyer, A. Pietrzyk[4], W. Poschenrieder, H. Rapp, A. Rudy, F. Schneider, C. Setzensack, G. Siller, E. Speth, F. Söldner, K. Steinmetz, K.-H. Steuer, N. Tsois[5], S. Ugniewski[6], O. Vollmer, D. Zasche

Max-Planck-Institut für Plasmaphysik,
EURATOM Association, Garching, FRG

and

O.J. Kwon and P.H. Diamond, The University of Texas, Austin, USA

ABSTRACT Confinement studies of runaway electrons have been performed in order to elucidate the nature of electromagnetic turbulence and its role in ohmically and beam heated L- and H-plasmas. Under ohmic conditions, the confinement time τ_R of runaway electrons depends strongly on the choice of q_a; in the L-mode, τ_R degrades with beam power; in the H-phase, runaway electrons are again well confined. With plausible assumptions, a correlation length of the underlying microturbulence of 0.1 cm is found which requires a magnetic perturbation $\tilde{B}_r/B_0 \sim 10^{-4}$ to be consistent with L-mode confinement.

The confinement of runaway electrons (R.E.) has been studied in ASDEX in ohmically and beam heated L- and H-mode plasmas. R.E. are produced within the first hundred ms when the loop voltage reaches values up to 10V.

---

[1] University of Stuttgart; [2] Ioffe Institute; [3] University of Heidelberg; [4] University of Washington, Seattle, USA; [5] N.R.C.N.S. "Democritos", Athens, Greece; [6] Inst. for Nuclear Research, Swierk, Poland;

Thereafter, the R.E. production rate decreases sharply; at 0.3s $n_e^{-1} dn_R/dt$ $\sim 4 \times 10^{-4}$ s^{-1} and is still decreasing. In the birth phase of R.E., the plasma T_e- and n_e-profiles are still very broad probably resulting in a largely homogeneous R.E. density. During the current ramp-up phase (typically 600-800 ms), R.E. are continuously accellerated. After about 1 s (with the plasma current being in the plateau phase) the R.E. distribution reaches steady state at a mean energy of about 1 MeV and with maximal energy around 10 MeV.

R.E. are measured via the thick target hard X-ray bremsstrahlung emitted when their orbit intersects a molybdenum target placed at the plasma mid-plane a few cm outside the separatrix on the low field side. During the current ramp-up phase the hard X-ray radiation increases because the electrons become increasingly energetic though their number does not further increase. The transition of rational q-surfaces across the plasma surface destabilizes the magnetic field topology resulting in transiently enhanced R.E. losses. Fig. 1a shows the initial discharge phase when current and density are ramped up and Fig. 1b displays the hard X-ray radiation indicating the sequence of rational q-surfaces moving from the interior across the separatrix. It is interesting to note that despite the anomaly of the magnetic field topology at the plasma surface of the magnetic limiter configuration (with q equal to infinity at the separatrix and a narrowly spaced sequence of rational q-surfaces at the plasma edge), the transit of a rational q_a-surface (q_a corresponding to the cyclindrical one ignoring the anomaly) still affects the quality of the magnetic field topology. During the subsequent plateau phase, R.E. are continuously lost; from the exponential decrease of the hard X-ray radiation a characteristic time is inferred which is interpreted as the confinement time of R.E. since the population and energy distribution of the R.E. is invariant during this period. Figure 2 plots the R.E. confinement time τ_R versus q_a in an ohmic B_0-scan. τ_R is generally a few 100 ms; for comparison, the global energy confinement time is between 80 and 90 ms. τ_R is clearly correlated with q_a and has a sharp minimum at $q_a \simeq 3$ (the actual MHD q-value is only slightly larger because of the low β_p-values of the ohmic plasma). The confinement of R.E. is sensitively correlated with the quality of the magnetic field configuration. Away from $q_a = 3$, τ_R has improved by at least a factor of 2. At the unfavourable case of $q_a \simeq 3$, the hard X-ray radiation is strongly

modulated by the sawteeth occurring in the plasma center /1/. Away from q_a=3, no distinct modulation is observed both at lower and higher q_a-values. This observation indicates the possibility that the resonant condition $q_a \simeq 3$ at the edge destabilizes the plasma further in (probably at rational q-surfaces with smaller q-values) leading to enhanced transport of R.E. from the center through the edge.

The traces of Fig. 2 clearly demonstrate that the magnetic field configuration is disturbed throughout the plasma by a rational edge q_a-value. Although the R.E. respond to this degradation sensitively, the bulk plasma properties are not affected at all as shown in Figure 2 for the global energy confinement time τ_E. There is no other known global quantity of the main or the divertor plasma (which are known to sensitively respond to confinement changes of the main plasma, such as shown in Fig. 5) which is affected by the degraded field topology.

Figure 3 shows the variation of the hard X-ray radiation during a neutral injection pulse into the ohmic plateau phase. τ_R is sharply reduced and R.E. are quickly lost. (A second beam pulse later in the discharge does hardly show any increased radiation confirming the expectation that no R.E. are produced in the plateau phase). With NI, there is a simultaneous degradation of the confinement of R.E. along with the one for energy and particles (see Fig. 4). The sensitivity of the R.E. confinement on the quality of the magnetic field topology clearly indicates a substantial degradation already at low beam power causing a sharp drop in τ_R. Furthermore, sawteeth strongly modulate the hard X-ray radiation in the beam phase for all q_a-values (see Fig. 3) in a way it was only observed for rational q_a-surfaces at the edge in the OH-phase.

It is interesting to note that τ_R in the degraded L-regime of a NI-heated plasma does not depend on q_a like in the OH-phase. With NI, τ_R is sharply reduced but increases monotonously with B_0 without a notch at q_a=3. Evidently, NI degrades the quality of the magnetic field structure to suchan extent that the additional geometrical disturbance is negligible. The uncorrelated q_a-dependence of τ_R and τ_E in the OH-phase raises doubts whether the OH confinement of the bulk plasma is indeed caused by the magnetic turbulence which is evidently responsible for the confinement of R.E. The question remains whether under beam heating conditions magnetic turbulence primarily determines transport or whether it accompanies dominant

drift-like fluctuations simply because of rising β_p. In this context it is important to note that the confinement of R.E. sharply improves at the H-transition though β_p further increases due to improved global confinement. Both in the L- and H-phases we observe a clear correlation in the confinement properties of the bulk plasma and R.E.
Fig. 5 plots the time dependence of the hard X-ray flux together with the H_α-radiation in the divertor chamber (a measure of the energy flux into the divertor) and the flux ϕ_D of particles backscattered from the target plates (a measure of the particle flux). The simultaneous OH→L and L→H-transition is shown in the three signals all governed by different confinement properties. The sharp onset of the L-phase a few ms after beam initiation also indicates that the magnetic turbulence is obviously not due to rising β_p.

With the hypothesis that unlike the ohmic confinement, the degradation in the L-phase is predominantly due to magnetic turbulence, we can characterize the structure of the underlying mode from the ratio τ_E/τ_R. It is known that the ratio of τ_E/τ_R is not given by the inverse ratio of the electron velocities since the coupling of the R.E. to the mode is reduced by the shift of the k·B resonance due to magnetic drift effects /2/. These effects can be considered by a radial structure function S such that

$\tau_E/\tau_R = V^R/V^{th} \cdot S$ (V^R, V^{th} are the R.E. and thermal velocities, respectively). S depends on $L_S V_D^R/\delta X V^R$ (L_S= shear length, V_D^R = R.E. drift velocity, δX = radial correlation length) and can be approximated by $\exp-(L_S V_D^R/\delta X\, V^R)^{2/3}$/. With the ratio of τ_E and τ_R at high beam power (see Fig. 4), $\delta X \simeq 0.1$ cm is calculated. This value is used to estimate the relative amplitude of the fluctuation

$\tilde{B}_r/B_o = (\chi_e^{th} \tilde{k}_\theta \delta X/\pi\, V^{th} L_s)^{1/2}$ (χ_e^{th} = thermal heat diffusivity, $\tilde{k}_\theta$ = average poloidal wave number) necessary to fully explain the level of thermal heat transport. Assuming poloidal mode number m=8 (Ref. /4/), the result $\tilde{B}_r/B_o \sim 10^{-4}$ is in agreement with the level of magnetic field fluctuations at the plasma edge deduced from measurements outside the separatrix (Ref. /4/). Scaling studies indicate that $\delta X \propto n^{0.2} B_0^{-1.3} P^{0.1}$ and $\tilde{B}_r/B_o \propto n^{-0.1} B_0^{-0.1} P^{0.6}$. Thus c/ω_{pe}-turbulence /5/ is an unlikely candidate while a model along the line of resistive pressure driven modes offers more promise.

References

/1/ G. Fußmann et al., in Plasma Phys. and Contr. Nucl. Fusion Research, 1978, Vol. 1, IAEA, Vienna (1979) 401.

C.W. Brown and J.D. Strachau, Nucl. Fus. 22 (1982) 1090.

/2/ H.E. Mynick and J.D. Strachan, Phys. Fluids 24 (1981) 695.

/3/ O.T. Kwon and P.H. Diamond, to be published.

/4/ G. Dodel, F. Holzhauer et al., this conference.

/5/ B.B. Kadomtsev, O.P. Pogutse in Plasma Phys. and Contr. Nucl. Fusion Research, 1984, Vol. 2, IAEA, Vienna 81985) 69.

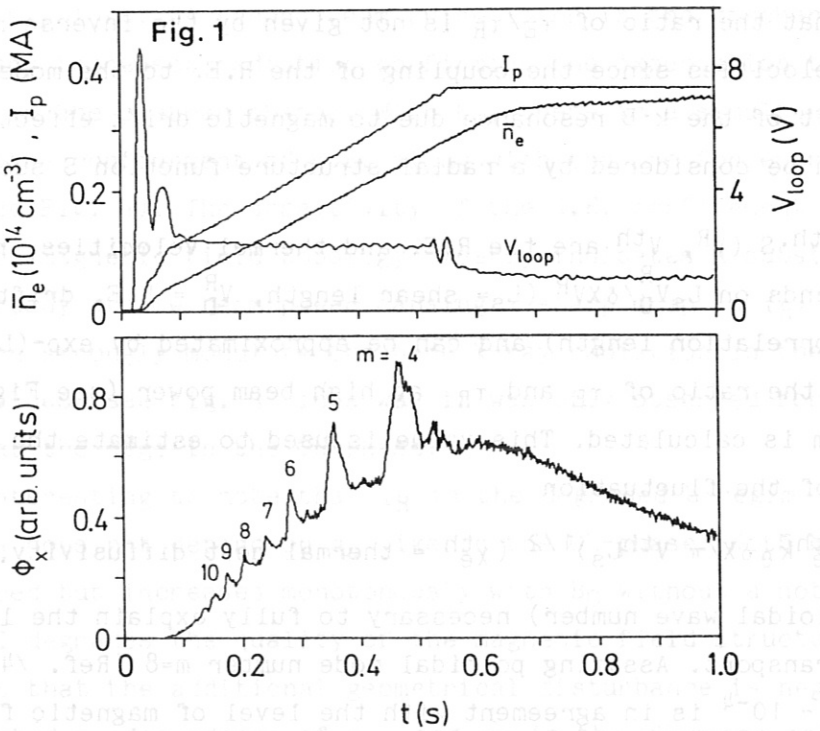

Fig.1: Current, density $\bar{n}_e$, loop voltage and hard X-ray radiation ϕ_x during current ramp-up.

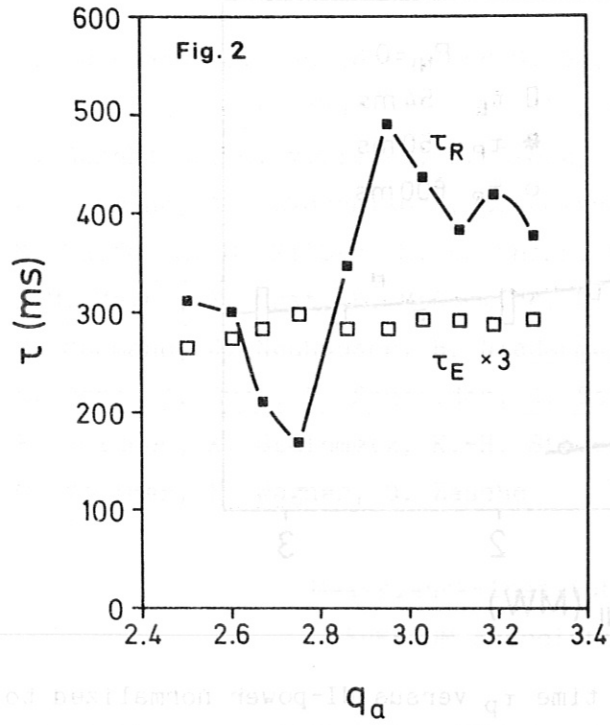

Fig.2: Global energy (τ_E) and runaway electron (τ_R) confinetime in an ohmic BT-scan.

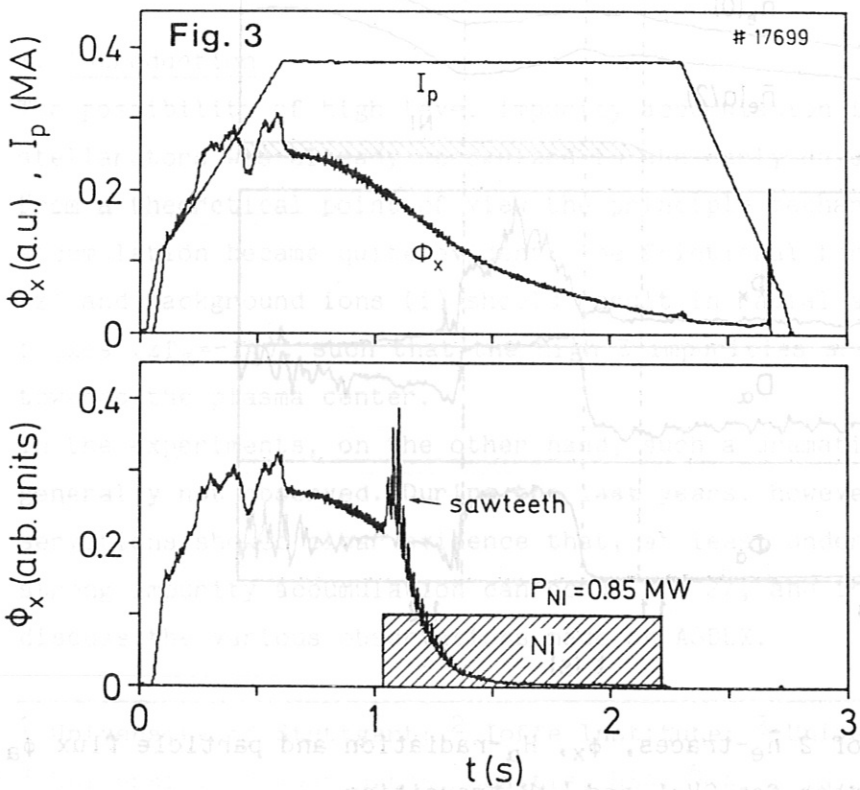

Fig.3: Comparison of ϕ_x in an OH- and NI-discharge; the sawtooth modulation of ϕ_x is indicated.

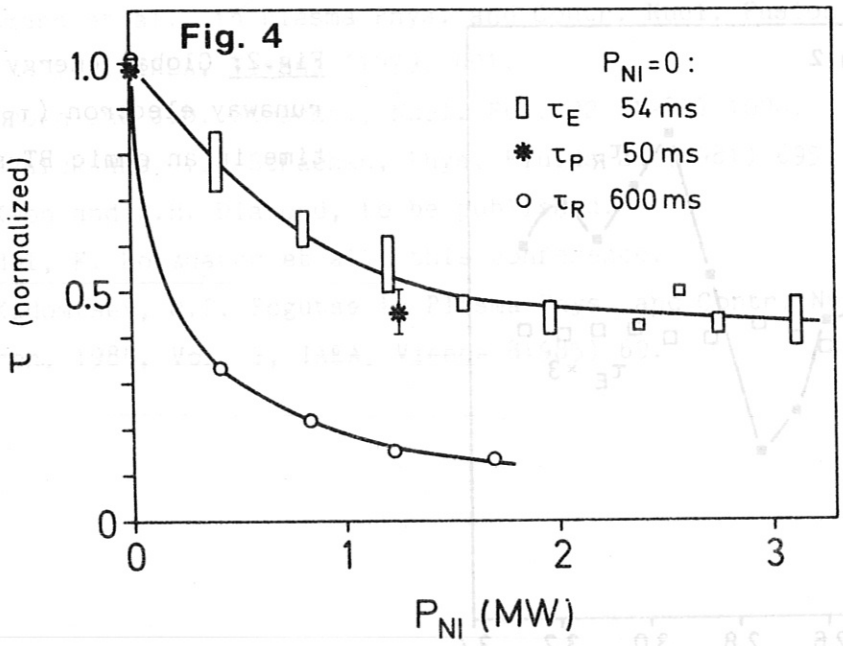

Fig.4: τ_E, τ_R and particle confinement time τ_p versus NI-power normalized to the OH-values (as given).

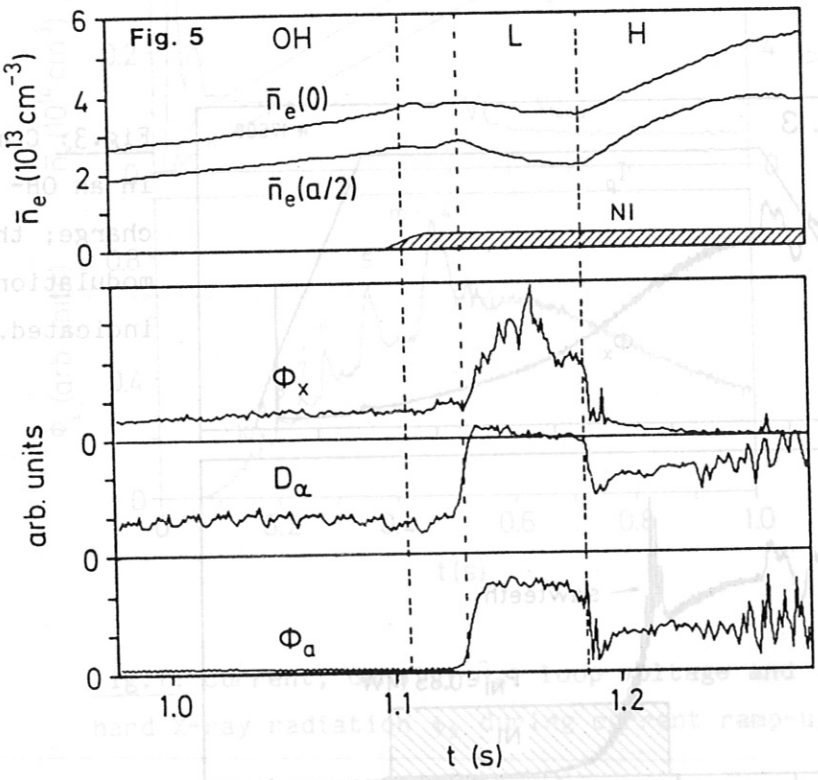

Fig.5: Time dependence of 2 $\bar{n}_e$-traces, ϕ_x, H_α-radiation and particle flux ϕ_a in the divertor chamber for OH→L and L→H transition.

STUDY OF IMPURITY ACCUMULATION IN THE ASDEX TOKAMAK

G. Fussmann, G. Janeschitz and G. Becker, H.S. Bosch, H. Brocken, A. Carlson, A. Eberhagen, G. Dodel[1], H.-U. Fahrbach, O. Gehre, J. Gernhardt, G. v.Gierke, E. Glock, O. Gruber, G. Haas, W. Herrmann, J. Hofmann, A. Izvozchikov[2], E. Holzhauer[1], K. Hübner[3], F. Karger, M. Kaufmann, O. Klüber, M. Kornherr, K. Lackner, M. Lenoci, G. Lisitano, H.M. Mayer, F. Mast, K. McCormick, D. Meisel, V. Mertens, E.R. Müller, H. Murmann, J. Neuhauser, H. Niedermeyer, A. Pietrzyk[4], W. Poschenrieder, H. Rapp, A. Rudy, F. Schneider, C. Setzensack, G. Siller, E. Speth, F. Söldner, K. Steinmetz, K.-H. Steuer, N. Tsois[5], S. Ugniewski[6], O. Vollmer, F. Wagner, D. Zasche

Max-Planck-Institut für Plasmaphysik,
EURATOM Association, Garching, FRG

Abstract: The internal disruptions are found to play an important role in preventing impurity accumulation. We describe several situations where strong peaking of metallic impurities in the plasma center is observed after suppression of the sawtooth activity.

I. Introduction

The possibility of high level impurity accumulation in tokamaks and stellarators was already recognized in the early days of these devices. From a theoretical point of view the principle mechanisms leading to accumulation became quite evident: The frictional forces between impurity (z) and background ions (i) should result in radial ambipolar interchange fluxes ($z\Gamma_z=-\Gamma_i$), such that the high Z impurities are rapidly driven towards the plasma center.

In the experiments, on the other hand, such a dramatic accumulation was generally not observed. During the last years, however, a number of observations showed clear evidence that, at least under certain conditions, strong impurity accumulation can occur /1, 2/, and in the following we will discuss the various observations made on ASDEX.

---

[1] University of Stuttgart; [2] Ioffe Institute; [3] University of Heidelberg; [4] University of Washington, Seattle, USA; [5] N.R.C.N.S. "Democritos", Athens, Greece; [6] Inst. for Nuclear Research, Swierk, Poland;

II. Impurity accumulation and counteracting mechanisms

Impurity accumulation was observed in ASDEX for the first time during the quiescent H-phase achieved by NI heating. As reported in /3/ these discharges collapse because of tremendous radiation losses in the plasma center. The quiescent H-mode differs from the normal one by the lack of bursts caused by edge localized modes (ELMs). It was originally assumed that accumulation can be prevented in the normal H-phase due to counterating mechanisms being correlated with the ELMs. A more detailed analysis, however, revealed that also in this case a quite similar accumulation of metallic impurities takes place /4/. The main difference between normal and quiescent H-phase is found in the Fe-impurity concentration (and hence the Fe influxes) during the preceding L-phase. This concentration is typically three times higher for the quiescent case. It is still unclear whether during the H-mode the ELMs effectively improve the screening efficiency of the plasma or if they are rather an indication of low metallic influxes.

Comparing ASDEX with other tokamaks /2/, we have to realize that in our experiments sawteeth do not occur during the H-phase. Therefore, the above accumulation is presumably more pronounced in ASDEX since the counteracting effect of the internal disruption is missing. The dispersing effect of sawteeth (st) has already been shown in a number of investigations /1, 5/. In ASDEX we have studied this effect by means of: a) current ramp-up to increasing plateaus, b) Kr gas puffing, c) pellet injection.

In addition, we have investigated sawtooth initiation during the early current build-up phase. Frequently, the first sawtooth is a very pronounced event (the so-called "Ereignis", further discussed in /6/). By comparison with discharges where the sawteeth grow continuously from noise level, some information on the transport induced by sawteeth can be obtained. Such a comparison is shown in Fig. 1. It is seen that the discharge exhibiting the "Ereignis" shows a substantial increase in the central soft X-ray (SX) intensities prior to the st-crash. After the crash, the SX-signal (dominated by Fe) approaches rapidly the trace of the reference shot. We also note that there is practically no effect to be seen on other spectroscopic signals (FeXVI, OVIII) emitted from outside half the minor radius. Taking further into account that central temperatures differ only by $\lesssim 1\%$ in the two cases, we conclude: Sawteeth expell in short pulses impurities out of the central region but do not lead to a net loss of particles from the plasma volume.

The effect of sawtooth suppression by current ramp-up has been described in /7/. Here it suffices to repeat the essential findings: Firstly, the procedure is not successful in any case. Depending on small changes of some unknown parameters, st may be suppressed or sustain with marked amplitude for the residual part (~2s) of the discharge. In case of suppression, only two changes are observed: 1) the n_e-profile is becoming more peaked, and 2) the central radiation losses are considerably increased (~ factor 10 for $q_a \leq 3$) and become comparable to the input power of ~0.2 W/cm^3, although the Z_{eff} determined by resistivity is as low as ≤ 1.5. Moreover, inspite of the high radiation losses, both the total energy content and the central energy density remain unchanged in comparison with the st case. Thus, a concomitant substantial reduction of the thermal conductivity is to be inferred.

Similar effects can be observed by applying Kr-puffing as demonstrated in Fig. 2. Shot #19691 is a discharge following a shot into which Kr had been blown. The SX-rays (as well as Kr-lines of highly ionized ions) are seen to increase monotonously. As to be seen from the st-amplitude $A=(\bar{n}_e - \langle\bar{n}_e\rangle)/\langle\bar{n}_e\rangle$ (with $\langle\bar{n}_e\rangle$ being the averaged line-density) plotted on top of Fig.2, there are no sawteeth developped in this discharge. The following shot had even less Kr and this time st occur after t=0.72 s. The reduction in the central soft X-rays is evident (whereas the non-central OVIII-radiation is nearly uneffected).

As mentioned above, another method for st-suppression is the injection of pellets with the centrifuge system. This has been done in ohmic discharges and also under carbonized conditions during counter-NI heating (see Ref. /8/ for more detail). The salient features to be observed during the post pellet phase, when the st activity is reduced or even quenched are as described before: Peaking of the n_e-profile, accumulation of metal impurities and improvement of energy confinement.

In the following, we concentrate on the accumulation aspects of two discharges with P_{NI}=0.45 MW (20032) and 0.9 MW (20033) counter NI (t=0.9 - 1.5s) into which 5 pellets have been injected (t=1.1 - 1.3s). In Fig. 3 we show the SX-signal of the second shot. The times of pellet injection are to be recognized from the $\bar{n}_e$ -trace depicted on top of Fig. 3. After the last pellet the sawteeth vanish (with one large exception) and the SX and TiXX intensities (λ=256 Å, peaking approximately at r=10 cm) are seen to rise exponentially. In Fig. 4 we compare the SX and TiXX radiation on log-scale for the two cited discharges. Each of the two signals is seen to rise very

similar with a multiplier of ~2 for the shot with doubled NI power. This proportionality to P_{NI} is also found from bolometer array measurements yielding very peaked profiles with central radiation losses as high as 0.5 and 0.9 W/cm^3 for the two discharges. Despite these large losses the central T_e drop is only about 10 % ($T_{e,max}$≈1.4 keV). Assuming Ti being the most abundant metallic impurity in these discharges (Fe being strongly reduced by carbonization) we need a central density of $n_{Ti}(0)/n_e(0)$≈1 - 2%. Invoking the collision parameter $\alpha=Z^2 n_Z/n_i>4$, we conclude that the interaction of the impurity ions among themselves is much larger than with the background ions - a situation imposing greatest difficulties in theory. However, the parallel development of the signals shown in Fig. 4 demonstrates that nonlinear impurity transport processes, with the possibility of enhanced impurity accumulation on account of the high impurity density (as discussed in /2/), are probably unimportant.

III. Transport simulation

Our observations suggest the following ansatz for the impurity fluxes:

$$\Gamma_Z(r,t) = \Gamma_S(r,t) + \Gamma_{an}(r) + \Gamma_{neo}(z,r)$$

with

$$\Gamma_S = \sum_k A_k P(t-t_k)\ V_S(r) n_Z$$

$$\Gamma_{an} = -D_{an}(r)\ n'_Z - v_{in}(r) n_Z$$

$$\Gamma_{neo} = -D_i(r) n_Z + Z(r) D(r) [n_i'/n_i - (o.5+1/Z) T_i'/T_i]$$

Γ_S represents the expelling effect of the sawteeth with P(t) being a pulse like-function Γ_{an} describes the underlying anomalous transport which is assumed equal for all particles, and finally Γ_{neo} is the neoclassical term /9/ (notation: '=∂/∂r).

We have simulated our experimental results using an impurity transport code applying measured $T_e(r,t)$ and $n_e(r,t)$. Particular emphasis has been devoted to the accumulation phase of #20033. In Fig. 3 we have included our results for the SX and TiXX chord integrals. All sawteeth were modelled in the same way: $\Gamma_{S,k}=V_{SO}\exp\{-[(t-t_k)/\tau]^2\}(r/r_o)\exp(-r/r_o)^2$ with r_o=15 cm, τ=1ms, V_{SO}= 1 000 cm/s. Most remarkably, these pulses control the peaking of the profiles very effectively at the beginning when the repetition time is still high. Assuming D_{an}=500 cm^2/s, V_{in}= 70 r/a cm/s, the peaking of the n_e-profiles could be roughly simulated by treating hydrogen in the code. Finally, in order to attain at least approximately the strong Ti peaking

observed from the radiation profiles, we had to double the neoclassical drift term and dropping the outward T_i'/T_i term therein.

References

/1/ R.C. Isler, Nucl. Fusion, 24, 1599 (1984)

/2/ K. Ida, et al., Phys. Rev. Lett., 58, 2, 116-119 (1987)

/3/ M. Keilhacker et al., Proceedings of the 10th Int. Conf. on Plasma Physics and Contr. Nucl. Fus. Research, London 1984, Vol. I, p. 71

/4/ E.R. Müller, IPP III/112 (1986) to be published in Nucl. Fusion)

/5/ TFR Group, Nucl. Fus. Lett. 25, 8, 981-986 (1985)

/6/ O. Gehre, this conference

/7/ F. Wagner, to be published in Nuclear Fusion

/8a/ V. Mertens, and /8b/ F. Mast this conference

/9/ S.P. Hirshman, Phys. Fluids, 19, 1, 155-158 (1975)

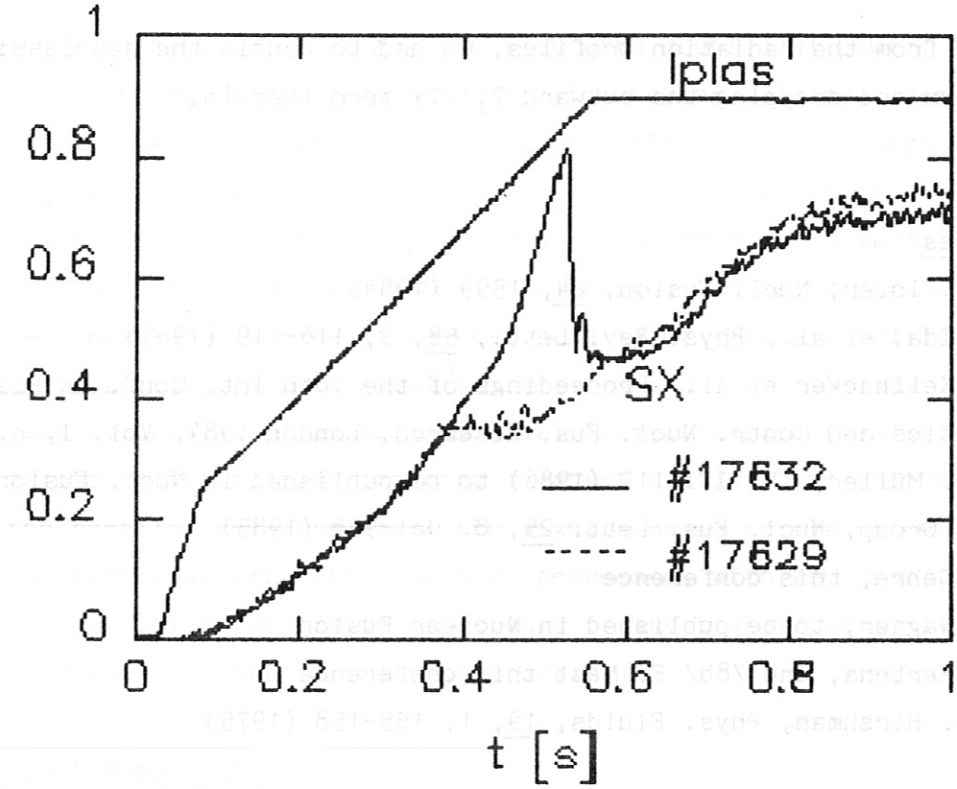

Fig.1: Soft X-ray emission in two discharges with different sawtooth initiation.

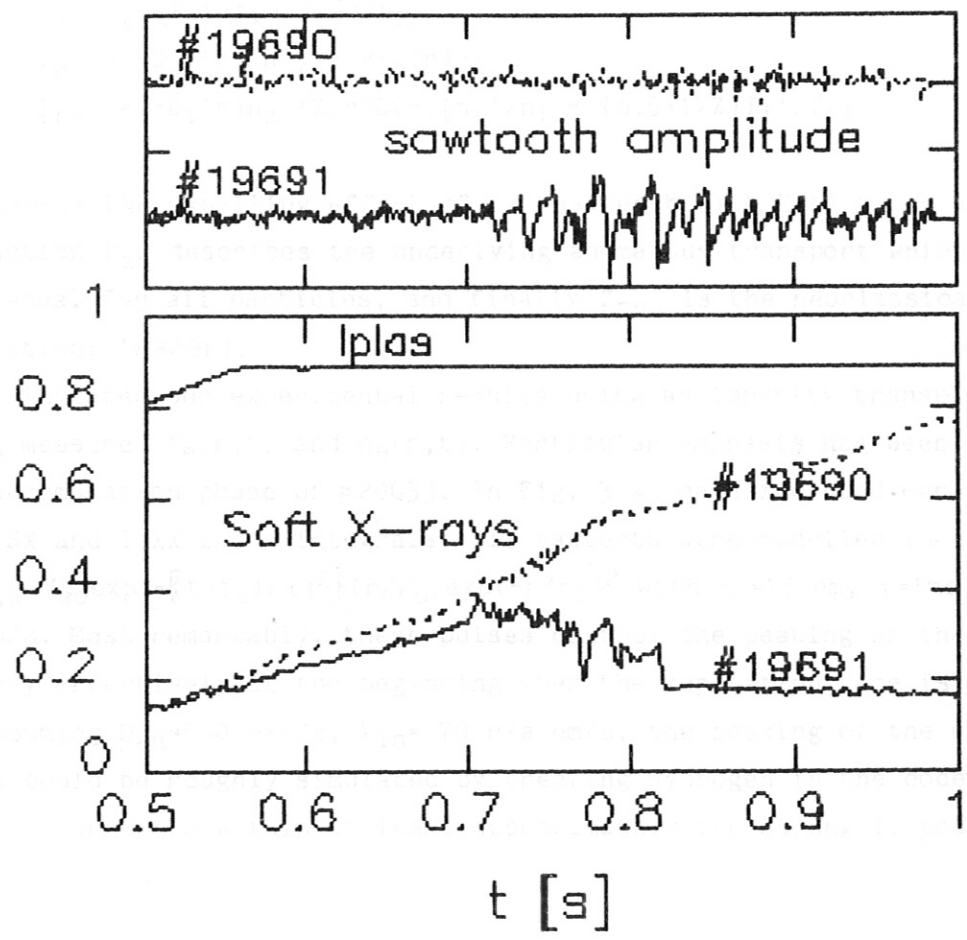

Fig.2: Increase of central SX radiation due to sawtooth suppression by means of Kr puffing.

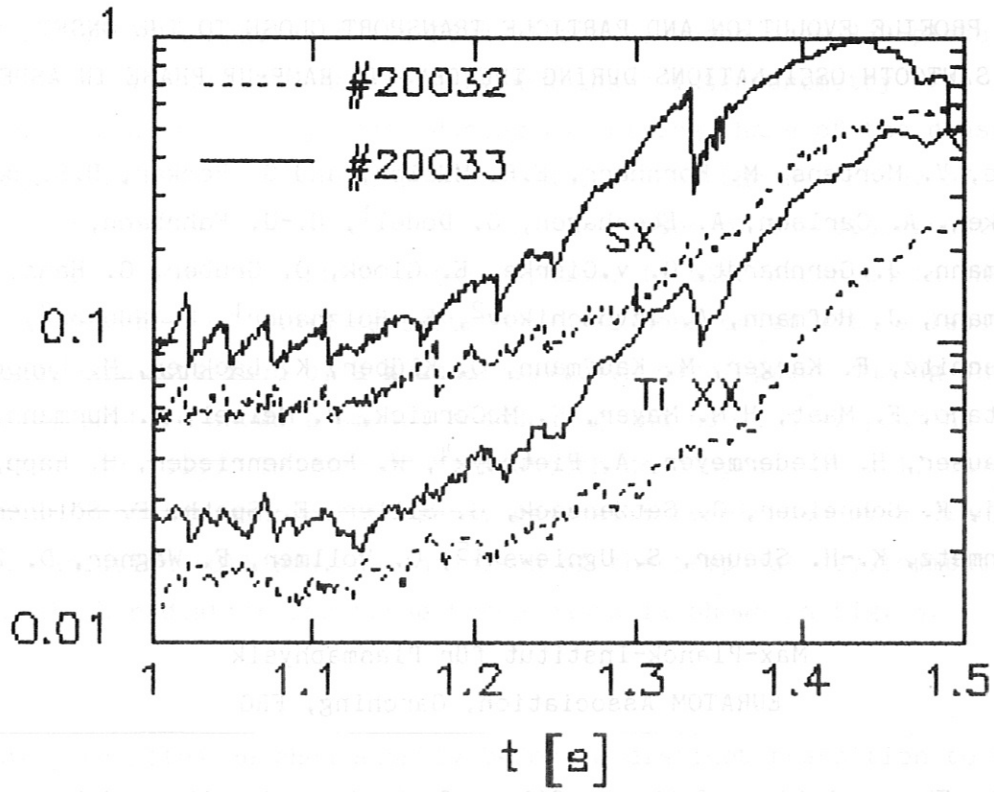

Fig.3: Development of SX and TiXX radiation, demonstrating the similarity of Ti accumulation in shots with different Ti influxes.

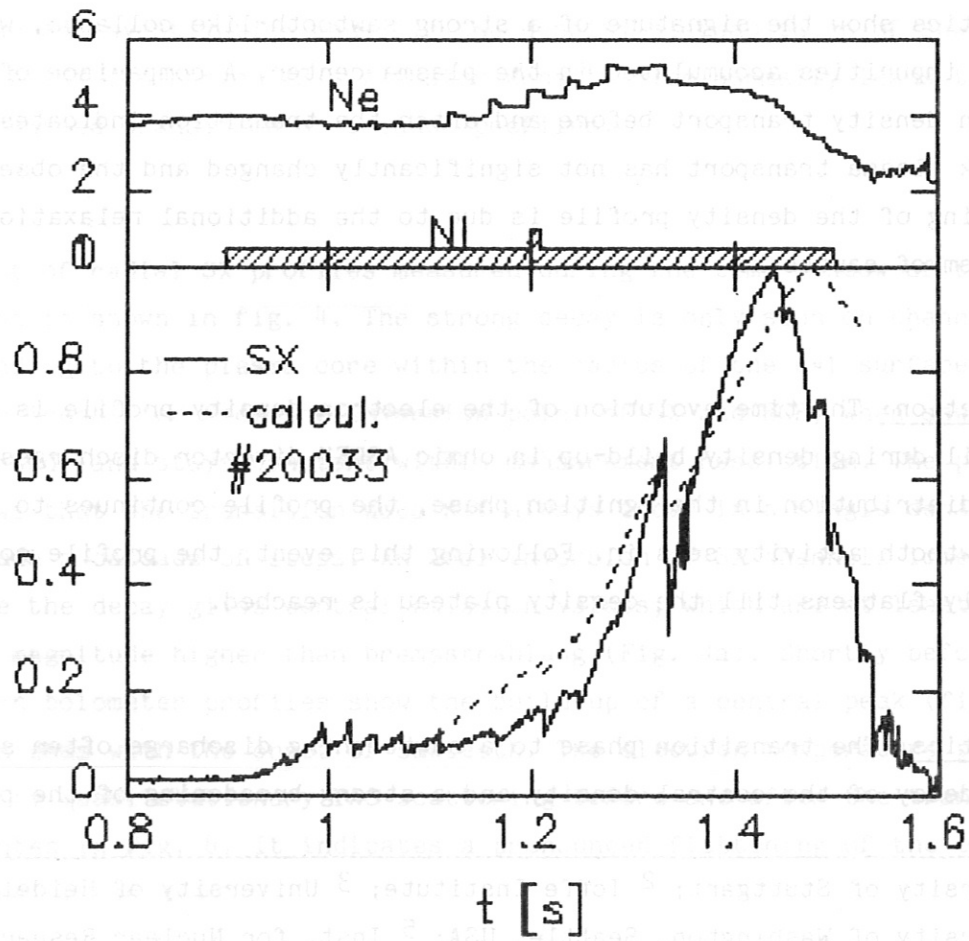

Fig.4: Impurity accumulation in case of pellet injection during the (counter) NI phase.
($\bar{n}_e$ in units of 10^{13} cm^{-3})

PROFILE EVOLUTION AND PARTICLE TRANSPORT CLOSE TO THE ONSET OF SAWTOOTH OSCILLATIONS DURING THE DENSITY RAMP-UP PHASE IN ASDEX

O. Gehre, V. Mertens, M. Kornherr, E.R. Müller, and G. Becker, H.S. Bosch, H. Brocken, A. Carlson, A. Eberhagen, G. Dodel[1], H.-U. Fahrbach, G. Fussmann, J. Gernhardt, G. v.Gierke, E. Glock, O. Gruber, G. Haas, W. Herrmann, J. Hofmann, A. Izvozchikov[2], E. Holzhauer[1], K. Hübner[3], G. Janeschitz, F. Karger, M. Kaufmann, O. Klüber, K. Lackner, M. Lenoci, G. Lisitano, F. Mast, H.M. Mayer, K. McCormick, D. Meisel, H. Murmann, J. Neuhauser, H. Niedermeyer, A. Pietrzyk[4], W. Poschenrieder, H. Rapp, A. Rudyj, F. Schneider, C. Setzensack, G. Siller, E. Speth, F. Söldner, K. Steinmetz, K.-H. Steuer, S. Ugniewski[5], O. Vollmer, F. Wagner, D. Zasche

Max-Planck-Institut für Plasmaphysik
EURATOM Association, Garching, FRG

Abstract: The evolution of the profiles of electron density and temperature, soft X-ray (SX) and bolometer radiation is investigated in ASDEX discharges close to the onset of sawteeth. For the transition phase these diagnostics show the signature of a strong sawtooth-like collapse, which removes impurities accumulated in the plasma center. A comparison of electron density transport before and after the transition indicates that the bulk plasma transport has not significantly changed and the observed broadening of the density profile is due to the additional relaxation mechanism of sawteeth.

Introduction: The time evolution of the electron density profile is studied in detail during density build-up in ohmic ASDEX divertor discharges. After a flat distribution in the ignition phase, the profile continues to peak till sawtooth activity sets in. Following this event, the profile continuously flattens till the density plateau is reached.

Diagnostics: The transition phase to a sawteething discharge often shows a sudden decay of the central density and a strong broadening of the profile.

---

[1] University of Stuttgart; [2] Ioffe Institute; [3] University of Heidelberg; [4] University of Washington, Seattle, USA; [5] Inst. for Nuclear Research, Swierk, Poland

This behaviour is demonstrated in figs. 1 and 2, which show 3-D-plots of vertical density profiles, measured by HCN-laser interferometry /1/. In fig. 1 the sawteeth already start during the rising phase of the density, while fig. 2 shows an even more pronounced onset at the beginning of the plateau, indicated by the sharp decay of the center of the distribution. A similar decay, after an initial peaking phase, is also observed in the SX radiation. The case of rapid sawtooth onset is confronted with a less common one, characterized by a gradual sawtooth development during which the density profile shows a smooth braodening and no central peaking of the SX radiation is found. In case of no sawtooth development at all, the density and SX profiles continue to peak, generally terminated by a disruption due to a radiation collapse. A comparison of the temporal development of the central SX radiation for these three cases is shown in fig. 3.

The density profiles reached shortly before a distinct transition to the sawtooth phase are characterized by a nearly constant shape, independent of plasma current I_p, toroidal field B_t, dI_p/dt and safety factor $q(a)$. For deuterium plasmas more peaked profiles are found as compared to hydrogen, similar to an investigation made for the density plateau phase of sawteething ASDEX discharges /2/. A faster density rise normally leads to a more pronounced transition at broader profiles.

A 3-D-plot of radial SX profiles measured during the time window of the transition is shown in fig. 4. The strong decay is only seen on channels corresponding to the plasma core within the radius of the q=1 surface. This radius is identified from the inversion point of SX and ECE, when sawteeth have started, and stays constant within measurement resolution. The picture also shows that the transition does not always occur in a single decay but may include a cascade of steps. An Abel inversion of SX channels immediately before the decay gives central emission values, which are at least one order of magnitude higher than bremsstrahlung (Fig. 4a). Shortly before the transition bolometer profiles show the build-up of a central peak (fig. 5), which vanishes with the onset of sawteeth. The electron temperature profile measured by quasi-stationary YAG scattering before and after the transition is presented in fig. 6. It indicates a pronounced flattening of the central region during the event.

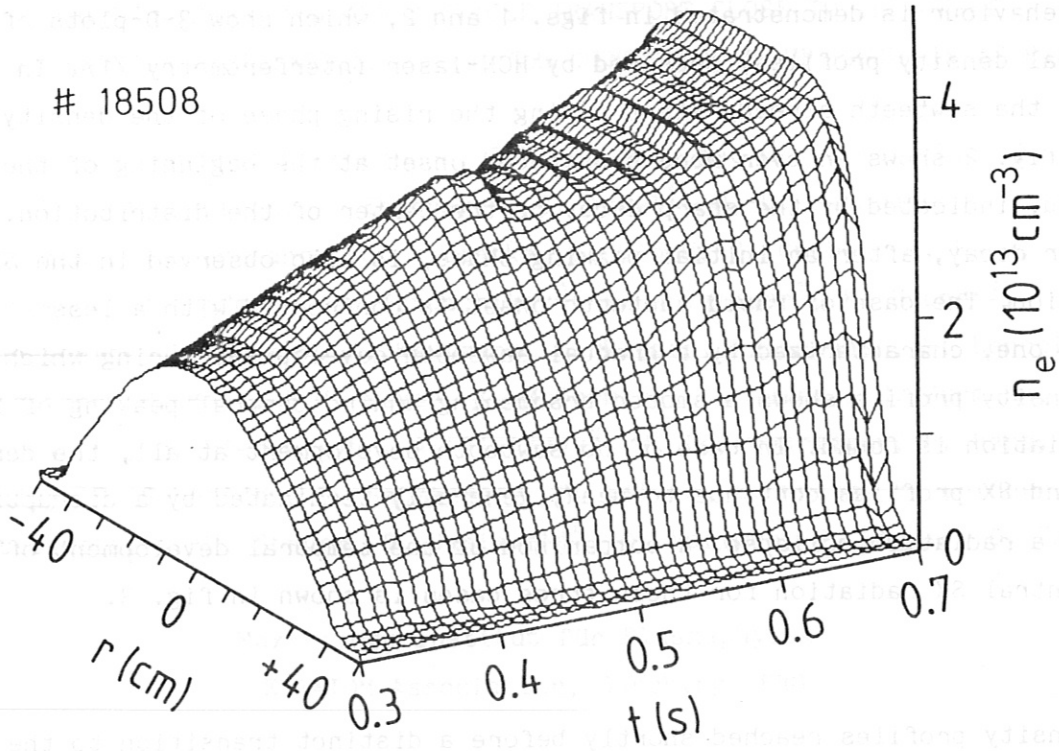

Fig. 1: Time evolution of the electron density profile close to the onset of sawtooth oscillations, transition to the sawtooth regime during the density build-up phase.

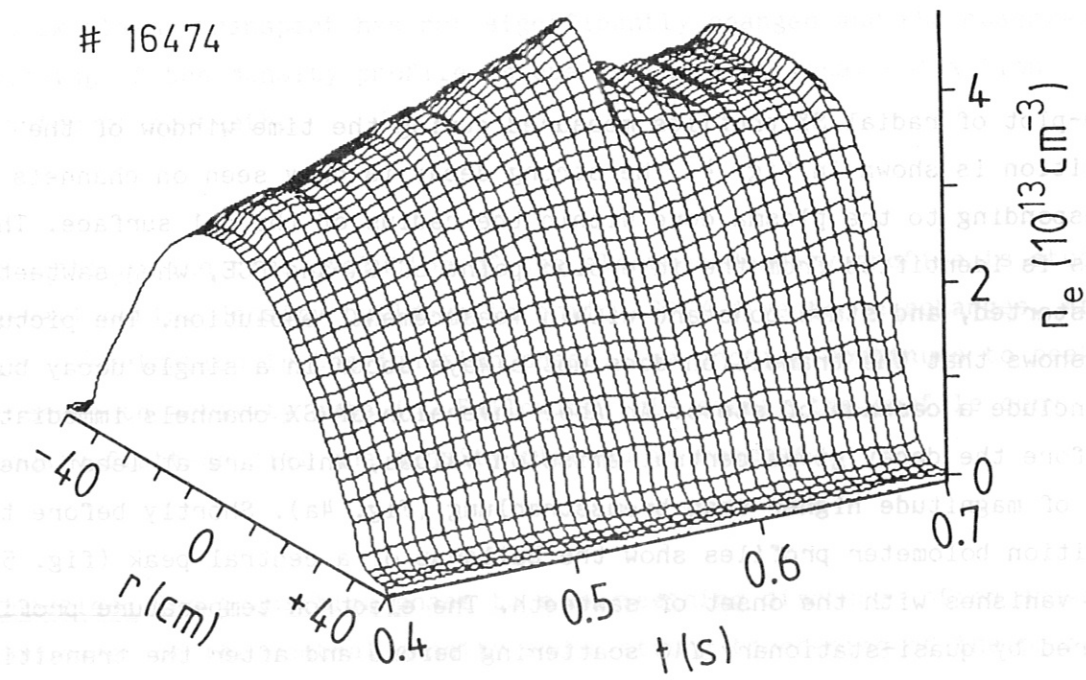

Fig. 2: As in fig. 1, but with more pronounced transition at the beginning of the density plateau.

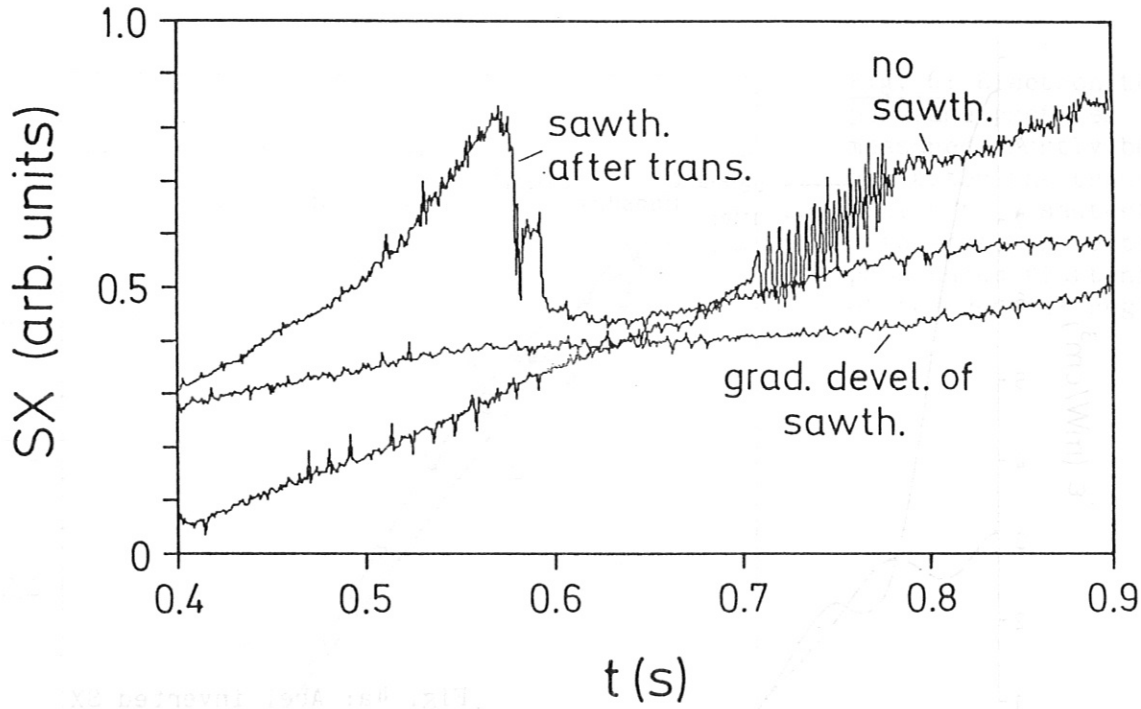

Fig. 3: Temporal development of the central SX radiation for a rapid sawtooth onset as compared to the cases of gradual sawtooth development and no sawteeth.

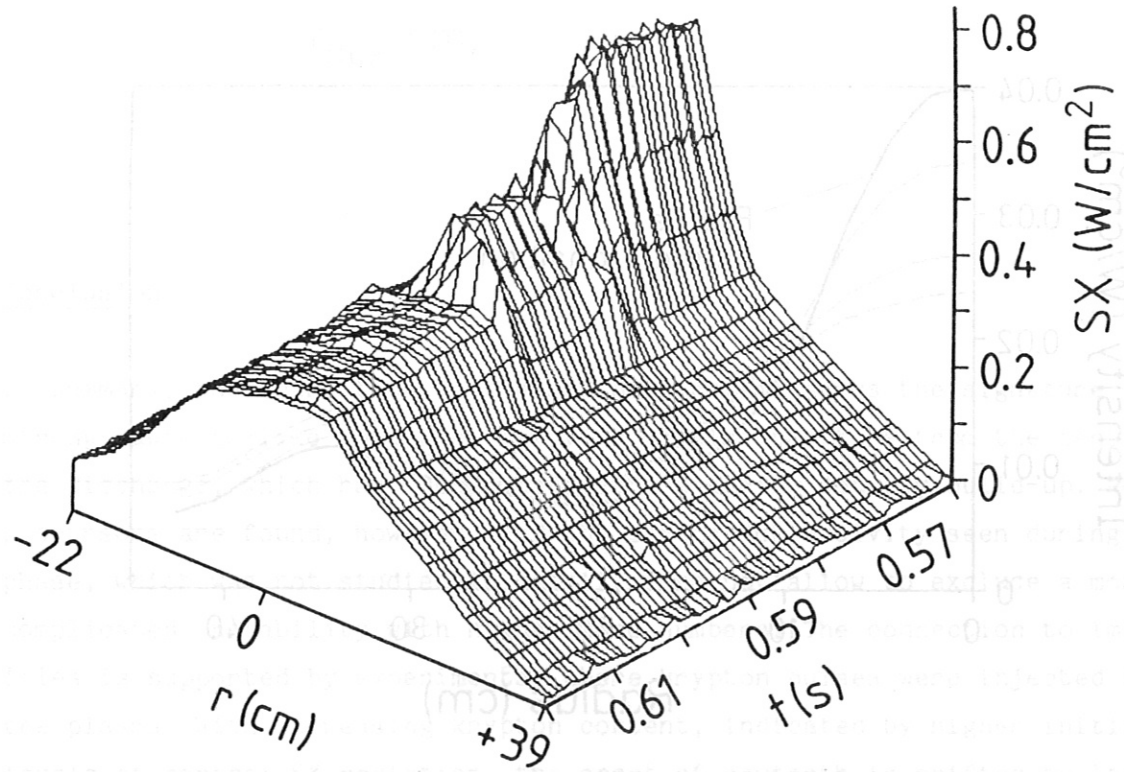

Fig. 4: SX radiation profiles during the transition to the sawtooth regime, showing a strong decay in the plasma core region.

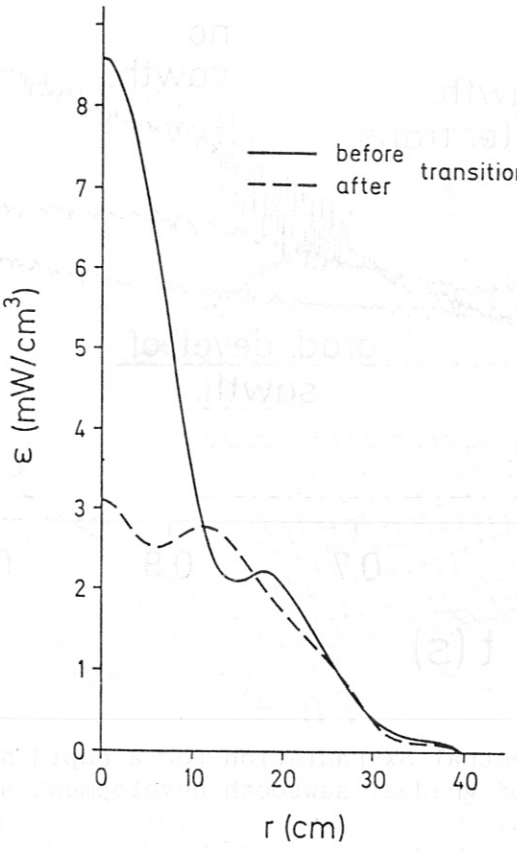

Fig. 4a: Abel inverted SX profiles before and after the transition.

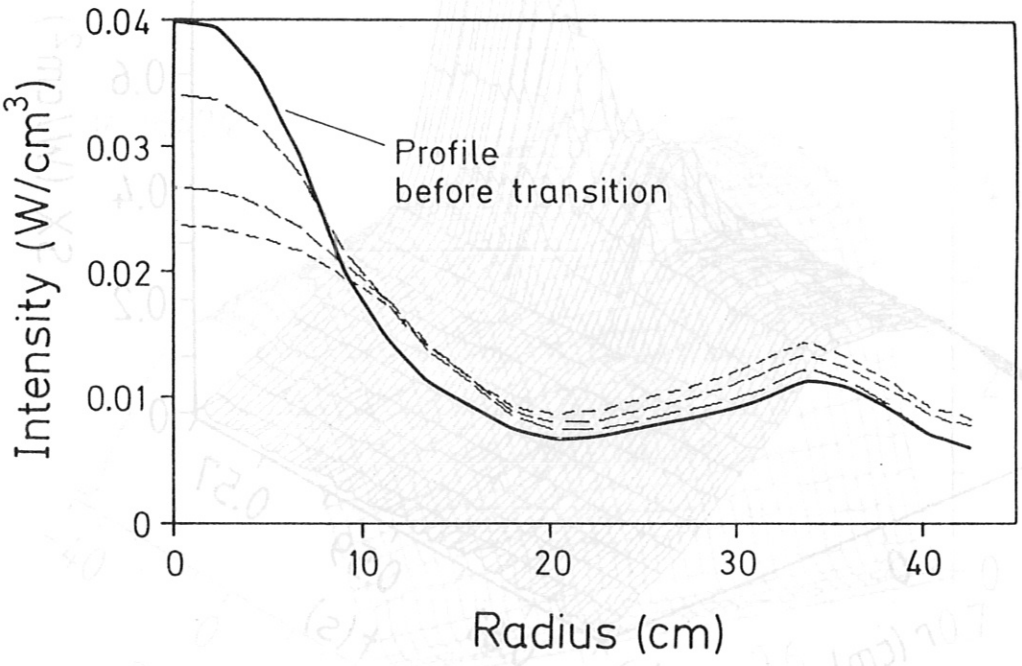

Fig. 5: Bolometer radiation profiles showing the build-up of a central peak before the transition. The solid curve gives the profile reached immediately before the onset of sawteeth.

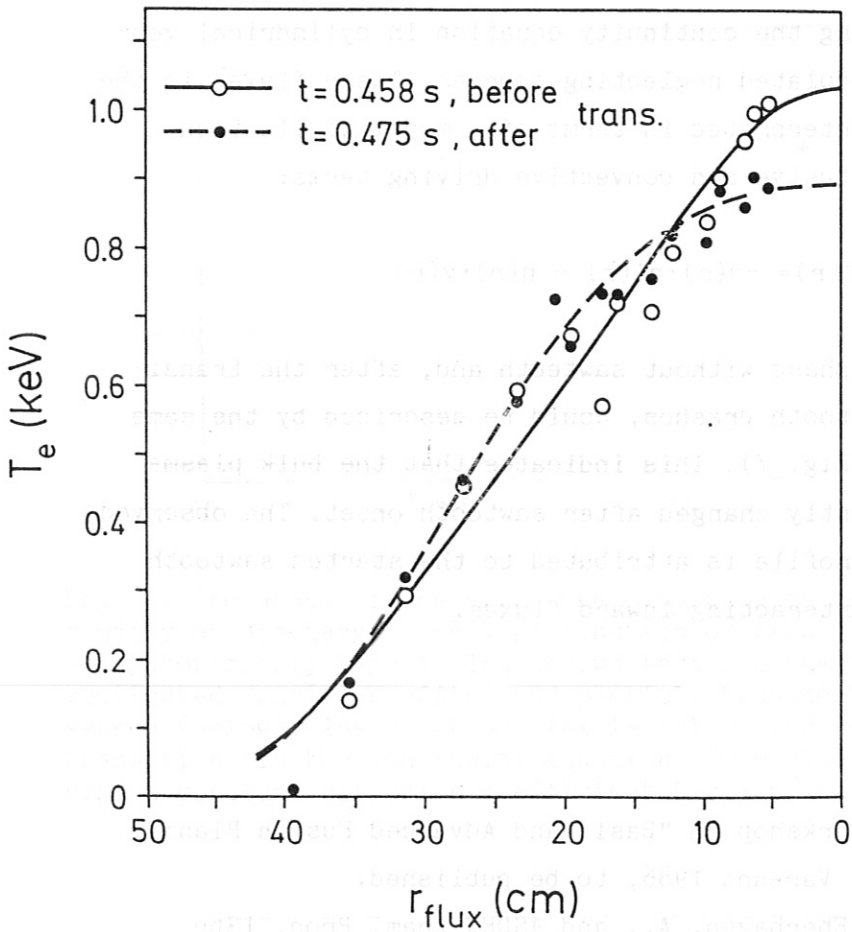

Fig. 6: Electron temperature profiles measured shortly before and after the transition to a sawteething discharge, indicating a pronounced flattening of the central region.

Conclusion

In summary, the transition to the sawtooth regime shows the signature of a strong sawtooth-like collapse, removing metal impurities from the center of the discharge, which have accumulated there during density build-up. No m=1 precursors are found, however, and the strong MHD activity seen during this phase, which was not studied in detail, does not allow to exclude a more complicated instability with higher mode numbers. The connection to impurities is supported by experiments, where krypton pulses were injected into the plasma. With increasing krypton content, indicated by higher initial levels of central SX radiation, the onset of sawteeth is shifted to later times and MHD activity during the transition increases. At too high impurity content no sawteeth develop and the discharge disrupts.

Transport: Electron density transport has been investigated shortly before and after the collapse. Using the continuity equation in cylindrical geometry, fluxes have been calculated neglecting sources. These fluxes in the plasma core region can be interpreted in terms of a model of electron transport consisting of diffusive and convective driving terms:

$$\Gamma(r) = -D(r) \cdot n'(r) - n(r) \cdot v(r).$$

The fluxes analyzed in the phase without sawteeth and, after the transition, averaging between sawtooth crashes, could be described by the same set of values for D and v (Fig. 7). This indicates that the bulk plasma transport has not significantly changed after sawtooth onset. The observed broadening of the density profile is attributed to the started sawtooth activity, balancing the counteracting inward fluxes.

References:

/1/ Gehre, O., Course and Workshop on "Basic and Advanced Fusion Plasma Diagnostic Techniques", Varenna 1986, to be published.

/2/ Gehre, O., Becker, G., Eberhagen, A., and ASDEX team, Proc. 13th Europ. Conf. on Controlled Fusion and Plasma Heating, Schliersee 1986, EPS Europ. Conf. Abstr. 10 C, part I, p. 220-223.

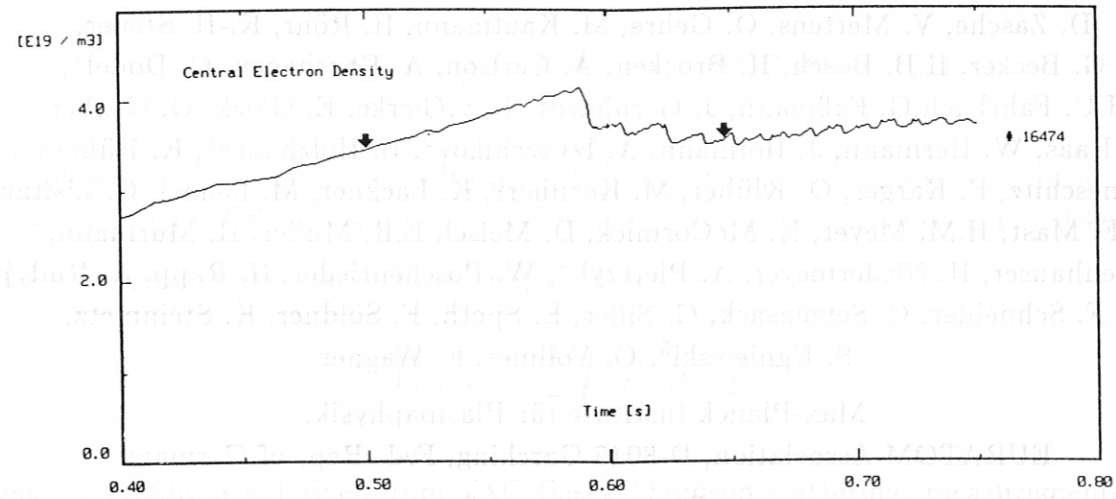

Fig. 7: The above figure shows the evolution of the central electron density of discharge 16474 as function of time. The transition happens at approximately 0.59 s. The arrows indicate the times where investigated density profiles and particle transport properties are presented (below). The electron flux is calculated before and after the transition via the continuity equation. To evaluate the inward velocity v(r) a constant diffusion coefficient D=0.4 m^2 is assumed.

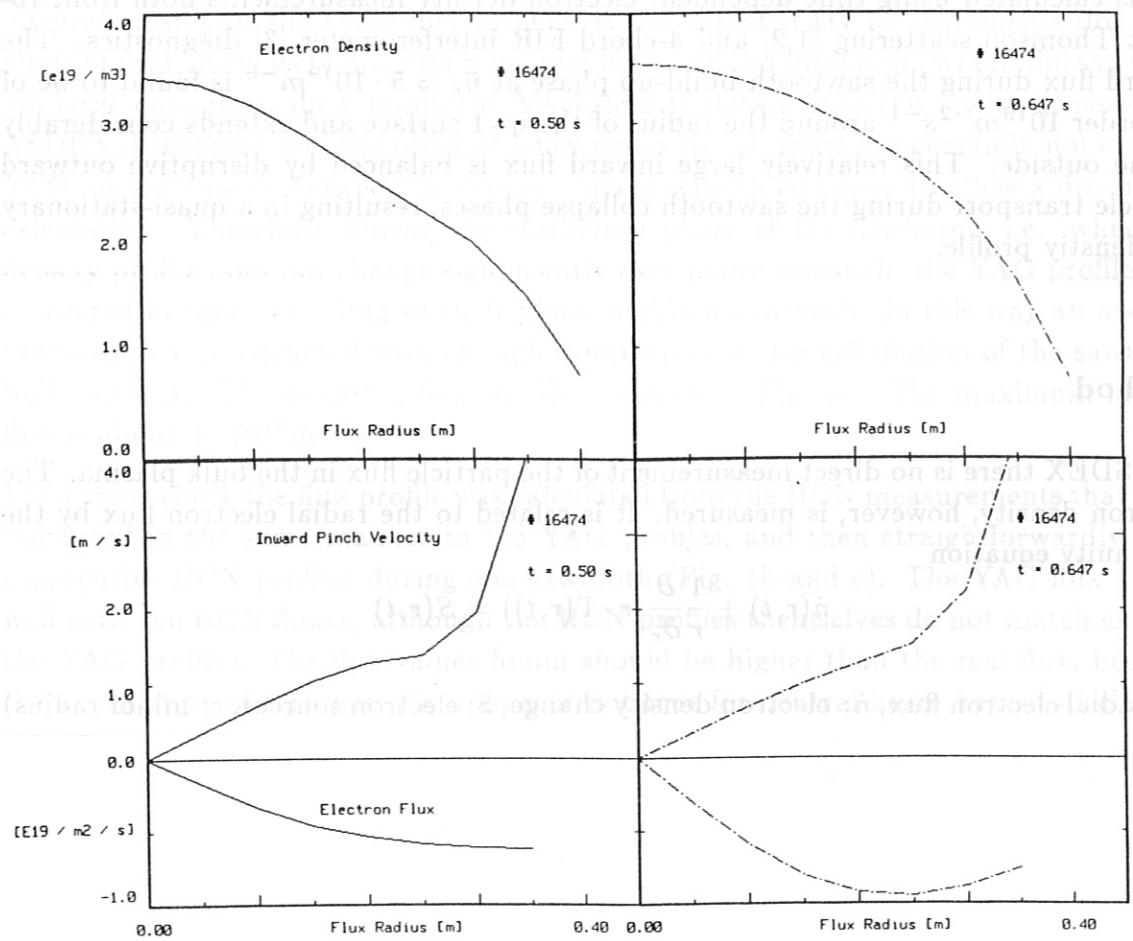

PARTICLE TRANSPORT IN SAWTEETH

D. Zasche, V. Mertens, O. Gehre, M. Kaufmann, H. Röhr, K.-H. Steuer, G. Becker, H.B. Bosch, H. Brocken, A. Carlson, A. Eberhagen, G. Dodel[1], H.U. Fahrbach,G. Fußmann, J. Gernhardt, G. v.Gierke, E. Glock, O. Gruber, G. Haas, W. Hermann, J. Hofmann, A. Izvozchikov[2], E. Holzhauer[1], K. Hübner[3], G. Janeschitz, F. Karger, O. Klüber, M. Kornherr, K. Lackner, M. Lenoci, G. Lisitano, F. Mast, H.M. Meyer, K. McCormick, D. Meisel, E.R. Müller, H. Murmann, J. Neuhauser, H. Niedermeyer, A. Pietrzyk[4], W. Poschenrieder, H. Rapp, A. Rudyj, F. Schneider, C. Setzensack, G. Siller, E. Speth, F. Söldner, K. Steinmetz, S. Ugniewski[5], O. Vollmer, F. Wagner

Max-Planck Institute für Plasmaphysik,
EURATOM Association, D-8046 Garching, Fed. Rep. of Germany

[1]University of Stuttgart, [2]Ioffe Institute, [3]University of Heidelberg,
[4]University of Washington, Seattle, USA, [5]Inst. for Nuclear Research, Swierk, Poland

Summary

The particle transport in ASDEX discharges with sawtooth oscillations is investigated on time scales comparable to and smaller than the sawtooth period. The net particle flux is calculated using time dependent electron density measurements both from 16-point Thomson scattering [1,2] and 4-chord FIR interferometer [3] diagnostics. The inward flux during the sawtooth build-up phase at $\bar{n}_e \approx 5 \cdot 10^{19} m^{-3}$ is found to be of the order $10^{19} m^{-2} s^{-1}$ around the radius of the q=1 surface and extends considerably to the outside. This relatively large inward flux is balanced by disruptive outward particle transport during the sawtooth collapse phases, resulting in a quasi-stationary flat denstiy profile.

Method

At ASDEX there is no direct measurement of the particle flux in the bulk plasma. The electron density, however, is measured. It is related to the radial electron flux by the continuity equation

$$\dot{n}(r,t) + \frac{1}{r}\frac{\partial}{\partial_r}(r \cdot \Gamma(r,t)) = S(r,t)$$

(Γ: radial electron flux, $\dot{n}$: electron density change, S: electron sources, r: minor radius)

The radial particle flux ($n_i \approx n_e$) is then

$$\Gamma(r,t) = \frac{1}{r}\int_o^r r'[S(r',t) - \dot{n}(r',t)]dr'$$

For ohmic ASDEX discharges with $n_o \geq 10^{19}m^{-3}$ the particle sources resulting from recycling are negligible inside minor radius $r \approx 0.30m$ [4] (separatrix at r = 0.4 m).

With the density n(r,t) known, the flux is then

$$\Gamma(r,t) = -\frac{1}{r}\int_o^r r'\dot{n}(r',t)dr'$$

Density profiles are derived from YAG (laser Thomson scattering) measurements and HCN (laser interferometric) measurements. The YAG data are available for 16 points with minor radius from 0.055 ...0.39 m every 0.017 s, with a resolution $\Delta_{YAG} \approx 5 \cdot 10^{18}m^{-3}$. HCN data (line integrated densities) are available for 4 horizontal chords with minor radius 0, +0.21, -0.21, -0.30 m every 0.001 s, with a resolution $\Delta n_{HCN} \approx 2 \cdot 10^{17}m^{-3}$. Although the density profiles from the 16 direct YAG measurements are more detailed, and hence better suited for flux calculations than profiles from the 4 inverted line integrals, the higher sensitivity and sampling rate of the HCN density profiles make them better suited for investigations of small and fast density changes characteristic for sawtooth oscillations. To find out whether the inverted HCN line integrals result in the same flux profiles as the direct YAG measurements do, both kinds of evaluation were done for a neutral beam-heated discharge, where the sawteeth are large enough to show up on the YAG density data. Since the sawtooth period in ASDEX discharges is of the order of a few times $10^{-2}s$, there are generally not enough YAG measurements between two consecutive sawtooth collapses to allow a direct flux calculation. Therefore, during the stationary phase of the discharge, i.e. when the density profile does not change significantly over many sawteeth, the YAG profiles are reordered in time according to their phase within a sawtooth. In this way an average sawtooth is reconstructed with enough sample profiles for calculation of the sawtooth build-up flux. The resulting flux profile is shown in Fig. 1a. The maximum inward flux is about $1 \cdot 10^{19}m^{-2}s^{-1}$.

For a cross-check the flux profile was calculated from the HCN measurements that were reordered in the same manner as the YAG profiles, and then straightforwardly from consecutive HCN profiles during one sawtooth (Fig. 1b and c). The YAG flux agrees well with the HCN fluxes, although the HCN profiles themselves do not match exactly the YAG profiles. The flux values found should be higher than the real flux, because the assumption of zero particle sources is not true for neutral beam heated discharges

(10^{20} ions/s injected for $P_{NBI} \approx 10^6 W$), but the error introduced is systematic and the same in both YAG and HCN measurements.

The good agreement lends confidence to the calculation of sawtooth build-up fluxes from HCN data alone in an ohmic discharge with sawteeth too small to be detected in the YAG data. In this case, the plasma is source-free. The inward flux is found to be on the order of $\approx 10^{19} m^{-2} s$ around the radius of the q=1 surface and extends considerably to the outside (see fig. 2).

Conclusions

Since the density profile is generally quasi-stationary in the presence of sawteeth, we must conclude that the inward flux is compensated for by the violent, disruptive particle transport in the opposite direction which takes place in the sawtooth collapses. This ensures that the net particle flux, averaged over times long compared to the sawtooth period, is zero, and the density profile remains unchanged as long as the sawteeth continue.

The inward flux seen during the sawtooth build-up phases is not marginal. A simple estimate shows that the observed inward flux could double the central density within 0.1 ... 0.2 s, if there were no opposing mechanism. There are indeed some cases, when the balancing effect of the sawtooth collapses is obviously absent. This is found, for example, in the early stages of a discharge, before sawteeth have started [5], or during successful pellet refuelling [6]. The observed peaking of the density profile in these cases is of a magnitude that is compatible with the profile peaking during the sawtooth build-up.

References

/1/ H. Röhr, K.-H. Steuer, et al., Nucl. Fusion 22, (1982) 1099.

/2/ H. Röhr, K.-H. Steuer, H. Murmann, D. Meisel, IPP internal report, IPP III/121, in print.

/3/ O. Gehre, Int. Journal of Infrared and Millimeter Waves, Vol. 5 (1984), 369.

/4/ V. Mertens, private communication.

/5/ O. Gehre, V. Mertens, M. Kornherr, E.R. Müller, this conference.

/6/ V. Mertens, M. Kaufmann, et al., this conference.

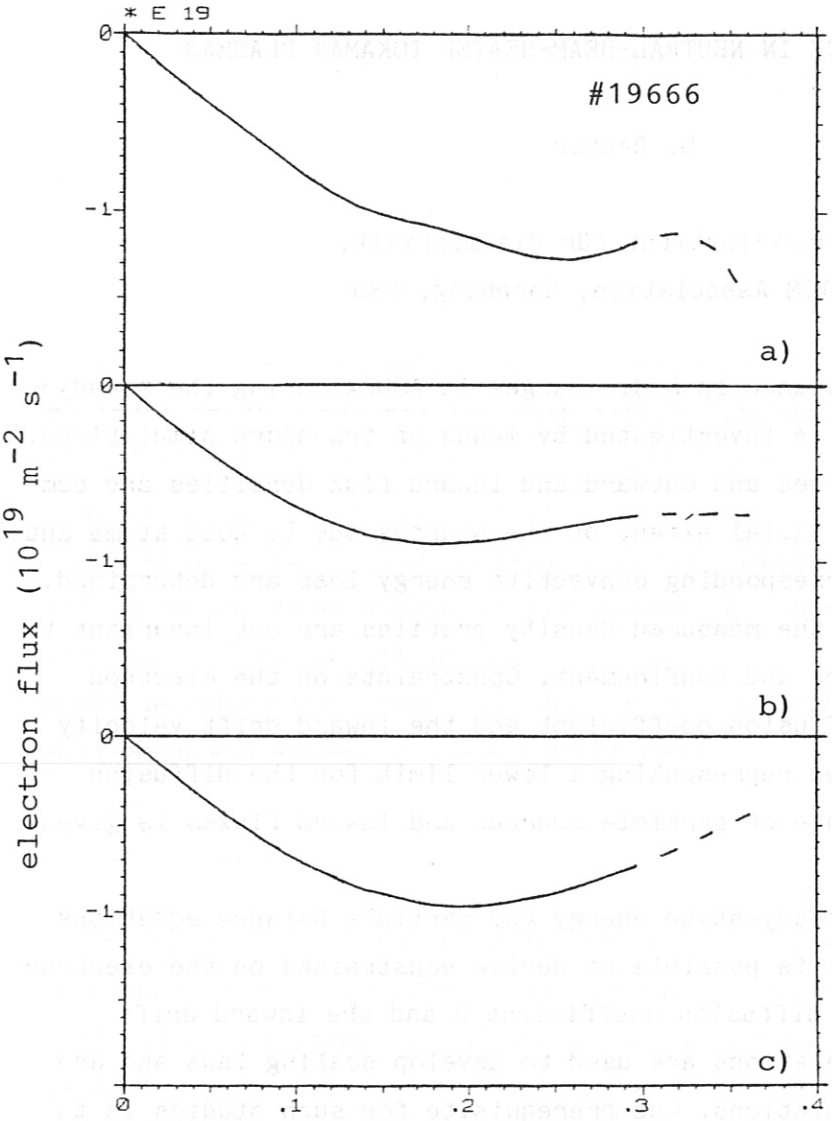

Fig. 1:

Inward flux during sawtooth build-up in neutral beam heated discharge

a) calculated from YAG data, re-ordered, average over 7 sawteeth

b) from HCN data, re-ordered, average over 7 sawteeth

c) from HCN data, consecutive samples, single sawtooth

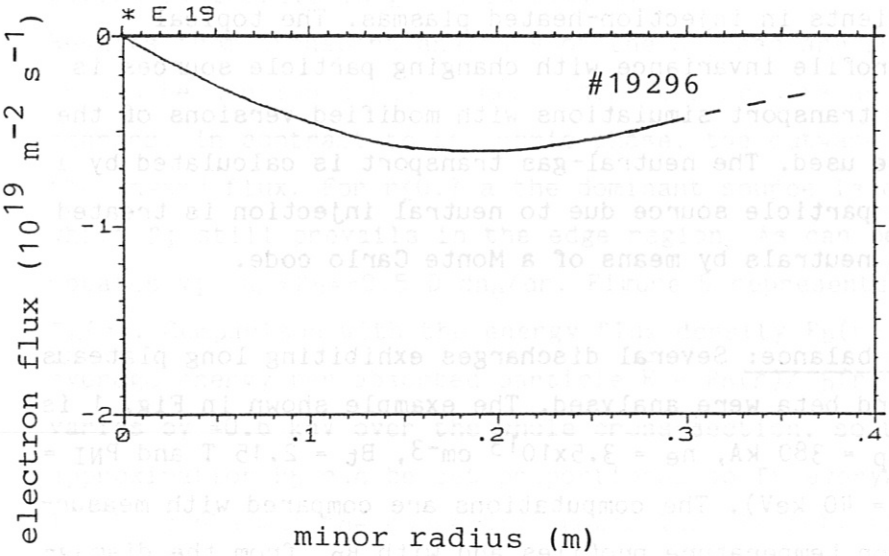

Fig. 2:

Inward flux during sawtooth build-up in ohmic discharge

HCN data, average over 5 sawteeth

PARTICLE BALANCE IN NEUTRAL-BEAM-HEATED TOKAMAK PLASMAS

G. Becker

Max-Planck-Institut für Plasmaphysik,
EURATOM Association, Garching, FRG

ABSTRACT: The particle balance in H discharges in ASDEX during the steady-state ohmic and H phases is investigated by means of transport simulations. Profiles of particle sources and outward and inward flux densities are computed. The magnitude and radial extent of the sources due to cold atoms and beam fuelling and the corresponding convective energy loss are determined. It is further shown that the measured density profiles are not invariant to changes in particle source and confinement. Constraints on the electron heat diffusivity, the diffusion coefficient and the inward drift velocity are derived. An expression representing a lower limit for the diffusion coefficient in the presence of particle sources and inward fluxes is given.

Introduction: From the steady-state energy and particle balance equations with neutral injection it is possible to derive constraints on the electron heat diffusivity χ_e, the diffusion coefficient D and the inward drift velocity v_{in} /1/. Such relations are used to develop scaling laws and are applied in transport simulations. One prerequisite for such studies is to know the radial extent of the particle and energy sources due to neutral injection and the corresponding convective energy losses. The paper deals with the particle sources, particle confinement and resulting constraints for transport coefficients in injection-heated plasmas. The topical question of density profile invariance with changing particle sources is studied. Results from transport simulations with modified versions of the BALDUR code /2, 3/ are used. The neutral-gas transport is calculated by a Monte Carlo code. The particle source due to neutral injection is treated by following the fast neutrals by means of a Monte Carlo code.

Steady-state particle balance: Several discharges exhibiting long plateaus of current, density and beta were analysed. The example shown in Fig. 1 is an H discharge with I_p = 380 kA, $\bar{n}_e = 3.5 \times 10^{13}$ cm^{-3}, B_t = 2.15 T and P_{NI} = 3.45 MW ($H^o \rightarrow D^+$, E_o = 40 keV). The computations are compared with measured density and electron temperature profiles and with $\beta_{p_\perp}$ from the diamagnetic loop. Good agreement is obtained by applying the coefficients /4, 5/

$$\chi_e^{OH}(r) = 1.6\times10^{16} A_i^{-1/2} B_t n_e(r)^{-1} T_e(r)^{-1} q(r)^{-1} \text{ cm}^2 \text{ s}^{-1} \quad (1)$$

$$D^{OH}(r) = 0.4 \ \chi_e^{OH}(r) \quad (2)$$

in the ohmic phase and

$$\chi_e^{H}(r) = 2.6\times10^{6} \ r_n(r)^{-1} q_a B_t(R_o)^{-1} \text{ cm}^2 \text{ s}^{-1} \quad (3)$$

$$D^{H}(r) = 0.4 \ \chi_e^{H}(r) \quad (4)$$

in the H phase. The inward drift velocity is given by $v_{in}(r) = 0.5\ D(r)\ r_{Te}(r)^{-1}$ cm s^{-1}, and the ion heat diffusivity used is three times the neoclassical values according to Chang and Hinton. The ion mass number is denoted by A_i. The toroidal magnetic field B_t is in kG, n_e is in cm^{-3}, T_e is in keV, q_a is the cylindrical q at the plasma radius a=40 cm and R_o = 167 cm is the major radius of the plasma. The quantities $r_n = -n_e/(\partial n_e/\partial r)$ and $r_{Te} = -T_e/(\partial T_e/\partial r)$ are in cm.

Under steady-state conditions the particle balance with anomalous outward diffusion and anomalous inward drift reads

$$-D \frac{dn_e}{dr} - v_{in} n_e = \Gamma_i + \Gamma_b \quad (5)$$

where Γ_i and Γ_b are the flux densities due to the ionisation of cold atoms and due to the beam fuelling, respectively. The particle balance in the ohmic phase is shown in Fig. 2. Since the plasma is impermeable to cold neutrals ($\lambda_o << a$ with mean free path λ_o), the interior of the plasma is almost source-free. This gives rise to nearly equal outward and inward fluxes, the typical difference being only 10 % of each of these fluxes. Obviously, the main contribution due to Γ_i occurs outside $r \approx 0.8$ a. The detailed Γ_i profile is given in Fig. 3.

Results from transport analysis of the H phase are presented in Fig. 4. It should be mentioned that almost identical results are obtained in L discharges. In contrast to the ohmic phase, the outward flux clearly exceeds the inward flux. For $r \lesssim 0.7$ a the dominant source is due to beam fuelling, while Γ_i still prevails in the edge region. As can be seen, at r= a/2 one obtains $v_{in} n_e \approx \Gamma_b \approx -0.5\ D\ dn_e/dr$. Figure 5 represents a detailed plot of $\Gamma_b(r)$. Comparison with the energy flux density $P_b(r)$ shows that the average energy per absorbed particle $\bar{E} = P_b(r)/\Gamma_b(r)$ = 23.8 keV only varies by ±0.6 keV over the whole cross-section, so that to very good approximation P_b can be set proportional to Γ_b everywhere.

In ohmic plasmas the convective power loss is only significant in the edge region, where Γ_i is large. With neutral injection, however, high con-

vective losses $P_c \approx 2.5\ (T_e+T_i)\ \Gamma_b$ also occur in the plasma bulk owing to the large particle source and high temperatures. The ratio $P_c/P_b \approx 2.5\ (T_e+T_i)/\bar{E}$ amounts to about 30 % at $r=2a/3$. With increasing heating power the fraction of P_b lost by convection grows with the temperature sum to unacceptably high values, unless E_o and $\bar{E}$ are correspondingly raised. The response of the density profile shape to changes in the particle source distribution is demonstrated in Fig. 6. During the ohmic phase the measured density profile is parabolic, while it is more triangle-shaped in the H phase. Evidently, the density profile shape is not invariant to changes in particle source and confinement.

Constraints on transport coefficients with injection heating: General expressions for transport coefficients are derived from approximate particle and energy balance equations. Using $\Gamma_i \ll \Gamma_b$ for $r \lesssim 0.7$ a in Eq. (5) yields

$$\frac{v_{in}}{D} \approx r_n^{-1} - \frac{\Gamma_b}{n_e D} \qquad (6)$$

Unlike in the source-free case ($v_{in}/D = r_n^{-1}$), the ratio v_{in}/D is here determined by the beam-fuelling profile as well, which has to be taken from code calculations. To avoid this disadvantage, we eliminate Γ_b with the help of the energy balance.

For $r \lesssim 0.7$ a the losses due to charge exchange and radiation are negligibly small. At injection powers much higher than the ohmic input and negligible ion heat conduction one obtains

$$q_e(r) \approx P_b(r) - P_c(r) \qquad (7)$$

where q_e is the flux density due to electron heat conduction. With $P_b(r) = \bar{E}\Gamma_b(r)$ and $P_c \approx 2.5\ (T_e+T_i)\ \Gamma_b$ it follows that

$$\Gamma_b \approx -\bar{E} - 2.5(T_e+T_i)^{-1}\, n_e \chi_e \frac{dT_e}{dr}. \qquad (8)$$

Replacing the particle source in Eq. (6) yields

$$\frac{v_{in}}{D} \approx r_n^{-1} + [\bar{E} - 2.5(T_e + T_i)]^{-1} \frac{\chi_e}{D} \frac{dT_e}{dr} \qquad (9)$$

This relation holds under stationary conditions for $P_{OH} \ll P_{NI}$ and $\Gamma_i \ll \Gamma_b$. An even simpler formula is obtained by setting χ_e/D equal to a constant. It was shown above that $\bar{E}$ is a constant which is usually large compared with the temperature sum. The ratio v_{in}/D can be determined from measured density and temperature profiles without knowing the beam-fuelling source. Using, for instance, the approximations $n_e(r) = n_e(0)\,(1-r/a_1)$ and $T_e(r) = T_e(0)\,(1-r/a_2)$ yields $v_{in}/D \approx (a_1-r)^{-1}$ - const, i.e. the increase of v_{in} with radius is much stronger than that of D.
The weak radial dependence of $P_b = \bar{E}\Gamma_b$ in the range $0.25 \leq r/a \leq 1$ (see Fig. 5) results in $q_e = -n_e \chi_e dT_e/dr \approx$ const (see Eq. (7)). With the above T_e profile one thus obtains $\kappa_e = n_e \chi_e \approx$ const and $D(r) \sim \chi_e(r) \sim n_e(r)^{-1}$.
According to Eq. (5) the diffusion coefficient reads $D = -(\Gamma_i + \Gamma_b + v_{in} n_e)/(dn_e/dr)$. In the case $v_{in} = 0$ one obtains the expression

$$D(r) = - \frac{\Gamma_i(r) + \Gamma_b(r)}{\frac{dn_e}{dr}(r)} \qquad (10)$$

which represents a lower limit, since for given particle sources and density profile a finite inward flux always corresponds to a higher diffusion coefficient. The minimum D can also be given when the anomalous inward flux is unknown. Equation (10) is especially useful for predictive code simulations, because it yields the minimum D values which are able to produce the measured density gradients.

References

/1/ Becker, G., in Controlled Fusion and Plasma Heating (Proc. 13th Europ. Conf. Schliersee, 1986), Part I (1986) 224.

/2/ Post, D.E., Singer, C.E., McKenney, A.M, BALDUR: A One-dimensional Plasma Transport Code, PPPL Transport Group, TFTR Physics Group, Rep. 33 (1981).

/3/ Becker, G., ASDEX Team, Neutral Injection Team, Analysis of Local Transport in Neutral-beam-heated L and H Plasmas of ASDEX, Max-Planck-Institut für Plasmaphysik, Garching, Rep. IPP III/98 (1984).

/4/ Becker, G., Nucl. Fusion 27 (1987) 11.

/5/ Becker, G., Nucl. Fusion 24 (1984) 1364.

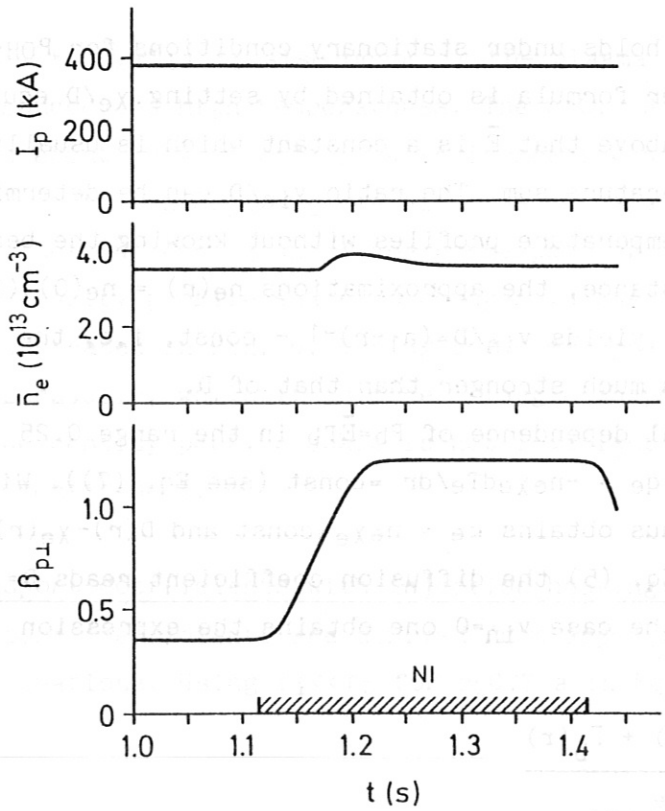

Fig. 1: Time evolution of plasma current, line-averaged density and poloidal beta in an H discharge.

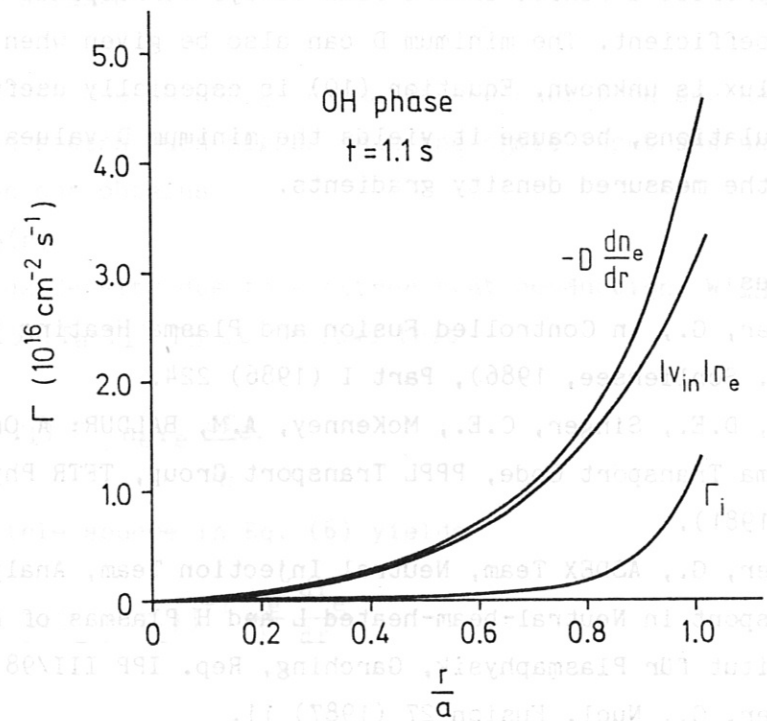

Fig. 2: Particle balance in the steady-state ohmic phase.

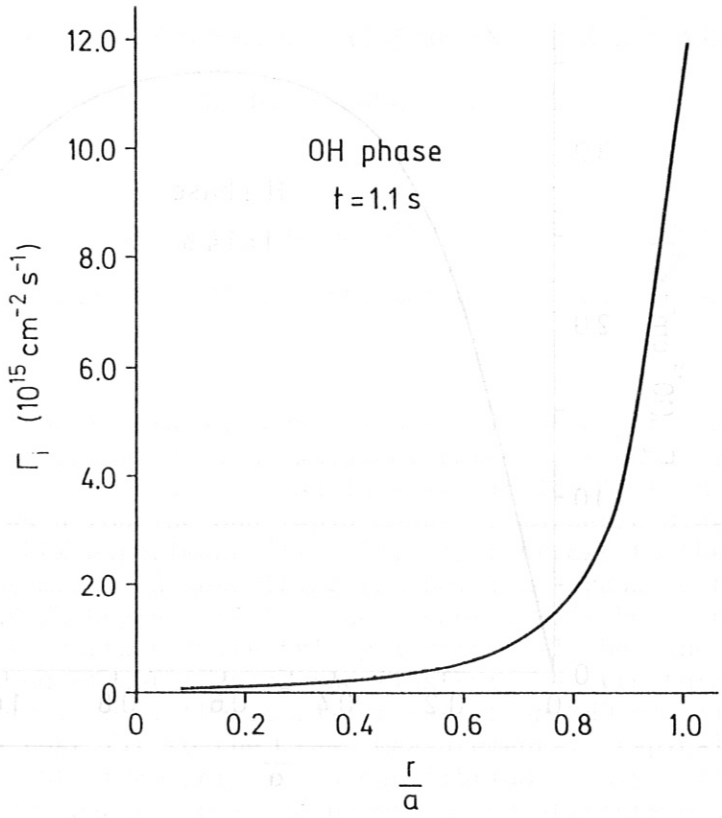

Fig. 3: Γ_i profile in the ohmic phase.

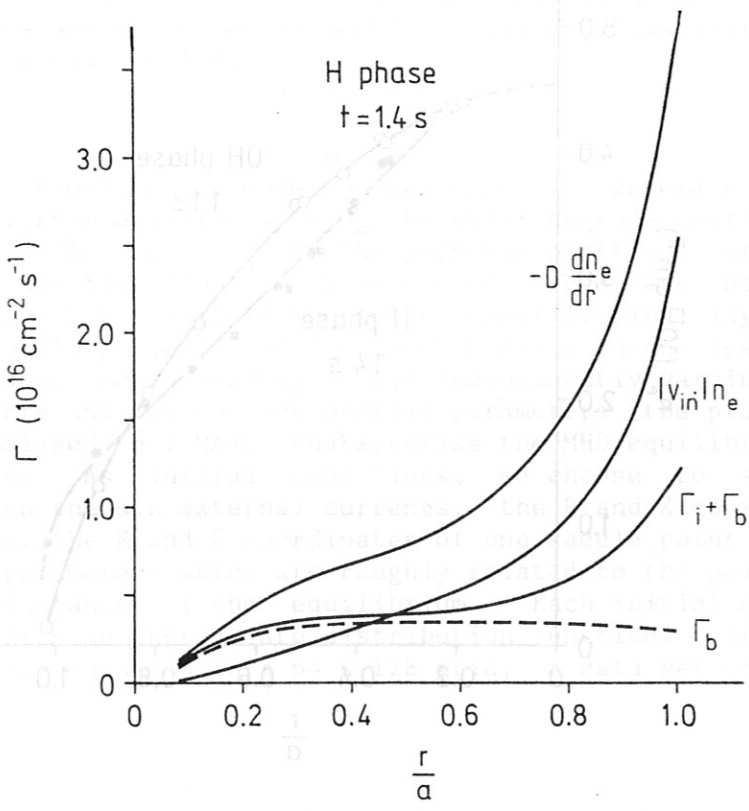

Fig. 4: Particle balance in the steady-state H phase.

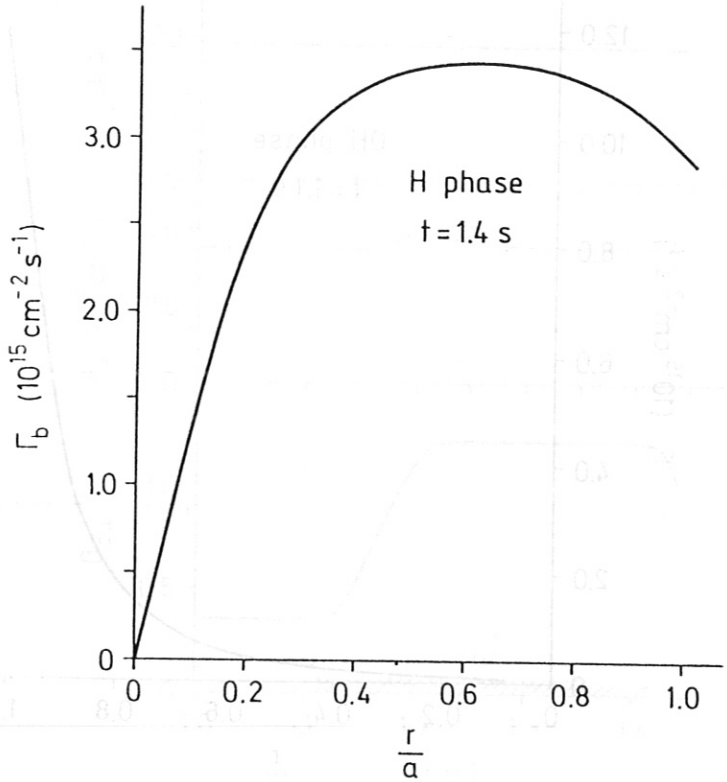

Fig. 5: Γ_b profile in the H phase.

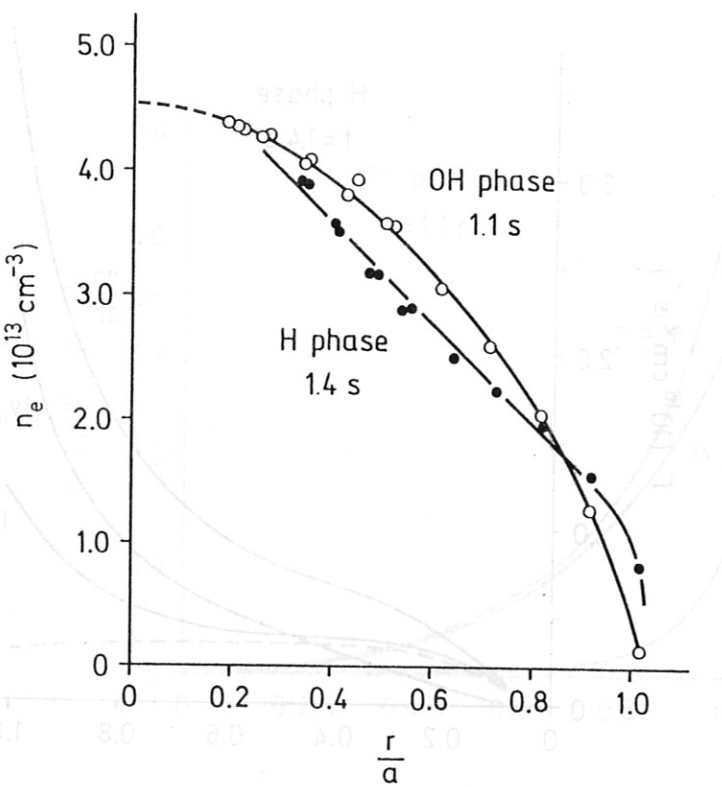

Fig. 6: Density profiles with ohmic heating and neutral-beam injection.

FAST DETERMINATION OF FLUX SURFACE STRUCTURE IN ASDEX AND ASDEX UPGRADE USING FUNCTION PARAMETERISATION

P.J. Mc Carthy*

Max-Planck-Institut fur Plasmaphysik, Garching bei Munchen.

*On attachment from University College, Cork, Ireland.

1. INTRODUCTION

The method of Function Parameterisation (FP), whereby the dependence of a simulated data base of desired physical parameters on a corresponding set of raw measurements is determined in a statistically robust manner, is now established as a routine and rapid means of magnetic diagnostic data analysis on the ASDEX experiment /1/, /2/. In contrast to the adequacy of the nested circles model in describing the poloidal cross-section of ASDEX MHD equilibria, ASDEX Upgrade field line geometry will be more general and non-circular flux surfaces with triangularity will be the norm. The conventional method of determining the flux surface structure (FSS) from magnetic diagnostics, i.e. the iterative use of an MHD equilibrium solver to arrive at a best fit to the raw measurements, typically requires several seconds of CPU time per fitted equilibrium. Only a limited number of time points may then be analysed under the constraints of between-shot analysis. Knowledge of the FSS will be, however, a prerequisite for the evaluation of many ASDEX Upgrade diagnostic data with spatially varying profile information. Hence it would be very desirable to have a means of recovering the FSS sufficiently fast to yield, on a between-shot time scale, a comprehensive time history of the latest discharge. An FP solution to this problem is proposed in the following sections. Some tabulated results are presented in Section 4 and some qualifying remarks are noted in the final Section.

2. THE DATABASE

The Garching Equilibrium Code /3/ was used to generate some 5000 limiter and divertor equilibria using the ASDEX Upgrade configuration of poloidal field coils together with the proposed positions of in-vessel magnetic probes and flux loops which were used to generate corresponding raw measurements. Fig. 1 shows the not necessarily final layout for 40 probes and 30 flux loops inside of the ASDEX Upgrade vacuum vessel. Eight degrees of freedom, corresponding to six independently varying poloidal field coil currents and two current profile parameters (the plasma current itself is normalised to 1 MA), characterise the MHD equilibrium in the present instance. As initial conditions, we choose to specify two relations between the six external currents, the R and Z coordinates of the magnetic axis, the R and Z coordinates of one saddle point and the two current profile parameters which are roughly related to the poloidal beta and internal inductance of the equilibrium. Each initial condition is chosen randomly from an appropriate distribution function. After solving the Grad-Shafranov equation on a 64 x 128 grid, a data set of some 500

words is stored on disk for each equilibrium. It consists of the simulated raw measurements, a variety of equilibrium parameters and a set of approximately 250 coefficients of a bi-cubic spline fit to the solution flux function over a fixed subset of the grid large enough to enclose all possible plasma boundaries.

3. RECOVERY OF ARBITRARY CLOSED FLUX CONTOURS

We propose, using an FP approach, a straightforward method of recovering the contour of a given flux value or circular equivalent radius with the sole restriction that it be a single-valued function of polar coordinates with origin at the magnetic axis. The latter quantity will be accurately recoverable (see following section) and so the relative nature of the contour determination does not pose a problem. We parameterise the contour by finding the distance from the origin to its point of intersection with a number of radial chords spaced at fixed angular intervals (see Fig. 1) using the bi-cubic spline fit to the poloidal flux in conjunction with a routine to search along the chord in question for the appropriate flux value. The intersection distances are now stored as additional "plasma parameters" and the normal FP regression against linear and quadratic combinations of a limited number of principal components /1/, /2/ is performed.

4. RESULTS

The sample results depicted in Table 1 arise from a regression of each of the listed parameters on the ten most significant principal components (and their quadratic combinations) of 41 magnetic probe and 37 flux loop measurements. The regression was performed on a subset of the data base consisting solely of lower null divertor equilibria. Dimensioned quantities are in metres.

The first seven parameters and the last two are self explanatory. The intervening names are of the form D:CONTOUR TYPE:ANGLE where ANGLE is the angle (in degrees) made by the intersecting chord (see Fig. 1), D is a normalised distance-like label for the chosen contour (D = 100 for the separatrix) and CONTOUR TYPE indicates either a contour with a particular flux value (PSI) or a particular circular equivalent radius (RHO). Thus 66 RHO 55 is a parameter which takes the value of the distance (m) from the magnetic axis along a chord inclined at 55 degrees to the horizontal to the flux surface enclosing 4/9 of the plasma area (we can also use enclosed volume to label the flux surfaces). Similarly 33 PSI 45 is the distance (m) from the magentic axis along a 45 degree chord to the surface whose flux difference relative to the magnetic axis flux is 1/3 of the axis-separatrix flux difference. For each parameter, the uncertainty in recovery is quoted for noiseless and noisy raw measurements. The significance of the STANDARD DEVIATION and ERROR columns and the choice of error magnitude follows references /1/ and /2/.

5. DISCUSSION

The tabulated results indicate that we can recover individual points on a contour of a specified normalised flux difference or circular equivalent radius with a standard error of about 5 mm, rising to 10 mm in the neighbourhood of stagnation points. If N points on each of K contours are

deemed sufficient to define the FSS of the equilibrium, then the real-time computation using the 65 regression coefficients obtained for each parameter in the present study requires about NK/4 msec for 1 megaflop/sec computing power. Thus 20 contours each consisting of one point every 15 degrees of poloidal arc would require 0.12 sec calculation time. It should be noted in regard to the present results that

(a) The selection of lower null point divertor equilibria (or any specific equilibrium category) assumes that it will be possible in real time to adequately discriminate between categories and hence to select the correct set of FP regression coefficients - one set covering all possible equilibria is not adequate (see Ref./1/).

(b) As part of its vertical stabilisation system, ASDEX Upgrade has a number of passive conductors located inside the vacuum vessel. The effects of transient currents on magnetic measurements made near these conductors has not been included, but once accounted for is not expected to be a problem.

(c) The recovery of moments of the flux surfaces rather than individual points is potentially more time efficient, though this approach has not yet been fully investigated.

(d) Finally, the encouraging accuracy of the contour recovery suggests that it may be possible to infer information about the current distribution in ASDEX Upgrade from the currently proposed magnetic measurements. This is consistent with previous reports linking determination of the current distribution in elongated plasmas to knowledge of flux surface geometry (/4/, Chapter 3 and /5/).

REFERENCES:

/1/ BRAAMS, B.J. JILGE, W. AND LACKNER, K., Fast determination of plasma parameters by function parametrization, Nucl. Fusion 26 (1986), 699-708.

/2/ McCARTHY, P.J. AND SEXTON, M.C., Plasma profile recovery by function parameterisation, IPP Report 5/12, Max-Planck-Institut fur Plasmaphysik, 1986.

/3/ LACKNER, K., Computation of ideal MHD equilibria, Comput. Phys. Commun. 12 (1976), 33-44.

/4/ BRAAMS, B.J., Computational studies in tokamak equilibrium and transport, Ph.D. thesis, Max-Planck-Institut fur Plasmaphysik, 1986.

/5/ CHRISTIANSEN, J.P. AND TAYLOR, J.B., Determination of current distribution in a tokamak, Nucl. Fusion 22 (1982), 111-115.

TABLE 1

PARAMETER	MIN	MAX	RANGE	STANDARD DEVIATION	ERROR NOISE=0	ERR/S.D. NOISE=0	ERROR NOISE= .1xS.D.	ERR/S.D. NOISE= .1xS.D.
RAXIS	1.49	1.81	.32	.074	.001	1.4%	.003	4.5%
ZAXIS	- .15	.30	.45	.106	.003	2.8%	.006	5.4%
RGEO	1.42	1.74	.32	.063	.002	3.6%	.004	6.2%
ZGEO	- .22	.26	.48	.106	.003	2.9%	.005	5.2%
A MINOR	.30	.55	.25	.056	.003	5.7%	.006	11.0%
B MINOR	.44	1.02	.58	.100	.007	6.9%	.010	9.6%
KAPPA	1.03	2.80	1.77	.286	.022	7.6%	.042	14.7%
33 PSI 0	.13	.27	.14	.024	.003	11.5%	.004	15.7%
66 PSI 0	.20	.39	.19	.036	.003	9.3%	.004	10.1%
100 PSI 0	.24	.51	.27	.049	.003	7.0%	.005	9.7%
33 RHO 0	.10	.19	.09	.019	.001	7.1%	.003	13.3%
66 RHO 0	.18	.36	.18	.036	.002	6.0%	.004	11.3%
100 RHO 0	.24	.51	.27	.049	.003	7.0%	.005	9.8%
33 PSI 45	.15	.31	.16	.028	.003	11.8%	.004	13.6%
66 PSI 45	.23	.44	.21	.039	.003	8.9%	.004	9.9%
100 PSI 45	.32	.59	.27	.050	.003	6.0%	.004	8.2%
33 RHO 45	.12	.22	.10	.018	.002	10.7%	.003	13.2%
66 RHO 45	.23	.42	.19	.035	.002	6.3%	.004	9.7%
100 RHO 45	.32	.59	.27	.050	.003	6.0%	.004	8.3%
33 PSI 50	.16	.32	.16	.030	.003	11.4%	.005	14.4%
66 RHO 55	.25	.44	.19	.037	.002	6.7%	.004	9.7%
100 PSI 60	.37	.67	.30	.057	.004	7.3%	.005	9.1%
33 RHO 65	.14	.25	.11	.021	.002	9.4%	.002	10.8%
66 PSI 70	.28	.60	.32	.056	.004	7.8%	.007	11.6%
100 RHO 75	.37	.84	.47	.080	.006	7.4%	.009	10.4%
RLOW SADDLE	1.35	1.62	.27	.071	.008	11.7%	.010	13.9%
ZLOW SADDLE	-1.00	- .70	.30	.074	.007	9.5%	.009	12.8%

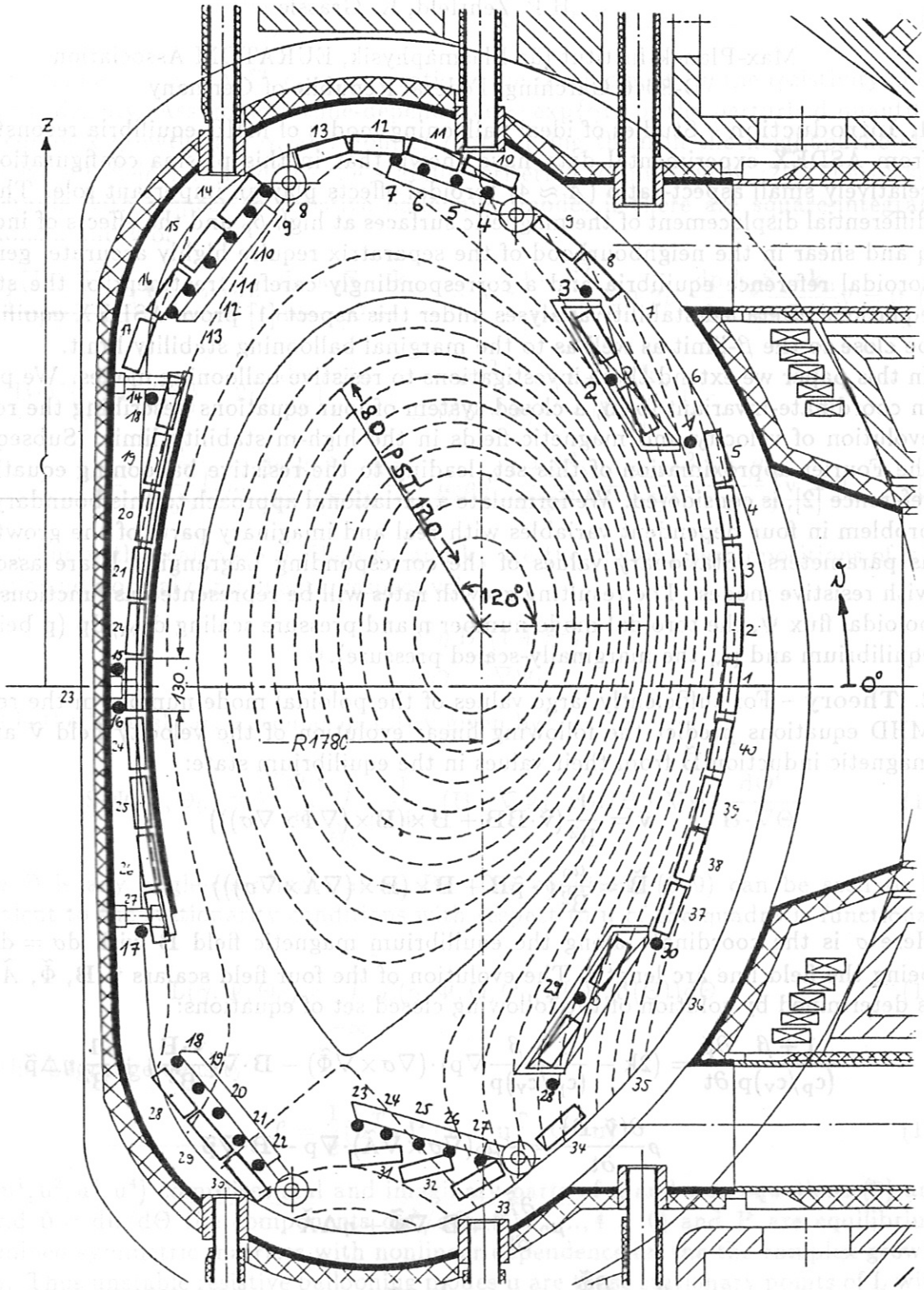

Fig. 1 Poloidal cross-section of the ASDEX Upgrade vacuum vessel showing in-vessel flux coils (black dots) and magnetic probes (open boxes).

RESISTIVE BALLOONING STABILITY OF ASDEX EQUILIBRIA

H.P. Zehrfeld, K. Grassie

Max-Planck-Institut für Plasmaphysik, EURATOM Association
D-8046 Garching, Federal Republic of Germany

1. **Introduction** – Studies of ideal ballooning modes of MHD equilibria reconstructed from ASDEX experimental data have shown that in this plasma configuration with relatively small aspect-ratio ($A \approx 4$) toroidal effects play an important role. The large differential displacement of the magnetic surfaces at high β_p and the effects of increased q and shear in the neighbourhood of the separatrix require highly accurate, genuinely toroidal reference equilibria and a correspondingly careful treatment of the stability equations. Detailed stability analyses under this aspect [1] prove ASDEX equilibria to be close to the β-limit as well as to the marginal ballooning stability limit.
In this paper we extend these investigations to resistive ballooning modes. We present, in coordinate-invariant form, a closed system of four equations describing the resistive evolution of velocity and magnetic fields in the high-m stability limit. Subsequently the Fourier approximation of this set, leading to the resistive ballooning equations of reference [2], is considered. We formulate a variational approach to this boundary value problem in four dependent variables with real and imaginary parts of the growth rate as parameters. Stationary values of the corresponding Lagrangian L are associated with resistive modes. The resulting growth rates will be represented as functions of the poloidal flux Ψ, the toroidal mode number n and pressure scaling dp_M/dp (p being the equilibrium and p_M the marginally-scaled pressure).

2. **Theory** – For sufficiently large values of the poloidal mode number m the resistive MHD equations predict the following linear evolution of the velocity field $\tilde{\mathbf{v}}$ and the magnetic induction $\tilde{\mathbf{B}}$ from their values in the equilibrium state:

$$\tilde{\mathbf{v}} = \frac{1}{B^2}(\tilde{\mathbf{v}}\cdot\mathbf{B}\mathbf{B} + \mathbf{B}\times(\mathbf{B}\times(\nabla\tilde{\Phi}\times\nabla\sigma))) \tag{1}$$

$$\tilde{\mathbf{B}} = \frac{\mu_0}{B^2}(-\tilde{p}\mathbf{B} + \mathbf{B}\times(\mathbf{B}\times(\nabla\tilde{A}\times\nabla\sigma))) \tag{2}$$

Here σ is the coordinate along the equilibrium magnetic field $\mathbf{B}$ with $d\sigma = ds/B$, s being the field line arc length. The evolution of the four field scalars $\tilde{\mathbf{v}}\cdot\mathbf{B}$, $\tilde{\Phi}$, $\tilde{A}$ and $\tilde{p}$ is determined by solution of the following closed set of equations:

$$\frac{1+\beta}{(c_p/c_v)p}\frac{\partial\tilde{p}}{\partial t} = (2k - \frac{1+\beta}{(c_p/c_v)p}\nabla p)\cdot(\nabla\sigma\times\nabla\tilde{\Phi}) - \mathbf{B}\cdot\nabla(\frac{\tilde{\mathbf{v}}\cdot\mathbf{B}}{B^2}) + \frac{1}{B^2}\eta\Delta\tilde{p} \tag{3}$$

$$\rho\frac{\partial(\tilde{\mathbf{v}}\cdot\mathbf{B})}{\partial t} = -\mu_0(\nabla\sigma\times\nabla\tilde{A})\cdot\nabla p - \mathbf{B}\cdot\nabla\tilde{p} \tag{4}$$

$$\mu_0\frac{\partial\tilde{A}}{\partial t} = \mathbf{B}\cdot\nabla\tilde{\Phi} + \eta\Delta\tilde{A} \tag{5}$$

$$\frac{\rho}{B^2}\Delta(\frac{\partial\tilde{\Phi}}{\partial t}) = \mathbf{B}\cdot\nabla(\frac{1}{B^2}\Delta\tilde{A}) + 2\mathbf{k}\cdot(\nabla\tilde{p}\times\nabla\sigma) \tag{6}$$

β is a local beta value and $\mathbf{k}$ the curvature vector:

$$\beta = \frac{\mu_0 (c_p/c_v) p}{B^2}\,, \qquad \mathbf{k} = (\mathbf{B}\cdot\nabla(\mathbf{B}/B))/B; \tag{7}$$

Δ is the Laplacian $\Delta = \nabla\cdot\nabla$, c_p/c_v the ratio of the specific heats, η the resistivity and ρ the mass density. Assuming a time-dependence $\sim \exp\{\gamma t\}$ of the perturbed quantities with complex growth rate γ, and Fourier representing them in the neighbourhood of a localization field line leads to the stability criterion formulated in [2]: The plasma is unstable with respect to resistive ballooning modes if there are square-integrable solutions u and v of

$$\mathbf{B}\cdot\nabla\Big\{\frac{(1+S^2)}{D|\nabla\Psi|^2}\mathbf{B}\cdot\nabla u\Big\} + \Big(2\mu_0\frac{dp}{d\Psi}\frac{k_g S - k_n}{|\nabla\Psi|} - \mu_0\rho\gamma^2\frac{1+S^2}{|\nabla\Psi|^2}\Big)u + 2\mu_0\frac{dp}{d\Psi}\frac{k_g S - k_n}{|\nabla\Psi|}v = 0 \tag{8}$$

$$\mathbf{B}\cdot\nabla\Big\{\frac{1}{B^2}\mathbf{B}\cdot\nabla v\Big\} - 2\mu_0\frac{dp}{d\Psi}\Big(\frac{n^2\eta}{\mu_0\gamma} + \frac{\rho\gamma^2}{\mu_0(dp/d\Psi)^2}\Big)\frac{k_g S - k_n}{|\nabla\Psi|}u -$$

$$- \Big\{\frac{n^2\eta}{\mu_0\gamma}\Big(2\mu_0\frac{dp}{d\Psi}\frac{k_g S - k_n}{|\nabla\Psi|} + \mu_0\rho\gamma^2\frac{1+S^2}{|\nabla\Psi|^2}\Big) + \frac{\mu_0\rho\gamma^2}{B^2}\frac{1+\beta}{\beta}\Big\}v = 0 \tag{9}$$

on that line with $\mathrm{Real}\{\gamma\} > 0$. Here $\mathbf{k}_g$ and $\mathbf{k}_n$ are the obvious decompositions of $\mathbf{k}$ in geodesic and normal components, respectively;

$$D \equiv 1 + \frac{n^2\eta}{\mu_0\gamma}\frac{B^2(1+S^2)}{|\nabla\Psi|^2} \tag{10}$$

and S is the local shear, a secular quantity given by

$$S(\Psi,\Theta,\Theta_0) \equiv \frac{|\nabla\Psi|^2}{B}\int_{\Theta_0}^{\Theta}\frac{1}{|\nabla\Psi|^4}(\mathbf{B}\times\nabla\Psi)\cdot\mathbf{rot}(\mathbf{B}\times\nabla\Psi)\frac{d\Theta'}{\mathbf{B}\cdot\nabla\Theta'} \tag{11}$$

where Θ is any angle-coordinate along $\mathbf{B}$. The equations (8–9) can be seen to be equivalent to the stationarity conditions with respect to $\mathbf{u}$ of the quadratic functional

$$L(\gamma,\Psi,\Theta_0) = \int_{-\infty}^{+\infty}\mathcal{L}(\gamma,\Psi,\Theta,\Theta_0,\mathbf{u}(\Theta),\dot{\mathbf{u}}(\Theta))d\Theta \tag{12}$$

with the Lagrange density

$$\mathcal{L} = \frac{1}{2}(\dot{\mathbf{u}}^T\cdot\mathbf{P}\cdot\dot{\mathbf{u}} - \mathbf{u}^T\cdot\mathbf{Q}\cdot\mathbf{u}) \tag{13}$$

$\mathbf{u} = (u^1, u^2, u^3, u^4)$ comprises real and imaginary parts of u and v in equations (8) and (9) and $\dot{\mathbf{u}} = d\mathbf{u}/d\Theta$ the components $du^k/d\Theta$, $k = 1,..,4$. $\mathbf{Q}$ and $\mathbf{P}$ are equilibrium determined symmetric matrices with nonlinear dependence on the the complex growth rate γ. Thus unstable resistive ballooning modes $\mathbf{u}$ are those stationary points of L with $\mathrm{Real}\{\gamma\} > 0$.

3. **Computational Procedure** – TRANSP code interpreted radial profile data are used for the calculation of distributions of toroidal current I and pressure p over the magnetic surfaces. Corresponding two-dimensional MHD equilibria are determined by iterative solution of the equilibrium partial differential equation

$$\mathrm{div}(\nabla\Psi/R^2) + 4\pi^2\mu_0(1/R^2\langle 1/R^2\rangle^{-1} + \beta_p(1 - 1/R^2\langle 1/R^2\rangle^{-1})\frac{dI}{dV} = 0 \qquad (14)$$

applying the Garching equilibrium code NIVA. R is the distance from the axis of symmetry, V the volume of the considered magnetic surface, $\langle..\rangle$ the usual flux surface average and $\beta_p \equiv (dp/d\Psi)(dV/dI)$. Resistivity profiles are calculated using experiment data on Z_{eff}, n_e and T_e [3]. Discretization of (1) on a sufficiently large interval of the localization line in finite elements [4] and appropriate numbering of function values lead to a finite-dimensional quadratic form $L = u^T \cdot S \cdot u$ with a growth-rate dependent system matrix $S(\gamma)$. For the investigation of resistive ballooning modes we perform a detailed singular-value analysis of S, the methods will be described elsewhere [5].

4. **Results** – Ideal ballooning stability results for a typical high-β_p ASDEX discharge are shown in Fig.1, where dp_M/dp is plotted as a function of $(V/V_B)^{1/2}$ at the maximum attained, code-calculated value of $\beta_p \simeq 2.26$.

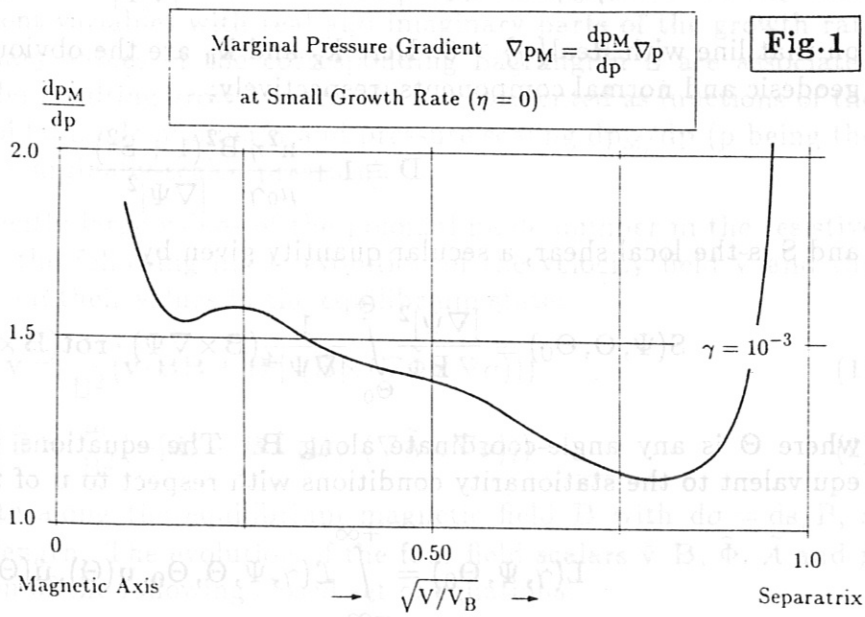

Fig.1

It can be seen that the plasma configuration is ballooning stable on all flux surfaces as $dp_M/dp > 1$ with a minimum value of 1.15. Fig.2 demonstrates the destabilizing effect of resistivity for a particular magnetic surface with a value of $r/a = (V/V_B)^{1/2} \simeq 0.65$ with $q \simeq 2.04$, where the right-hand scale refers to the second stability region. The η-value of $3.32 \cdot 10^{-8}$ Vm/A for this surface and the relatively high ideal ballooning stability of ASDEX – for comparison we have represented the results for $\eta = 0$ by the dashed curves – require an anomalous large toroidal mode number (n = 500) to make this effect plain. It is interesting to note that at small growth rates a minimum of dp_M/dp is observed which moves to smaller growth rates with decreasing resistivity. This effect must be ascribed to the stabilizing influence of the compressibility which is separately demonstrated plotting the undermost curve which is valid for a very small value of c_p/c_v. Finally, Fig.3 shows the radial dependence of the growth rate for different values of n, where γ was normalized by multiplication with the Alfven transit time $\tau_A = (\mu_0\rho)^{1/2}R/B_T$ (where ρ is taken on

the considered flux surface and R/B_T on the magnetic axis). As in the case of ideal ballooning modes (Fig.1) the most unfavourable flux surfaces with respect to stability are those with a r/a– value of about 0.8. Fig.3 illustrates that in the considered range of growth rates $\text{Real}\{\gamma\} \in (0.005, 0.1)$ and resistivities only modes with very high values of n are of remarkable effect.

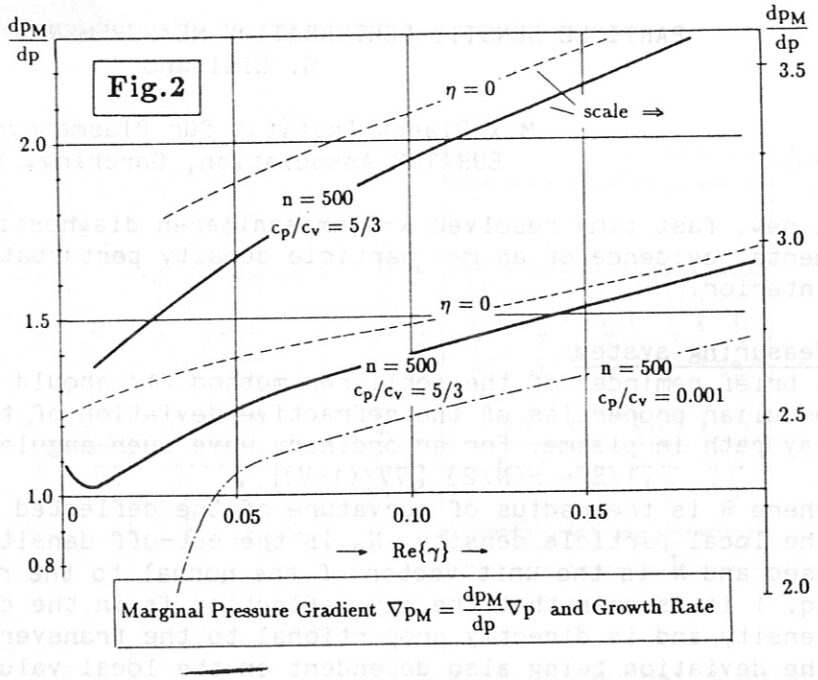

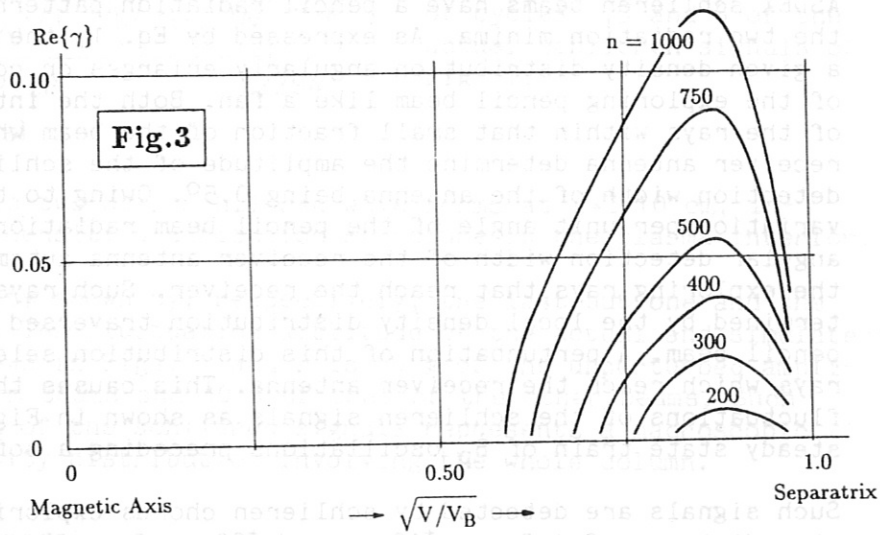

We would like to acknowledge useful discussions with D. Correa-Restrepo and K. Riedel. We also would like to thank O. Gruber for providing us with experimental results of ASDEX in TRANSP-code interpretation.

REFERENCES

[1] O. Gruber et al., "MHD Stability and Transport of Beam Heated ASDEX Discharges in the Vicinity of the Beta Limit", 11th International Conference on Plasma Physics and Controlled Nuclear Fusion Research, Kyoto 1986, paper IAEA-CN-47/A-VI-2.

[2] D. Correa-Restrepo, "Resistive Ballooning Modes in Three-Dimensional Configurations", Z.Naturforsch. **37a**, 848-858 (1982).

[3] S.P. Hirshman, R.J. Hawryluk, B. Birge," Neoclassical Conductivity of a Tokamak Plasma",Nucl. Fusion **17** (1977), 611.

[4] O. Axelsson, V.A. Barker, "Finite Element Solution of Boundary Value Problems", Theory and Computation, Academic Press 1984.

[5] H.P. Zehrfeld, K. Grassie, "Resistive Ballooning Stability of ASDEX Equilibria" (to be published).

PARTICLE DENSITY PERTURBATION MEASUREMENTS WITH SCHLIEREN

G. Lisitano

Max-Planck-Institut für Plasmaphysik,
EURATOM Association, Garching, FRG

A new, fast time resolved λ=2 mm schlieren diagnostic provides experimental evidence of an m=1 particle density perturbation in the plasma interior.

Measuring system

A brief reminder of the schlieren method /1/ should emphasize a few peculiar properties of the refractive deviation of the electromagnetic wave ray path in plasma. For an ordinary wave such angular deviation is given by

$$1/R = -(\vec{N}/2)\,[\nabla V/(1-V)]\ , \qquad (1)$$

where R is the radius of curvature of the deflected ray path, $V=N/N_c$, N is the local particle density, N_c is the cut-off density for the wave length used and $\vec{N}$ is the unit vector of the normal to the ray trajectory. From Eq. 1 it is seen that the ray deflection is in the direction of decreasing density and is directly proportional to the transversal density gradient, the deviation being also dependent on the local value of the density. The ASDEX schlieren beams have a pencil radiation pattern extending 30° between the two radiation minima. As expressed by Eq. 1, the local refractivity of a given density distribution angularly enlarges or compresses all the rays of the exploring pencil beam like a fan. Both the intensity and the density of the rays within that small fraction of the beam which reaches the receiver antenna determine the amplitude of the schlieren signal, the detection width of the antenna being 0.5°. Owing to the large intensity variation per unit angle of the pencil beam radiation pattern, the small angular detection width of the receiver antenna automatically identifies the exploring rays that reach the receiver. Such rays are uniquely determined by the local density distribution traversed by the exploring pencil beam. A perturbation of this distribution selectively varies the rays which reach the receiver antenna. This causes the amplitude fluctuations of the schlieren signals as shown in Fig. 1 during an almost steady state train of $\dot{B}_p$ oscillations preceding a soft disruption.

Such signals are detected by schlieren chords exploring the poloidal plane at a distance of Δ=0 cm, $\pm$10 cm and $\pm$20 cm from the midplane of the tokamak. The signals were recorded during an L-phase of deuterium injection into deuterium plasma dominated by the $m\geq 1$, n=1 mode /2/. The onset of the $\dot{B}$ oscillations occurs nearly at the line when β_p attains its maximum. At the time interval in Fig. 1, owing to a transition back into the L-phase, β_p decreases from its maximum value of 2.2 to 1. The injection power, plasma current and safety factor are NI=4 MW, I_p=0.32 MA and q(a) = 3.3 [$q(a) = 2\pi a^2 B_T/\mu_o R I_p$]. The mean value of the particle density increases from 3.5×10^{13} cm^{-3} at the start of injection up to 4.1×10^{13} cm^{-3} at the time of maximum β_p. It then decreases to 2.9×10^{13} cm^{-3} at the time interval in Fig. 1. Owing to their dependence on a fairly localized small region of maximum density gradient, the schlieren signals exhibit far more detailed information than the corresponding Mirnov oscillations and line-integrated

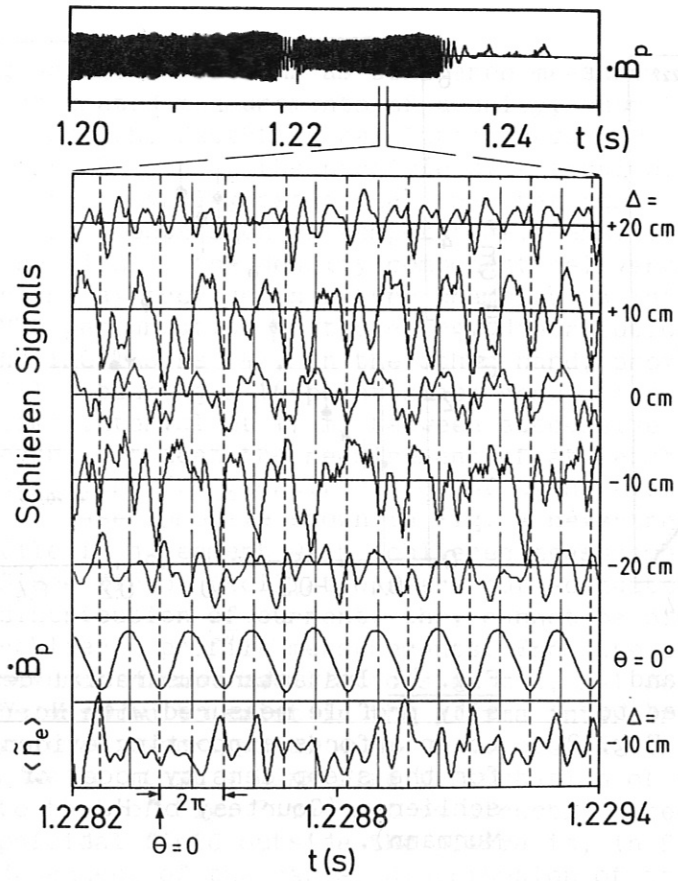

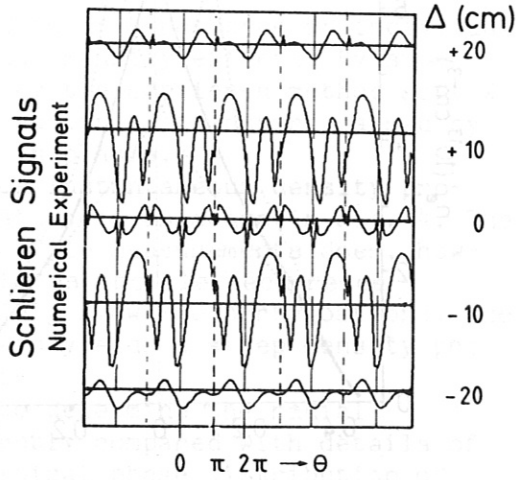

Fig. 2: Numerical simulation of cycles 1,5 and 6 of the actual schlieren signals of Fig. 1.

Fig. 1: Characteristic two-hump schlieren wave forms at $\Delta=\pm$ 10 cm, indicating an m=1-like density distribution structure in the plasma interior.

measurements of density shown by, respectively, the last but one and the last trace of Fig. 1. The fluctuation amplitude of the actual and simulated schlieren signals shown in Figs. 1 and 2 is 60 % of the unperturbed amplitude of the $\Delta = \pm$10 cm beams and 40 % of that of the other beams. Such amplitude fluctuation of the schlieren signals represents a macroscopic variation of the density distribution involving the whole column.

Density perturbation model

For quantitative evaluation of the schlieren signals all experimental facilities pertaining to the schlieren diagnostic were numerically simulated as in real space. Since the signals are directly dependent on the local gradient of density traversed by the schlieren beams, each beam is first used to determine the corresponding variations of the local gradient. A complete density distribution model for the whole plasma cross-section is then obtained from the individual gradients of density.

For each class of MHD perturbations a representative density model may then be adapted to simulate various details of the actual experiment on that class of perturbation. By this procedure, after modelling the density distribution of Fig. 3 by means of individual gradients, the actual schlieren wave forms of representative cycles 1,5 and 6 of Fig. 1 are numerically reproduced as shown in Fig. 2.

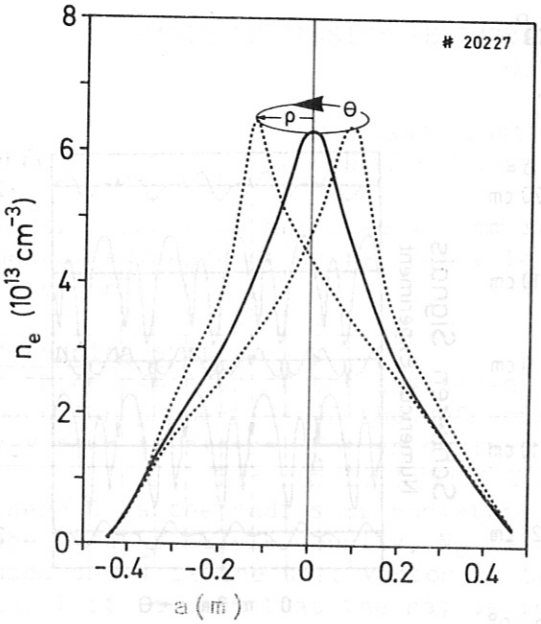

Fig. 3: Radial density profile and schlieren perturbation model used to obtain the simulated signals of Fig. 2.

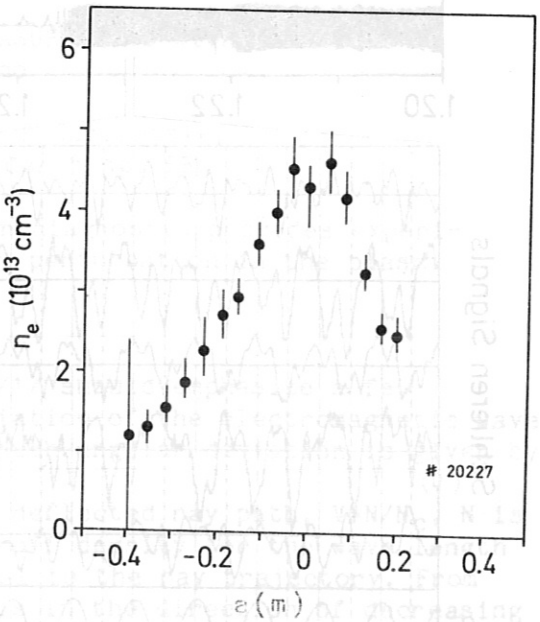

Fig. 4: Instantaneous radial density profile measured with Nd:YAG Laser affords supporting evidence for the steep density model of schlieren (Courtesy of H. Murmann).

Note in Figs. 1 and 2 that each negative hump indicates passage of a steep density gradient through the schlieren probing chords. Cycles 1, 5 and 6 of the actual signals in Fig. 1 and the simulated signals of Fig. 2 exhibit the two-hump wave forms on opposite schlieren channels. Opposite schlieren channels exhibit opposite phase relationships of their signals. The four passages on two opposite chords during a cycle are determined by a projected toroidal rotation of the density peak on the poloidal plane. The schlieren wave forms therefore establish at every instant the position of the density peak. The latter crosses the midplane of the machine, at $\theta=0$, between the last negative hump of the lower chord, $\Delta= -10$ cm, and the first one of the upper chord at $\Delta=+10$ cm. A peaked density profile as is derived from the schlieren analysis and as is observed from the Thomson scattering measurements (see Fig.4) is typical for the L-phase causing the sharp decrease of β. Such peaked profile may be due to an external resistive constraint of the particle density during the L-phase. As the peaked profile is also observed for T_e, the resistive constraint of the particle density and current reduces the safety factor value to $q=rB_T/RB_p<1$ in the plasma interior. This is conducive to the model of the helically perturbed centre core established by the schlieren measurements.

Simultaneous data from other diagnostics

Besides schlieren no other diagnostic can so far furnish reliable profile details on density during the instability. Line-integrated measurements of the particle density distribution with millimeter and submillimeter wave-interferometry cannot, in fact, distinguish such fine details of density

gradient variations as schlieren measurements do. Besides yielding line-integrated measurements of density, submillimeter laser beams do not yet afford the fast-time resolution required for identification of fast MHD perturbation of the particle distribution.
Soft X-ray diagnostics have not yet resolved their dependence on individual componenents such as temperature, density and impurity effects. By subtraction of the density component delivered by the schlieren method soft X-rays may provide in future unambiguous information on transport caused by MHD perturbation of the energy distribution in plasma.
Nd-YAG lasers /4/, on the other hand, provide instantaneous density profiles bearing a 16-point space resolution data set, as shown in Fig. 4. The time interval of 17 ms between successive profile measurements does, however, not meet the requirement of at least 10 µs profile recurrence necessary for identification of even relatively slow MHD perturbations. The YAG laser profile shown in Fig. 4 nevertheless yields a steep density profile in agreement with schlieren measurements.
Since Mirnov oscillations are not adequate to determine the radial distribution of current, they cannot be directly compared with details of schlieren profile measurements. From the poloidal phase distribution of several Mirnov oscillations an m=2, n=1 mode structure can therefore only be assumed to exist in the plasma interior without it being possible to give an experimental contour to such a structure. It should be noted, however, that a kink-like perturbation of the current centre core similar to that of Fig. 3 may not be directly detected by the Mirnov coils. The poloidal field outside the plasma is, in fact, up to a scale factor independent of the radial distribution of the current.
Supporting evidence for the schlieren perturbation model of Fig. 3 can, however, be derived by the m=2 Mirnov oscillations by assuming identical current and particle density distributions. In the presence of Shafranov pressure effect the poloidal field outside the plasma would then exhibit the m=2 variation /2/ inside and outside the location of the Mirnov coils. It should be noted that the density distributions of Figs. 3 and 4 are radial profiles perpendicular to the machine midplane. They therefore do not exhibit details of the Shafranov displacement towards the outer wall. Future work on this and on other varieties of MHD instabilities may also benefit from supplementary details of mutually supporting evidence yielded by different diagnostics, such as Mirnov, Thomson scattering, soft X-ray and schlieren.

Acknowledgement
The author is indebted to the ASDEX team for their experimental support and criticism of this work.

References
/1/ G. Lisitano, Rev. Sci. Instrum. 58, 249 (1987)
/2/ O. Klüber et al., Proc. 13th Europ. Conf. Contr. Fus. and Plasma Physics, Schliersee, Vol. I, 136 (1986)
/3/ J.L. Dunlop et al., Phys. Rev. Lett. 48, 538 (1982)
/4/ D. Meisel, et al., Proc. 13th Europ. Conf. Contr. Fus. and Plasma Physics, Schliersee, Vol. I, 97 (1986)

Parametric Behavior of the Density Profile in the Scrape-off Layer of ASDEX for Neutral-Beam-Heated Plasmas in the L-Regime

K. McCormick, Z.A. Pietrzyk[4], H. Murmann and G. Becker, H.S. Bosch, H. Brocken, A. Carlson, A. Eberhagen, G. Dodel[1], H.-U. Fahrbach, G. Fussmann, O. Gehre, J. Gernhardt, G. v.Gierke, E. Glock, O. Gruber, G. Haas, W. Herrmann, J. Hofmann, A. Izvozchikov[2], E. Holzhauer[1], K. Hübner[3], G. Janeschitz, F. Karger, M. Kaufmann, O. Klüber, M. Kornherr, K. Lackner, M. Lenoci, G. Lisitano, F. Mast, H.M. Mayer, K. McCormick, D. Meisel, V. Mertens, E.R. Müller, J. Neuhauser, H. Niedermeyer, W. Poschenrieder, H. Rapp, A. Rudy, F. Schneider, C. Setzensack, G. Siller, E. Speth, F. Söldner, K. Steinmetz, K.-H. Steuer, N. Tsois[5], S. Ugniewski[6], O. Vollmer, F. Wagner, D. Zasche

Max-Planck-Institut für Plasmaphysik,
EURATOM Association, Garching, FRG

Abstract: Characterizing the scrape-off layer (SOL) density profile by the density at the separatrix n_s and the e-folding length λ_n, the SOL is described for a wide variety of conditions: $\bar{n}_e$=1-5x10^{13} cm^{-3}, I_p=250-440 kA, B_t~22 kG, q_a=2.4-4.3 for injected powers P_{NI}~0.4-1.7 MW, which lead to L-type discharges. Generally, λ_n increases with P_{NI}, these changes becoming more dramatic for lower I_p and $\bar{n}_e$. For OH and NI plasmas n_s is roughly proportional to $\bar{n}_e$; the constant of proportionality increases with NI and is independent of P_{NI} over the range investigated.

Introduction: This paper is designed to furnish an initial data base for the critical evaluation of SOL models, as well as to investigate the premise that the SOL behavior during NI reflects global plasma transport properties as has been observed elsewhere /1, 2/. Statements are limited to the SOL n_e profile in the outer midplane of doubly-null diverted discharges sustained by gas puffing. The ASDEX neutral lithium-beam probe /3, 4/ is used to determine λ_n and the relative changes in n_s; previous experience gained with the edge Thomson scattering system /5/ furnishes an approximate absolute calibration of n_s.

---

[1] University of Stuttgart; [2] Ioffe Institute; [3] University of Heidelberg; [4] University of Washington, Seattle, USA; [5] N.R.C.N.S. "Democritos", Athens, Greece; [6] Inst. for Nuclear Research, Swierk, Poland;

To place matters in context, fig. 1a illustrates the effect of high power (2.75 MW) $H^0 \rightarrow D^+$ injection on $\bar{n}_e$, $\beta_{p\perp}$ (taken from the diamagnetic loop) and D_α as well as the Li-beam light signal outside the separatrix. $\bar{n}_e$ decreases going into the L-phase, followed by the H-phase increase and subsequent clamping correlated with the D_α bursts. The characteristic D_α signatures are closely paralled by Li [2p-2s] (~ proportional to n_e) /3/. The SOL n_e profiles for OH, L and H (fig. 1b) indicate that $n_s^L < n_s^{OH} < n_s^H$. Further, $\lambda_n^{OH} \sim 1.95$ cm, $\lambda_n^L \sim 2.8$ cm and $\lambda_n^H \sim 1.1$ cm. $T_{es} \sim 70$, 130 and 250 eV for the OH, L and H-regimes respectively /5/. $R-R_s$ is the distance from separatrix; R_s is derived from magnetic signals and underlies an uncertainty of perhaps 1 cm. This has an important bearing on scaling statements made about n_s; thus if R_s were in fact one cm further outwards, then $n_s^{OH} > n_s^L \sim n_s^H$ would be deduced.

Results: Fig. 2b depicts for $H^0 \rightarrow He^{2+}$ injection, λ_n vs. the total absorbed input power $P_{TOT} = P_{OH} + P_{NI}^{abs}$ for $\bar{n}_e = 1\text{-}4.9 \times 10^{13}$ cm^{-3} and $I_p = 420$ kA; the energy confinement time "τ_E" deduced from the steady-state NI phase using β_p to determine the total energy W and "τ_E"$= W/P_{TOT}$ (without correction for radiation effects) is plotted vs. $P_{TOT}/\bar{n}_e$ in fig. 2a.

Fig. 2b demonstrates that during OH (corresponding to the points at the left as in fig. 2a) λ_n is about constant for $\bar{n}_e > 1.9 \times 10^{13}$ cm^{-3}, and is much larger for lower $\bar{n}_e$, as has been previously reported /6/. Auxiliary heating leads to an increase in λ_n, the changes becoming more apparent for lower $\bar{n}_e$ and higher P_{TOT}, τ_E decreases with $P_{TOT}/\bar{n}_e$. Thus, at $\bar{n}_e = 4 \times 10^{13}$ cm^{-3} (1.9×10^{13} cm^{-3}), over the power range λ_n increases by ~10% (22%) and τ_E goes from ~100 to 50 ms (63→45 ms). n_s exhibits the interesting behavior that it is described by an offset-linear law of the form $n_s = a\bar{n}_e + b$, the constants depending only on the type of heating (OH or NI). No parametrical dependence of n_s on P_{NI} is evident; however, for higher P_{NI} a relationship must exist, as documented in fig. 1b where n_s is reduced rather than increased in the L-phase for $P_{NI} = 2.85$ MW.

The $H^0 \rightarrow D^+$ series of fig. 3 involve a q_a-($I_p = 270\text{-}420$ kA) and $\bar{n}_e$-scan (2.2, 3.5×10^{13} cm^{-3}). For any given q_a the NI-induced changes in λ_n (see fig. 3b) have the same qualitative behavior as for He: lower $\bar{n}_e$ and higher P_{NI} are both conducive to large alterations in λ_n. The slope of the λ_n vs. q_a curves is about the same for all conditions. With respect to τ_E, for in

jection with 4 sources τ_E is the same for $\bar{n}_e$=2.2 or 3.5x10^{13} cm^{-3}, whereas λ_n increases by 25% ($\bar{n}_e$ = 2.2→3.5x10^{13} cm^{-3}), demonstrating that λ_n does not necessarily mirror changes only in τ_E.

In fig. 3c there is no convincing dependence of n_s on q_a; also, the largest absolute δn_s is small, of the order ~0.15x10^{13} cm^{-3}. Nevertheless, a plot of n_s vs. $\bar{n}_e$ (not shown here) also reveals an offset-linear relationship, switching from one slope to another as with He, depending on the type of heating used.

Fig. 4 shows the results of another $H^0 \rightarrow D^+$ power scan with either $\bar{n}_e$ (fig. 4b,c) or I_p (fig. 4d, e) being held constant. The familiar variation of λ_n with P_{NI} and $\bar{n}_e$ is again found, but the changes are more extreme. For example, at $\bar{n}_e$~3x10^{13} cm^{-3} and q_a=4.3 (fig. 4d), λ_n varies from 2.8 to 4.3 cm for P_{TOT}~0.25 → 1.2 MW. In addition, the λ_n^{OH} values are larger than those normally observed on ASDEX by ~0.5 cm. n_s^{NI} clearly increases more strongly with $\bar{n}_e$ for q_a=4.3 than for n_s^{NI}(He) at q_a=2.4 of fig. 2c; on the other hand, the n_s^{OH} values are nearly identical.

Discussion and Summary: It is a common feature of NI-heated plasmas in the L-regime that λ_n increases with P_{NI}, the increase being less pronounced for higher $\bar{n}_e$, and possibly higher I_p. In any case for both OH and NI, λ_n is augmented with q_a: The OH λ_n-q_a scaling of fig. 3b agrees well with previous results /6/, whereas λ_n^{OH} of fig. 4b and 4d is anomalously large for a D^+ plasma. This may be indicative of a deviant wall-conditioning of the divertor. Also, "τ_E" for the series of fig. 4 is noticibly lower. Hence, this series should be regarded in a more qualitative manner.

Whereas it is true that a degradation in τ_E is accompanied by larger λ_n, the reverse conclusion that larger λ_n are synonymous with lower τ_E cannot be universely drawn. It appears that the NI-induced degradation in the cross-field diffusion coefficient D also extends into the SOL, but that this is only one component in determining λ_n. With respect to τ_E, plotting vs $P_{TOT}/\bar{n}_e$ leads to a surprisingly orderly unification of the OH and NI values, at least for this limited data set. Further, the τ_E scalings for He^{++} of fig. 2a and D^+ of fig. 3a are virtually identical, and of the form $\tau_E \sim \alpha(P_{TOT}/\bar{n}_e)^{-\beta}$ msec (α = 31-32.3, β=0.48, 0.51).

For n_s vs. $\bar{n}_e$, a very clear feature which emerges is that the OH offset-linear scaling switches promptly to a steeper gradient upon initiation of NI, but beyond that shows no dependence on the magnitude of P_{NI}. Higher I_p

might bring the OH and NI scalings closer together (compare fig. 2c and 4e): the data base is too small to allow definitive conclusions. As a comment, one of the quantities which should determine n_s for high recycling is the specific heat flux $q_{\parallel}$ into the divertor /7/, which is related to P_{TOT}, λ_n and λ_{Te}. λ_{Te} decreases ~10% /5/ over the P_{NI} range studied here, in contrast to the moderate (at low q_a and high $\bar{n}_e$) 10-20% enhancement in λ_n; therefore $q_{\parallel}$ should increase almost proportionately to P_{TOT}.

No Thomson data was available to calibrate the relative Li-beam determinations of n_s; to obtain n_s absolutely, experience from cross-calibrations of other series were used. Hence, strictly speaking, all absolute n_s values are provisional including the n_s vs. $\bar{n}_e$ scalings. Definitive conclusions can be drawn only with respect to the relative behavior of the switch in scaling between OH and NI discharges. λ_n is generally measured to an accuracy of $\pm$0.1 cm .

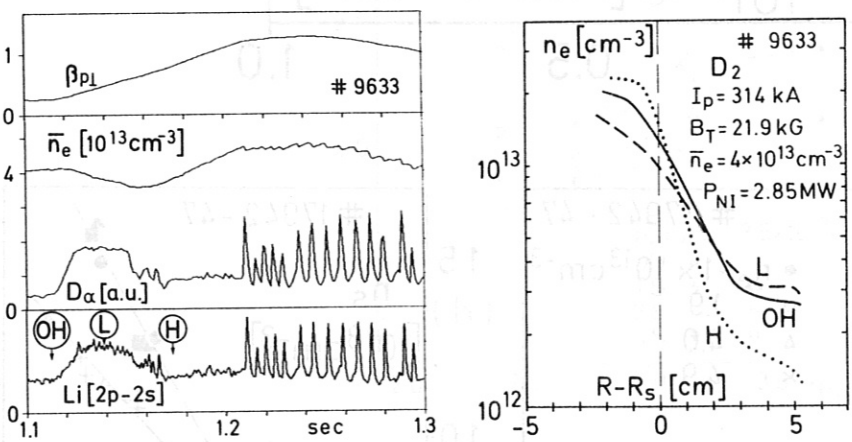

Fig.1 (a) Time behavior of $\beta_{p\perp}$, $\bar{n}_e$, D_α radiation in the divertor and the Li [2p-2s] light intensity several cm outside the separatrix, (b) n_e profiles for the OH, L and H-phases.

References

/1/ F. Wagner, Nucl. Fusion 25 (1985) 525.

/2/ F. Wagner, O. Gruber, et al. 12th EPS (Budapest 1985) 335.

/3/ K. McCormick, H. Murmann and El Shaer, J. Nucl. Mater. 121 (1984) 48.

/4/ K. McCormick, Rev. Sci. Instr. 56 (1985) 1063.

/5/ H. Murmann and M. Huang, Plasma Phys. 27 (1985) 103.

/6/ K. McCormick, Z.A. Pietrzyk, et al., J. Nucl. Mater. 145-147 (1987) 215.

/7/ J. Neuhauser and R. Wunderlich, in ref. /6/ (1987) 877.

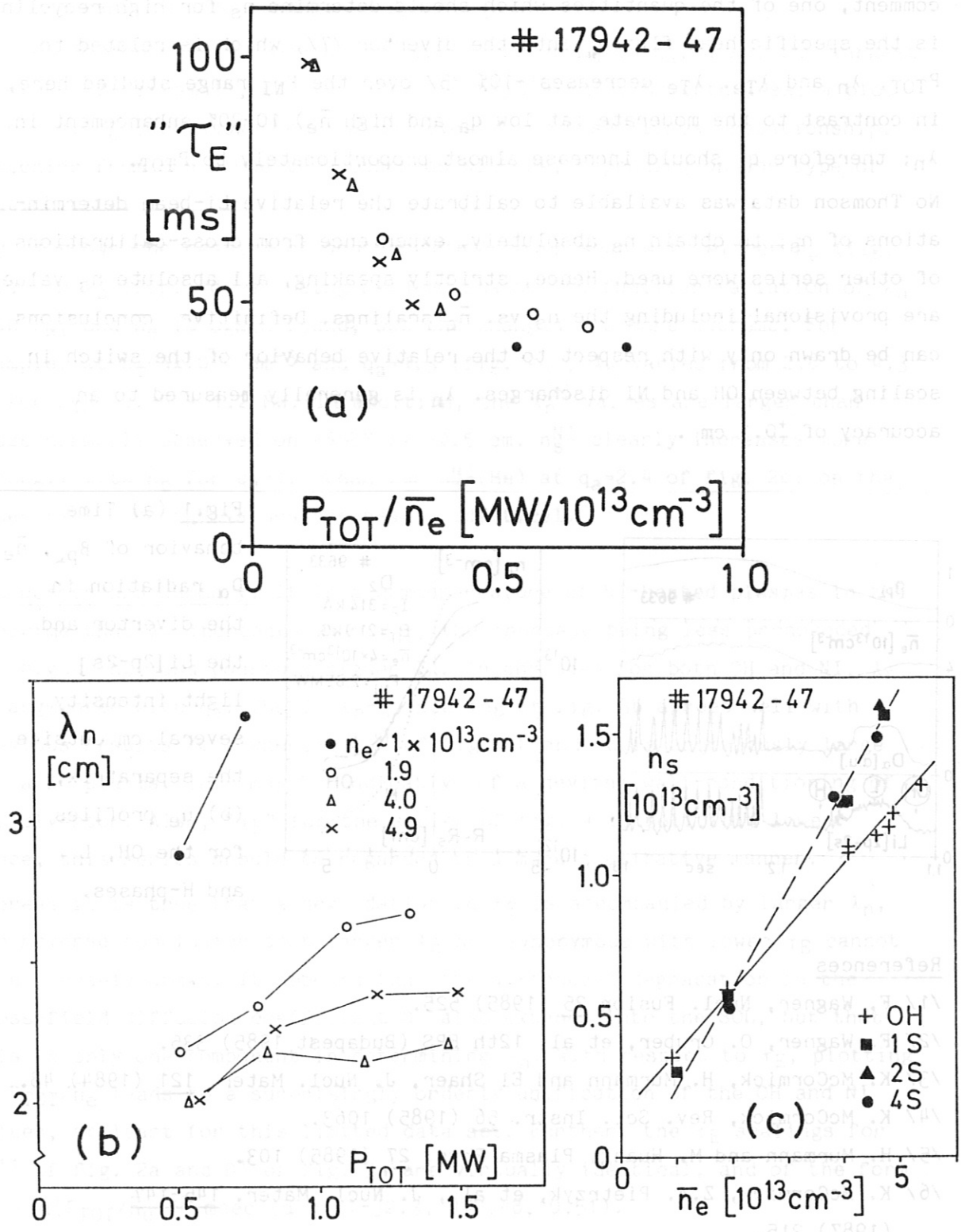

Fig.2 $H^0 \rightarrow He^{2+}$ with P_{NI}=0.41, 0.88, 1.24 MW (1, 2 and 3 NI sources), I_p=420 kA, B_t=21.7 kG: (a) energy confinement time "τ_E" vs. $P_{TOT}/\bar{n}_e$, (b) density e-folding length λ_n in the SOL vs. P_{TOT} with $\bar{n}_e$ as a parameter. (c) Separatrix density n_s vs. $\bar{n}_e$ during OH and NI.

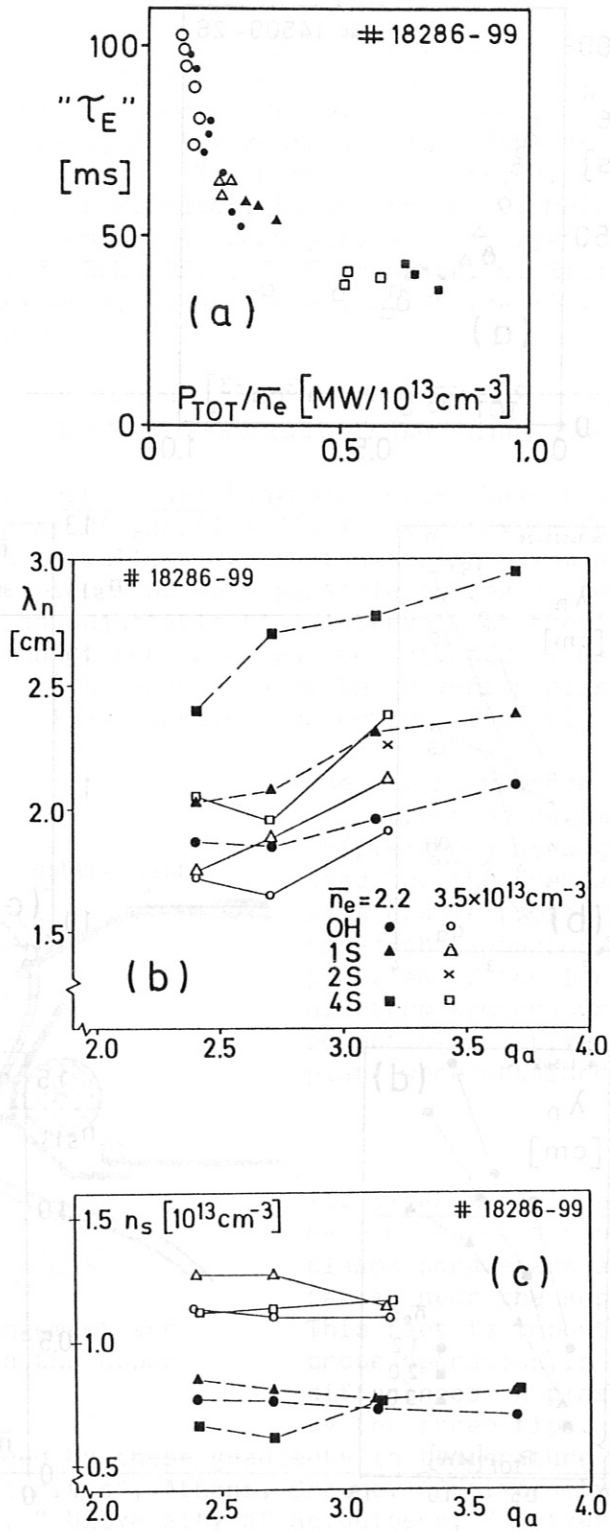

Fig.3 $H^0 \rightarrow D^+$ with P_{NI}=0.41, 0.83, 1.67 MW (1, 2 and 4 sources), $\bar{n}_e$=2.2, 3.5x10^{13} cm^{-3}, B_t=21.8 kG: (a) "τ_E" vs. $P_{TOT}/\bar{n}_e$, (b) λ_n vs. q_a (I_p=270, 320, 370, 420 kA) with $\bar{n}_e$ as a parameter, (c) n_s vs. q_a, symbols as in (b).

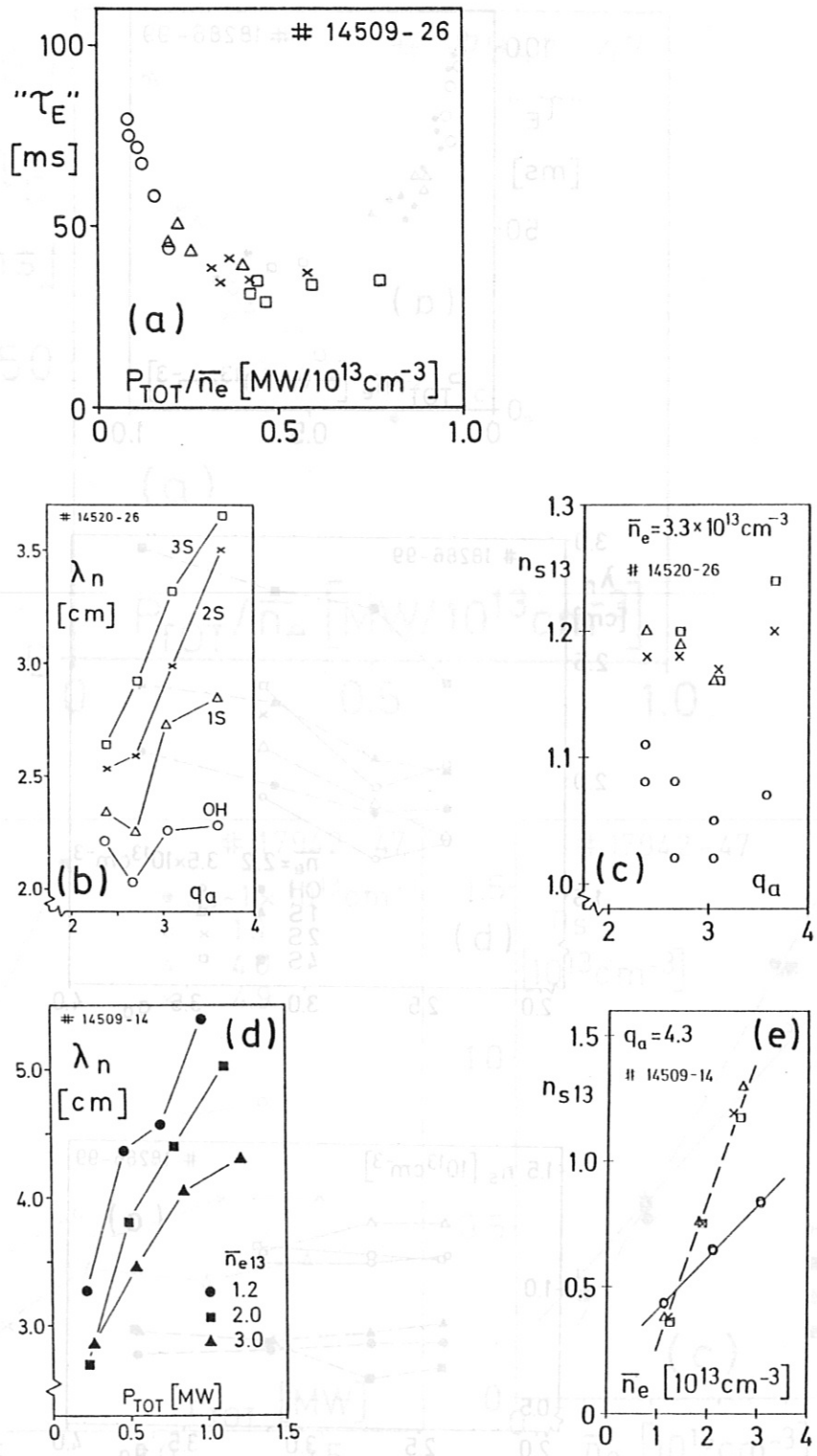

Fig.4 $H^0 \rightarrow D^+$ with P_{NI}=0.42, 0.87, 1.3 MW (1, 2 and 3 sources), B_t=22 kG: (a) "τ_E" vs. $P_{TOT}/\bar{n}_e$, (b) λ_n vs. q_a (I_p=290, 340, 390, 440kA) with P_{NI} as a parameter, $\bar{n}_e$~3.3x10^{13}cm^{-3}, (c) n_s vs. q_a for shots of (b); (d) λ_n vs. P_{TOT} with $\bar{n}_e$ as a parameter, q_a=4.3 (250 kA), (e) corresponding n_s vs. $\bar{n}_e$ plot.

LANGMUIR PROBE MEASUREMENTS IN THE ASDEX DIVERTOR PLASMA

N. Tsois[1], G. Haas, M. Lenoci, J. Neuhauser, and G. Becker, H.S. Bosch, H. Brocken, A. Carlson, A. Eberhagen, G. Dodel[2], H.-U. Fahrbach, G. Fussmann, O. Gehre, J. Gernhardt, G. v. Gierke, E. Glock, O. Gruber, W. Herrmann, J. Hofmann, A. Izvozchikov[3], E. Holzhauer[2], K. Hübner[4], G. Janeschitz, F. Karger, M. Kaufmann, O. Klüber, M. Kornherr, K. Lackner, G. Lisitano, F. Mast, H.M. Mayer, K. McCormick, D. Meisel, V. Mertens, E.R. Müller, H. Murmann, H. Niedermeyer, A. Pietrzyk[5], W. Poschenrieder, H. Rapp, A. Rudyj, F. Schneider, C. Setzensack, G. Siller, E. Speth, F. Söldner, K. Steinmetz, K.-H. Steuer, S. Ugniewski[6], O. Vollmer, F. Wagner, D. Zasche

Max-Planck-Institut für Plasmaphysik,
EURATOM Association, Garching, FRG

I. Introduction and apparatus: Langmuir probes have been used routinely in ASDEX divertor plasma diagnostics /1,2/. Recently, a fast movable probe carrier system was installed. Two fast sweeping movements with a speed of 1 m/s and 10 cm displacement were possible during a shot. The probe can also be kept, for an adjustable time interval, at the innermost position. The initial position of the probe can be adjusted by using the manipulator and a tilt mechanism. A large area of the divertor plasma can thus be scanned in the radial and vertical directions (see fig. 1).

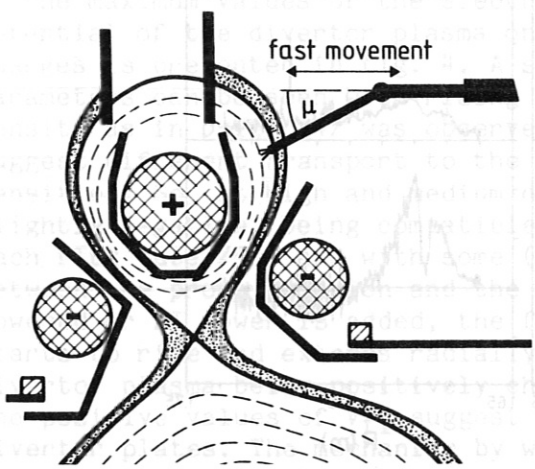

Fig.1: Probe arrangement and accessible area in the upper divertor.

The divertor probe system was used in all operation regimes of ASDEX. The triple-probe arrangement /3/ was mainly used but the probes were also operated as a double probe, especially for cross-check purposes. Up to four radial profiles of the ion saturation current, electron temperature and floating potential relative to the divertor plate were obtained during a shot.

II. Experimental results: Radial scans have revealed strong gradients of the plasma parameters across the flux surfaces, near the separatrix location. This fact is important since triple-probe operation is very sensitive to differences in plasma parameters seen by the three tips. In order to minimize the error introduced by these gradients in temperature and density evalu-

[1] N.R.C.N.S. "Democritos", Athens, Greece; [2] University of Stuttgart; [3] Ioffe Institute; [4] University of Heidelberg; [5] University of Washington, Seattle, USA; [6] Inst. for Nuclear Research, Swierk, Poland

ation, an optimum inclination of the probe arm was chosen so that the tips were as close as possible to the same flux surface. The data reported here were obtained with this optimum inclination ($\mu \approx 15^{o}$).

Ohmically heated discharges: Typical radial profiles of plasma parameters for two values of the main plasma densities are shown in fig. 2. The medium density profiles display the well-known characteristics of the ASDEX divertor plasma /1,2/: large maxima close to the separatrix, broad shoulders a few centimetres away in the ion saturation current and density profiles, and relatively flat temperature profile. The absolute values of the electron temperature and density are in good agreement with the double-probe cross-check measurements. The floating potential profiles are flat, with values slightly negative. At densities $\bar{n}_e \leq 5 \times 10^{13}$ cm^{-3}, a sharp negative "dip" develops close to the calculated position of the separatrix which cannot be attributed to a local temperature rise.

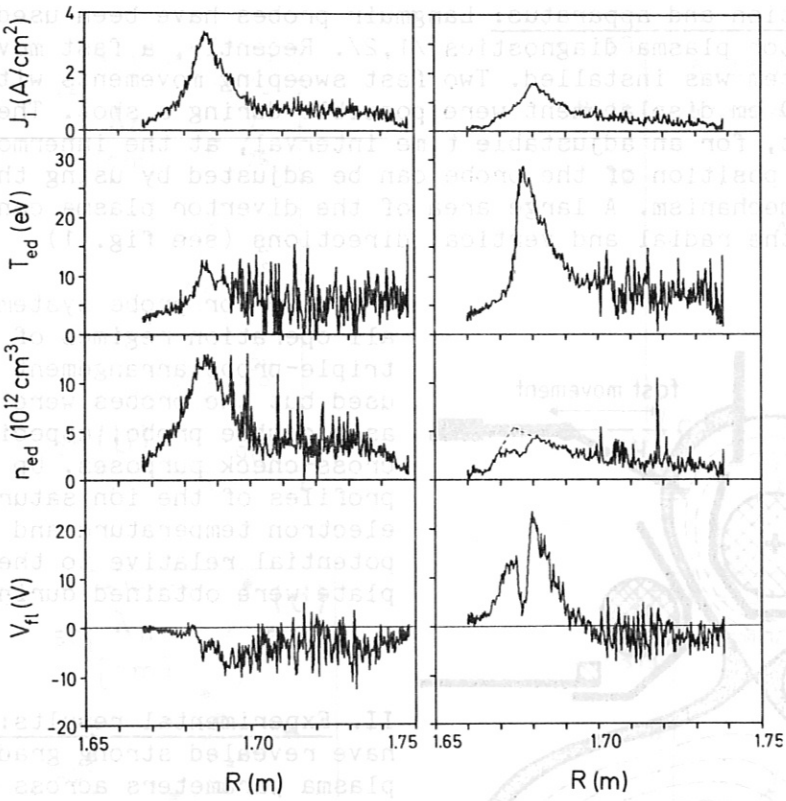

Fig.2: Profiles of ion saturation current, electron temperature, density and floating potential vs. major radius R for $\bar{n}_e = 4.3 \times 10^{13}$ cm^{-3} (left) and $\bar{n}_e = 1.4 \times 10^{13}$ cm^{-3} (right).

As the density is lowered, the floating potential becomes positive together with an increase of temperature around the separatrix, in a region which is more and more extended. Also the narrow "dip" is now well developed. Floating-potential gradients as high as ~100 V/cm can be observed in some low density shots. Even at the optimum inclination of the probe arm, floating

potential differences of 5 to 8 V between tips were measured in a narrow zone around the separatrix. These high gradients together with a presumably non-Maxwellian electron velocity distribution clearly affect the derivation of the electron temperature and density profiles (see fig. 2).

Additionally heated discharge: During the additional-heating phases of the discharges (NI, LH, ICRH) the divertor plasma also displays specific features. Besides the enhanced power flow (increased ion saturation current and electron temperature), some changes were also observed in the floating-potential and density profiles. In fig. 3 a few examples of floating-potential profiles are presented. In the L phase of a NI-heated discharge, the floating-potential profiles show positive charging of the plasma around the separatrix, similar to that in OH discharges of lower densities. The negative "dip" is also more pronounced.
In the H phase, the burst activity makes the interpretation of floating-potential data very difficult. The ion saturation current and electron temperature between bursts are comparable with the values for ohmic phases. The peak values of bursts are much larger and extend over the whole profile, including the shoulder.
The RF heating produces different effects on the density and floating-potential profiles, mainly depending on the plasma density and the injected power. At medium densities (~4×10^{13} cm^{-3}) and high powers (~2 MW), all the divertor plasma is positively charged, as can be seen in fig. 3.

III. Discussion: As seen above, all profiles show a pronounced structure depending on the density, heating power and heating method. The dependence of the maximum values of the electron temperature, density and floating-potential of the divertor plasma on the main plasma density for ohmic discharges is presented in fig. 4. A smooth evolution in all three measured parameters can be seen with rising density. No step-like change of V_{fl} with density as in D-III /4/ was observed. The floating-potential profiles suggest different transport to the divertor plates for different plasma densities. So, at high and medium densities, the floating potential stays slightly negative, being compatible with locally ambipolar transport on each flux tube /5/, and with some (few eV) drop in the electron temperature between the probe position and the divertor plate. As the density is lowered or NI power is added, the floating potential around the separatrix starts to rise and extends radially, the whole cross-section of the divertor plasma being positively charged at densities below 1×10^{13} cm^{-3}. The positive values of V_{fl} suggest locally non-ambipolar transport to the divertor plates. The mechanism by which the divertor plasma is charged is not yet clear. Non-Maxwellian electrons close to the separatrix (see below) together with vertically asymmetric plasma position and divertor recycling etc. could be candidates for explanation. Further experiments are needed to clarify these aspects.
The negative "dip" displayed very close to the calculated position of the separatrix, although expected, was surprising in some respects. Firstly, it implies strong gradients in floating potential which perturbs any multiple-tip probe measurements. Then, it is very narrow so that we believe that it can be used for separatrix position determination (as done in Fig. 3) with a better accuracy than magnetic measurements.

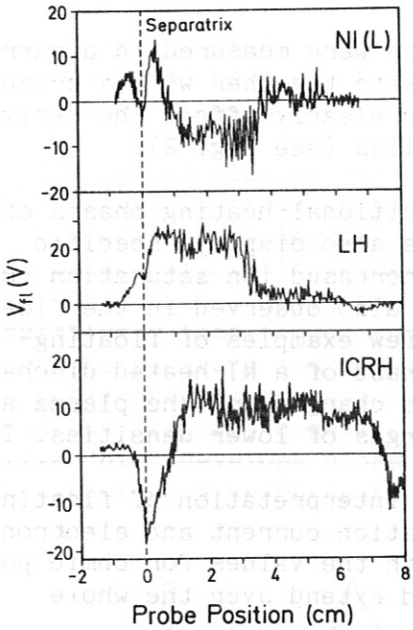

Fig.3: Floating potential profiles for different heating methods.

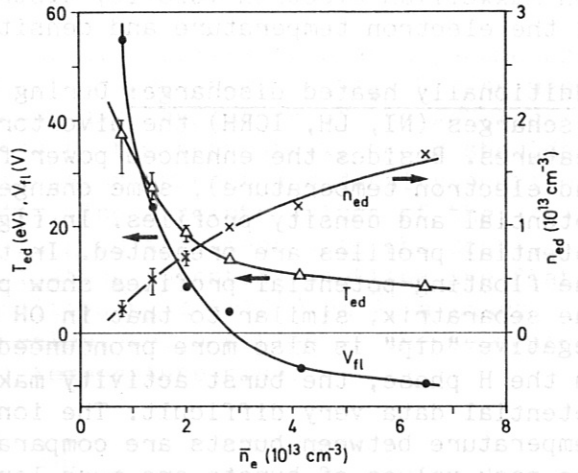

Fig.4: Peak values of electron temperature, density and floating potential vs. main plasma density $\bar{n}_e$.

Some estimation of the current density and energy of electrons responsible for the "dip" can be made by combining the available data. Values of 0.2 - 0.5 A/cm^2 and $E_e \geq 100$ eV were obtained in low-density discharges. At higher densities, these numbers are significantly lower and only upper limits can be estimated. The values obtained at low densities are in good agreement with those expected from a diffusive loss of fast electrons across the separatrix which can reach the divertor /6/. It is therefore concluded that the negative "dip" in floating-potential profiles as well as some distortion in ion saturation current profiles at very low densities are due to fast electrons which flow almost collisionless from the main chamber to the divertor very close to the separatrix.
The amounts of energy carried by these electrons can be locally important. Some comparisons with thermographic data have shown that the correction implied by these fast electrons has the right direction.

References

/1/ Y. Shimomura, M. Keilhacker, K. Lackner and H. Murmann, Nucl. Fus. 23, 869 (1983).
/2/ G. Fussmann et al., J. Nucl. Mater. 128/129, 350, (1984).
/3/ S.L. Chen, T. Sekiguchi, J. Appl. Phys. 36, 2363, (1965).
/4/ M. Shimada et al., in Plasma Phys. and Contr. Nucl. Fus. Res. 1984 (Proc. 10th Int. Conf. London, 1984), Vol. 1, IAEA, Vienna (1985) 281.
/5/ P.C. Stangeby, G.M. McCracken, S.K. Erents, J.E. Vince and R. Wilden, J. Vac. Sci. Technol. A1, (2), 1302 (1983).
/6/ U. Ditte, T. Grave, Probe and Thermographic Measurements in ASDEX Divertor, IPP Report, III/102 (1985).

NUCLEAR EMULSION NEUTRON DIAGNOSTICS AT ASDEX

K. Hübner, R. Bätzner, H. Hinsch, J. Hubele, B. Wolle
Institut für Angewandte Physik, Universität Heidelberg
D-6900 Heidelberg

B. Bomba, H. Rapp, H. Wurz, ASDEX Team, NI Team
Max-Planck-Institut für Plasmaphysik
EURATOM Association, D-8046 Garching

We are using nuclear emulsions at ASDEX to investigate neutron energy spectra and emission profiles and to determine the absolute neutron yield of a discharge. The emulsions are exposed in collimators which define the observed plasma region and shield them against neutrons emitted and scattered in the rest of the experiment. Two collimators view radially and two others tangentially to the plasma axis, one in the direction of injection (co-collimator), the other in the counter-direction (counter-collimator). An unshielded emulsion was used for the emission profile measurement. One of the radial collimators observes the plasma through the wall of the vessel; all others are positioned in front of the quartz window at the large port.

Neutron diagnostics with nuclear emulsions

In emulsions neutrons are detected by their recoil protons. Measurement of the track length (proton energy) and scattering angle delivers the neutron energy. The energy

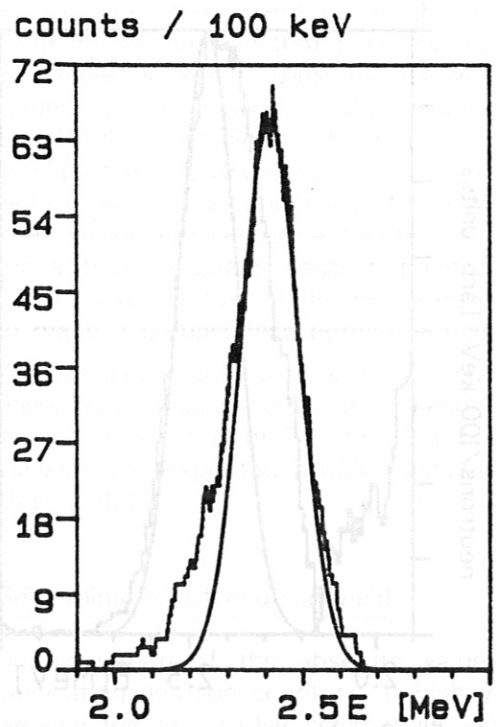

Fig.1: Neutron energy spectrum measured with co-collimator

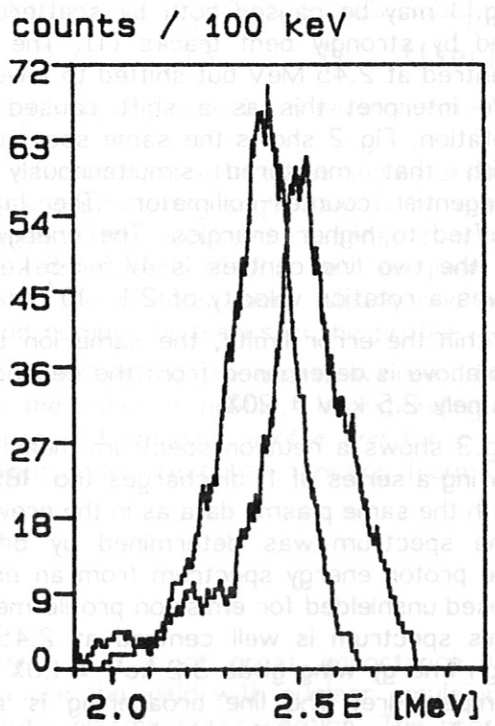

Fig.2: Neutron energy spectra measured with both collimators

resolution is determined by range straggling of the proton tracks and the statistical errors in the measurement of the length and angle. The tracks are bent and therefore good resolution requires measurement of the tangent at the beginning of the track and restriction to small scattering angles. For large track numbers this can be avoided because the neutron energy spectrum could also be obtained by differentiating the proton energy spectrum. Furthermore for flux measurements energy resolution is not essential and it is sufficient to determine the scattering angle from the start and end point of the track. Examples of spectra measured in this way are used and discussed in [1].

Neutron spectra during H-injection

We studied neutron emission from many ASDEX H-type discharges with plasma currents of 380 kA and injection powers of 3.6 MW. Fig. 1 gives the neutron energy spectrum measured with the tangential co-collimator. It is integrated over five disruption-free discharges (no. 16744-16748). The FWHM of the line determined from a fit to a Gaussian is 180 ± 10 keV. Defolding the broadening caused by counting the neutrons in 100 keV intervals reduces the FWHM to 165 ± 11 keV.

Our energy resolution was determined from measurements at the Gothenburg accelerator. It depends on the maximum scattering angle of the tracks used. Here we have choosen $\Theta_{max} = 10^{\circ}$, which gives an energy resolution of 86 ± 8 keV.

We thus get a temperature broadening of 141 keV ± 10%, corresponding to an ion temperature of 2.9 keV ± 20%. The electron temperature determined from ECE measurements is 2.4 keV.

The hump at the low-energy wing of the line in Fig. 1 may be caused both by scattered neutrons and by strongly bent tracks [1]. The line is not centred at 2.45 MeV but shifted to lower energies. We interpret this as a shift caused by plasma rotation. Fig. 2 shows the same spectrum together with that measured simultaneously with the tangential counter-collimator. The later one is shifted to higher energies. The energy difference of the two line centres is 47.5 ± 5 keV, and this gives a rotation velocity of $2.1 \cdot 10^7$ cm/s ± 10%.

Within the error limits, the same ion temperature as above is determined from the second spectrum, namely 2.5 keV ± 20%.

Fig.3 shows a neutron spectrum measured radially during a series of 11 discharges (no. 18949-18959) with the same plasma data as in the previous series. The spectrum was determined by differentiating the proton energy spectrum from an emulsion exposed unshielded for emission profile measurement. This spectrum is well centred at 2.45 MeV. The high-energy wing gives 3.2 keV ± 20% for the ion temperature. The line broadening is asymmetric, being stronger in the low-energy part. This may be caused by two effects. First, the bent shape of the tracks causes a systematic reduction of

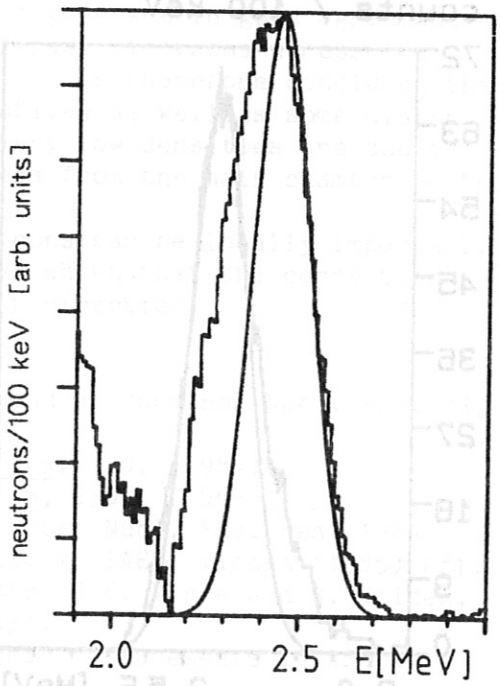

Fig. 3: Neutron energy spectrum from uncollimated exposure near quartz window

the measured track length. This effect is much stronger here than in the spectra in Fig. 1 and Fig. 2 because here we are also using tracks with large scattering angles. Second, due to our work on neutron scattering in the ASDEX device [1] we have to expect in the low-energy wing a strong contribution of neutrons scattered in the quartz window.

n_D/n_H ratio from neutron rate

Having measured the ion temperature, we can determine the mean ion density and thus, in the case of H-injection, the mean value of the ratio n_D/n_H from the measurements of the neutron rate. Using our interpretation code for the neutron rate [2], we calculated for 4 discharges of the series considered the n_D/n_H ratios which are given in Fig. 4 as a function of time. The shaded region indicates the injection pulse. The bars give the errors due to our temperature determination.

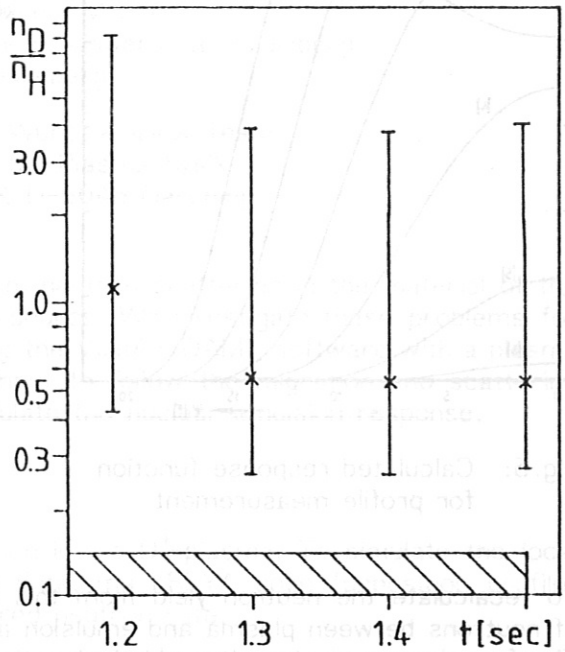

Fig. 4: n_D/n_H ratio from neutron rate

Neutron emission profile

The direction of the longest proton tracks, i.e. of the protons with maximum energy, is precisely the direction of the incident neutrons because in that case the scattering angle is zero. Thus by following the longest tracks back into the plasma, it is in principle possible to obtain the emission profile of the neutron source. In reality the number of protons scattered at angles around zero is very small and so certain ranges of energy and scattering angle have to be used. They define the response function of the measurement. The calculated response function for a thermonuclear neutron point source with a temperature of 2.5 keV is given in Fig. 5 as a function of the indicated energy range for the protons used. Clearly one has to make a compromise between angle resolution and number of tracks in the profile.

We scanned 8,000 tracks in an emulsion exposed unshielded at the quartz window. This track number allowed an angle resolution of 5^o for the emission profile, corresponding to a radial resolution of 9.6 cm. Fig. 6 shows the measured emission profile and for comparision the expected profile calculated with the appropriate response function from the plasma data.

Determination of neutron yield

Determination of the absolute value of the neutron yield is of great importance for calibrating neutron counters at high yields. To measure the yield with nuclear emulsions, we use the two radial collimators, observing the total plasma cross-section. The proton track density delivers the neutron flux at the position of the emulsion during its exposure.

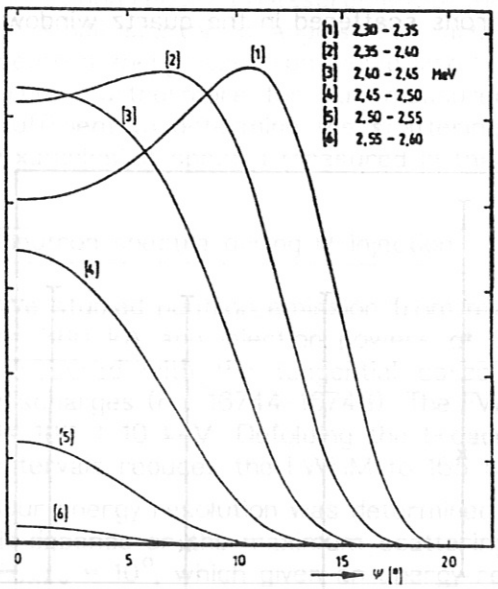

Fig. 5: Calculated response function for profile measurement

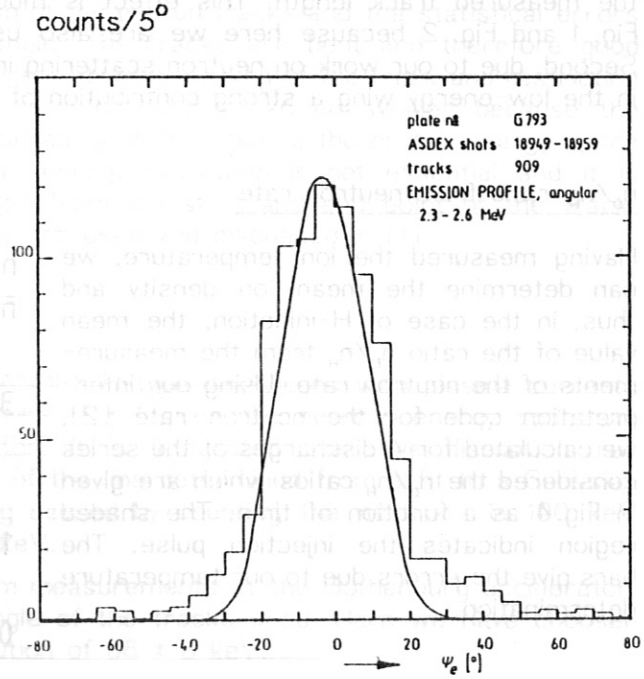

Fig. 6: Measured and calculated emission profile

To recalculate the neutron yield from this value, one has to account for the absorption of neutrons between plasma and emulsion and for the background of scattered neutrons. The former may be done by analytical estimation but for the latter one needs a detailed calculation of the neutron scattering in the experiment. From our calculations with the VINIA-3DAMC software we determine the neutron flux arriving at the emulsion per emitted neutron in the ASDEX plasma [1]. From the VINIA calculation and the neutron flux measured with the emulsion we get the following results. They agree well with the values measured with a U-counter calibrated by a neutron source and successive plasma discharges.

ASDEX discharge	no. 16910, coll. 1	no. 19111, coll. 2	
VINIA calculation	$0.250 \cdot 10^{-7}$ ± 3.7%	$0.891 \cdot 10^{-7}$ ± 8%	cm^{-2}
measured flux	$3.41 \cdot 10^{5}$ ± 13%	$2.55 \cdot 10^{6}$ ± 13%	neutrons/cm^2
resulting yield	$1.36 \cdot 10^{13}$ ± 14%	$2.86 \cdot 10^{13}$ ± 17%	neutrons
measured yield	$1.3 \cdot 10^{13}$ ± 15%	$3.2 \cdot 10^{13}$ ± 15%	neutrons

References

[1] B.V.Robouch, et al, this conference
[2] K.Hübner, et al, 12th Europ. Conf. on Controlled Fusion and Plasma Physics, Budapest 1985, part 1, p. 231-23

VINIA AND NEPMC CODE NUMERICAL EVALUATION OF NEUTRON SCATTERING FOR NEUTRON DIAGNOSTICS ON ASDEX

B. V. Robouch
Associazione EURATOM-ENEA sulla Fusione
Centro Ricerche Energie Frascati, I-00044 Frascati

K. Hübner, R. Bätzner, M. Roos
Institut für Angewandte Physik II, Universität Heidelberg
D-6900 Heidelberg

L. Ingrosso, H. Rapp, H. Wurz, ASDEX Team
Max-Planck-Institut für Plasmaphysik
EURATOM Association, D-8046 Garching

Neutron diagnostics near a tokamak suffer from neutron scattering in the material of the facility and the large extension of the neutron source. We investigate these problems for nuclear emulsion measurements at ASDEX using the VINIA-3DAMC software with a plasma neutron source and the ASDEX structure as input to follow the migration and scattering of neutrons, and the NEPMC software to calculate the nuclear emulsion response.

Input data

We consider ASDEX discharges with D^0-injection into a D^+-plasma. To simulate the local neutron production, we use measured plasma data, the FREYA code (deposition profile) and our interpretation code [1] for the measured neutron rate.

The material structure of the ASDEX facility is represented by its vacuum vessel, a quartz window with support, 16 toroidal field coils, the ohmic coils, the central core of 3 different regions, the collimator for exposing and shielding a nuclear emulsion, as well as the glass support of the emulsion. To check for special effects, we also introduced for some calculations certain parts of the divertor, material between toroidal field coils, and the experimental torus hall.

We consider measurements with two different collimators, viewing radially to the plasma, one in front of a large port closed with a quartz window (collimator 1), the other beside a toroidal field coil in front of the vessel (collimator 2).

VINIA-3DAMC software

The software, a strict analogical Monte Carlo, uses the nuclear data bank files in ENDF/B4 format in extenso in order to avoid imparing the precision of avaliable data: no truncation (of Legendre polynomials or tables), no discretization of either energy (no group treatment) or space (no ray effects), both taken as continua. This Monte Carlo follows the neutrons from birth as long as its story is relevant to the problem (absorption, loss or energy threshold) through each "forced" collision as to: position, weight attenuation, nuclide and reaction branch, anisotropic reemission with definite or continuous energy selection. The "flux-at-a-point" method is used with due account at each event (emission/collision) of all probabilistically determined possible contributions. Complimentary to this basic Monte Carlo, is a built-in data extracting software that gathers information pertinent to the specific problem under study.

NEPMC–software

To calculate the response function of the nuclear emulsion, we use a Monte Carlo code taking into account the proton track statistics and the statistical errors of track measurement. Furthermore the real angle of incidence for each neutron is used and thus the effects caused by the large extension of the neutron source for both emitted and collided neutrons are included.

Results

The shape of the collimator 1 defines 3 distinct spatial regions important for interpreting the results: the free aperture (zone 1) defining the observed plasma volume, a "soft edge" of the aperture (zone 2) with shine-through from the neighbourhood of the observed region, and a well-shielded region (zone 3).

The VINIA calculations deliver the spectral neutron flux per emitted neutron arriving at the emulsion, resolved into contributions of emitted and collided neutrons from each of the 3 zones and each of the different structural parts of the ASDEX device. From a calculation with 34,575 emitted neutrons we get the following fluxes (in cm^{-2}):

neutron energy [MeV]		$1.0 < E < 2.1$	$2.1 < E < 3.0$		
flux total		$0.265 \cdot 10^{-8} \pm 15.1\%$	$2.50 \cdot 10^{-8} \pm 2.4\%$	$\hat{=}$	100%
emitted,	zone 1		$1.55 \cdot 10^{-8} \pm 3.0\%$	$\hat{=}$	62.1%
	zone 2		$0.21 \cdot 10^{-8} \pm 6.5\%$	$\hat{=}$	8.4%
	zone 3		$0.551 \cdot 10^{-11} \pm 11.5\%$	$\hat{=}$	0.02%
collided,	zone 1	$0.227 \cdot 10^{-8} \pm 17.3\%$	$0.586 \cdot 10^{-8} \pm 6.3\%$	$\hat{=}$	23.4%
	zone 2	$0.035 \cdot 10^{-8} \pm 19.1\%$	$0.146 \cdot 10^{-8} \pm 12.1\%$	$\hat{=}$	5.8%
	zone 3	$0.002 \cdot 10^{-8} \pm 29.6\%$	$0.004 \cdot 10^{-8} \pm 31.1\%$	$\hat{=}$	0.16%

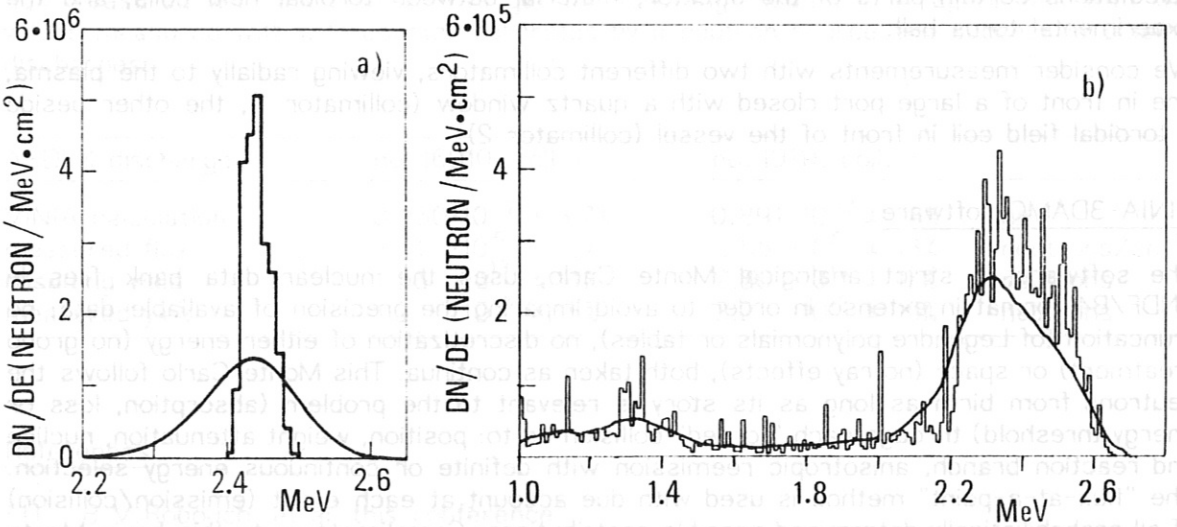

Fig.1: Energy spectra for emitted (a) and collided (b) neutrons from VINIA and NEPMC calculations

Fig.1 shows for collimator 1 the energy spectra for the emitted and collided neutrons (summed over all zones) from the VINIA calculation as well as the expected response of the nuclear emulsion calculated with the NEPMC software. As expected, the spectrum of emitted neutrons is centred at 2.45 MeV, but the spectrum of collided neutrons also substantially contributes to this region.

For nuclear emulsion diagnostics it is only the energy region above 2.1 MeV that is of interest. Here we find in the case of collimator 1 a contribution of 31.8% from the scattered flux. This flux originates in zones 1 and 2. The shine-through of the collimator in zone 2 may be reduced by proper design, but the contribution in zone 1 is unavoidable. The scattered component in zone 1 is mainly produced in the quartz window (73%), the rest coming from the inner wall of the vessel (15%), the window support (7%), the ohmic coils (3%), and the toroidal field coils in the core (2%).

Weighted emission of neutrons

For the VINIA calculations the neutrons are emitted with the radial distribution and the energy spectrum defined by the input parameters. Now, the dominant contributions to the neutron flux at the emulsion are produced in zone1 and here the few collisions in the material between plasma and emulsion are the main source for the collided component.

To adequately fill the distribution for these components, we resort to a weighted emission: half of the neutrons are emitted in front of the considered collimator in a region with centre angle ±10° or ±30°; half of these are emitted into the solid angle defined by a sphere circumscribing the quartz window (collimator 1) or the collimator 2.

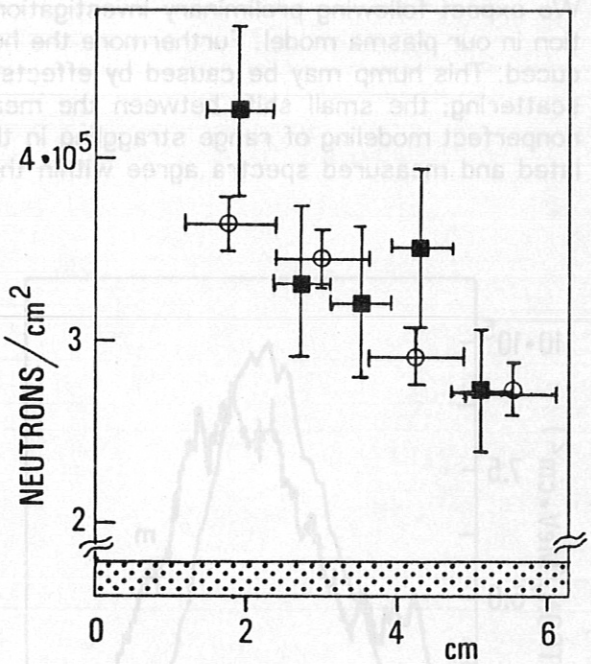

Fig.2: Calculated (o) and measured (■) neutron flux,
horizontal bars: scanning range,
vertical bars: uncertainty

Comparision with measurements

The calculated integral fluxes per emitted neutron are multiplied by the measured total neutron yield (U-counter) to get the neutron fluxes at the emulsion. These are now compared with the fluxes measured by the emulsions for two discharges for which the two different collimators were used.

ASDEX discharge	no. 16910, coll. 1	no. 19111, coll. 2	
neutrons in VINIA	34,575	4,000	
neutron yield	$1.3 \cdot 10^{+13}$ ± 15%	$3.2 \cdot 10^{+13}$ ± 15%	neutrons
VINIA calculation	$0.250 \cdot 10^{-7}$ ± 2.4%	$0.891 \cdot 10^{-7}$ ± 8%	cm^{-2}
resulting flux	$3.25 \cdot 10^{5}$ ± 15%	$2.85 \cdot 10^{6}$ ± 17%	neutrons/cm^2
measured flux	$3.41 \cdot 10^{5}$ ± 13%	$2.55 \cdot 10^{6}$ ± 13%	neutrons/cm^2

Considering that the three values from the U-counter, the VINIA calculation, and the emulsion are completely independent, the agreement is extremely good. This is further demonstrated in Fig.2, where the decrease of the neutron flux along the x-axis of the emulsion is shown for both measured and calculated (5,500 neutrons per point) values. This decrease is due to the reduction of zone 1 as the distance from the plasma increases.

Figs.3 and 4 give the calculated and measured neutron spectra for both ASDEX discharges. For these spectra the scattering angles of the protons are determined from the start and end point of the tracks and scattering angles up to 20° are used; thus the energy resolution is deteriorated compared with the spectra discussed in [2].

The line width tends to be larger for the measured spectra than for the calculated ones. We expect following preliminary investigations, that this is caused by neglecting ion gyration in our plasma model. Furthermore the hump on the low-energy wing is not well reproduced. This hump may be caused by effects in the proton track statistics or by enhanced scattering; the small shift between the measured and calculated spectra may be due to nonperfect modeling of range straggling in the NEPMC software. Nevertheless, the calculated and measured spectra agree within their errors.

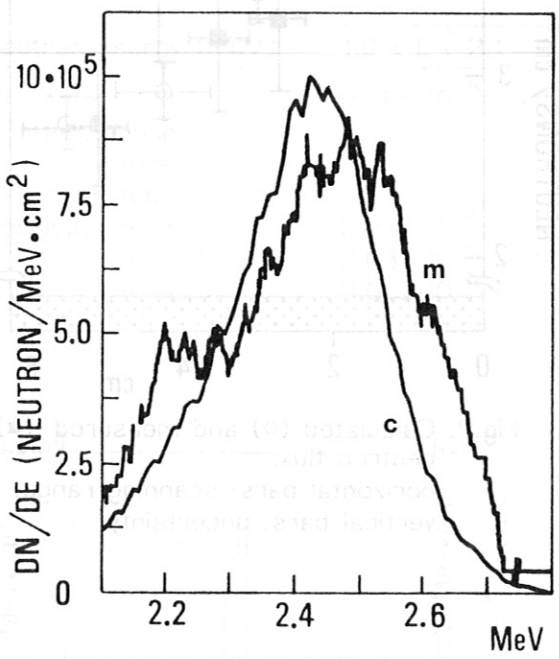

Fig.3: Calculated (c) and measured (m) absolute neutron spectra, discharge no. 16910

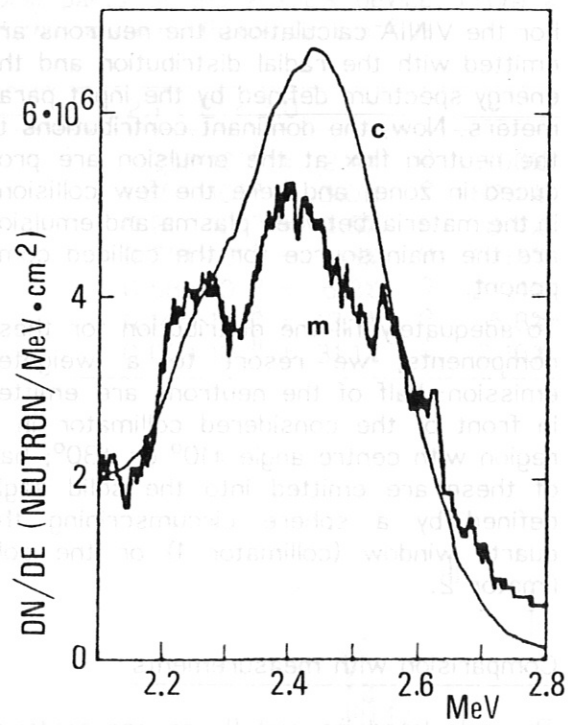

Fig.4: Calculated (c) and measured (m) absolute neutron spectra, discharge no. 19110

References

[1] K. Hübner, et al, 12th Europ. Conf. on Controlled Fusion and Plasma Physics, Budapest 1985, part 1, p. 231-234

[2] K.Hübner, et al, this conference